UNIVERSITY OF SOUTHAMPTON

FACULTY OF ENGINEERING AND THE ENVIRONMENT

National Centre for Advanced Tribology at Southampton (nCATS)

The development of a wear resistance aluminium bronzes (Cu-Al-Fe) coating

by

Pawee Kucita

October 2016

UNIVERSITY OF SOUTHAMPTON

ABSTRACT

FACULTY OF ENGINEERING AND THE ENVIRONMENT

National Centre for Advanced Tribology at Southampton (nCATS)

Thesis for the Degree of Doctor of Philosophy

THE DEVELOPMENT OF A WEAR RESISTANCE ALUMINIUM BRONZE (Cu-Al-Fe) COATING

Pawee Kucita

Aluminium bronze alloys (Cu-Al-Fe) with Al > 14 wt. % are known to have high wear resistance and low friction coefficient against ferrous metals thus making it an ideal material for forming dies application. However, the use of these alloys has been restricted by the high cooling rate required to prevent embrittlement of the alloy during production. The plasma transferred arc technique (PTA) is an attractive production technique that offers the required high cooling rate, however the resulting microstructure is strongly dependent on the composition change induced during deposition. Therefore to optimise the microstructure for application such as forming dies, thorough understanding of the effects of PTA induced composition change on the microstructure, wear and corrosion resistance properties are required. The composition change induced by PTA involves primarily an increase in Fe. Therefore, in the present research four aluminium bronze coatings with 9, 20, 27 and 35 wt. % Fe were produced from a gas atomized Cu-Al-Fe powder by deposition on to an E.N. 10503 steel substrate by PTA. Microstructure characterisation was carried out using complementary techniques involving SEM, EDS, XRD, EBSD and depth-sensing nano-indentation on etched and electro-polished specimen. The results show that Fe content above 9 wt. % leads to a phase change from the Cu_3Al martensitic β_1' to solid solution (Cu) phase. This is also accompanied by an increase in size of the Fe_3Al intermetallic κ_1 phase. The re-distribution of Al solute during cooling was identified as the main factor for the observed phase change. These microstructure changes lead to a hardness increase from 4.9 GPa in the coating with 9 wt. % Fe to 5.6 GPa in the coating with 35 wt. % Fe, however hardness mapping using depth-sensing nano-indentation shows that in the high Fe content coating, the hardness distribution is not uniform. This is due to the large volume fraction of the intermetallic κ_1 phase which has high hardness of ~7 GPa. The wear resistance of the coating was found to be strongly influenced by the Cu-rich matrix phase. In the coatings with 20, 27 and 35 wt.% Fe, delamination and abrasive wear are the dominant wear mechanisms.

SEM observations show that pile-up of slip at the hard intermetallic phase leads to the formation of surface cracks. Coalescence of these cracks coupled with the adhesion between the coating and the ferrous counter material were found to be responsible for promoting delamination wear, which results in high wear rate. The coating with 9 wt.% Fe has the lowest specific wear rates of 2.11-2.87 x 10^{-4} mm^3/Nm against AISI 316, 420 and 440 stainless steel. This is significantly lower than the specific wear rates of 5.95-15.36 x 10^{-4} mm^3/Nm measured for the currently used AISI D2 tool steels at the same condition. This is due to the uniform hardness and retention of the martensitic β_1' phase. The effects of PTA induced microstructure change on the corrosion resistance were investigated by electrochemical and immersion corrosion tests in an aerated 3.5 % NaCI solution. The results show that the corrosion resistance of the coating is strongly dependent on complete formation of Al_2O_3 protective layer. The Al content in the coating is a critical factor in the formation of the protective layer. In the coating with high Fe content where limited Al solutes are available, high corrosion rates of 300-400 x 10^{-3} mm per year were observed. The 9 wt.% coating which contains the highest Al solute, the lowest corrosion rate of 22.5 x 10^{-3} mm per year was measured. This corrosion rate is comparable to the more expensive and highly alloyed nickel aluminium bronze. Based on the results obtained in the present research, the coating with a martensitic β_1' phase and submicron size intermetallic κ_1 phase has the highest wear and corrosion resistance. Such a structure can be achieved by controlling the PTA parameters to minimize the composition change promoted by melting of the steel substrate during deposition. The results from the present research also highlight the importance of interface properties, which have been shown to have a significant influence on properties such as adhesion, wear and corrosion. As more composite materials are utilised, further understanding of the microstructure and properties near the interfaces between materials becomes ever more important. It is hoped that the methodology and results presented in this thesis will provide the initial groundwork for future experimental and modelling work on multiphase material.

Table of Contents

List of Tables

List of Figures

xix

xxiii

DECLARATION OF AUTHORSHIP

I, Pawee Kucita declare that the thesis entitled

THE DEVELOPMENT OF A WEAR RESISTANCE ALUMINIUM BRONZE (Cu-Al-Fe) COATING

and the works presented in the thesis are both my own, and have been generated by me as the result of my own original research. I confirm that:

- this work was done wholly or mainly while in candidature for a research degree at this University;

- where any part of this thesis has previously been submitted for a degree or any other qualification at this University or any other institution, this has been clearly stated;

- where I have consulted the published work of others, this is always clearly attributed;

- where I have quoted from the work of others, the source is always given. With the exception of such quotations, this thesis is entirely my own work;

- I have acknowledged all main sources of help;

- where the thesis is based on work done by myself jointly with others, I have made clear exactly what was done by others and what I have contributed myself;

- parts of this work have been published as: P. Kucita, S.C. Wang. W.S. Li, R.B. Cook and M.J. Starink, Journal of Physics: Conference Series 644 (2015) 012010

Signed:

Date: ………………24/11/2016………………….…..

Acknowledgements

I would like to express my sincere gratitude to my supervisors Prof. Marco J Starink and Dr. Shuncai Wang for their continual support, guidance and patience throughout this research. I would also like to thank Dr. Wensheng Li for his warm welcome and valuable discussions during the visit to Lanzhou and throughout this research.

I would like to thank Dr. T.J. Harvey, Dr. R.B. Cook and Dr. J. Walker for their supports. I would also like to thank my friends and colleagues at Southampton, in particular, Alex Richardson, Timothy Kamp, and Dr. Maria Fabiola Leyva-Mendivil for their support and motivations through the good and tough times. I would also like to thank my family for always being there for me. Lastly, I would like to end this acknowledgement with a speech (in Thai) given by HRH King Bhumibol Adulyadej of Thailand, which motivates me throughout this Phd.

การจะพัฒนาทุกสิ่งทุกอย่างให้เจริญนั้นจะต้องสร้างและเสริมขึ้นจากพื้นฐานเดิมที่มีอยู่ก่อนทั้งสิ้น   ถ้าพื้นฐานไม่ดี หรือคลอนแคลนบกพร่องแล้ว ที่จะเพิ่มเติมเสริมต่อให้เจริญขึ้นไปอีกนั้น ยากนักที่จะทำได้ จึงควรจะเข้าใจให้แจ้ง ชัดว่า นอกจากจะมุ่งสร้างความเจริญแล้ว ยังต้องพยายามรักษาพื้นฐานให้มั่นคง ไม่บกพร่อง พร้อมๆ กันไปด้วย

พระบรมราโชวาทของ พระบาทสมเด็จพระเจ้าอยู่หัวรัชกาลที่ 9 ในพิธีพระราชทานปริญญาบัตรแก่นิสิตจุฬาลงกรณ์ มหาวิทยาลัย ณ จุฬาฯ 10 ก.ค.2523

<div align="center">Translation</div>

Complete understanding of fundamental concepts is critical for a successful development work. A weak foundation and flawed fundamental knowledge are difficult to build upon; therefore it is important to maintaining deep understanding of the fundamental concepts that underline the work at hand while continuously pushing the boundaries of knowledge.

Royal Guidance speech at the graduation ceremony at Chulalongkorn University 10th July 1980

List of Abbreviations

AISI	American Iron and Steel Institute
APS	Atmospheric plasma spraying
CDA	Copper Development Association
CP	Chlorinated Paraffin
CVD	Chemical vapour deposition
D-Gun	Detonation Gun
EBSD	Electron backscattered diffraction
EDS	Energy dispersive X-ray spectroscopy
EIS	Electrochemical Impedance Spectroscopy
HVOF	High velocity oxygen fuel spraying
OCP	Open circuit potential
PVD	Physical vapour deposition
PTA	Plasma transferred arc techniques
REACH	Registration, Evaluation, Authorisation and Restriction of Chemicals
SEM	Scanning electron microscope
SMF	Sheet metal forming
TEM	Transmission electron microscope
XRD	X-ray diffraction

1. Introduction

Wear of components is a significant problem for all industrial sectors. Dimensional loss, corrosion and increase in energy consumption are examples of wear induced problems, which promote premature component failures, increase down time and accidents. The economic cost of wear is significant, in the United Kingdom it is estimated that 1.6% of the country's gross domestic product is lost every year through wear related problems in several industrial sectors such as transport, manufacturing and energy [1]. The manufacturing industry is one of the largest industrial sectors and is responsible for production of a wide range of commodities that are critical to modern society. Within the manufacturing industry, drawing and deep drawing are important sheet metal forming (SMF) processes used for production of high volume components such as cans and automotive parts [2]. In the drawing and deep drawing process, the sheet metal is drawn into the forming dies by a mechanical punch where it plastically deforms and takes the shape of the forming dies.

Wear of forming dies and surface defects on the formed parts are major problems that limit the efficiency of the process. Due to the high contact pressure induced during forming, adhesive wear resulting in transfer of sheet material onto forming die surface often occurs. This leads to severe scratching of the sheet metal, wear of the forming dies and in the worst case jamming of the tooling. This problem is commonly referred to as galling, which can be classified as a severe form of adhesive wear. Galling is particularly severe during the forming of high strength stainless steel and titanium alloys [3]. The forming dies is a high value asset; its value is dependent on the geometrical complexity of the part, some forming dies cost in excess of USD $ 100,000 [4]. The current solution to prevent galling is to employ lubricant containing chlorinated paraffin (CP). The lubricant reacts with the sheet metal and creates a boundary film that prevents contact between the forming dies and the metal sheet [3]. CP contains short and medium chain chloroparaffins, which are suspected to have harmful effects on human health and on the environment [5].

With the introduction of REACH (Registration, Evaluation, Authorisation and Restriction of Chemicals) [6] and increase in environmental concerns from the consumers, the use of such lubricant will be limited in the near future. The lubricants also account for more than 15% [7] of the total cost of SMF process. The cost includes purchasing the lubricant, cleaning lubricated parts after forming and disposal of the waste lubricant. Therefore in the interest of environmental protection and cost saving there is drive towards dry/semi dry SMF process. The current research and development to minimise the environmental impact of SMF and wear of the forming dies can be largely grouped into three main categories [3]: (i) the development of new lubricant, (ii) anti-galling material and (iii) application of surface coatings. The current research is part of category (iii). The feasibility of various ceramics such as zirconia and alumina for dry deep drawing of stainless steel has been investigated [8]. The performance improvements offered by these ceramics were found to be limited to specific types of sheet metal.

Alternative lubricants which are less harmful to the human health are currently being developed [9]. However, disposal of these lubricants still pose significant concerns to the environment as well as incurring additional cost. Furthermore, for some industries such as food processing, sanitary systems and medical systems, the use of lubricant is not permitted due to contamination issues [10]. Surface coating is an attractive solution towards an environmentally friendly wear protection. In the metal cutting process, hard PVD and CVD coatings such as TiN, TiAlN and CrN have been successfully used to provide significant improvement in the wear resistance of the cutting tool [11]. However, the use of such hard coatings for protection of forming dies is limited as the contact between the hard coatings and the soft sheet metal such as austenitic stainless steel, Al, Ni and Ti-based alloy has been reported to result in unstable friction coefficient and galling [12]. Therefore, there exists a need for further coating development to prevent wear of the forming dies.

Aluminium bronzes are copper-based alloys known for their high strength, wear resistance and good sliding properties [13]. The alloys are widely used in applications requiring low friction under compressive load such as bushings and guide plates [14]. Standard aluminium bronzes contain up to 12 wt. % Al and have a hardness of ~ 200 HV [15][16]. This level of hardness has been reported to be insufficient for deep forming dies applications [17]. Cu-Al-Fe alloys with Al >14 wt.% are known to have high hardness in the range of 320-420 HV [17] and high wear resistance [18]. Furthermore, due to the low solubility of Cu in Fe, the tendency for adhesive junctions to form during contact is also low [19]. This makes the Cu-Al-Fe alloy with high Al content an ideal candidate for forming dies material, in particular for forming of Fe-based sheet metal. However, there are manufacturing challenges associated with the production of alloys with high Al content. This is due to the narrow solidification range and eutectoid reaction, which leads to the embrittlement of the alloy [17]. The eutectoid reaction can be suppressed by ensuring high cooling rate during production. However, for complex 3D shape components such as a forming dies, the high cooling rate may not be achievable as cracks may develop due to temperature differences between the outer surface and the core of the material. For this reason, the use of Cu-Al-Fe alloys with high Al content is still limited.

To resolve this problem and to utilize the advantages offered by Cu-Al-Fe alloys with high Al content, deposition of the alloy in the form of surface coating is envisaged as an ideal solution for wear protection of forming dies. However, there are further challenges in development of a wear resistance coating based on Cu-Al-Fe alloys with high Al content. In SMF, the high stresses during service demand coating with high bond strength to avoid failure in service. Aluminium bronze coatings have been successfully produced using several techniques such as ion-plating [20], plasma vapour deposition (PVD) [13] and different forms of plasma spraying [21][22]. However, with these methods, limited bond strength is established between the coating and substrate. Plasma transfer arc (PTA) is another deposition process that is widely used to deposit protective coatings. The technique offers many key advantages that are critical for the deposition of high aluminium bronze alloys such as high cooling rate, minimal thermal distortion to

the formed part and low porosity [23]. More importantly the technique also promotes metallurgical bonding between the coating and the substrate, which is expected to result in significantly higher bond strength compared to other deposition method such as PVD. However, the microstructure and mechanical properties of the coating produced by PTA technique is strongly dependent on the composition change induced by melting of the substrate during deposition. This change in composition is commonly referred to as dilution. The dilution can be controlled by the PTA process parameters such as transferred arc current, powder feed rate and current intensity [24].

In Co-based coating, high dilution has been reported to decrease the hardness of the coating [25]. However, for wear protection of forming dies, it is common to promote high dilution in order to enhance the bond strength even though the mechanical and wear resistance properties may be compromised [26]. Therefore to achieve an optimal solution for adhesion and wear resistance, complete understanding of the effects of dilution on the microstructure and mechanical properties is required. Additionally, deposition of Cu-Al-Fe alloys with high Al content using rapid solidification also involves complex phase transformations that are also of theoretical interests [27]. The high cooling rate can result in formation of martensitic, intermetallic and solid solution phases leading to complex microstructures, which have not been previously investigated. Due to the differences in composition and electrochemical potential of these possible phases, the coating may be prone to galvanic corrosion when subjected to certain corrosion media in service. For this reason, it is also important to understand the effects of the microstructure on the corrosion resistance of the coating.

1.1. Research aims and objectives

The aim of the research presented in this research is to develop a wear resistance coating to protect the forming dies and enable dry/semi dry sheet metal forming operation.

The coating is based on Cu-Al-Fe aluminium bronze alloys with Al >14 wt.% and is produced by deposition on to an E.N. 10503 steel substrate by using plasma transferred arc technique (PTA). The research is collaborative between the University of Southampton and Lanzhou University of Technology, China. The coatings were fabricated at Lanzhou University of Technology during a one-month visit by the author. The objectives of the present research are to study the influence PTA deposition on the microstructure and properties of the PTA aluminium bronze coating, with particular attention to:

- The effects of elevating heat input during PTA deposition on microstructure and hardness of the resulting coating.
- The microstructural influence on the friction and wear characteristics of the coatings under dry sliding conditions.
- The electrochemical corrosion of the coating in 3.5% NaCI solution.

1.2. Novelty of the present research

The majority of the previous research on Cu-Al-Fe aluminium bronze is focused on the microstructure and properties of cast alloys with Al < 12 wt.% and Fe < 5 wt.%. There are few investigations on Cu-Al-Fe aluminium bronze coating, particularly on those with high Fe content. Deposition of aluminium bronze coating using high cooling rate is of theoretical and industrial interest as the high cooling rate can result in non-equilibrium microstructures and novel properties, which have not been previously investigated. A significant portion of previous work on Cu-Al-Fe aluminium bronze is also directed at the effects of Al content. However, there are few investigations detailing in effects of Fe content. Iron is known to have a grain refining effects. The addition of Fe also promotes formation of an intermetallic phase with high hardness that can contribute to the wear resistance of the alloy. Therefore, complete understanding of the role of these intermetallic phases is critical for designing the most wear resistance microstructure. In the present research, the composition of the coatings investigated is on the high Fe and spans across a wide range of Al content as shown in Figure 1.1.
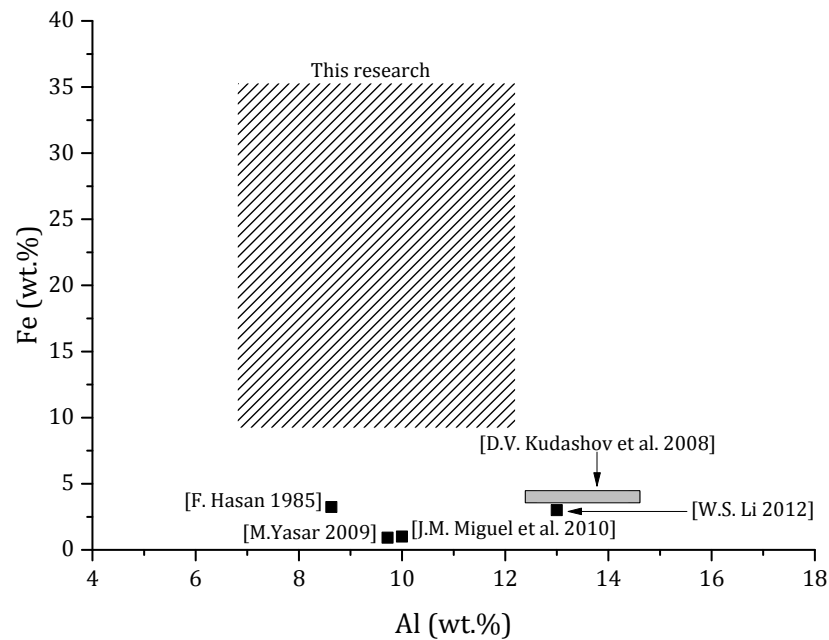
Figure 1.1: The compositions of the coatings investigated in relation to other works on Cu-Al-Fe aluminium bronzes (balance Cu for all compositions shown)

The completion of the objectives will contribute knowledge to the field of surface coatings, dissimilar metal joining and copper alloy development particularly in the following areas;

- Identification and confirmation of the constituent phases in rapidly solidified Cu-Al-Fe alloy with high Fe content.
- The significance of microstructure features, in particular, the intermetallic phase on the dry sliding friction and wear characteristics of Cu-Al-Fe aluminium bronze coatings produced by rapid solidification technique.
- Evaluation of the benefits of and effects of high Fe content (above solubility limit of Fe in Cu) on the electrochemical corrosion characteristics.
- Characterisation of the interface microstructure and hardness between Cu-Al-Fe alloy and Fe-based substrate.
- Optimization of the microstructure for improved wear resistance.

2.   Literature review

2.1   Sheet metal forming processes: Current practice and recent developments

Sheet metal forming (SMF) is an important group of industrial processes. It is used in many industries to produce component with complex 3D shapes by controlled plastic deformation of flat sheet metal using tools or dies. There are several techniques in SMF. These include drawing, stretching, bending, rolling and stamping. The usage of these processes is dependent on the geometrical requirement of the parts being formed. Amongst the SMF processes, deep drawing is one of the most widely used SMF process in the automotive industry to manufacture car body parts [28]. The other products that are commonly produced using drawing process include cans, sinks and drums for washing machines. The majority of these products are produced in large quantities, for example, it is estimated that the world produced 400 billion cans per annum [3]. Due to the industrial importance of drawing and deep drawing, these two processes are the main focus of the present research. Mass production requires continuous operation at maximum efficiency to meet the demand. In drawing and deep drawing, the efficiency of the process is governed by the operational limits of the forming dies. Faster production speed is accompanied by increase mechanical and thermal loading on the forming dies, resulting in higher wear and reduced service life of the dies. Therefore, to meet the increasing production target, there exists a need to increase wear resistance of the forming dies. This is the aim of the present research. In this section, the fundamentals of drawing process will be introduced. The current problems and wear mechanism of drawing process will be discussed. The section ends with a review of recent and on-going solutions for wear protection of forming dies.

2.1.1   Drawing and deep drawing processes

The three main steps of the drawing process are illustrated in Figure 2.1. In the first stage, the sheet metal is vertically constrained at both edges using the pressure ring (see Figure 2.1 left). In the deep drawing process, the sheet metal is vertically and horizontally constrained at both edges and is not allowed to slide. The term deep drawing is used when the depth of the parts formed exceeds its diameter. In the second stage, the central portion of the sheet metal is mechanically pressed into the die opening where it is plastically deformed and takes the shape of the forming dies [29] (see Figure 2.1). The conditions at the contact between the die and the work piece are severe. For deep drawing process, the typical contact pressure is $\sim$ 800 MPa and relatively velocity of $\sim$ 200 mm s^{-1} [3]. Higher wear rates are expected in the region near the die and pressure ring (highlighted by the black box in Figure 2.1), this due to the high contact pressure and the relative movement generated by the bending and unbending of the sheet metal [30]. The large contact pressure and pure sliding friction leads to high temperature on the sheet metal as shown in Figure 2.2. Furthermore, insufficient heat dissipation, faster production speed and forming of high strength materials can also promote high temperature on the surface of the forming dies and the sheet metal during processing. In the final stage, the formed sheet metal is removed and the process is repeated for a new sheet. This makes drawing process an "open tribological system" where the forming dies is in contact with fresh sheet metal surface at the beginning of each forming cycle. Consequently, the wear processes involved are non-steady wear, which results in highly stochastic wear rates. This makes the Archard model [31] for adhesive wear (see Equation 2.2 in section 2.1.2) not applicable for predicting wear in drawing processes [32].
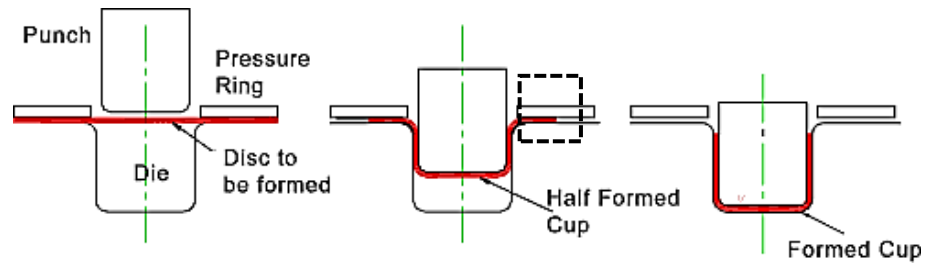
Figure 2.1: Schematic showing a typical drawing process, dotted black box highlights region of maximum contact pressure and highest wear rate (adapted from [33])
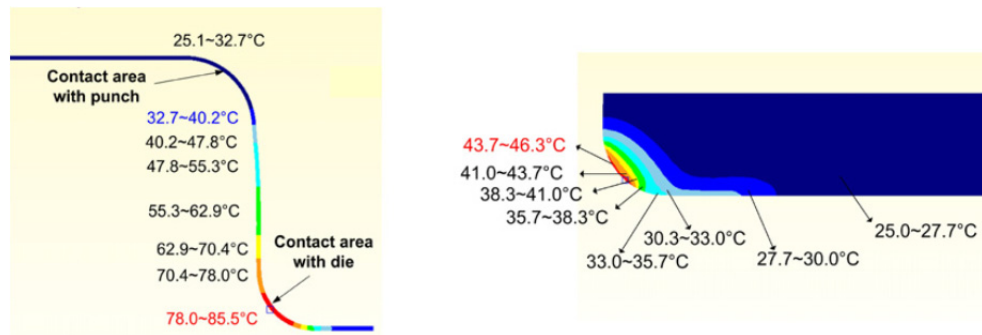
Figure 2.2: Typical temperature distribution in the stainless steel sheet material (left) and drawing dies (right) during lubricated deep-drawing process [34]

High carbon Fe-C alloys such as AlSI D2 and AlSI A2 are currently the most widely used materials for drawing dies [8][35][34][29]. These alloys typically contain 0.6-1.4 wt. % C with Cr, V, W and Mo as other alloying elements. These alloying elements combined with C to form hard, wear-resistance carbides such as WC, $Cr_{23}C_6$. This gives the alloy strength and hardness, but low ductility [36]. To prevent adhesion and build-up of transfer layers on the forming dies, liquid lubricant is essential to the drawing process, particularly for forming complex shapes and for certain materials such as stainless steel and titanium alloys [3]. Lubricant is normally applied to the sheet metal prior to pressing by the punch where it is retained in the sheet metal holder and the punch-rounding region (see Figure 2.1). The lubricant chemically and/or physically bonded to the surface of the forming dies and the sheet metal [28]. The lubricant works by reacting with the metal and creating a boundary film, which prevents contact between the forming dies and the sheet metal as well as providing low shear strength layers that reduce friction and wear [3].

The lubricant also reduces the interfacial temperature between forming dies and sheet metal. Introduced in the 1930s, chlorinated paraffin (CP) is a lubricant additive for cutting fluids and metalworking. CPs is classified as polychlorinated alkanes with general formula $C_xH_{(2x+2)-y}CI_y$ (where x represents the number of C and y represents the number of CI). Short chain CPs are used for extreme pressure additives in metal working fluid such as that used in drawing process [37]. However, CPs are toxic to human and the environment. The United Nations Environmental Program (UNEP) listed short chain CPs as toxic in 2003, while the International Agency for Research on Cancer (IARC) listed it as a possible carcinogenic to humans. CPs are also classified by the International Maritime Organization (IMO) as severe marine pollutant [37]. In the European Union, introduction of new regulations such as Registration, Evaluation, Authorisation and Restriction of Chemicals (REACH), will limit the use of CPs in the near future [6]. Furthermore, when lubrication is insufficient the currently used AISI D2 tool steel is known to suffer from severe failure characterised by the transfer of sheet metal onto the forming dies surface and severe scratching of the sheet metal [38]. This problem is commonly known as galling, which is generally accepted as a severe form of adhesive wear. This leads to high and fluctuating friction coefficient, accelerated wear of the forming dies and surface defects on the sheet metal. Therefore, there is a need to reduce the reliance on CP based oil in drawing process. Dry/semi-dry drawings are environmentally friendly solutions, however it is difficult to achieve without advanced tribological design of the forming dies. Tribological aspects of drawing and deep drawing processes without the use of lubricant are discussed in the next section.

2.1.2 Tribology of drawing and deep drawing without the use of lubricant

Tribology is the term that encompasses the science of friction, wear and lubrication. The term was first introduced in 1964 by David Tabor and Peter Jost who recognised the problems associated with increasing friction in machinery [39]. Due to the multidisciplinary nature of a tribological problem, it is common to introduce the concept of a tribological system.

In drawing and deep drawing processes where lubricant is not present, the tribological system consists of the forming dies in contact with the sheet metal surrounded by humid air as shown schematically in Figure 2.3. Application of tangential force leads to relative movement between the two solids. The combinations of the normal and tangential forces lead to friction and wear of the surfaces due to:

- The interlocking of the asperities (unevenness of the surface). This can lead to resistance against relative movement (friction) or deformation of the asperities.
- Elastic/plastic deformation of the asperities, which upon contact can modify the topography of the surface and may change its load carrying capacity in a case where work hardening took place.
- The hardness difference between the two solids, one solid may penetrate into the other leading to ploughing and transfer of materials (wear).
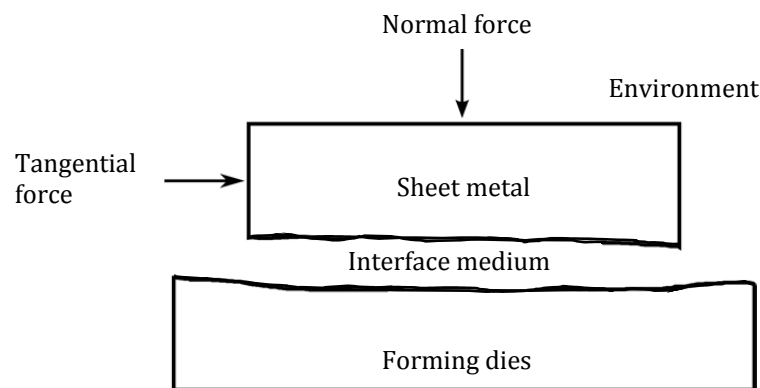
Figure 2.3: Schematic showing the unlubricated drawing and deep drawing tribological system

Friction in drawing and deep drawing processes

Friction coefficient between the forming dies and the sheet metal controls the plastic flow of the sheet metal during forming and thus influences the quality of the formed product as well as wear of the forming dies [40]. Although low friction coefficient reduces the energy required during each forming cycle, ultra-low friction coefficient leads to handling problems associated with slipping of the sheet metal as well as wrinkles on the formed product.

In contrary, high friction coefficient leads to cracks of the formed part. In general, a stable friction coefficient is required during forming. Friction may be defined as the "resistance encountered by a body as it moves tangentially over another material in which it is in contact" [41]. It is normally expressed in terms of the ratio between the tangential F_t and normal force F_n as shown in Equation 2.1.

$$\mu = \frac{F_t}{F_n}$$ Equation 2.1

In the absence of lubricating liquid, there are two main factors that contribute to friction: (i) the adhesion between the solids and (ii) deformation of the solid surface [42]. Under the applied load, only the asperities of the solids are in contact, therefore the real area of contact is substantially smaller than the geometric area. Consequently, the pressure at these locations is also higher than the nominal value. This can lead to localize plastic deformation and formation of junctions. To sustain or enable relative motion, shearing of these junctions is necessary. The tangential force required contributes to the adhesive friction force. The presence of oxide films or local melting of the surface due to frictional heating can influence the strength of the junction and thus on the friction force due to adhesion. Deformation of the surface is another main contribution to friction. This is due to the macroscopic interaction at the asperities on the two surfaces. Under normal load, the differences in hardness between the two materials can lead to penetration of the harder material into the softer material. During sliding the ploughing action plastically deforms the softer material. The force required for this to occur contributes to the deformation friction force. In addition, the deformation of the asperities also increase the real contact area, resulting in an increase in friction [43]. The other possible situation leading to deformation friction is when hard materials become entrained between the two surfaces and damaging the softer surface. Therefore, optimizing the hardness and roughness of the surface can reduce friction.

Wear mechanism during sheet metal forming process

The degradation of material can take place in several ways as shown in Figure 2.4. Surface deterioration as a result of wear accounts for a significant portion of material degradation. Wear may be defined as a "progressive loss or displacement of material as a result of relative motion between the surfaces or a surface of another substance" [44]. In SMF processes, the dominant wear mechanisms are adhesive and wear and abrasive wear. In the next sections, these mechanisms will be discussed.
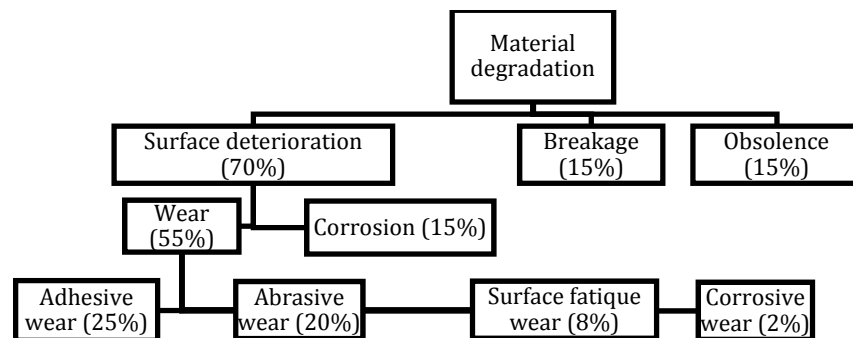
Figure 2.4: Sources of material degradation (the percentage shown is an estimate of the economic importance of each source of deterioration) [45]

A schematic showing the solid surface is shown in Figure 2.5 . The surface of a solid plays a critical role in dictating the friction and wear during sliding. The mechanical properties of the surface can differ from those in the bulk. This is due to the disruption to the symmetry of the atomic structure and the influence of the environment.   The applied load and temperature can also cause considerable changes to the surface and creates concentration of elements, which can be very different to the bulk concentration. This can influence the attractive forces between the two surfaces.
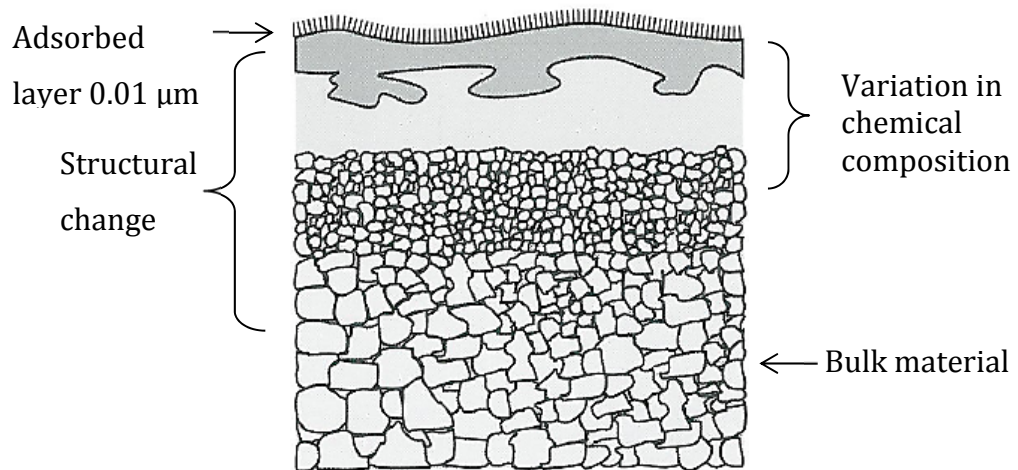
Figure 2.5: Schematic of a solid surface (adapted from [46])

Attractive forces exist between the atoms on the surface of two materials. Upon contact, these forces promote the tendency in which the surfaces will adhere together to form a junction. For relative motion to occur, these junctions must be broken. This can occur at the junction or within one of the materials as shown in Figure 2.6.
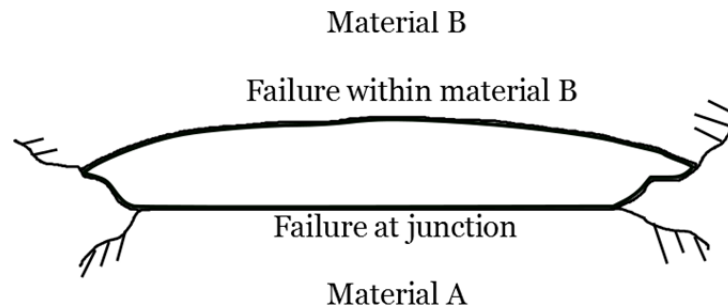
Figure 2.6: Schematic showing possible failure mode during shearing of a junction between two solids

Failure will occur at the junction if the shear strength of the junction is weak compared with the cohesive strength of both materials. This type of failure typically results in negligible wear on both solids. In other cases, where the shear strength of the junction is strong, failure will occur in the weakest material, which leads to formation of a fragment. The fragment can be transferred to the harder material or it can be detached as loose debris.

Failure under this situation is known as adhesive wear and can be modelled using Archard's equation [31] that relates the volume loss to the hardness of the softer material and the normal load as shown in Equation 2.2.

$$Q = K_{ad} \frac{W}{H}$$
<div align="right">Equation 2.2</div>

Where, Q is the volume loss produced per unit sliding distance, W is the load in Newton, H is the hardness of the softer material and K_{ad} is the empirical wear coefficient to account for the fact that not all asperities will be able to produced wear particle. The typical value of K_{ad} is << 1.

Galling is a severe forms of adhesive wear. The ASTM G40 standard defined galling as "a form of surface damage arising between sliding solids, distinguished by macroscopic, usually localized roughening and creation of protrusion above the original surface; it often includes material transfer, plastic flow or both" [44]. Budinski [10] noted that this definition of galling does not include the role of adhesion or solid state bonding between the two surfaces, which have been noted by several authors to have a fundamental role in the initiation of galling. Additionally, some materials do not exhibit localized roughening even after substantial amount of material transfer takes place [32]. Based on the standard definition and review of previous works, galling mechanism may be divided into three main stages (as shown in Figure 2.7). Strong adhesion between the sheet metal surface and the forming dies is a major factor required to initiate galling [47]. Additionally, other factors such as poor fitting, miss-alignment, insufficient lubrication, surface roughness of the forming dies [29] and frictional heating [48] have also been reported to induce galling. The initial stage of galling may be characterized by the bonding between the two surfaces as shown in Figure 2.7 a.
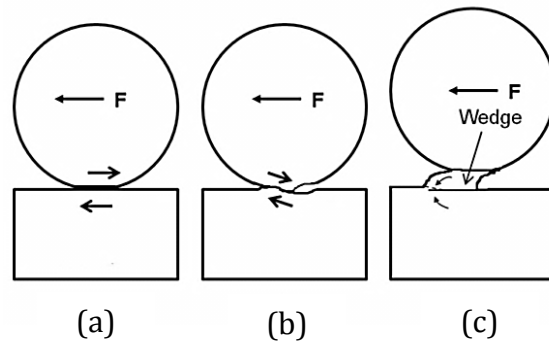
Figure 2.7: The three main stages of galling: (a) initiation, (b) wedge formation and (c) wedge detachment [47]

In the second stage of galling, the bond between the two surfaces is broken as a result of the shear force induced by the relative motion. The bond breaks within the bulk of one material (typically the sheet metal) as shown in Figure 2.6, leading to material transfer. Note that the adhesive wear theory discussed previously doesn't account for the subsurface damage that is expected to take place during sliding. The theory also doesn't account for the deformation of the material during sliding. The delamination theory of wear [49] postulate that stresses induced during sliding leads to pile-up of dislocation at a finite distance from the surface, leading to formation of voids. Void formation is enhanced if the material contains hard secondary phase in which dislocation can pile-up against. Formation of the void is due to plastic flow of the matrix material around the hard particle. As the sliding progresses, coalescence of these voids can occur by growth or by shearing, leading to cracks parallel to the wear surface as shown in Figure 2.8. When the crack reaches a critical length the surface will shear. This results in sheet-like particles, which due to adhesion can be transferred to the counter material.
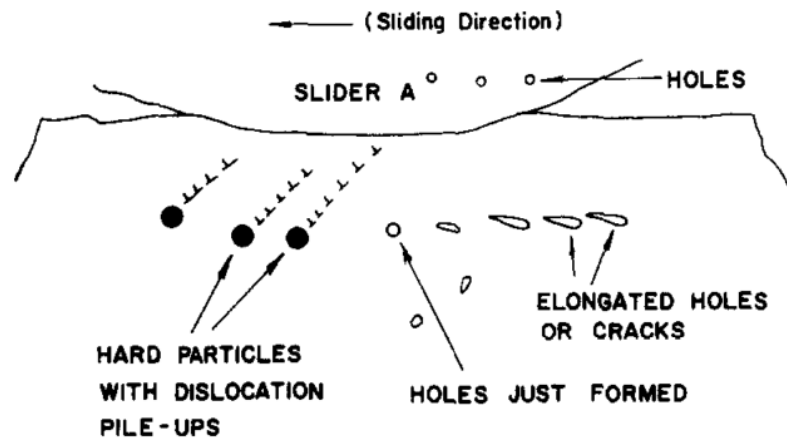
Figure 2.8: Schematic showing the wear particle formation by shear deformation of voids [49]

At the beginning of the third stage of galling, the wedge of transferred material is formed as shown in Figure 2.7 c. The size of the wedge increases with sliding distance, which leads to separation of the two surfaces. Finally, the wedge reaches a critical size and shape where it breaks off and caused damage to the sheet metal by abrasive wear. Abrasive wear is caused by ploughing action on the soft surface by hard asperities or by hard particles trapped between the contacts. The former is often referred to as two-body wear, while the latter is known as three-body wear.

2.1.3   Existing solutions and current research on galling problem

Several solutions have been proposed to alleviate the effects of galling without the use of CP-based oil. These solutions can be largely classified into four main groups; (i) development of alternative lubricant, (ii) development of new tool materials, (iii) surface modifications and (iv) surface coatings as shown in Table 2.1. As part of the global drive to reduce the use of toxic lubricant such as CP-based oils, the recent developments tend towards the use of solid lubricants. Less toxic liquid lubricant based on boric acid also exhibits some promising properties. Boric acid has been reported to adhered strongly with an aluminium surface and provides an ultra-low friction coefficient of 0.04 [50]. The low friction coefficient is due to the layered structure of the of the boric acid [51].

Wurong et al. [52] compared the severity of galling of tool steel that has been treated by plasma nitriding and thermal diffusion in a wear test against galvanised high strength steel. Their results show that the nitriding treatment can reduce the initiation of galling due to the formation of complex Fe_3N and Fe_4N phase. However, significant delamination of the zinc from the sheet metal was also observed. Several coating systems have been examined for reducing galling. DLC coatings have been investigated by several authors [53] [54] [55] [56] using both laboratory and field testing. The tests show promising results for reducing galling during forming of zinc coated steel, stainless steel and high strength stainless steel. Teisuku et al. [56] compared the performance of DLC coating against MoB-based cermet and cermet carbide forming dies during the forming of Al sheets using CP-based and non-CP-based oil. Their results show that DLC coatings were able to prevent galling as indicated by a low surface roughness of the specimen even when non-CP base oil was used.

However, the anti-galling performance of both cermet-based materials only holds when the CP-based oil is used. Taube [7] evaluated the performance of different carbon-based coatings and concluded that for forming aluminium sheets, DLC coating exhibits the best anti-galling properties. However, DLC coatings have also been reported to delaminate high load due to insufficient adhesion [57]. Additionally the low heat resistance of DLC also limits its use for forming at elevated temperature [3]. The anti-galling performance and wear resistance of TiN, VN and TiAlN have been investigated by several authors. Daodon et al. [58], evaluated the anti-galling behaviour of TiN and VN coating during wear test against 1050 aluminium alloy. Their results showed that the TiN has lower amount of material transfer compared with the VN coating. Zirconium carbide coated forming dies have also been investigated [59], the results show that galling can be reduced by using biodegradable lubricant instead of CP-based oil. Other coating systems such as CrN have also been investigated. CrN is known for its high thermal stability, wear and corrosion resistant, however it has also been reported to have high friction and high surface roughness when sliding against zinc-coated steel [60].

Adamus et al. [61] investigated the performance of different coatings on forming of titanium sheet by using strip drawing test. Four coatings were investigated, these include: TiN and Cr overlaid by electrolytic method, aluminium bronze coating overlaid by surface welding, single layer Cr/CrN and Cr/CrN-(a-C:H) multi-layer coating. Their results show that the multi-layer Cr/CrN-(a-C:H) and aluminium bronze overlaid coatings were found to be effective at preventing adhesive wear in titanium sheet forming. However, the multi-layer Cr/CrN-(a-C:H) suffered from void formation during deposition and poor adhesion to substrate, which leads to delamination and crack initiation. The aluminium bronze coating was found to be intact during the test. Based on the review of the literature, two main issues are clear: (i) the anti-galling performance of the coating is strongly dependent on the type of sheet metal. This issue was also highlighted by Podgornik et al. [62] who also proposed a methodology for selection of coating to improve galling performance. Their results suggested that carbon based coatings such as DLC provide the best protection against material transfer during forming of stainless steel, while nitride based coatings such as TiN are best suited for forming of aluminium and titanium alloys. (ii) It appears that PVD and CVD based coatings do not have adequate adhesion for sheet metal forming application. This might require further development or change in the deposition technique to improve adhesion and avoid delamination failure. In section 2.2, the different deposition techniques and the bonding mechanisms are reviewed

Table 2.1: Summary of existing and recent development on wear protection of forming dies
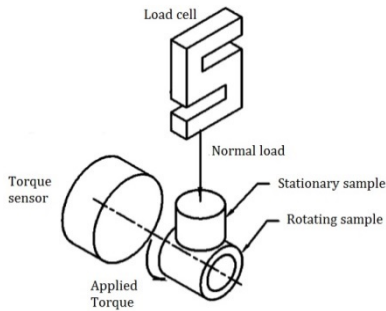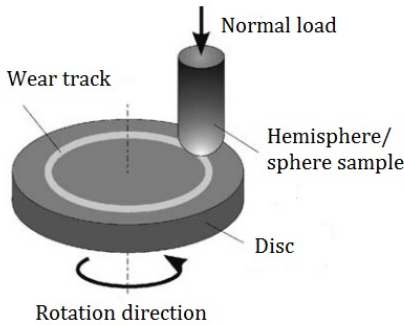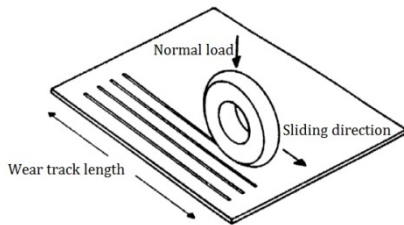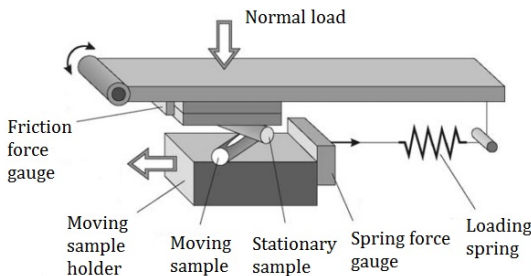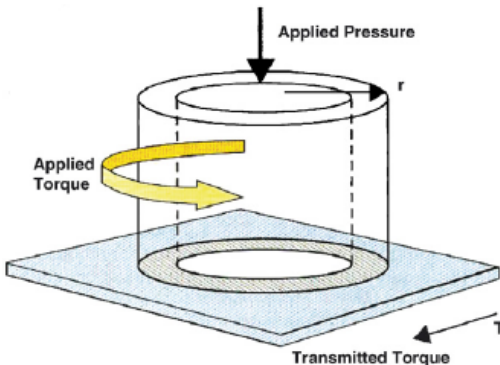
Solutions	
Alternative lubricant system	1. Dry-film lubricant system[63] [64] [65] 2. Boric acid [9] 3. Formation of oxide layers through electrochemical treatment [66]
Development of alternative tool materials	1. Powder metallurgical nitrogen alloyed tool steel [67] 2. High speed tool steel (Z85WD06) [68] 3. Non-metallic materials such as engineering plastics and laminated wood [69] 4. Technical ceramics such as Al_2O_3, ZrO_2 and Si_3N_4 [8]
Surface coatings	1. WC-Co [70][71] 2. TiN and TiAlN [72][73] 3. DLC [74] 4. Polymer based coating [75]
Surface modification	1. Macro and micro structured tools [76][77] 2. Surface texturing [78]

2.1.4   Tribological tests used to simulate drawing process

Full scale simulations of deep drawing processes have been used to test new materials [8][59][70], however it requires complex set up and is not economical, therefore laboratory tests are performed. One of the most widely used test to evaluate the galling resistance of a material is the ASTM G98-91 button-on-block test [79]. In this method, the end of the cylindrical button is loaded against flat block. The button is rotated one revolution before it is removed for visual inspection for evidence of galling. This method relies on large number of samples and the galling criteria are based solely on visual inspection. To overcome these draw backs other test methods have been developed, these are shown in Table 2.2. In addition, other test procedures such as strip drawing tests [35] and pin-on-flat [80] are also employed. The button-on-cylinder, pin-on-disc and twist compression have the advantages of being simple and are readily available. However, they require large number of samples to complete all the load range and thus are time consuming.

The load scanning test allows the load range expected in service to be simulated in one single test run [81], this reduces the time and samples required, however the instrument is complex and not widely available. The slider-on-flat system is the only system that can simulate an open tribological system such as those found in service. The slider-on-sheet system is highly specialized, requires large sample to operate and due to its availability, comparison of results between laboratories is limited. During galling test, parameters such as specimen temperature and friction coefficient are continuously monitored and later evaluated for onsets of galling. One of the threshold for galling is a sudden rise in friction coefficient [82]. In [81] a coefficient of friction of 0.5 was used as a threshold for galling, this value was based on microscopic observations of the surface at different friction level. An increase in temperature can also be associated with the onset of galling. The temperature rise can lead to break down of low shear strength layer (solid or liquid) that separate the two surfaces, leading to formation of wedge and galling [48].

Table 2.2: Test methods used to simulate sheet metal forming processes

Method	Principle	Reference
Button-on-cylinder		[83]
Pin-on-disk		[81]
Slider-on-sheet		[48] [47]
Load-scanning test		[81]
Twist compression test		[34] [84]

2.2   Surface engineering solutions for SMF process and their limitations

Surface coating is a surface engineering method where the coating material is deposited onto the base material known as the substrate or by reactions involving the substrate material and the coating material. In addition to enhancing the surface properties, surface coatings also enable specific properties to be allocated where they are most needed [85]. The substrate material can be selected to provide toughness, while the coating can be responsible for resistance against wear, corrosion, thermal load or to achieve the required friction characteristics [86]. The design and selection of surface engineering solutions for a given combination of operating conditions are challenging. As discussed in section 2.1.3, a range of surface engineering solutions for SMF have been proposed, each with their own advantages and limitations. The main limitation highlighted by review of existing solutions is inadequate bond strength between the coating and the substrate. The bond strength between the coating and the substrate is an important parameter that controls the performance and quality of the coating. The bond strength is influenced by several factors such as the chemistry of the coating, characteristics of interface zone, the microstructure and most importantly the deposition technique [87]. The deposition technique strongly influences the type of bonding mechanism between the coating and the substrate. The coating can be bonded to the substrate by several mechanisms such as mechanical, chemical and electrostatic bonding. Additionally some deposition processes also promote diffusion. In this section, the bond strength of different types of deposition techniques are discussed with reference to the deposition parameters.

2.2.1   Surface coating deposition techniques

Surface coatings can be deposited using many techniques. These techniques can be divided into four main categories depending on the state of the material being deposited as shown in Figure 2.9. For wear resistance application, thin films produced from gaseous state process are frequently employed. This section focuses on the advantages and limitations of gaseous state and molten/semi-molten state deposition.
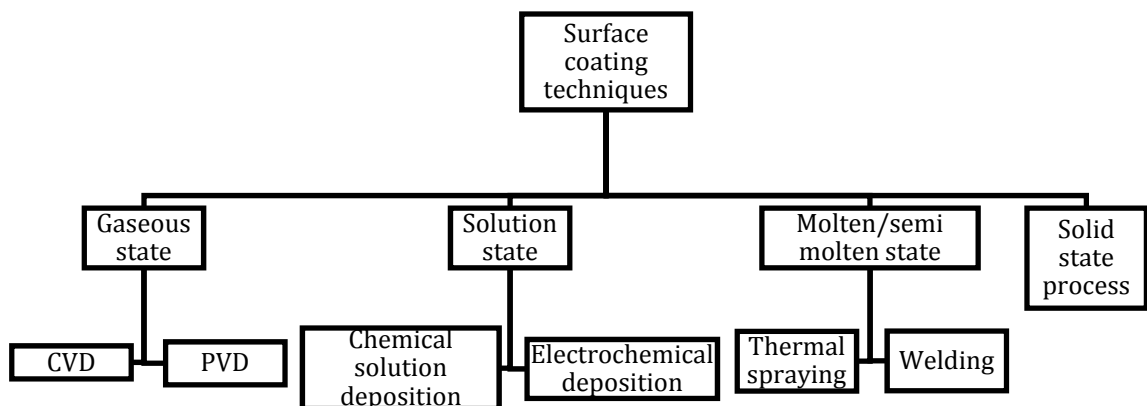
Figure 2.9: Surface coating deposition techniques (adapted from [86])

2.2.2   Gaseous state deposition

Chemical Vapour Deposition (CVD) and Physical Vapour Deposition (PVD) are commonly used gaseous state deposition techniques. In CVD process, the material to be deposited is formed by chemical reactions between one or more gaseous species in the vicinity of the substrate. Variants of CVD processes differ by methods in which the energy for the chemical reaction is supplied. For conventional CVD, the energy is often supplied in the form of hot filament or laser. This results in deposition temperature between 500 °C - 1500 °C [4][46]. The typical thickness of the coating ranges from 0.1-10 μm. The main advantage of CVD is the ability to coat deep holes and complex geometry as it is not a line-of-sight process. The main disadvantage of the CVD process is the high deposition temperature, which can lead to dimensional changes and effects existing heat treatment.

In the PVD process, the material to be deposited is condense into vapour under reduced pressure and is later transferred to the substrate material. Reactive gases can be introduced into the chamber to form compounds. The typical deposition temperature is in the range of 200 °C - 500 °C [46] at an operating pressure of 0.1-1 Pa [88]. The typical coating thickness is ∼ 10 µm. The main advantage of PVD compared with CVD process is the low deposition temperature. This reduces the risk of dimensional changes and effects on the mechanical property of the substrate. In addition, localized coating is also possible by masking. CVDs and PVDs are commonly used to deposit hard coatings such as diamond like carbon (DLC) and carbides. For both processes, chemical bonding is the primary bonding mechanism. The adhesion of hard thin coatings such as those produced by PVD and CVD is typically measured by scratch testing. During the scratch test, a spherical indenter tip slides over the surface of the coating at a constant or incremental load. After each scratch, the surface is examined for signs of failures such as cracking and delamination. The load at which the coating fails is defined as the critical load L_c. It is worth noting that the L_c is also dependent on several other parameters such as: substrate hardness and roughness, coating hardness and roughness, friction coefficient between the indenter and the coating as well as the internal stress of the coating [89]. The typical *Lc* value for some PVD and CVD coatings are given in Table 2.3.

Table 2.3: Adhesion force measured by scratch testing of selected CVD and PVD coatings

Coating	Deposition method	Thickness	L_c	Reference
Silicon containing DLC	CVD	2 ± 1 µm	30-33 N	[90]
AlCrN	PVD	3 ± 0.2 µm	55 N	[91]
DLC	CVD	0.1,0.3 and 0.5 µm	75,175,235 mN	[92]
DLC	CVD	4 µm	4-6 N	[93]

2.2.3   **Thermal spraying**

Thermal spraying is a group of processes in which metallic, ceramic, cermet and polymeric materials in the form of powders, wires, or rods are fed into a torch/gun where they are heated to a temperature near or above their melting point. The resulting molten/semi-molten droplets of materials are then accelerated in a gas stream and projected towards the substrate [94]. The different types of thermal spraying processes are shown in Figure 2.10 together with typical deposition parameters in Table 2.4.
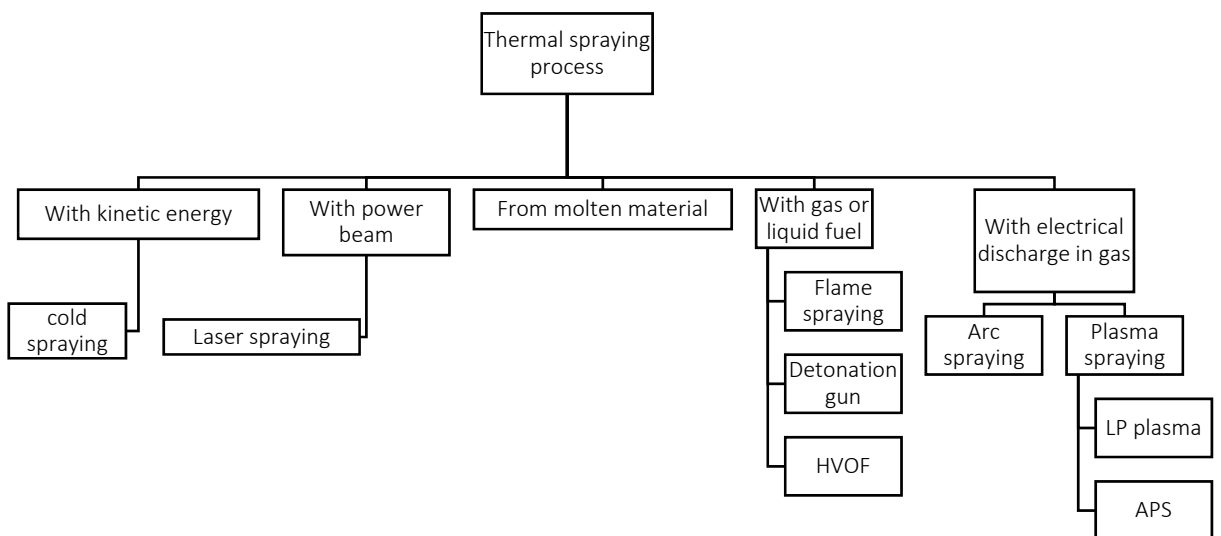
Figure 2.10: Schematic showing classification of thermal spraying techniques by energy source (adapted from [87])

Table 2.4: Typical process parameters for thermal spraying process [95]

Thermal spraying process		Flame spraying (powder)	Electric arc/wire	Plasma /APS	D-GUN	HVOF	LP plasma
Process parameters	Flame/Gas temperature (x 10^3°C)	2.2-3.2	4-5.5	5.5-15	3-4	2.5-3.1	6-15
	Droplet velocity (m/s)	30-100	30-240	150-400	500-910	400-900	200-700
Materials that can be sprayed	Metals	✓	✓	✓	✓	✓	✓
	Ceramics	✓	x	✓	✓	✓	N/A
	Nitrides and carbides	x	x	✓	✓	✓	✓
	Cermets	x	x	✓	✓	✓	✓

Due to the heat input and cooling rates achieved during the deposition process, the composition and structure of the coating can be significantly different from the precursor material. Hence, the microstructure and properties of the coating can be extremely diverse. In thermal spraying processes, metallurgical bonding is the main mechanism. Increasing the flame temperature and droplet velocity leads to an increase in the bond strength and reduction in porosity of the coating shown in Table 2.5. The adhesion of thermal sprayed coating is measured by standard method such as ASTM C633-01 (2008) [96] [97]. Note that the maximum adhesion measureable by ASTM C633 method is limited by the adhesive strength of the bonding agent used. For the data shown in Table 2.5, an epoxy resin was used, hence the results are limited to the strength of the epoxy which is ~ 70 MPa [97]. However, the adhesion of plasma spraying, D-Gun and HVOF can exceed value as indicated in Table 2.5. Compared to the adhesion of the CVD and PVD coatings (c.f. Table 2.3) the adhesion of the thermal spraying process is significantly higher.

Table 2.5: Typical adhesion and porosity of thermal sprayed coating [95]

Thermal spraying process		Flame spraying (powder)	Electric arc/wires	Plasma/ APS	D- GUN	HVOF	LP plasma
Coating properties	Adhesion (MPa)	7-15	10-20	20-70	>70	>70	20-70
	Adhesion* (x 10^3 N)	3.5-7.6	5.1-10.1	10.1-35.5	>35.5	>35.5	>35.5
	Porosity (%)	8-20	6-15	1-10	< 0.5	<1	<1

*based on standard specimen diameter of 25.4 mm

2.2.4   Plasma transferred arc deposition technique (PTA)

Plasma transferred arc deposition (PTA) of powders was developed as a modification to the plasma arc welding method. The technology is based on the same principle as traditional welding techniques such as oxygen fuel and gas welding. The technique falls under the molten/semi molten category as shown in Figure 2.9. During PTA deposition a non-transferred arc is initiated between a tungsten cathode and a water-cooled copper anode by a low current. An inert gas, typically argon, is passed through the cathode and the anode via the inner annulus. The gas is ionised and forms a plasma arc column that is then transferred to the work piece via an orifice and completes the DC circuit (see Figure 2.11). The temperature of the plasma can reach 20,000-30,000 °C [98][99][46][25], which allows a wide range of materials to be deposited. The powder precursor materials are transported within the PTA gun and exit via the orifice into the collimated plasma at a set distance from the substrate and subsequently into the molten pool that forms on the surface of the substrate. A metallurgical bond [100] is formed between the coating and the substrate.

Additionally, PTA also offers low thermal distortion to the substrate, high deposition speed and minimal release of ultra-fine powders into the environment. Consequently PTA is a widely used deposition technique for deposition of protective coating such as Stellite [101], boron-based coating [102] and Fe-based coating [103]. The technique has also been used to deposit Ti-based composite coatings with self-lubricating properties [104][105]. PTA is also commonly used for deposition of wear resistance coating for moulds and forming dies [26]. Due to the metallurgical bonding formed during PTA deposition, the bond strength achieved is extremely high and is comparable to the tensile strength of the weakest material. Su et al. [106] used PTA for restoration of Ni-based super alloy, their results show that the tensile strength of the joint is 96 % of the nominal tensile strength of the base material.
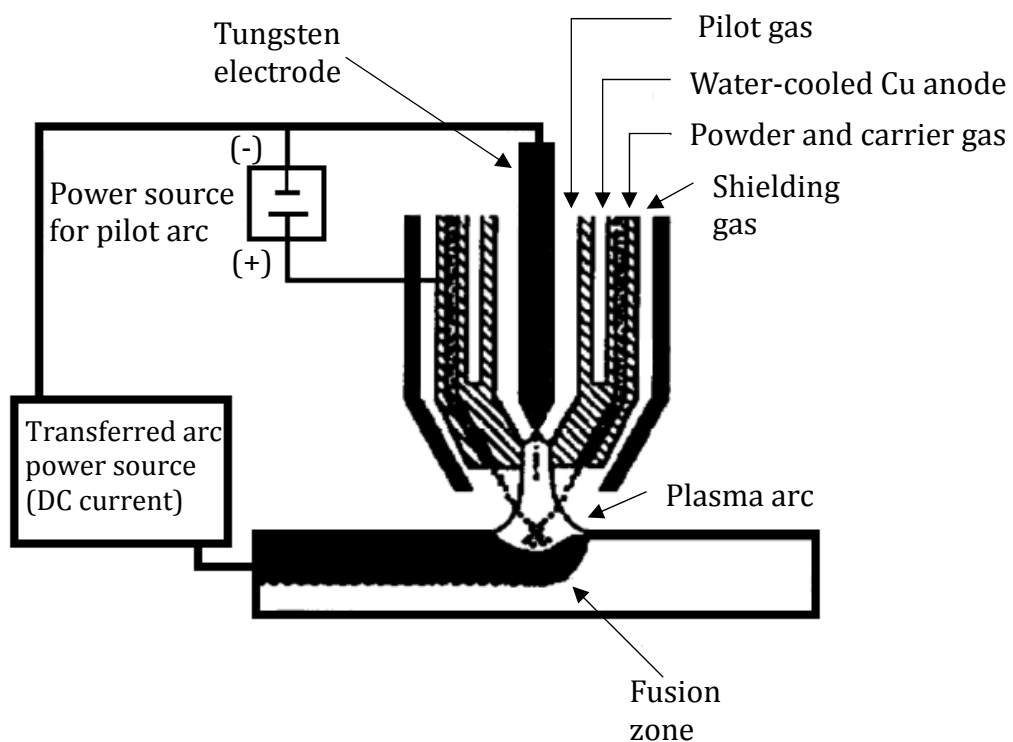
Figure 2.11: Schematic showing the cross section of the plasma transferred arc deposition process (adapted from [100])

Effects of PTA deposition parameters on the resulting coatings

The composition change due to melting of the substrate material during PTA deposition has significant effects on the properties of the coating. This change in composition is known as dilution. The typical substrate dilution level for PTA is 5-10 % [24]. The control of dilution is complex as it is influenced by several deposition parameters. The effects of PTA parameters on the dilution level has been investigated by several authors [24][100][107][108] some of the key findings are summarized as follow:

- Plasma nozzle diameter: The nozzle diameter affects the concentration of the plasma column. Decreasing the nozzle diameter increases the plasma concentration that leads to deeper substrate penetration, which has been reported to increase adhesion [98].
- Plasma gas flow rate: The plasma gas flow rate effects heat generation within the plasma arc. High flow rate increases the velocity of the plasma arc as well as the plasma force on the substrate. This can lead to porosity and oxides within the coating.
- Transferred arc current: The transferred arc current is directly related to the dilution level. Increasing the transferred arc current leads to an exponential increase in dilution. At higher current, more heat is generated and therefore excess heat is available to melt the substrate material, which leads to higher dilution.
- Powder feed rate: The powder feed rate has a complex relation to the dilution. At low powder feed rate, less heat is utilized for melting the powder and thus more heat is used to melt the substrate, which leads to higher dilution. At higher melting powder feed rate, a significant amount of heat generation is used to melt the powder. Therefore substrate melting is lower. However, some molten metal are known to melt the substrate this can also lead to high dilution.
- Stand-off distance: The stand-off distance between the PTA orifice and the substrate is inversely proportional to the dilution. At higher stand-off distance the plasma arc length increases. This spreads the heat input over a larger area, which leads to lower dilution.

The microstructure, mechanical properties and wear resistance of PTA coatings have been investigated by several authors [109][110][111][112][102]. However, there are few reports on the influence of dilution on the microstructure. Deuis et al. [100] reported that high dilution leads to a large heat affected zone and reduction of the coating hardness. However, low dilution leads to poor adhesion. This suggests that a compromise between adhesion and mechanical properties is needed. Fernandes et al. [25] investigated the effects of substrate dilution on the room temperature and high temperature tribological properties of Ni-based coatings deposited by PTA on grey cast iron. Their results show that high dilution level increases the wear resistance of the coating at high temperature. This is due to the agglomeration of high amount of oxide debris, which acts as a protective tribo-layer.

2.2.5   Summary

The main limitations of the existing coating deposition technique such as PVD and CVD are the coating thickness (maximum of 10 μm) and the low toughness. PTA technique offers thick coating (up to several millimetres) with high bond strength due to the strong metallurgical bonding between the coating and the substrate. The strength of the bond is comparable to the tensile strength of the coating material. However, due to melting of the substrate material during deposition, the microstructure of the resulting coating can deviates substantially from the expected structure of the precursor powder. Detailed investigation on the effects of PTA induced microstructure change is required.

2.3   Aluminium bronze alloys

Copper alloys are of technological importance and have a long history of continual development. The global production of copper increases constantly from 11,140 thousand tons in 1995 to 21,103 thousand tons in 2015 [113]. The primary use of Cu is in the areas of building and construction, electrical and electronics products, industrial and machinery equipment, transportation equipment and for consumer products. This section focuses on copper alloys used for industrial and machinery equipment; in particular the alloys used for wear resistance application. Aluminium bronzes are copper based alloys with aluminium as the main alloying element. Small addition of Fe, Ni, Mn and Si are often added to create alloys with different properties. Aluminium bronze alloys can be classified by the alloying elements into three main types as shown in Table 2.6. The extensive lists of the commercially available cast and wrought alloys can be found in Appendix 1.

Table 2.6: Aluminium bronze alloys classification

Classification	
Binary	Cu-Al
Ternary	Cu-Al-Fe, Cu-Al-Ni, Cu-Al-Mn, Cu-Al-Si, Cu-Al-Be, Cu-Al-Sn and Cu-Al-Co
Complex	Cu-Al-Fe-Ni, Cu-Mn-Al-Fe-Ni

Aluminium bronzes are well known for their high strength (comparable to medium carbon steel) and exceptional resistance to corrosion and fatigue. The alloys are also highly resistant to wear and can retain strength up to a temperature of 400 °C [16]. The U.S. Environmental Protection Agency also listed the alloy as being anti-microbial [114]. Other key properties of aluminium bronze are:

- Low friction coefficient against steel ~ 0.15 (lubricated) [19]
- Good machinability and weldability
- High impact resistance
- Non-sparkling and low magnetic permeability
- Attractive appearance

Aluminium bronzes are mainly used in marine applications such as propellers and sea water transport system [115][116]. The alloys are also used in applications such as bushings and guide plates where hardness and wear resistance are key requirements. This section focuses on Cu-Al-Fe aluminium bronzes with high aluminium content. These alloys are known for their high hardness but low ductility, hence are suited for applications such as forming dies where the load is mainly compressive. In the next subsections, the effects of Al and Fe on Cu will be discussed.

2.3.1   Effects of Al addition to Cu

The addition of Al to Cu has significant effects on the mechanical, tribological and corrosion properties. Consequently the Al content is usually controlled to within ± 0.1 wt. % of the design value. Binary Cu-Al alloys are the simplest form of aluminium bronzes. The microstructure features and transformation that occur in Cu-Al alloys also form the base for understanding more complex alloys such as Cu-Al-Fe and Cu-Al-Fe-Ni alloys. Studies on the microstructure of aluminium bronzes started in the 1920s [117]. The microstructure features present in the alloy are diverse. Various features related to martensitic [118] [119], ordering reactions [120] as well as occurrence of unique metastable precipitates [27] have been reported. This makes the aluminium bronze system highly complex. The microstructures of Cu-Al alloys have been studied extensively. Several phase diagrams for Cu-Al systems have been produced and revised, the phase diagram presented by Murray [121] (see Figure 2.12) is one of the most widely used, however some high temperature phases and reactions couldn't be confirmed by subsequent authors [117] [122] and were consequently excluded. The generally accepted Cu-Al phase diagram is shown in Figure 2.12. The characteristics of the equilibrium phases in Figure 2.12 are detailed in Table 2.7. At Al content between 0 – 30 at.% (0 - 15 wt.%) the alloy can be classified into two types. The microstructure of the alloys with Al content up to ~17 at.% (~6 wt.%) remains the same as that of Cu and is composed of homogeneous (Cu) phase, which is solid solution of Al in Cu. Such alloys are known to have high ductility but low hardness [15].

Alloys with Al content above 17 at. % ($\sim$ 6 wt.%), the second phase known as the β phase appears in the microstructure. The β phase is a high temperature Cu_3Al compound with a wide solubility range [21]. The β phase alloys are known to have higher strength and hardness than (Cu) phase alloy; however the ductility at room temperature is lower. In the present research, the composition of the coating used is within the (Cu)/ β phase region as highlighted in Figure 2.12. In the next section, the solidification sequence and transformations of (Cu)/ β alloy will be discussed.
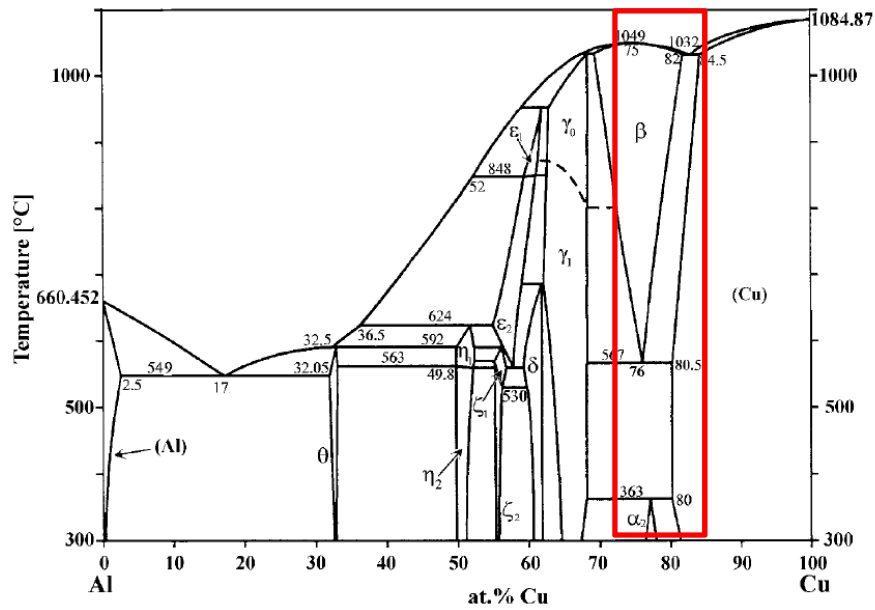
Figure 2.12: Generally accepted Cu-Al phase diagram[123] (The red box indicates approximate Cu-Al compositions relevant to coating used in the present research)

Table 2.7: Characteristics of equilibrium phases in the Cu-Al phase diagram

(adapted from [122] and [123])

Phase	Composition range (at. % Cu)	Temperature range (°C)	Lattice parameters (nm)	Space group	Crystal system
(Al)	0-2.48	<660	a = 0.40496	$Fm\bar{3}m$	Cubic
θ	31.9-33.0	<592	a = 0.6063, c = 0.4872	I4/mcm	Tetragonal
η_1	49.8-52.4	624-560	a = 0.4807, b = 1.204 c = 0.8635	Pban or Cmmm	Orthorhombic
η_2	49.8-52.3	<563	a = 1.2066, b = 0.4105 c = 0.6913	C2/m	
ζ_1	55.2-59.8	590-530	a = 0.8127, b = 1.4985 c = 0.9992	P6/mmm [123] Fmm2 [122]	Hexagonal Orthorhombic
ζ_2	55.2-56.3	<570	a = 0.4097, b = 0.7031 c = 0.9979	Imm2	Orthorhombic
ε_1	59.4-62.1	958-850	-		
ε_2	55.0-61.1	850-560	a = 0.4146, c = 5.063	$P6_3/mmc$	Hexagonal
δ	59.3-61.9	<686	a = 0.8706	R3m	Trigonal
γ_0	59.8-69.0	~1040-800	-	$I\bar{4}3m$	Cubic
γ_1	52.5-59.0	<~900	a = 0.8702	$P\bar{4}3m$	Cubic
β	70.6-82.0	1049-567	a = 0.2950	$Im\bar{3}m$	Cubic
α_2	76-5-78.0	<~367	a = 0.3668, c = 0.3680	-	
(Cu)	80.3-100	<1084	a = 0.3641	$Fm\bar{3}m$	Cubic

Solidification sequence of β phase alloys

For β phase alloy, the microstructure transformation during slow cooling from the high temperature disordered β phase region through the eutectoid temperature can be described as follow. At the temperature $\sim 1049°C$ the alloy solidified as a disordered β phase, which is the equilibrium phase at high temperature. Upon further cooling it undergoes an ordering reaction:

$$\beta_{\text{disordered (A2)}} \rightarrow \beta_{1 \text{ ordered (DO}_3)} \qquad \text{Equation 2.3}$$
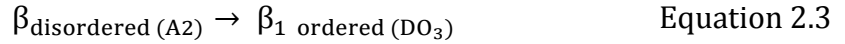
The structure of the ordered β_1 phase is reported as DO_3 type [124][125] (see Table 2.8 for more details). As the temperature decreases further, the ordered β_1 phase undergoes eutectoid decomposition at ~ 567 °C:

$$\beta_1 \rightarrow (\text{Cu}) + \gamma_1 \qquad \text{Equation 2.4}$$

The eutectoid reaction takes place in two stages [118]. First, the ordered β_1 phase transforms into the Cu_9Al_4 compound designated as the γ_1 phase, the formation of the γ_1 phase causes a decrease in solute aluminium concentration in the matrix. This leads to the formation of (Cu) phase as the Al content in the matrix decreases below ~ 19 at. % (~ 10 wt.%). The eutectoid reaction is controlled by the solid state diffusion of Al in the matrix phase [126] and thus require a substantial amount of time for completion. Therefore in rapid solidification process such as plasma transferred arc deposition, the high temperature β phase follows a non-equilibrium transformation.

Non-equilibrium transformation of the high temperature β phase

Cu-Al alloys with aluminium content between 18.9 at.% and 27.7 at.% (9 and 14 wt. % Al) are known to show a martensitic transformation when rapidly cooled from high temperature [118]. The ordering reaction (see Equation 2.3) precedes the martensitic transformation [120], which leads to formation of metastable phases [125]. The metastable phases obtained are dependent on the Al content [120]. At high aluminium content > 21 at. % (> 12 wt.%) the martensitic transformation is reported to occur after the completion of the ordering reaction. Two ordered martensitic phases have been reported, these are denoted as β_1' and γ' [125] [118] [120].

At lower aluminium content < 21 at. % Al (< 12 wt.%) a disordered martensite designated as β' is obtained [125][118] (see Figure: 2.13). The effects of Al content on the type of martensite formed are summarised in a partial Cu-Al phase diagram shown in Figure: 2.13. The reported crystal structures of β_1', γ' and β' martensite are detailed in Table 2.8. TEM images of β_1' and β' martensite are shown in Figure 2.14 and Figure 2.15 respectively.
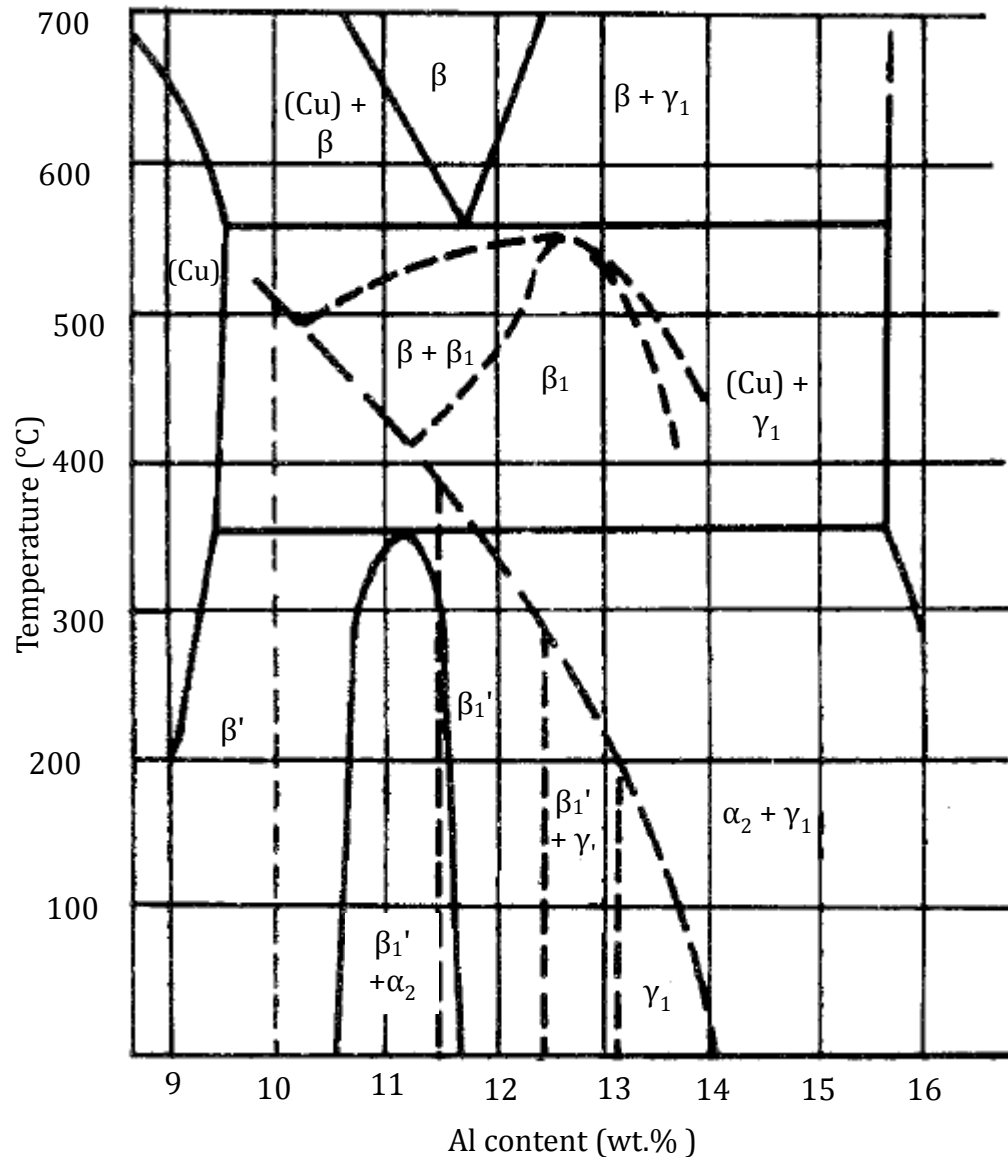
Figure 2.13: Partial Cu-Al phase diagram in showing the presence of martensitic phases and metastable phases (adapted from [118])

Table 2.8: Crystal structures of β_1', γ' and β' martensite and the ordered β_1 phase

Al content	Phase	Crystal system	Lattice parameter	Remarks	Reference
Al >21 at. % (> 12 wt.%)	β_1'	Orthorhombic	a = 04494 nm, b/a =2/√3 , $c/a = \frac{22}{3}\sqrt{2}$	The primitive cell was described as monoclinic with compact DO$_{22}$ basal plane	[125] [127]
	γ'	Hexagonal	a = 0.2505 nm, c/a = 1.619	It has been reported in [128] that martensite phase with high aluminium content has the crystal structure approaching HCP	[129] [130]
Al< 21at. % (< 12 wt.%)	β'	Cubic	-	-	[125][118] [131]
	Ordered β_1	Cubic	a = 0.596 nm	Ordered-FCC	[124][125]
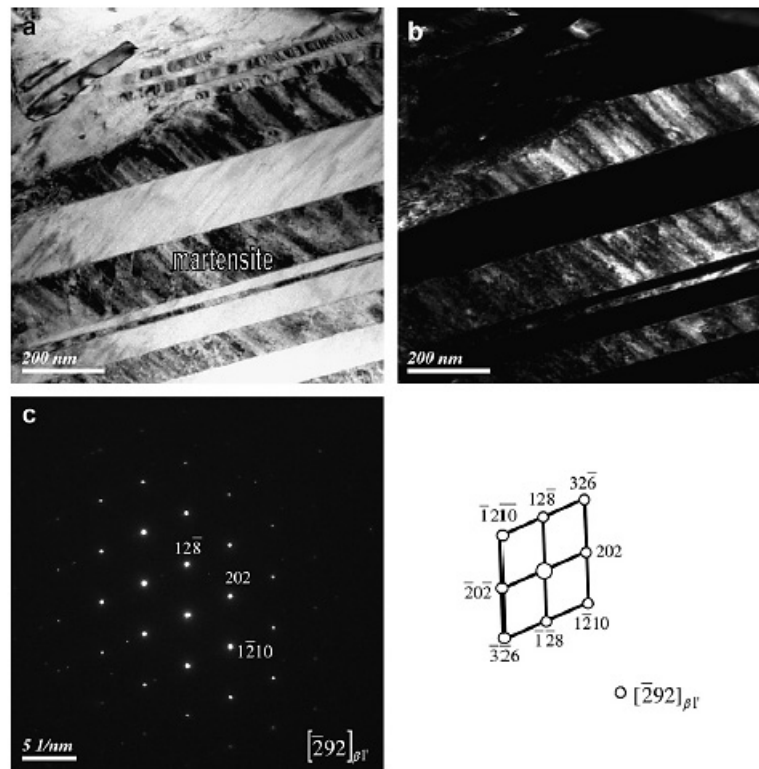
Figure 2.14: (a) TEM bright field image, (b) TEM dark field image and (c) SADP of the β_1' martensite obtained by infrared brazed Fe_3Al using Cu braze foil at 1000 °C for 30 s [130]

(a)   (b)
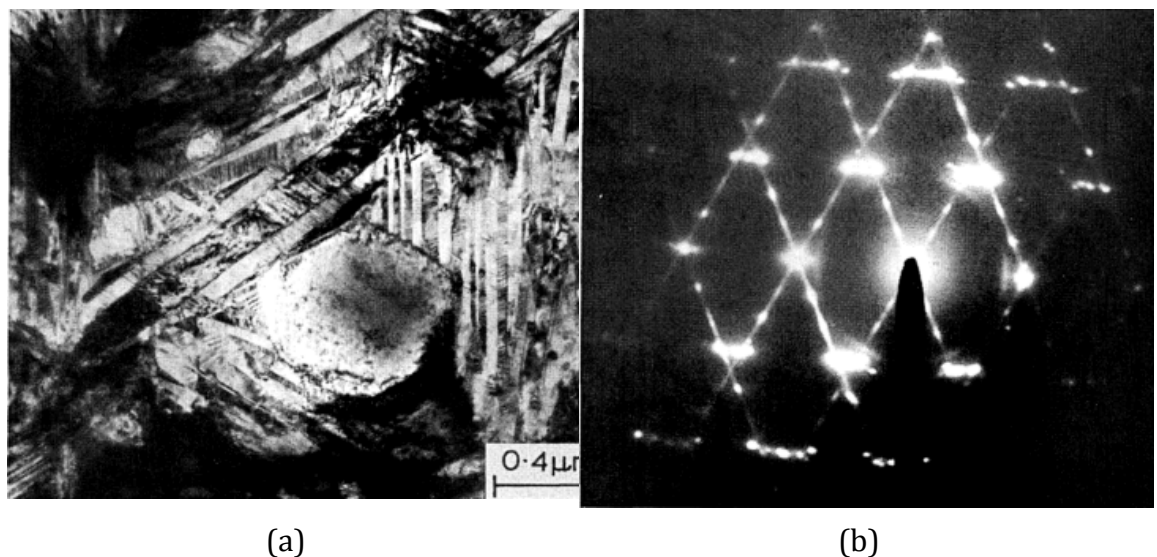
Figure 2.15: TEM image showing the presence of β' martensite in a cast alloy with composition in wt. % Cu-8.63Al-3.23Fe (a), diffraction pattern showing the structure of β' martensite [131]

39

The effects of Al content on the mechanical properties

The addition of aluminium to copper reduces the stacking fault energy (SFE) as shown in Figure 2.16. The stacking fault is an interfacial defects characterised by a disruption in the staking sequence of the close-packed plane. The decrease in stacking fault energy limits the mobility of dislocation in the material and cross slip becomes more difficult. Consequently the alloy becomes increasingly more brittle as more slip systems must be activated to accommodate the deformation.
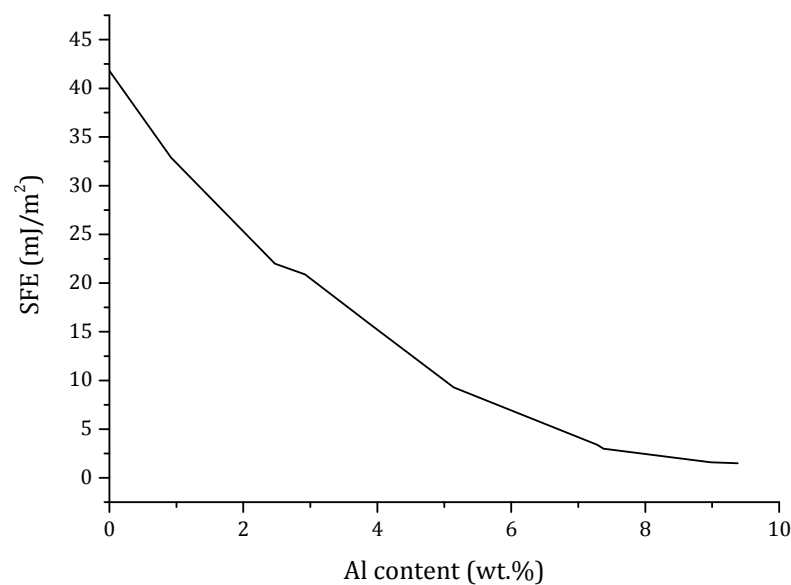
Figure 2.16: Effects of Al content on stacking fault energy of Cu (data from [132])

The mechanical properties of the alloys are strongly influenced by the Al content. The effect of increasing Al on tensile strength is shown in Figure 2.17. Between 0 – 8 wt. % Al the tensile strength increases linearly. This can be associated with solid solution strengthening. Above 8 wt. % the tensile strength increases more rapidly owing to formation of the β phase
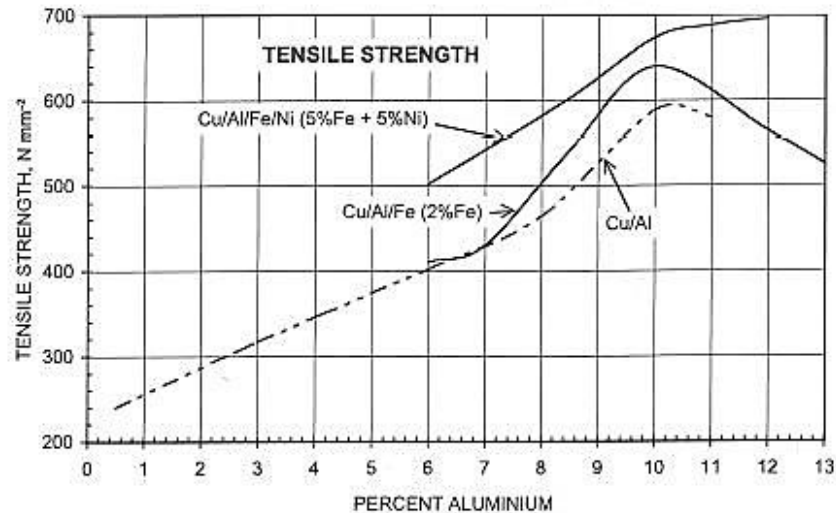
Figure 2.17: Effects of Al content on tensile strength of Cu alloys [16] (the amount of Al shown is in wt.%)

The effects of increasing Al content on percentage elongation are shown in Figure 2.18. Addition of Al up to 5 wt.% leads to an increase in percentage elongation, which reaches a maximum value of 74 % between 5-7 wt.% Al. Above ~ 8.5 wt. % Al the percentage elongation decreases significantly and approaches ~ 0 % at 11.4 wt.% Al. Up to 8.5 wt.% Al, the elongation decreases mainly due to the increase solid strengthening caused by the increase in Al content. This increases the energy required for slip to occur thereby reducing the % elongation of the alloy. Above 8.5 wt. % Al the decrease in elongation can be attributed to the formation of brittle martensitic β phase upon fast cooling or formation of eutectoid (Cu) + γ_1 upon slow cooling. Consequently, wrought alloys typically contain 4.5-7.5 wt. % Al for optimum formability. The majority of the cast alloys typically contain 8 – 11 wt. % Al to avoid casting difficulties associated with a narrow solidification range and the eutectoid reactions. Alloys with 11-13 wt. % Al have high hardness and low ductility. These alloys are also significantly harder to produce by conventional casting techniques.
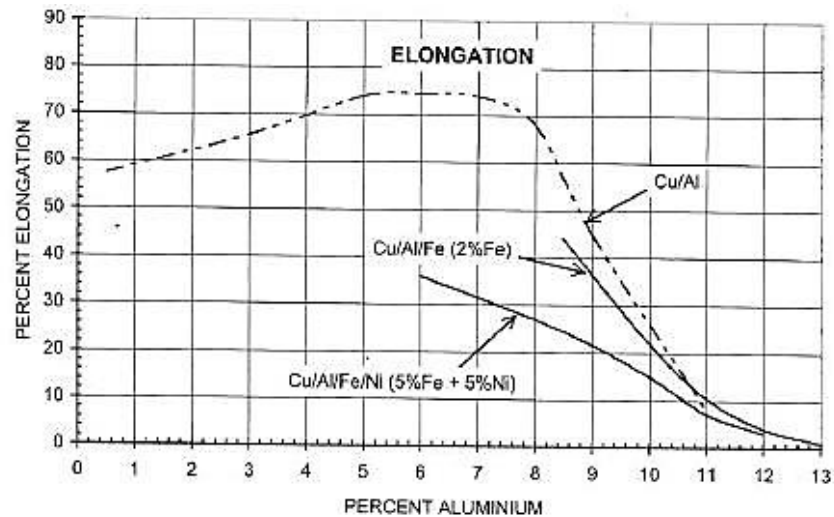
Figure 2.18: Effects of Al content on percentage elongation[16]

2.3.2   Effects of Fe addition to Cu-Al alloy

The addition of Fe to Cu-Al alloy refines the (Cu) phase grain size, which improves the toughness of the alloy. Iron also retards formation of the brittle γ_1 phase during solidification [15]. The addition of Fe has also been reported to enhance the corrosion resistance as long as the iron remains in solid solution and does not precipitate as pure Fe [133]. The hardness of (Cu) phase alloys has also been reported to increase linearly with the addition of Fe up to 7.8 wt.%. This is due to solid solution strengthening caused by Fe [133]. Unlike the effects of Al, the influence of Fe is not well studied, particularly when the Fe content exceeds ~ 5 wt.% which represents a typical limit for commercial alloy (see Appendix 1). This is due to the limited solubility of Fe in aluminium bronze, which is ~ 3.5 wt.% [15]. The solid solubility of Fe in aluminium bronze can be increased by using rapid solidification techniques. Collins et al. [133] used spin melting to retain 11.50 wt.% Fe in Cu-6 wt.% alloy. The majority of the Fe is retained in solid solution, however some Fe-rich particles were also observed. TEM observations identified them as the bcc αFe.

This result by Collins et al. [133] and the vertical section of the Cu-Al-Fe phase diagram (see Figure: 2.21) suggests that the retention of high Fe content in the (Cu) phase alloy is not expected to cause a change in the matrix phase. However, for the β phase alloys, the effects of high Fe content on the microstructure have not been reported. The computed isothermal section of the Al-Cu-Fe system is shown in Figure 2.19. In the composition range relevant to the present coating system, no ternary Cu-Al-Fe phase is known. Due to the low solubility of Cu in Fe as shown in Figure 2.20, no Cu-Fe phases are known, however a miscibility gap exists as highlighted by the dotted lines in Figure 2.20. This indicates the tendency for liquid phase separation into Fe-rich and Cu-rich parts during rapid cooling. Liquid phase separation has been previously observed in work on rapid solidification of a Cu-Fe alloy [134][135].
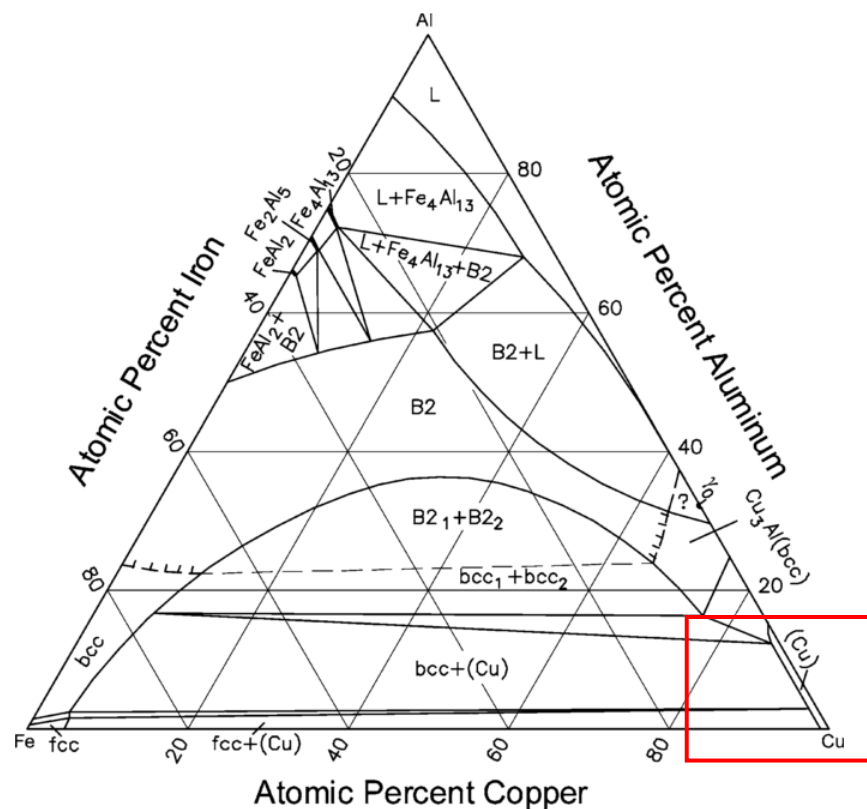
Figure 2.19: Computed Al-Cu-Fe isothermal section at 1000 °C [136] (the red box indicates compositions relevant to coating used in the present research)
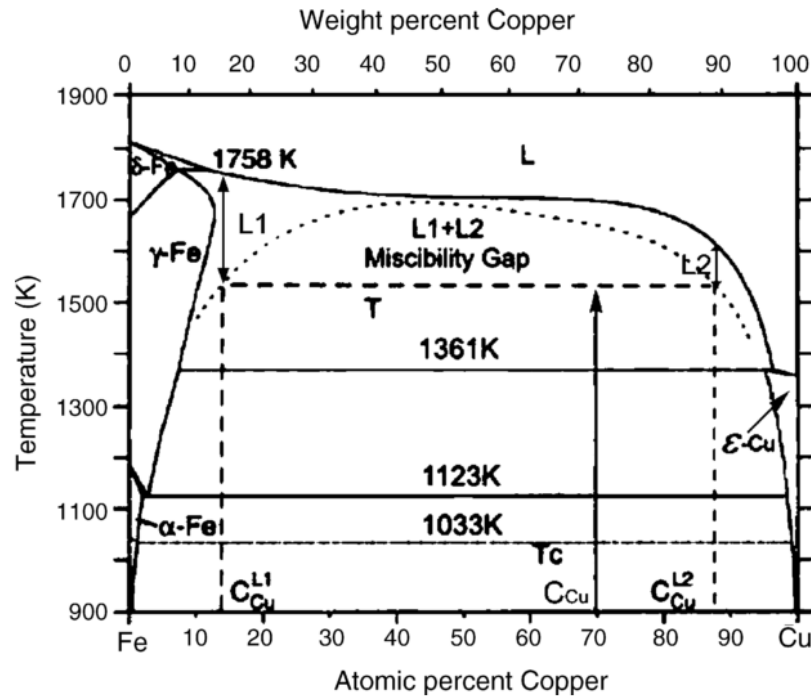
Figure 2.20: Fe-Cu phase diagram (dotted line represents calculated metastable
miscibility dome) [137]

The Cu-Al-Fe phase diagram is shown in Figure 2.18. Compared to the Cu-Al phase
diagram (see Figure 2.21) it is clear that addition of a small amount of Fe (3 wt. %)
only leads to the addition of the intermetallic Fe_3Al κ_1 phase to the Cu-Al system.
Since the alloy consists largely of Cu and Al, the solidification sequence described
in section 2.3.1 is still applicable. Formation of the Fe_3Al κ_1 precipitate can be
explained by considering the reaction between Fe and Al as well as the solubility of
Fe in Cu-Al phases.
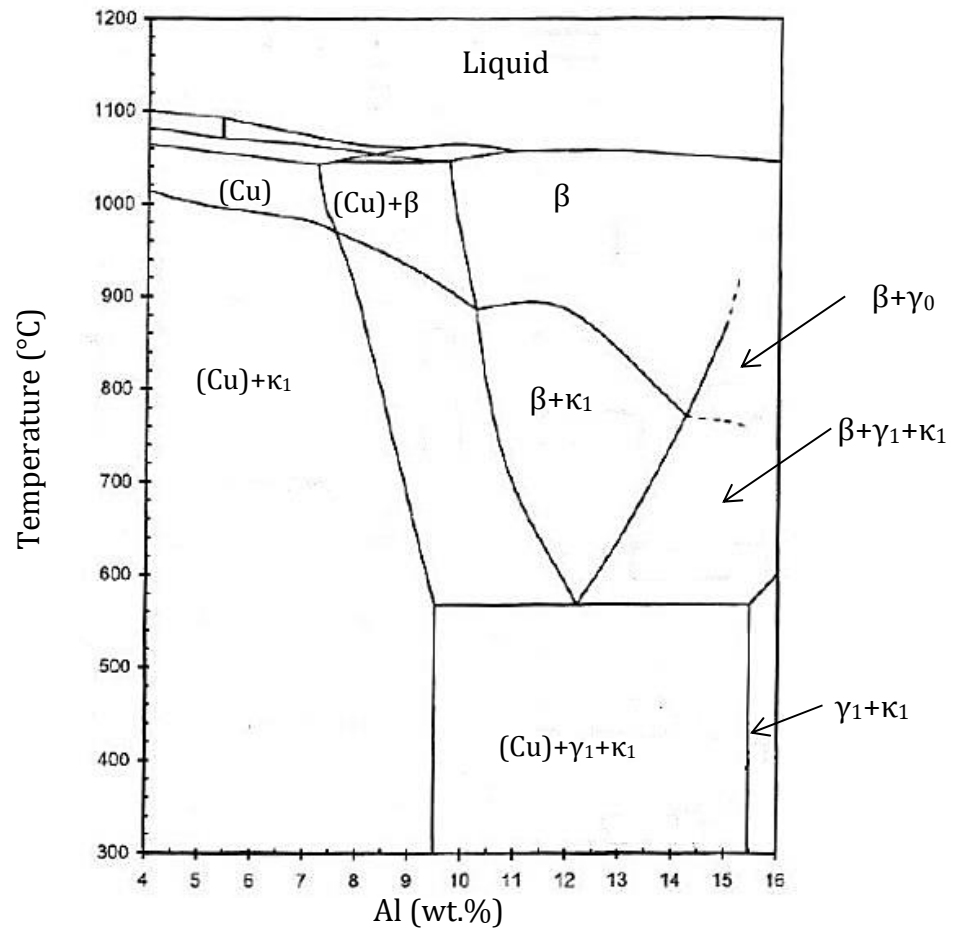
Figure 2.21: Vertical section of the Cu-Al-Fe system at 3 wt.% Fe (adapted from [138])

Solubility of Fe in Cu-Al phases

The solubility of Fe in Cu-Al phases as a function of temperature is shown in Table 2.9. With the exception of the γ_1 phase, the solubility of Fe in Cu-Al phase decreases with temperature. Iron in excess of 3 wt. % will precipitate in (Cu) and β phase when the temperature drops below 1000 °C as shown in Figure 2.23. Hence quenching the alloy from higher temperature allows more Fe to be retained. Krzanowski et al. [139] have shown using magnetron sputtering that is it possible to produce aluminium bronze alloy with an Fe content of 9 wt.% .

Table 2.9: Solubility of Fe in Cu-Al phase as a function of temperature (data from [16])

Temperature (°C)	wt.% of Fe soluble in		
	(Cu) phase	β phase	γ_1 phase
500	0.6	-	0.9
600	0.9	1.1	1.3
800	1.5	2.6	
1000	2.6	6.0	

Reaction between Fe and Al

The Fe-Al phase diagram is shown in Figure 2.22. Nine phases and two metastable phases have been identified. Within the composition applicable to the present research (highlighted by red box in Figure 2.22), the bcc αFe phase is the first to solidify. The bcc αFe phase is known to exist in both disordered A2 as well as the ordered B2 and DO$_3$ forms [136]. As the temperature decreases below $\sim$ 540°C the bcc αFe phase transforms into intermetallic Fe$_3$Al κ_1 phase with DO$_3$ structure [130].The characteristics of the Fe-Al phases in the composition range applicable to the present research are detailed in Table 2.10.
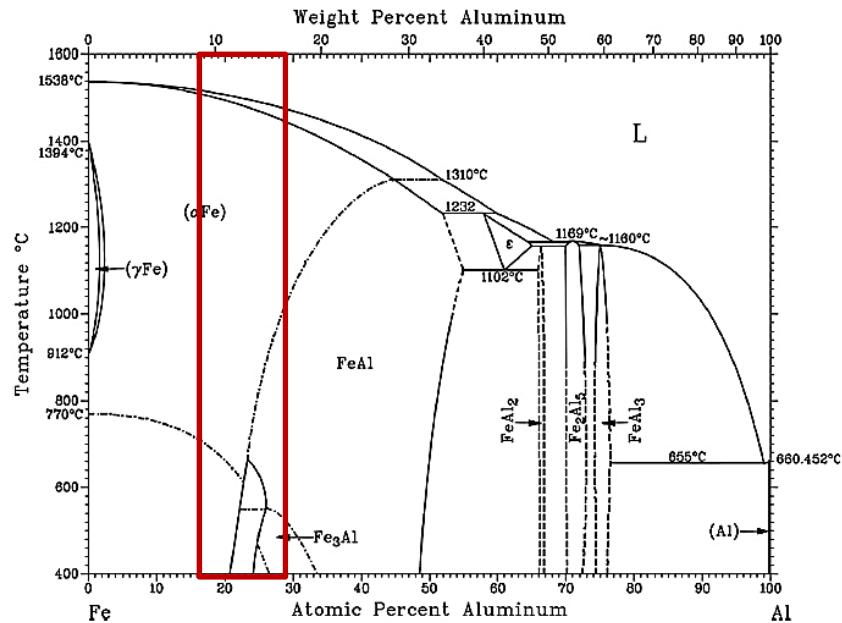
Figure 2.22: Fe-Al phase diagram [140] .The red lines marks the composition relevant to the present research

Table 2.10: Characteritics of Fe-Al phase in the range applicable to the present study [140]

Phase	Composition range (at. % Al)	Lattice parameter (nm)	Space group	Crystal system
bcc αFe	0-44.0	a = 0.286	Im$\bar{3}$m	Cubic
FeAl	23.3 – 54.9	a = 0.291	Pm$\bar{3}$m	Cubic
Fe$_3$Al	23.6 – 34.1	a = 0.579	Fm$\bar{3}$m	Cubic

Microstructure of Cu-Al-Fe alloys

Based on the preceding discussions the microstructure of the Cu-Al-Fe alloy with 11-14 wt.% Al and small amount of Fe addition can be explained as follows. At 1538 °C the Fe solidifies as the bcc αFe phase. At ~ 1060 °C the remaining liquid solidifies as the high temperature disordered β phase. As the temperature drops to ~ 900 °C the disordered β under goes an ordering reaction into the ordered β$_1$ phase as previously described in Equation 2.3. On slow cooling through the eutectoid temperature (~ 567 °C) the ordered β$_1$ phase undergoes eutectoid decomposition into (Cu) and γ$_1$ phase. As the temperature decreases below 540 °C the bcc αFe precipitate transforms into Fe$_3$Al κ$_1$ intermetallic phase. The crystal structure of κ$_1$ phase has been investigates using TEM by Hasan et al. [131] and was reported to be DO$_3$ (see Figure 2.24). On quenching the alloy from high temperature, martensitic phase and κ$_1$ phase can be expected in the microstructure. The type of martensite form is dependent on the Al content as detailed in Table 2.8.

(a)   (b)
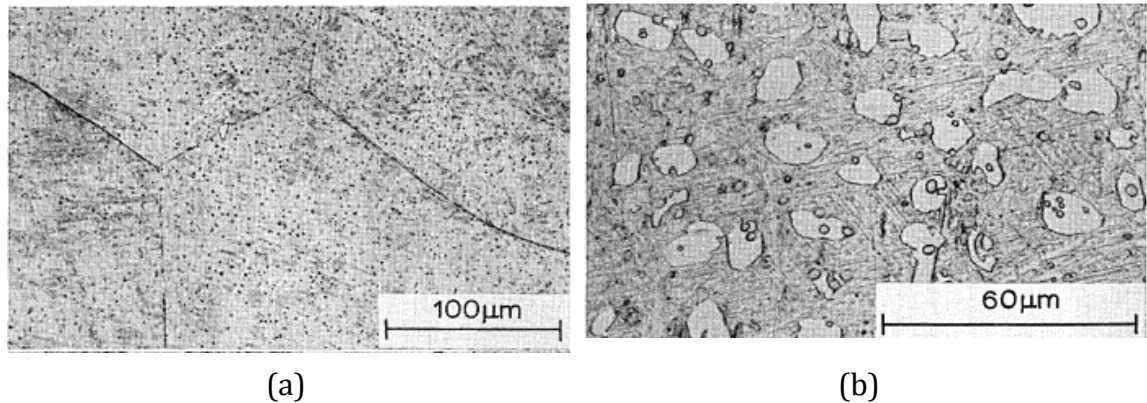
Figure 2.23: Microstructure of a Cu-8.63Al-3.23Fe (all in wt.%) alloy quenched from 900° (a) and 860°C (b) [131]

Figure 2.24: TEM diffraction of Fe_3Al κ_1 phase showing DO_3 structure [131]

Mechanical properties of Cu-Al-Fe alloy

The addition of 2 wt. % Fe to the Cu-Al alloy with Al content 9 – 12 wt.% increases the tensile strength from 590 N mm^{-2} to 640 N mm^{-2} as shown in Figure 2.17. The hardness of the alloy also increases due to formation of hard intermetallic Fe_3Al κ_1 phase. However, this also leads to a reduction in percentage elongation as shown in Figure 2.18. Formation of the κ_1 phase is a possible reason for the reduction in percentage elongation. Cu-Al-Fe alloys with high aluminium content (12 – 14 wt.%) are known to have high hardness. Roucka et al. [141] investigation the properties of cast aluminium bronzes with composition in wt.% Cu-15.1Al-3.5Fe-1Mn-1.2Ni. They reported that an alloy with martensitic structure could be achieved by rapid cooling in air. The alloy was reported to have a maximum hardness of 424 HV. Kudashov et al. [17] uses spray forming to fabricate alloys with composition in wt.% Cu-12-5-14.5Al-4Fe-Mn-Co. Their results show that the increase in Al content from 12.5-14.5 wt.% leads to an increase in hardness from 340-380 HV. This is due to the formation of the hard Cu_9Al_4 γ_1 phase.

2.3.3   Influence of other alloying elements and impurities

In addition to Al and Fe, other alloying elements such as Ni, Mn, Ti, and Zn are also used. Ternary Cu-Al-Fe alloys with addition of 1 wt.% each of Ni and Mn have microstructures very similar to a Cu-Al-Fe alloy. Mn and Ni remain in solid solution and have an effect in strengthening the (Cu) phase. The (Cu) phase grain size can be refined by addition of Ti and B [18]. The addition of Si has a grain refining effect and increases the tensile strength, proof strength and hardness of the alloy. It has been reported that the addition of 1 wt.% of Si is equivalent to 1.6 wt.% of Al [16]. However, in commercial alloys Si is limited to < 1 wt.%. For bearing application a small amount (~1 wt.%) of Pb is often added to aluminium bronzes to improve sliding properties and machinability. However, alloys with addition of Pb were found to have low strength and elongation. Zn and P are some of the impurities found in aluminium bronzes, these elements are known to decrease the mechanical properties of the alloy when present in quantity greater than 1 wt. % and 0.08 wt.% respectively. Magnesium has a deoxidizing effects, which may be beneficial during casting, however its presence in small quantities of 0.01 wt.% leads to reduction in ductility [142].

2.3.4   Summary

The microstructure of aluminium bronze alloys is strong dependent on the cooling rate during production and the Al content. The effects of these two factors on the microstructure of Cu-Al alloys are summarised in Figure 2.25. Based on the review, the addition of Fe into the solid solution alloys doesn't lead to significant phase change. However, the effects of high Fe content on alloys with high Al content have not been reported.
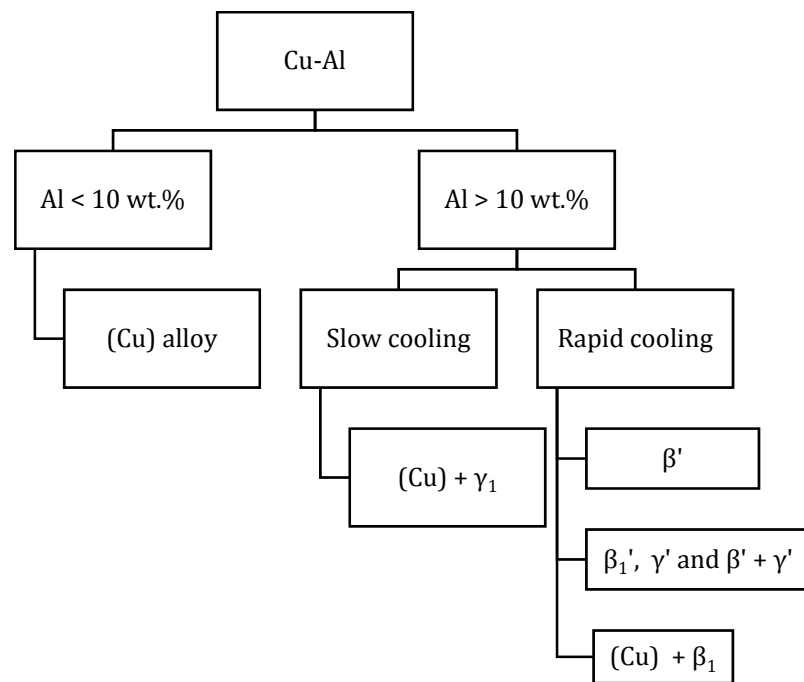
Figure 2.25: The effects of Al content and cooling rate on the microstructure of the Cu-Al alloy

2.4   Tribology of aluminium bronze alloys

Copper-based alloys such as aluminium bronze and phosphor bronze are commonly employed in sliding surfaces where the lubrication is not ideal. Aluminium bronze alloys offer higher loading capacity and fatigue resistance than phosphor bronze. However, during dry sliding against steel, aluminium bronze has higher friction coefficient (0.45) than phosphor bronze (0.35) [15]. The friction coefficient of aluminium bronze alloys can be improved by fabricating the alloy with embedded solid lubricant particles [143] and/or polymers [144] in the form of surface coating. For applications involving compressive loading and high wear resistance, aluminium bronze alloys with Al > 12 wt.% are particularly well suited. The high wear resistant of alloys with high Al content makes them highly suitable for forming dies application. However, these alloys are also known to be brittle and are thus difficult to machine into the desired complex shape, which limits its use for industrial application. This is due to the formation of the brittle (Cu) + γ_1 structure (see section 2.3.1). To alleviate this problem, aluminium bronze alloys with high Al content (above 12 wt.%) can be fabricated by combining it with a suitable substrate in the form of surface coating. The rapid cooling during deposition is expected to prevent the eutectoid decomposition of the high temperature β phase and retains it in the form of martensite. In the next section, the factors affecting the wear resistance of the aluminium bronze alloys are discussed.

2.4.1   Influence of microstructure on wear resistance properties

Microstructure of aluminium bronze alloys for wear resistance applications can be classified into two main categories: the single-phase solid solution (Cu) alloy and the duplex (Cu)/β alloy. In this subsection, the influence of the microstructure on wear resistance properties of the alloy will be discussed.

Wear of solid solution (Cu) phase alloy

The solid solution (Cu) phase alloys contain a maximum of ~ 8 wt.% Al. The microstructure of the alloy is characterised by a solid solution (Cu) phase matrix with fcc crystal structure. The friction and wear behaviour of the solid solution alloys are well studied. In this type of alloy, the wear resistance increases with the Al content up to approximately 3-5 wt.%. Further addition of Al content up to the limit of the solid solution phase (7.5-8.0 wt.% Al) leads to a reduction in the wear resistance. Delamination and abrasive wear are the two dominant wear mechanism of the solid solution alloy [145]. The friction coefficient of the alloy has been reported to decrease linearly with increasing Al content [146]. The improvement in the wear resistance and reduction in friction coefficient with Al content (up to 3-5 wt.% Al) can be explained by the increase in the hardness of the alloy. The hardness increase can be attributed to the solid solution strengthening of the Al solute. The increase in hardness reduces the ploughing component of friction (see section 2.1.2). This reduces the tangential force needed to cause relative motion, resulting in a reduction in friction coefficient. The reduction in friction coefficient also reduces the shear stress at the contacting asperities thus minimizing the subsurface deformation. The increase in hardness also increases the resistance against adhesive wear, which contributes to the increase in wear resistance. The subsurface deformation of the solid solution alloy is characterised by a highly deformed mechanically mixed layer below the contacting asperities. Beneath the highly deformed mechanically mixed layer is a layer of cold worked material as shown in Figure 2.26.

Subsurface crack →

Highly deformed layer

Work hardened layer

1 μm
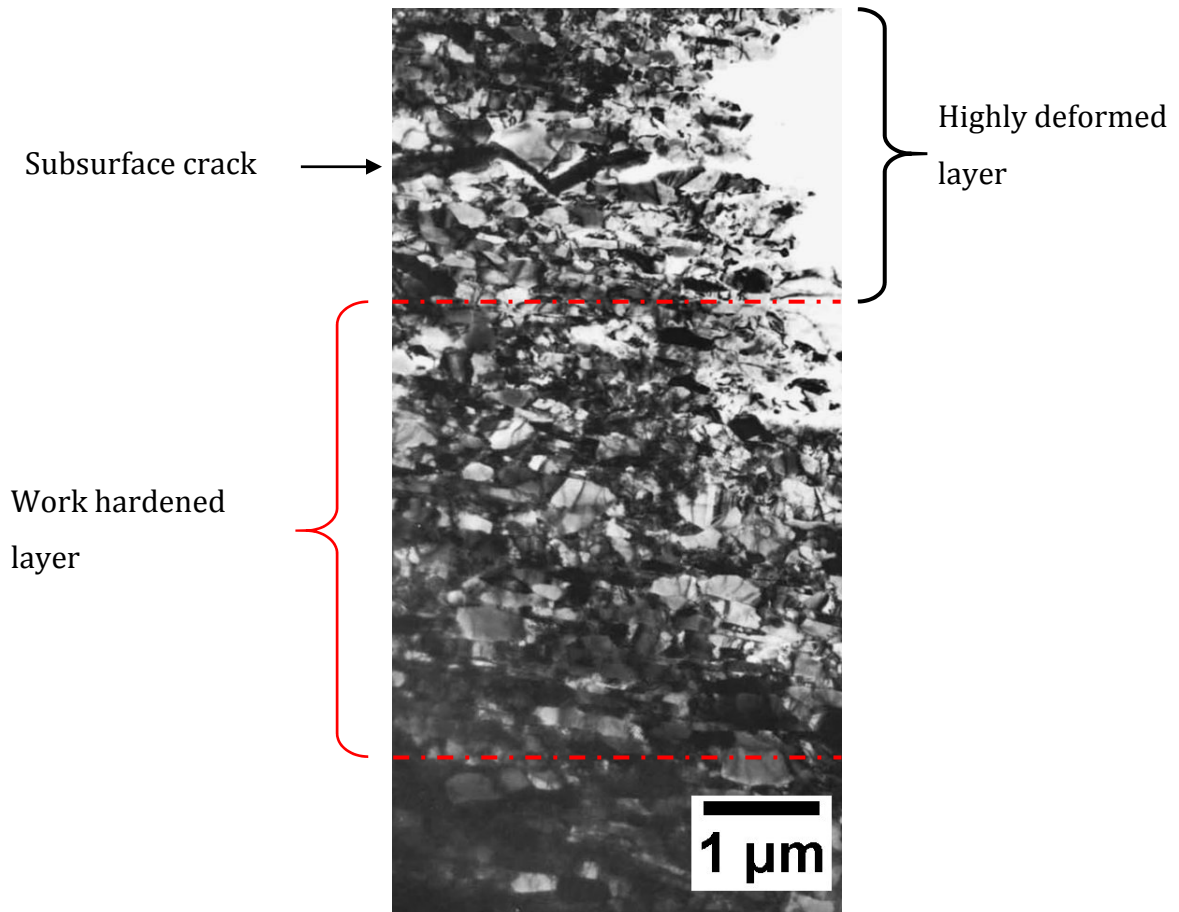
Figure 2.26 Electron micrograph showing a the presence cracks in the of highly deformed layer and a work hardened layer (adapted from [147])

Within the highly deformed layer, fine grains were observed. Formation of the highly deformed layer is a combined effects of local plastic strain induced by the tangential force and the formation of new nuclei due to dynamic recrystallization [148]. Under reciprocating motion such as during SMF, the material beneath the contact and ahead of the contact in the direction of sliding experienced a compressive load, while the material behind the contact experienced tension as shown schematically in Figure 2.27. This cyclic loading leads to generation of crack as shown in Figure 2.26, which eventually leads to the removal of the material from the surface.
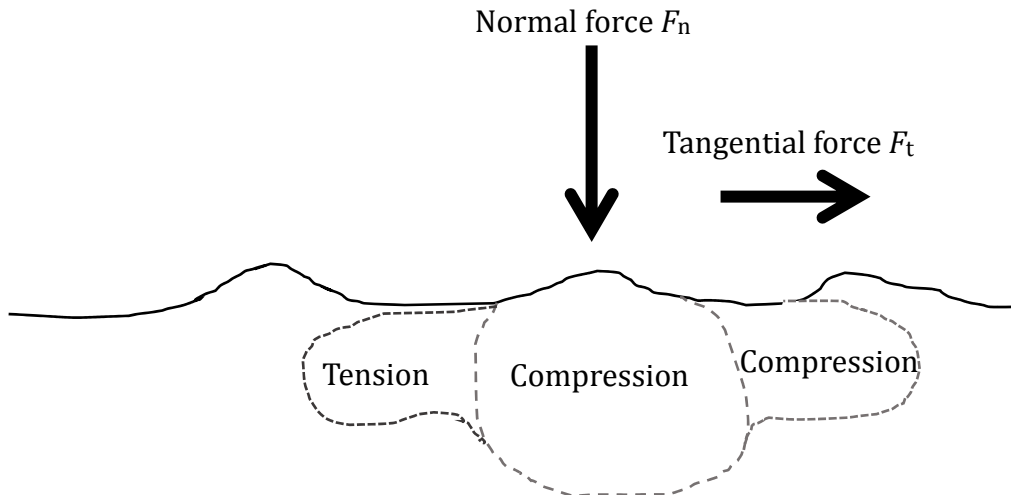
Figure 2.27: Schematic showing the cyclic loading involving tension and compression during reciprocating motion

As the Al content increases above 5 wt.% the wear resistance of the alloy decreases. At this composition range the stacking fault energy also falls below 25 mJ/m^2 as shown in Figure 2.16. This reduction in stacking fault energy has been reported to promote deformation by twinning, which was associated with an increase in the depth of the deformed layer beneath the worn surface [146]. As the depth of the deformed layer increases, the depth in which cracks propagate also increases. This leads to an increase in the size of the material removed, resulting in the increase in wear. Additionally, the presence of inclusions or secondary phases can also act as crack nucleation points, which leads to an increase in wear. The addition of Fe to (Cu) alloys leads to a (Cu) + κ_1 structure that have been reported to have high wear rates [149].

Wear of duplex (Cu)/ β alloy

Above the solid solution limit of Al in Cu, the microstructure of aluminium bronze alloys become more complex. Depending on the cooling rate during fabrication, the microstructure of the alloy can be large grouped in to three types:

- The eutectoid (Cu) + γ_1 structure
- The martensitic β' (for Al < 12 wt.%) and β$_1$' and/or γ' (for Al >12 wt.%)
- The α + β$_1$ structure

Compared to the solid solution alloys, investigations on the wear resistance of (Cu)/β alloys are more limited. Blau [146] investigated the wear resistance of hot rolled (>700 °C) Cu-12 wt.% Al alloys with an eutectoid structure and a martensitic β_1' structure. The eutectoid structure was obtained by slow cooling through the eutectoid temperature water quenched at 512 °C. The martensitic structure was obtained using two methods: (i) water quench from 800 °C and (ii) by electron beam melting of the hot rolled alloy. In the alloy with martensitic structure micro-twins and acicular plates were observed as shown in Figure 2.28. The microstructure of the alloy with the eutectoid structure is characterised by the solid solution (Cu) phase surrounded by the γ_1 phase as shown in the backscattered electron image in Figure 2.29.
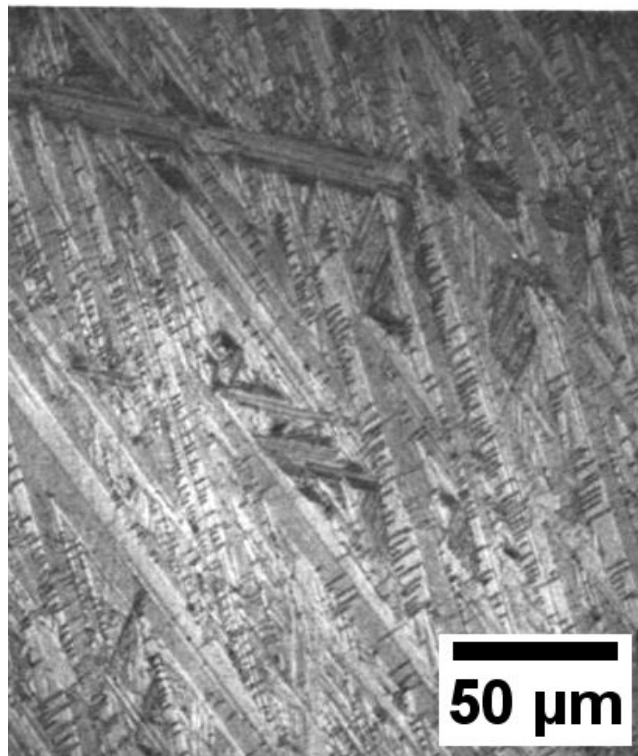
Figure 2.28: Etched microstructure of the martensitic β_1' showing fine twinning structure within the martensite plates (adapted from [146])
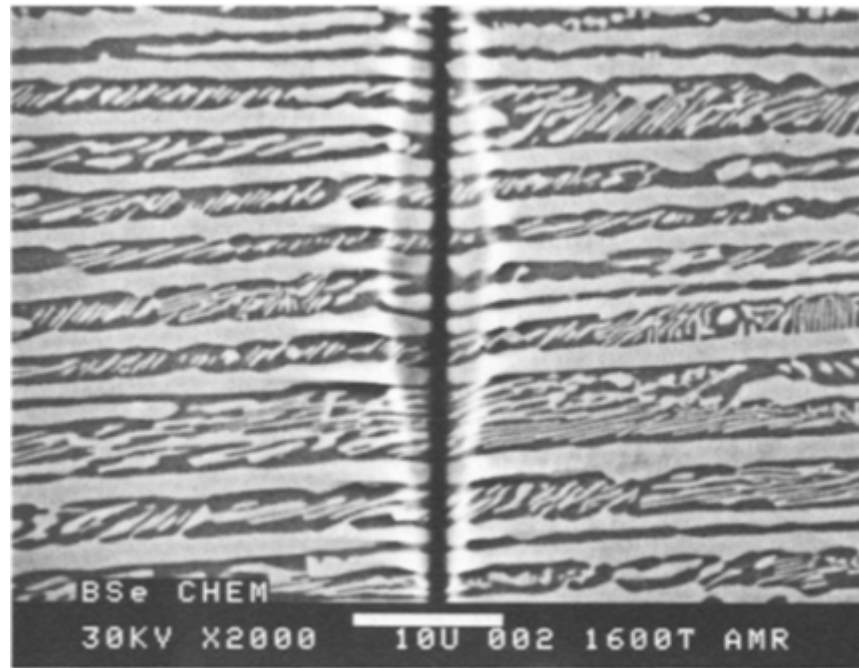
Figure 2.29: Backscattered electron image showing the microstructure of the Cu-12 wt.% Al alloy with eutectic structure [146]

The results from dry sliding wear tests show that the alloy with eutectoid microstructure has higher specific wear rate (1.86×10^{-4} mm^3/Nm) than the alloy with martensitic structure (1.40×10^{-4} mm^3/Nm for water quench and 1.44×10^{-4} mm^3/Nm for electron beam melted). This is due to the presence of subsurface cracks, which were observed to form in the brittle γ_1 phase. Propagation and coalescence of these cracks lead to the higher wear rates observed. In the alloy with martensitic structure, subsurface cracks were not observed. Post-test characterisation of the alloy with martensitic β_1' phase showed that the deformation is localized to within the twin boundaries. The energy dissipation through the interfaces between the martensite plates-matrix and the micro twins-central martensite laths, are thought to dissipate the stress induced by sliding, which contributes to the reduction in deformation. This leads to the lower specific wear rate [146].

The wear characteristic of the alloy with martensitic β' structure was investigated by Shi et al. [149]. The martensitic structure was obtained by electron beam melting of Cu-9.2Al-4Fe alloy. Compared to the alloy with solid solution (Cu) phase structure, the crack length and the depth of the deformed layer is lower in the alloy with martensitic β' structure as shown in Figure 2.30. The presence of these subsurface cracks leads to the failure by delamination as discussed in section 2.1.2. Unlike the β₁' martensite, the β' martensite undergoes a transformation into the solid solution (Cu) phase after the wear process [149]. This observation suggests that the β₁' martensite is more stable than the β' martensite.
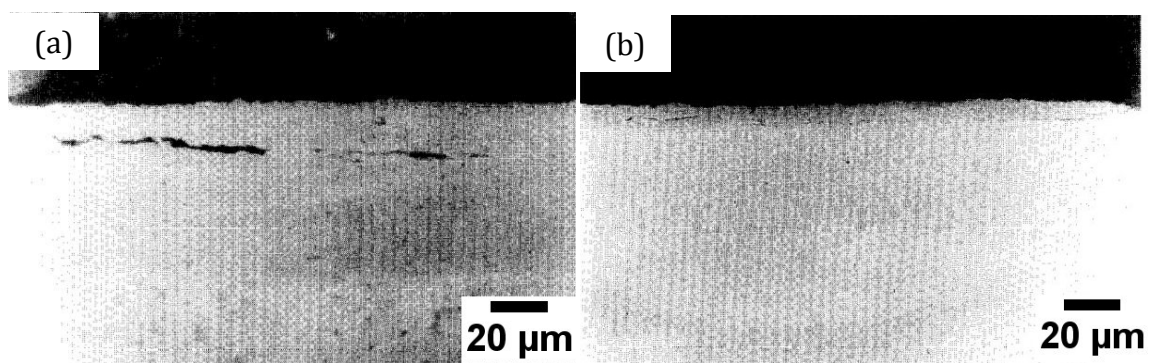
Figure 2.30: Optical images showing the subsurface microstructure of the Cu-9.2Al-4Fe alloy with (a) (Cu)+κ₁ structure and (b) martensitic β' structure after dry sliding wear test

2.4.2   The influence of surface oxide on the friction and wear resistance of aluminium bronze alloys

In addition to the microstructural features, surface oxides also have strong influence on the friction and wear resistance of the alloy. In alloys with high Al content, surface segregation of Al by diffusion through the grain boundaries increases the concentration of Al near the surface as shown in Figure 2.31 [150]. The concentration of Al at the surface increases with the temperature and the amount of Al present in the alloy. The main driving force behind the segregation of Al to the surface is to minimize free energy. Differences in atomic radii between the solute Al and Cu lead to micro-stress and high free energy.

This can be minimized by diffusion to region with low free energy such as near the surface or grain boundaries. The other factor that can promote high free energy is vacancy in the solute metal. Consequently, these solute metals are attracted to regions in the material with high electron density by coulomb interaction. Regions near the surface are reported to have higher electron vacancy than in the bulk of the material [150] . This attracts high vacancy solute metal to the surface.
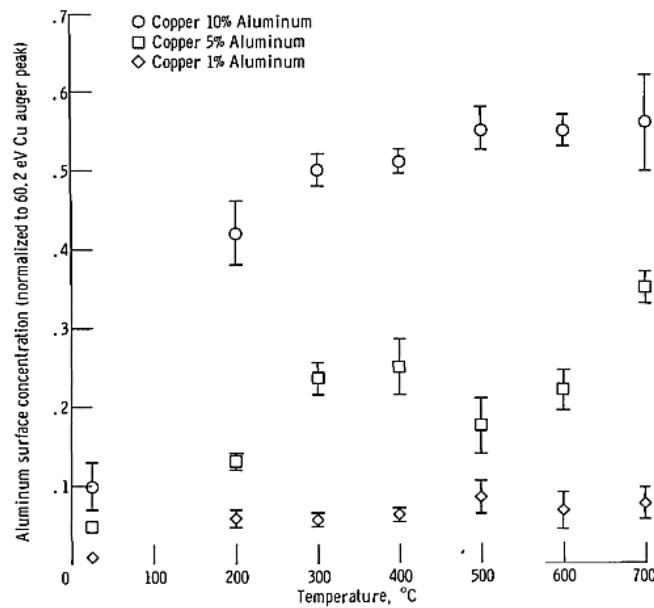
Figure 2.31: Effects of temperature on the concentration of Al at the surface for different Cu-Al alloys [150] (error bars represent standard deviation of repeated experiments)

The increase in Al content at the surface promotes formation of Al_2O_3 [151]. Poggie et al. [152] investigated the effects of Al segregation on the adhesive wear behaviour of solid solution aluminium bronze alloys with Al content of 1 wt.%, 4 wt.% and 6 wt.% during dry sliding wear test against sapphire. Their results show that presence of Al_2O_3 increases the adhesive wear and transfer of materials to the sapphire counter material. This is due to the differences between the mechanical properties and the crystal structure of the Al_2O_3 oxide the solid solution alloy. The compatibility of the oxides to the substrate is governed by the thermodynamic stability of the oxides formed.

Oxides formed from elements, which are active in oxygen such as Al, form stable oxide layer over the surface of the substrate. As the stability of the oxides layer increases, adhesive wear also increases. This is because the adhesive strength between the oxide layers and the counter material is greater than the cohesive strength of the substrate material. Thus during sliding, the shearing takes place within the substrate material (see Figure 2.4), this leads to transfer of material from the substrate material to the counter material.

2.4.3   Summary

Wear of aluminium bronze alloy is influenced by the microstructure and the properties of the surface oxide. Abrasive and delamination wear are the two primary wear mechanisms. The alloys with martensitic β_1' structure appears to have the highest wear resistance due to the absence of subsurface cracks which are present in all other microstructures. It is also worth noting that there is very limited information on the wear properties of the alloy with $(Cu)+\beta_1$ structure. The presence of the intermetallic κ_1 phase in solid solution (Cu) phase alloy was reported to have detrimental effects the wear resistance. However, the effects of the κ_1 phase in martensitic alloy remains to a large extent unknown. Regarding the optimum microstructure for maximum wear resistance, for solid solution alloy Li et al. [99] postulated that the optimum microstructure has soft phase to hard phase of 67:33 (volume fraction) and an average α phase grain size between 33 and 46 μm. Further investigations are required to confirm if this microstructural optimization approach also holds for martensitic alloys.

2.5   Corrosion resistance of aluminium bronze alloy

The corrosion resistance of aluminium bronze is a result of a stable surface oxide film, which readily reforms when damaged. The chemical composition and heat treatments have a strong influence on the corrosion rate of the alloy. This section begins with a discussion on the effects of alloying elements and heat treatments on the corrosion of aluminium bronze alloys.

2.5.1   Surface oxide on aluminium bronze alloy

The surface oxide film on aluminium bronze alloy is approximately 900-1000 nm thick and mainly consists of aluminium-rich oxide layer adjacent to the base metal and a Cu-rich layer in the outer region. Additionally, oxides of Ni and Fe may also be present [151]. In Cu-10 wt.% Al alloy, formation of the oxide is achieved by rapid formation of the Cu_2O from which a layer of Al_2O_3 is formed at the interface between the oxide and the base metal as shown by the schematic in Figure 2.32. The Al_2O_3 acts as a protective layer that is highly impermeable. Ionic transport across the oxide layer is limited. This reduced the corrosion rate. The corrosion resistance of the alloy increases with the Al content [153].
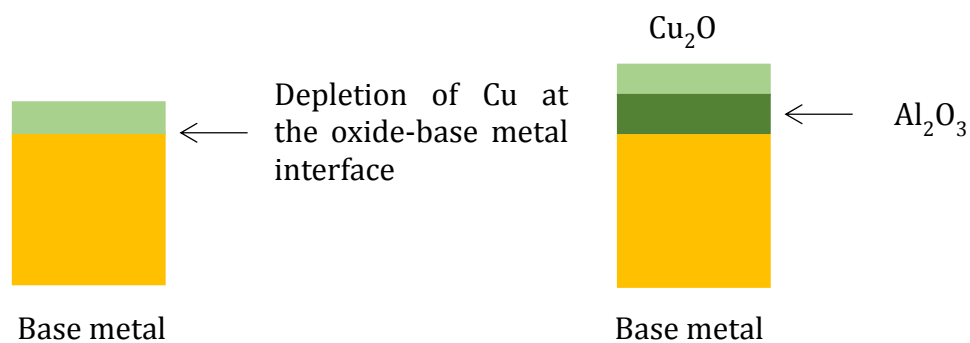
Figure 2.32: Schematic showing formation of surface oxide on aluminium bronze alloys

2.5.2   Influence of alloying elements and heat treatments on the corrosion resistance

Similarly to the mechanical properties, the alloying elements have a strong influence on the corrosion resistance of aluminium bronze alloy. In this subsection, the effects of alloying elements on the corrosion resistance of the alloys will be discussed.

The effects of Al on corrosion resistance

The influence of Al content on the corrosion resistance of the aluminium bronze alloys has not been investigated over a while range [15]. The corrosion resistance of the Cu-Al alloy increases with the Al content up to approximate 8 wt.%, which represents the limits for the solid solution (Cu) phase alloy (see Cu-Al phase diagram in Figure 2.12). These alloys are commonly used in pumps, valve and impeller due to their resistance to cavitation erosion and impingement attack [154]. As the Al content increases above 8 wt.% the high temperature β phase appears as shown in the Cu-Al phase diagram in Figure 2.12. Duplex (Cu)/β alloys have higher strength than the solid solution alloys, however, upon slow cooling the eutectoid decomposition of the high temperature β phase leads to the formation of the highly corrosive (Cu)+γ_1 structure. The γ_1 with nominal composition Cu_9Al_4 has substantially higher Al content than the (Cu) and β phase. This has significant effects on the electrochemical potential. The potential difference between the cathodic (Cu) phase to the anodic γ_1 is reported to be as high as 100 mV [16]. Therefore, the presence of these two phases in the microstructure leads to high corrosion rate. Alloys with continuous γ_1 were found to have 5-6 times higher corrosion rates than alloy with (Cu)/β structure, while isolated γ_1 only result in minor pitting [155]. To avoid this corrosion structure, several measures can be applied. The addition of Ni, Fe and Mn are known to stabilized the β phase and enables lower cooling rate to be used [15]. The influence of cooling rates and Al content on the formation of the corrosion (Cu) + γ_1 structure is shown in Figure 2.33. To utilize the advantages of high Al content, the maximum cooling time from 900 - 400 °C must be less than 2 minutes. For large section, this cooling rate might not be possible.

However, with the introduction of rapid cooling technique such as PTA, the high cooling rates of $10^2 - 8 \times 10^3$ K s^{-1} can be achieved [100] . This opens up new possibility for potential improvement in the corrosion resistance of the Cu-Al alloy.
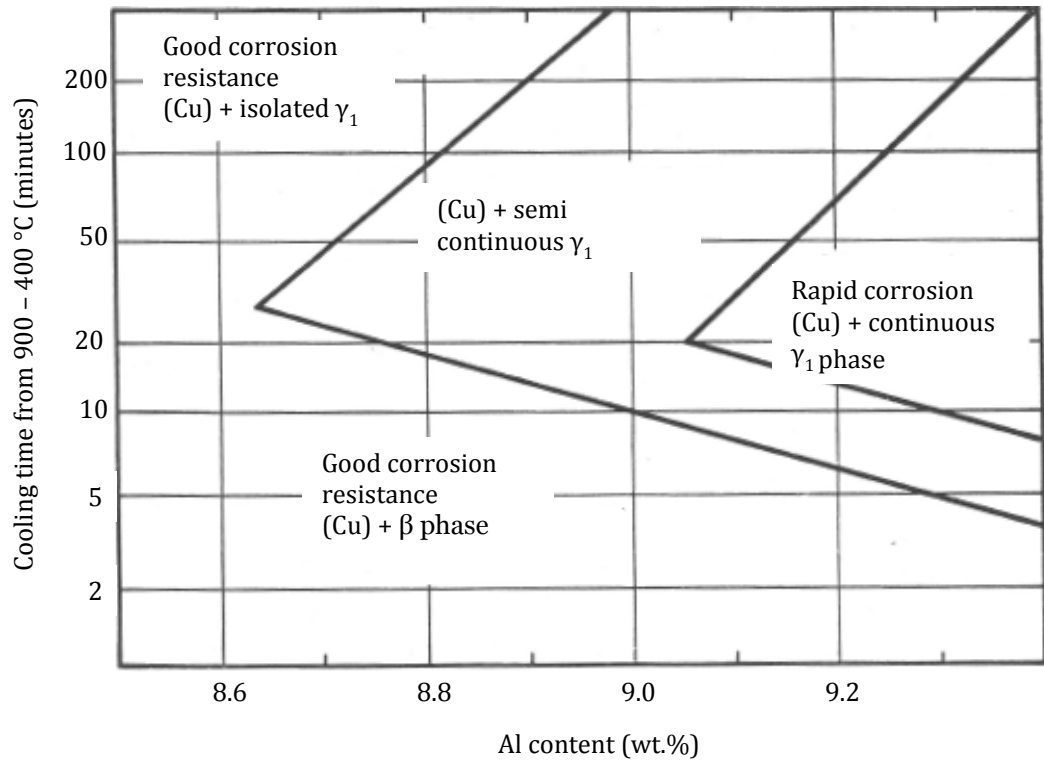
Figure 2.33: Effects of Al content and cooling rates on the corrosion resistance of Cu-Al alloy (adapted from [15])

The effects of Fe on corrosion resistance

The solubility of Fe in the Cu-Al alloys is limited as indicated by the Cu-Fe phase diagram in Figure 2.20. Macken and Smith [15] reported that for (Cu) phase alloy, the addition of 3.5 wt.% Fe has no effects on the corrosion resistance of the alloy. However, Collins et al. [133] reported that for rapidly solidified (Cu) phase alloy, the retention of up to 8 wt.% Fe by rapid solidification leads to an increase in corrosion resistance. For the duplex (Cu)/β, the addition of Fe enables the β phase to be retained at a much lower cooling rate. The formation of Fe-rich phases also prevents continuous formation of the γ_1 [15]. However, this effect has not been studied over a wide composition range of Fe, particularly for alloys with Al > 10 wt.%.

The effects of Ni on the corrosion resistance

The addition of small amount of Ni to duplex (Cu)/β alloy significantly reduced the decomposition of β phase in to the corrosive (Cu) + γ_1 structure and enables it to be retained at a significantly slower cooling rate. This effect is the most pronounced in Cu-Al-Fe-Ni alloy, which are also known as nickel aluminium bronze (NAB) with a typical nominal composition Cu-10Al-5Fe-5Ni. In NAB alloys the β breaks down progressively at 950 °C – 750 °C into a finely distributed Fe-Ni-Al phase in the (Cu) phase matrix. This microstructure contains very little β phase and no γ_1 phase which results in high corrosion resistance and high tensile strength. Consequently, NAB is one of the most widely used aluminium bronze alloys in corrosive environment. Its microstructure and corrosion resistance has been investigated by a number of authors [156][157][158][159][159]. Due to the wide composition range of the Fe-Ni-Al phase, this phase can be anodic or cathodic to the matrix phase. However, in alloy containing 4-5 wt.% each of Ni and Fe, this effect is not significant.

The effects of Mn on the corrosion resistance

Similarly to the Fe and Ni, the addition of Mn enables the β phase to be retained at a lower cooling rate. The addition of 6 wt.% Mn has been reported to be sufficient to prevent the eutectoid decomposition of the β phase for all commercial cooling rates [15]. However, under condition of limited oxygen, alloys containing Mn are susceptible to crevice corrosion. The depth of corrosion penetration was is proportional to the content of Mn in the alloy (up to 2 wt.%). Therefore, in Cu-Al-Fe alloy, the Mn content is typically limited to 0.75 wt.%.

2.5.3   Dealuminification and electrochemical corrosion of aluminium bronze alloys

The corrosion of aluminium bronze alloys can take place by several mechanisms depending on the operating environment. These include: dealuminification, stress corrosion, impingement corrosion and electrochemical corrosion. Joining of aluminium bronze alloys to another metal such as in the form of surface coating can lead to galvanic effects that can result in dealuminification and electrochemical corrosion. In this section, effects of aluminium bronze microstructure on its resistance to dealuminification and electrochemical corrosion will be discussed.

Dealuminification of aluminium bronze

The preferential removal of aluminium from aluminium bronze exposed to an aggressive environment is termed dealuminification. This corrosion mechanism is analogous to the dezincification observed in brasses. Dealuminification is promoted by the lack of oxygen. The corroded surface damaged by dealuminification process is characterised by a porous copper structure and loss of mechanical strength. Alloys in the α phase region of the Cu-Al phase diagram is not effected by dealuminification [160]. However, in duplex (Cu)/β alloy dealuminification is observed. Han and Zhao [161] reported that the in Cu-9Al-2Mn alloy, the β phase is preferentially attacked during dealuminification process. Duplex alloys with continuous γ_1 network in α matrix are also known to suffer from dealuminification. The interconnected highly anodic γ_1 phase is known to form a path for selective dealuminification to occur through the entire structure [162]. This results in high corrosion rate.

Previous works on the electrochemical corrosion of aluminium bronze alloys

Although the electrochemical corrosion of Cu-based alloys such as Cu-Ni and NAB have been extensively studied in a various environment [163], there has been little work directed to the study of the electrochemical behaviour of the Cu-Al alloy, particularly those with martensitic microstructure. In chloride media, the de-alloying rate of Al from the alloy is proportional to the Al content and is also dependent on the kinetic rate of solid-state diffusion of Al atom to the outer

surface of the alloy [164]. This situation is expected to occur in condition where there is insufficient oxygen for the protective oxide layer to reform. Alfantazi et al. [164] investigate the electrochemical behaviour of Cu-8Al-2Fe alloy, Cu-Zn, Cu-Ni and Cu in 1M NaCI solution. Their electrochemical corrosion results show that the Cu-8Al-2Fe alloy suffered from dealuminification. This observation is also consistence with that of Benedetti et al. [165] who investigated the electrochemical corrosion of Cu- 5.2 wt.% alloy in 0.5M NaCI solution. Elsayed et al. [166] investigated the electrochemical behaviour of Cu- 7 wt.% Al alloy in concentrated 1-8 M NaOH solution. Their results also show that the alloy suffered from selective dealuminification. The electrochemical potential and the alkaline concentration were reported as being the dominant factors that control the dealuminification. Grains orientated parallel to the {111} plane was reported to be selectively dissolved. Based on the review of the literature the electrochemical corrosion of aluminium bronze is dependent on the following factors: (i) the standard reversible potentials of the major alloying element has a strong influence on the electrochemical corrosion behaviour. Some of the standard reversible potential of Cu, Al, Fe and Ni are shown in Table 2.11. Due to the closer potential between Cu and Ni compared with Cu and Al, de-alloying of Ni in Cu-Ni alloy is more difficult. Therefore, minimizing the potential difference between the phases or eliminative the presence of different phases is expected increase resistance to de-alloying.

Table 2.11: Standard electrode potential of Cu, Al, Fe and Ni [36]

Electrode reaction	Standard electrode potential (V)
$Fe^{3+} + e^- \rightarrow Fe^{2+}$	+ 0.771
$Cu^{2+} + 2e^- \rightarrow Cu$	+ 0.340
$Ni^{2+} + 2e^- \rightarrow Ni(s)$	- 0.250
$Al^{3+} \; 3e^- \rightarrow Al$	- 1.662

The kinetic of the solid-state diffusion is also another important factor. In aerated NaCI solution the electrochemical corrosion of aluminium bronze alloy can be, at first approximation, the same as that of Cu [167]. The anodic dissolution of Cu is the dominant reaction. The anodic and cathodic reactions involved in the corrosion process are [167]:

Anodic dissolution of Cu $Cu - e^- + 2Cl^- \rightarrow CuCl_2^-$ Equation 2.5

Cathodic reduction of oxygen $O_2 + 2H_2O + 4e^- \rightarrow 4OH^-$ Equation 2.6
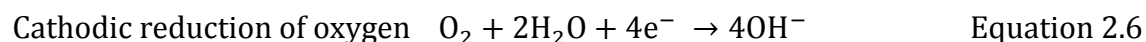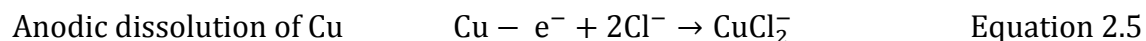
The presence of protective oxide film prevents the transport of species from the base metal to the surrounding solution; this limits the reaction rate, which reduces the corrosion current. Previous electrochemical studies of Cu-Al alloy and pure Cu in different media [165] [166] shows that the nature of the oxide is also dependent on the media in which the sample is immersed. The effects of the solution on the type of oxide formation are outside the scope of the present research. The review of the literature thus far shows that the majority of the previous works focus mainly on the corrosion of Cu-rich phases; however it is also important to consider the role of the constituent phases such as the Fe_3Al intermetallic κ_1 phase. García-Alonso et al. [168] investigate the corrosion behaviour of Fe_3Al type intermetallic phase in chloride solution. Their results show that the intermetallic phase has higher pitting corrosion resistance than 316L stainless steel; however its capacity to passivate is less than that of the stainless steel.

The presence of non-metallic inclusions on the surface of the intermetallic has been found to prevent passivation and increase the pitting corrosion. Rao [169] reviewed the electrochemical corrosion of Fe aluminides and showed that the corrosion resistance of Fe aluminide intermetallic is higher than that of its alloying elements (Fe and Al). However, its ability to re-passivate is slower than that of stainless steel. The additions of Cr and Mo have been reported to improve the passivation of the Fe aluminide. The condition of specimen surface finish is also known to have an influence on the electrochemical behaviour. The majority of the works reported in the literature were obtained from specimens that have been polished flat. Preparation of the specimen effects the composition and thickness of the air form oxide film. For as-polished pure copper at room temperature, a layer of Cu_2O 2.5 nm thick is formed [163]. Since the oxide layer has strong influence on the corrosion behaviour, careful consideration of the preparation technique should be made. In the present research the surface of the specimen were polished flat and were left in air for 24 hours prior to all tests.

2.5.4   Summary

The corrosion resistance of aluminium bronze alloys is dependent on formation of protective Al_2O_3. This is dependent on the presence of Al solute in the alloy. However, as the Al content in the alloy increased, the faster cooling rates are also needed to prevent the eutectoid decomposition of the high temperature β phase into a highly corrosive (Cu) + γ_1 structure. Therefore, rapid solidification techniques such as PTA can be used to prevent the eutectoid decomposition and utilized the advantages offered by alloys with high aluminium content.

3. Experimental methodology

This chapter begins with a description of the coating production process and a brief discussion on the effects of Ce addition on the morphology of the powder. Test methodologies used for microstructure characterisation, tribological and corrosion tests are presented at the end of the chapter.

3.1   Coating production

There are two stages in the coating production process. The Cu-Al-Fe aluminium bronze powders were first produced by gas atomisation in nitrogen atmosphere with cooling water and subsequently deposited onto an E.N. 10503 steel substrate using the plasma transferred arc (PTA) technique.

3.1.1   Gas atomisation of Cu-Al-Fe powder

Primary component metals consisting of Cu, Al and Fe with electrolytic purity of 99.95 % were melted in an induction furnace shown in Figure 3.2. Rare earth element Ce was added to the molten alloy prior to the final deoxygenating stage (see Figure 3.1) to reduce impurities such as O, H and S that may be present in the molten alloy. Due to the high thermal conductivity of the molten alloy, it is critical to heat the alloy to 1180 °C – 1240 °C before pouring into the gas atomisation chamber via a ceramic funnel as shown in Figure 3.2. Further details on the melting process used can be found in reference [170]. During atomisation, nitrogen gas is introduced to the stream of molten alloy. This creates turbulent flow as the gas expands into the large collection volume. The turbulent flow separates the stream of molten metal and rapidly reduces its temperature, which leads to formation of spherical powder that is collected in the bottom of the large expansion volume (see Figure 3.3 b). The powders formed are then separated into different sizes by centrifugal particle separator shown in (Figure 3.3 b)
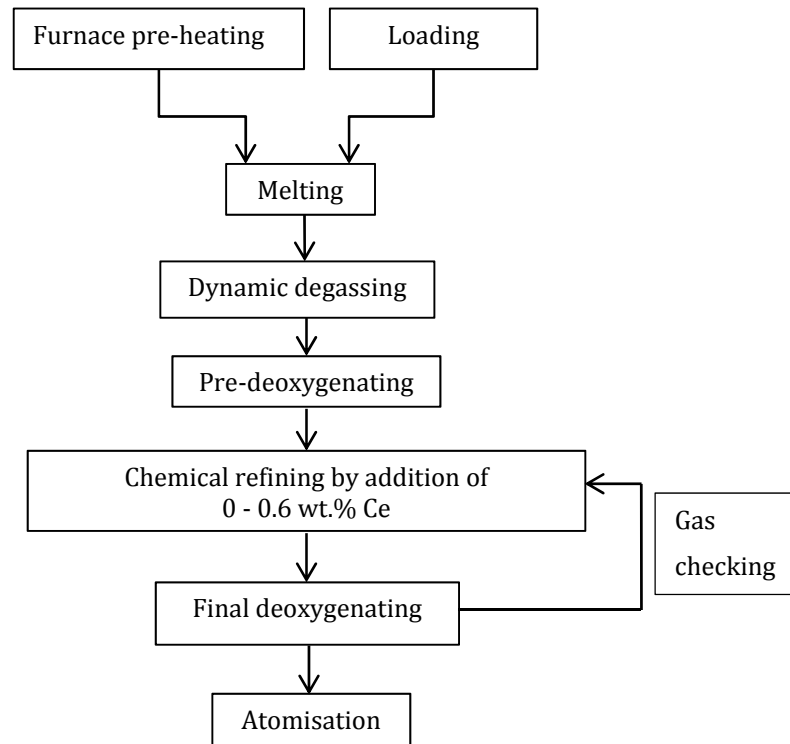
Figure 3.1: Schematic showing the joint charging single-melt technique (adapted from [170])

Figure 3.2: An induction furnace loaded with component metal, an atomisation chamber inlet with ceramic funnel attached
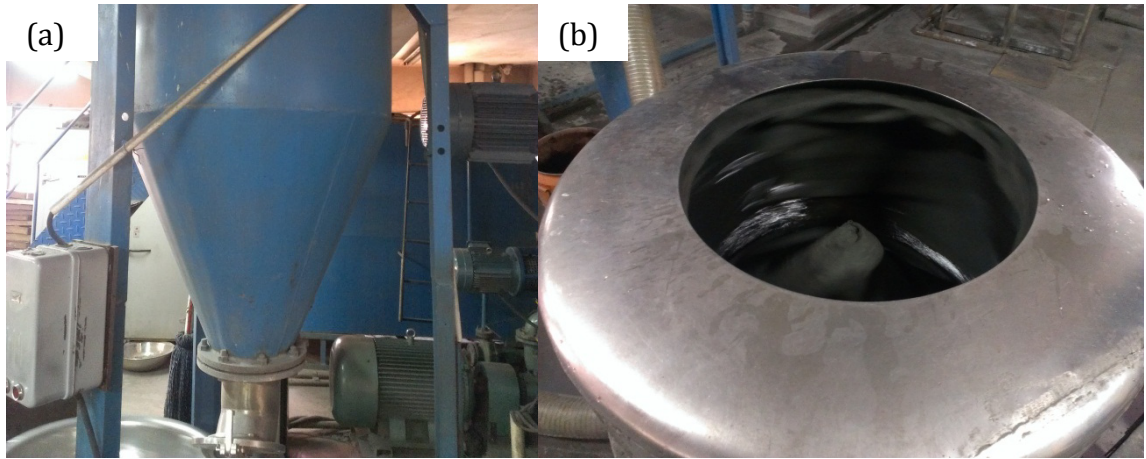
Figure 3.3: (a) The bottom section of the large collection volume and (b) a centrifugal powder separator

Effects of Ce on the morphology of the powder

The effects of Ce addition on the powder morphology are shown in Figure 3.4. The addition of Ce decreases the powder size and increases the number of powder with spherical geometry. The addition of 0.3 wt.% Ce leads to the powder with the smallest diameter. Further increase in Ce addition leads to an increase in powder size as shown in Figure 3.5.
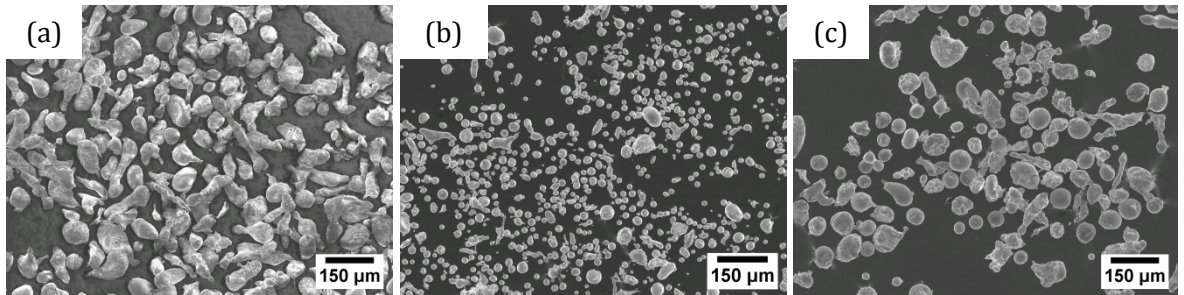
Figure 3.4: Secondary electron images showing the effects of Ce addition on the morphology of the Cu-Al-Fe powder with (a) 0 wt.% Ce, (b) 0.3 wt.% Ce and (c) 0.6 wt.% Ce

The chemical composition of the powders as determined by EDS analyses is shown in Table 3.1. The results show that an insignificant amount of Ce is present in the powder.

Due to the high reactivity of Ce, it is expected to combine with impurities in the molten alloy to form oxides such as Ce_2O_2S and CeS through these possible reactions shown in Equation 3.1 and Equation 3.2 respectively [171]:

$$2Ce + 3O + S \rightarrow Ce_2O_2S \qquad \text{Equation 3.1}$$

$$Ce + S \rightarrow CeS \qquad \text{Equation 3.2}$$

These oxides have high atomic mass (344.295 g/mol and 171.181 g/mol respectively [172]) and are expected to remain at the bottom of the furnace and thus are not transferred to the atomization stage. This chemically refines the motel alloy the molten alloy.
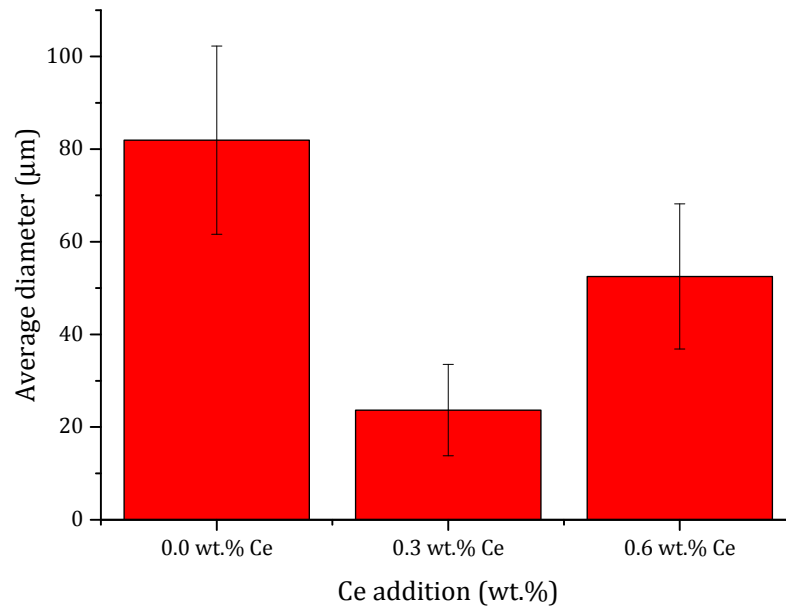
Figure 3.5: The effects of Ce addition on the diameter of the gas atomized powder

Table 3.1: Chemical compositions of the Cu-Al-Fe powders (all in wt.%)

Ce addition	Cu	Al	Fe	Mn	Ni	Si	Ce
0.0	76.9	16.2	4.4	0.6	1.3	0.5	0.0
0.3	77.4	14.4	5.7	1.0	1.3	0.8	0.0
0.6	76.2	15.7	4.7	1.0	0.7	0.2	0.2

In the present research all coatings were produced from spherical powder with diameter between 50-150 μm was used. This is to increase the deposition efficiency [100]. Spherical geometry allows regular alignment of the powder during the injection stage of the PTA deposition.

3.1.2   PTA deposition of the coating onto steel substrate

In the second stage, the coating was produced from the gas-atomized powder by deposition onto an E.N. 10503 steel substrate disks (Ø 108 mm x 20 mm) using plasma transferred arc technique (PTA) shown in Figure 3.7. The composition of the E.N. 10503 steel substrate as determined by EDS analysis is shown in Table 3.2. The steel is used in as received condition with hardness of ~ 200 HV.

Table 3.2: Averaged EDS composition of the E.N. 10503 steel substrate (all in at.%)

Fe	C	Si	P	Cr	Mn
98.22	0.63	0.27	0.05	0.09	0.73

Prior to deposition by PTA, the surface of the steel substrate was roughened using a hand grinder with wheel roughness of 300 mesh as shown in Figure 3.6 a. This is to remove existing oxide layers and to assist mechanical bonding between the coating and the steel substrate.
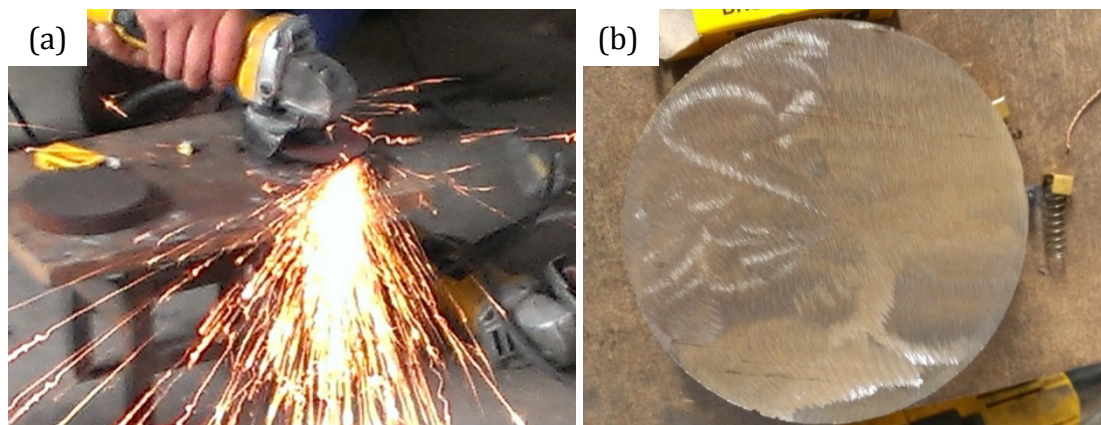
Figure 3.6: (a) Use of hand grinder to increase the surface roughness of the steel substrate (b) surface of the steel substrate prior to PTA

The steel substrate was loaded into the PTA system as shown in Figure 3.7. Argon gas shielding was used to minimize oxidation during the deposition process. During the deposition process, the nozzle moved in a reciprocating motion in the x-direction and the stage is rotated in a clock-wise direction.
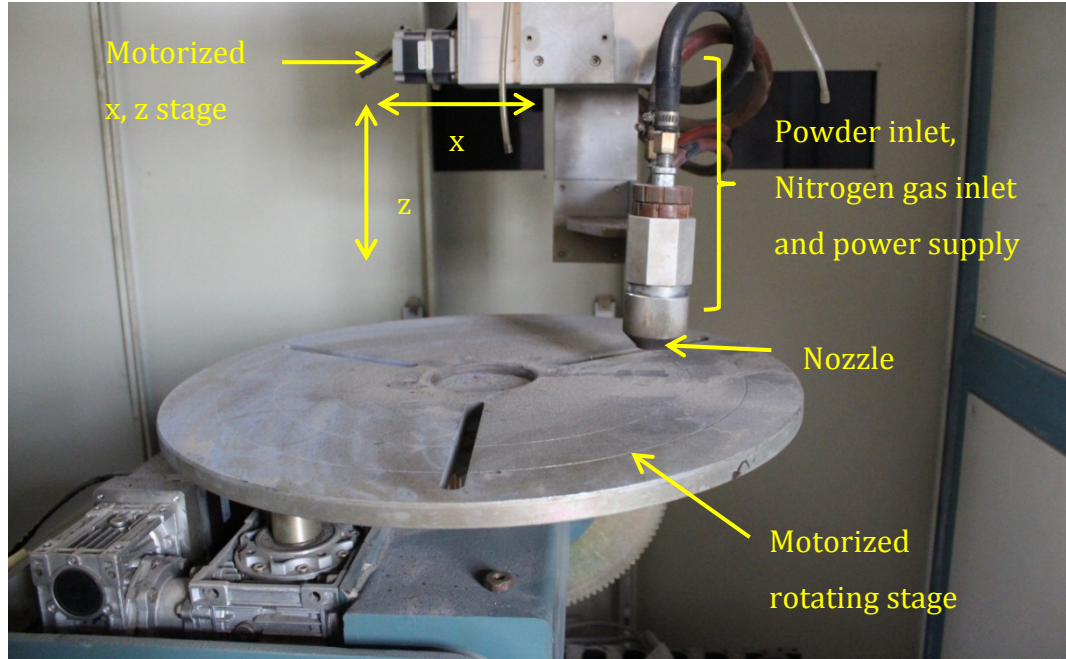
Figure 3.7: PTA configuration used for the deposition of the aluminium bronze coatings

To evaluate the effects of substrate melting on the microstructure and properties of the resulting coating, the PTA parameters (current, nitrogen flow rate, powder feed rate and spray distance) were adjusted in the range given in Table 3.3 to increase the heat input during deposition. Four levels of heat input during deposition were employed resulting in four coatings. The time taken for the deposition process is ~ 60 minutes per sample. Following the deposition the coating was air cooled to ambient temperature.

Table 3.3: PTA parameters used for deposition of the aluminium bronze coating

Parameters	
Current	165-170 A
Nitrogen flow rate	3-6 L min^{-1}
Powder feed rate	1-3 g s^{-1}
Spray distance (z)	5-10 mm
Stage rotation speed	0.05 rpm
Nozzle speed (x-direction)	15 mm s^{-1}
Final thickness	3 mm

3.2   Microstructure and mechanical properties characterisation

3.2.1   Sample preparation procedure

Specimen for microstructure and mechanical properties characterisation were sectioned using electrical discharge machining (EDM) into cylindrical sample from which a cross section and a top surface sample where obtained as shown in Figure 3.8. Following the sectioning, the samples were then prepared for characterisation using three different techniques described in Table 3.4. Due to the different phases expected in the coatings, several preparation techniques are required to reveal the different microstructures.
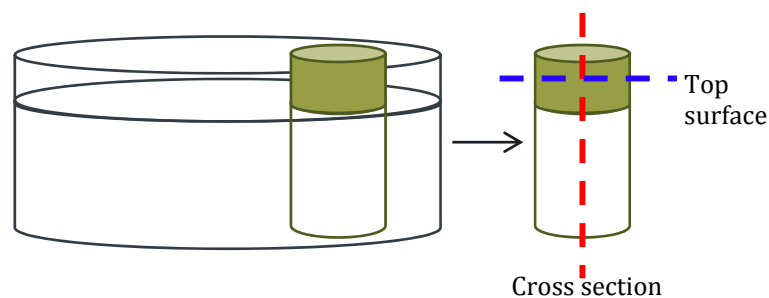
Figure 3.8: Schematic showing sectioning of specimen for microstructure and mechanical properties characterisation

Table 3.4: Summary of specimen preparation techniques

Techniques	Description	Usage
Metallographic preparation	Specimen was ground on 120, 800, 1200, 4000 grit SiC paper followed by polishing with 6 μm and 1 μm diamond polishing	Phase identification, friction tests, hardness tests and corrosion tests
Electro-polishing	Specimen was electro-polished using 20 % HNO_3 + 15 % 2-butoxyethanol + 65 % methanol solution cooled to -30°C. Polishing time was 30 s at 20V	EBSD and phase identification
Etching	Specimen was etched using solution containing 5 g $FeCl_3$ + 10ml HCI + 250 ml distilled water	Phase identification

3.2.2   SEM, EDS, EBSD and XRD

The microstructures were examined using a JEOL-JSM6500F scanning electron microscope (SEM) operating at 15 kV and a working distance of 10-11 mm. The SEM is equipped with a HKL Channel 5 EBSD system and an Oxford Inca EDS system. The EBSD analyses were used to provide crystallographic information on individual grains and the associated grain boundary misorientation angles. EBSD mapping was carried out with an accelerating voltage of 15 kV, the specimen was tilted to 60 ° with a working distance of 18 mm. Step sizes of 500 and 1000 nm were employed. EDS analyses were used to obtain quantitative and qualitative compositional information. Point, line and area EDS analyses were carried out with an accelerating voltage of 15 kV and working distance of 10-11 mm. With regards to the detection limits of EDS, a value of ± 0.1 wt.% has been reported in the literature [173]. For phase identification, X-ray diffraction was carried out using PXD Benchtop D2 Phaser with Cu K_α ($\lambda = 0.154056$ nm) radiation. The scanning rate used was 0.02 °/s and step of 5 s.

3.2.3   Depth-sensing nano-indentation

The depth-sensing nano indenter shown in Figure 3.9 was used to produce a hardness map of the top surface of the coating and across the interface between the coating and the steel substrate. The top surface map consists of 196 (14 x 14 indents) and the map across the interface consists of 150 or 200 indents (10 x 15 or 10 x 20 indents). The values chosen were based on sample size and time restriction. The nano indenter was operated in depth control mode using a Berkovich indenter tip with a face angle of 65.3° and a typical tip radius of 50-100 nm [174]. The other parameters used are shown in Table 3.5.
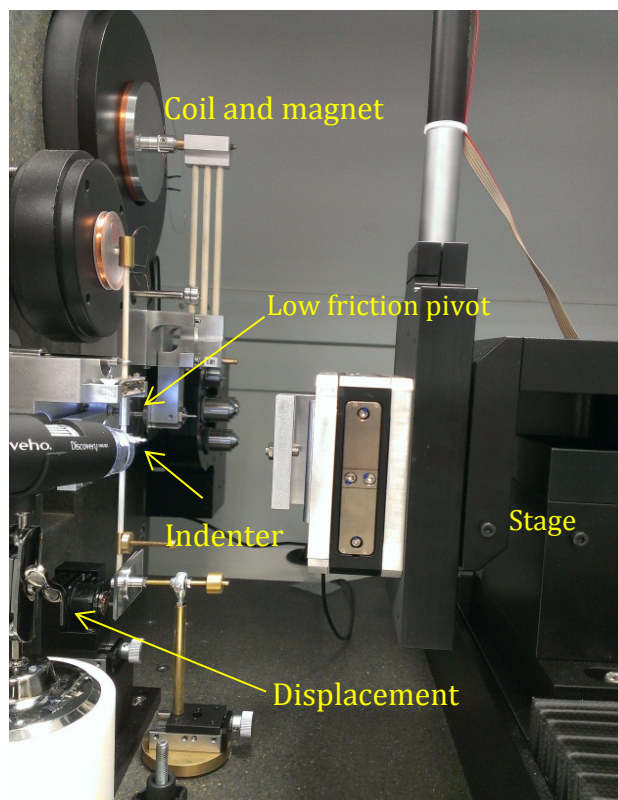
Figure 3.9: Micro Materials NanoTest® Depth sensing nano-indenter

In each cycle, the indenter is brought into contact with the specimen surface. A capacitive transducer is used to monitor the position of the indenter. The load is applied by an electromagnetic force from the coil and magnet located at the top of the pendulum, which is supported by a low friction spring fixture (see Figure 3.9).

Due to the small residual imprint of the indent, the load F versus displacement h hysteresis (shown in Figure 3.10) was recorded for each indent and was subsequently used to calculate the indentation hardness and reduced modulus.

Table 3.5: Parameters used for depth control indentation

Parameters	
Initial load	0.02 mN
Cut off load	0.1 mN
Loading and unloading rate	1 mN s^{-1}
Maximum depth	500 nm
Dwell time at maximum depth	40 s
Number of indents	196 (surface), 150 and 200 (cross section)
Spacing between each indent	15 μm
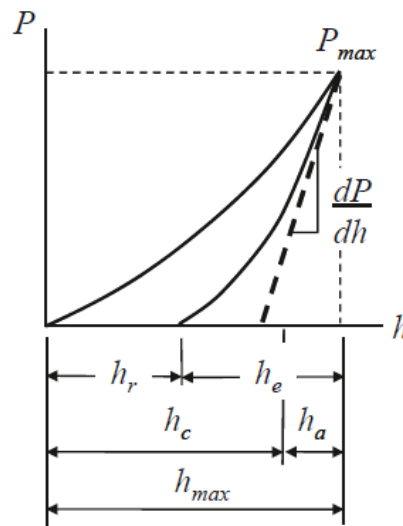
Figure 3.10: Generic load vs. displacement curve [174]

h_c	Depth beneath contact
h_r	Depth of residual impression
h_{max}	Total indentation depth to maximum load
h_e	The elastic displacement during unloading
h_a	Distance from the edge of the contact to the specimen surface at full load

The indentation hardness H (Pa) is defined as:

$$H = \frac{F_{\text{Max}}}{A_{\text{p}}}$$

<div align="right">Equation 3.3</div>

Where, F_{max} is the maximum load and A_{p} is the projected or cross sectional area of the contact at depth h_{r} beneath the contact. For an ideal Berkovich indenter with a face angle of 65.3° A_{p} is related to the depth beneath the contact h_{c} as follow;

$$A_{\text{p}} = 3\sqrt{3h_{\text{c}}^2 \tan^2 65.3} = 24.5 h_{\text{c}}^2$$

<div align="right">Equation 3.4</div>

Upon knowing h_{c} the hardness can be calculated from Equation 3.3 and Equation 3.4 by using the slope of the initial part of the elastic unloading section $\frac{dp}{dh}$ as shown in Figure 3.10. For the present study, this process is done automatically using the built-in software on the nano-indenter. However, prior to the automatic process, each load versus displacement hysteresis was individually checked to make sure that the elastic unloading section does not overlap with the loading section. If such situation occurs then the data is excluded from the analysis. The reduced modulus E^* was calculated using Equation 3.5.

$$E^* = \frac{dp}{dh} \frac{1}{2h_{\text{c}}} \frac{1}{\beta} \sqrt{\frac{\pi}{24.5}}$$

<div align="right">Equation 3.5</div>

The term β is a yield correction factor and has a typical value 1.034 for a Berkovich indenter. This value was deduced from finite element calculations and accounts for the non-symmetrical pyramidal shape of the Berkovich indenter [174].

3.3 Tribological test methodology

3.3.1 Pre-test and post-test characterisation methodology

Specimens for tribological tests were prepared by metallographic techniques as detailed in section 3.2.1. The surface roughness, micro hardness and the mass were measured before and after the wear test using the following methods.

Surface roughness measurement

Surface roughness is a measure of the surface's texture, which is quantified by the vertical deviation of the real surface from its ideal form. The form of the surface defined as the low frequency, long wavelength component of the surface. The roughness is a high frequency, short wavelength component. The roughness of the surface can be measured using a profilometer. In the present research, a stylus based and an optical profilometer were employed.

Stylus-based profilometer

The roughness of the as-polished coating surface was evaluated using a Taylor-Hobson 120L stylus-based profilometer. During the measurement, the stylus travels across the surface and its movement is amplified and recorded. Both the form and the roughness were obtained. For each sample, three line profiles were obtained using a sliding speed of 0.02 mm s^{-1} and profile length of 4.1 mm. Post-test analyses of the measured profile were conducted in compliance with ISO 4288:1966 standard [175]. The result of the all analyses is expressed in terms of the average value of the deviation of the measured profile from the ideal form R_a. Note that the R_a value does not differentiate between peaks and valleys. Therefore different profiles can have similar R_a value. However, for the present investigation, all surfaces were prepared used identical method and have similar roughness (see appendix 1), thus the R_a value provides sufficient confidence for quantitative evaluation and comparison of the as polished surface roughness.

Optical profilometer

The 3D morphology of the worn coating surfaces and the corroded coating surfaces were evaluated using an Alicona Infinity Focus IFM 2.1 optical profilometer. The 3D image is formed by combining a series of 2D images taken over a range of vertical distance between the lens and the specimen. The distance information is obtained by illuminating the specimen with a light source, which is transmitted through the optics and focused through the beam splitter.

The light reflected off the specimen is detected by a sensor that uses light interference to measure the change in sharpness as the distance between the specimen and the objective lens is varied. The specimen is in focus when the sharpness is at maximum. The distance at maximum sharpness is then recorded and the cycle is repeated until the end of the specified vertical scan range. The specification of the Alicona Infinity Focus IFM 2.1 as provided by the manufacturer is shown in Table 3.6. For all analyses the 10x objective was used. This is to ensure sufficient field of view and vertical resolution.

Table 3.6: Technical specification of an Alicona Infinity Focus IFM 2.1

Objectives	2.5x	5x	10x	20x	50x	100x
Optical lateral resolution (µm)	5.6	2.2	1.1	0.8	0.6	0.4
Minimum scan speed (µm s^{-1})	112	20	5	2.5	1	0.5
Vertical resolution at minimum scan speed (µm)	2.3	0.41	0.1	0.05	0.02	0.01
Lowest measurable Ra (µm)	7	1.2	0.3	0.15	0.06	0.03

Micro hardness measurement

The micro hardness was measured using a Matsuzawa Seiki MHT-1 micro hardness tester (certified according to BS EN ISO 6507-2 standard). A load of 1 kg and dwell time of 15 s were used for micro hardness measurement of the as polished PTA aluminium bronze coatings, the AISI D2 tool steel and the counter material pins (AISI 52100 bearing steel and AISI 316, 420 and 440 stainless steel). A load of 0.1 Kg and dwell time of 15 s was used for the micro hardness measurement of the worn surfaces.

Mass measurement and specific wear rate

All mass measurements were performed using a Sartorius ME-2355 high precision scale with sensitivity ± 0.01 mg. The specific wear rate was determined using gravimetric method. The change in mass was measured using the precision scale and is then converted into a change in volume by using the density of the material. The coatings and the AISI D2 tool steel are assumed to have density values of 8.70 g cm^{-3} and 7.76 g cm^{-3} respectively. The specific wear rate is calculated by dividing the volume by the load and sliding distance. It has a unit mm^3/N m.

Subsurface characterisation using Focused Ion Beam (FIB) and SEM-EDS analysis of the worn surfaces

The subsurface microstructure of selected worn surfaces was characterised by sectioning using Carl Zeiss Gemini NVision 40 SEM equip with a gallium ion source FIB system. For the cross sectioning the FIB was operated at 30 KeV at a working distance of 5.1 mm and specimen was tilted at 54 °. A milling current between 10-80 pA was used. All cross-sections have a maximum depth of 10 μm; this was chosen due to time restriction. Prior to the milling process, some of the surface was covered with a layer of carbon to protect the surface during the milling process. The morphology and chemical composition of the worn surfaces were also observed using SEM and EDS analyses.

3.3.2   Contact geometry and initial contact pressure

In the present research, a point-contact (spherical ball on flat plate) was used for all wear tests. The spherical ball has a diameter of 6 mm. The coating is a flat plate with radius equal to infinity. The wear characteristics of the coatings were evaluated by dry sliding test against AISI 52100. The AISI 52100 counter material was selected because it has a significantly higher hardness (~700 HV) than the coating and thus the majority of the wear is expected to be on the coating. In this part of the test four loads 5 N, 10 N, 15 N and 20 N were used to investigate the effects of the change in load on the wear characteristics of the coatings. To investigate the effects of sheet metal hardness on the coating's resistance galling, stainless steel balls made from AISI 316, 420 and 440 grades were used. For comparison, the stainless steel balls were also tested against the industrial standard AISI D2 tool steel. All tests were carried out at room temperature with no lubrication. This is to simulate the starve lubrication condition, which the coating might experience in service. For the wear tests against stainless steel, a load of 5N was used. The initial contact pressure between the coating and the counter material was calculated by using the Hertzian contact theory with the material parameters shown in Table 3.7. The Young's moduli of the coatings were obtained from nano-indentation data as detailed in section 3.2.3.

The Poisson's ratio of the coating was obtained from review of the literature [149], a value of 0.3 was used. The initial Hertzian contact pressure and indentation are presented in Table 3.8 and Table 3.9 respectively

Table 3.7: Young's moduli and Poisson's ratio used for the calculating the initial contact pressure

Material	E (GPa)	v
AISI 316SS ball	193	0.3
AISI 420SS ball	200	0.3
AISI 440SS ball	200	0.3
AISI 52100 ball	210	0.3
AISI D2	207	0.3
9Fe coating	121.7	0.3
15Fe coating	147.6	0.3
20Fe coating	165.1	0.3
37Fe coating	160.6	0.3

Prior to determining the contact pressure, the reduced radii and reduced Young's moduli were first calculated using Equation 3.6 and Equation 3.7. Body A is the stainless steel/bearing steel ball and body B is the PTA aluminium bronze coatings/AISI D2 tool steel.

$$\frac{1}{E'} = \frac{1}{2}\left[\frac{1 - v_A^2}{E_A} - \frac{1 - v_B^2}{E_B}\right] \qquad \text{Equation 3.6}$$

$$\frac{1}{R'} = \frac{1}{R_x} + \frac{1}{R_y} \qquad \text{Equation 3.7}$$

Where:

E' Reduced modulus

E_A Young's modulus of body A

E_B Young's modulus of body B

v_A Poisson's ratio of body A

υ_B Poisson's ratio of body B

R' Reduced radius of curvature

R_x Reduced radius of curvature in x direction

R_y Reduced radius of curvature in y direction

The contact area has radius a, maximum contact pressure P_{max}, average contact pressure P_{mean}, maximum indentation δ, the applied load W in N, the radius of the ball R and the maximum shear stress τ_{max} at depth Z were calculated using Equation 3.8 - Equation 3.13 which are based on Hertz's theory [117].

Contact area
$$a = \left(\frac{3WR}{E'}\right)^{\frac{1}{2}}$$
Equation 3.8

Maximum contact pressure
$$P_{max} = \frac{3W}{2\pi a^2}$$
Equation 3.9

Mean contact pressure
$$P_{mean} = \frac{W}{\pi a^2}$$
Equation 3.10

Maximum indentation
$$\delta = 1.0397\left(\frac{W^2}{E'^2 R'^2}\right)$$
Equation 3.11

Maximum shear stress at depth Z
$$\tau_{max} = \frac{1}{3}P_{max}$$
Equation 3.12

Depth at which maximum shear stress occurs
$$Z = 0.638a$$
Equation 3.13

The Hertzian theory is based on the following assumptions:

1. The two materials are homogenous
2. The yield stress is not exceeded
3. The contact stress is caused solely by the normal load and tangential forces are negligible
4. The contact area is small compared to the dimensions of two materials
5. The two materials are at rest in equilibrium and the effects of surface roughness is negligible

Assumptions 3-5 were met by controlling experimental parameters. The coatings were also polished flat and the pins were aligned to ensure it is normal to the coating surface. However, as it will be shown by the hardness mapping in section 4.1.5, the hardness of the coatings is not homogeneous. There are specific regions on the coatings that are significantly harder than the others. Hence the values obtained may underestimate the actual maximum contact pressure value. Based on the hardness results the 27Fe coating is predicted to have the highest wear resistance as shown by the low indentation in Table 3.9.

Table 3.8: Calculated initial contact pressure at 5-20 N load

Mean contact pressure (GPa)				
Load (N)	9Fe	20Fe	27Fe	35Fe
5	0.61	0.66	0.69	0.68
10	0.77	0.83	0.87	0.86
15	0.88	0.95	1	0.99
20	0.97	1.05	1.1	1.08

Table 3.9: Calculated initial indentation at 5-20 N load

Indentation (10^{-6} m)				
Load (N)	9Fe	20Fe	27Fe	35Fe
5	0.87	0.8	0.77	0.78
10	1.38	1.27	1.22	1.23
15	1.81	1.67	1.6	1.62
20	2.19	2.02	1.94	1.96

3.3.3   Dry sliding wear tests using high frequency reciprocating tribometer

Room temperature dry sliding wear tests were carried out using TE-77 high-frequency reciprocating tribometer shown in Figure 3.11. The TE-77 allows for evaluation of two specimens. The stationary specimen is mounted with two screws on a stainless steel plate. The moving specimen is mounted in a carrier head, which can accommodate a range of geometries by using a two screws clamping fixture (see Figure 3.11). The reciprocating motion is provided by a variable speed electric motor, which drives a mechanical drive unit. The mechanical drive unit (see Figure 3.12) consists of an eccentric cam, a scotch yoke and plane guide bearings that convert the eccentric motion of the cam on the drive shaft into pure sinusoidal motion.
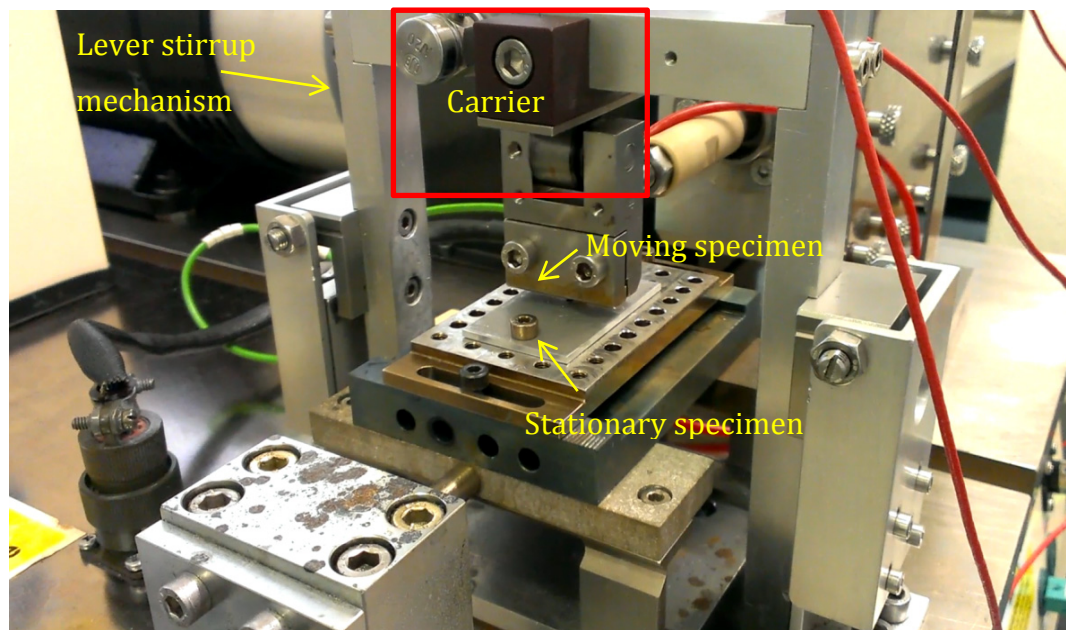
Figure 3.11: TE-77 high frequency reciprocating tribometer
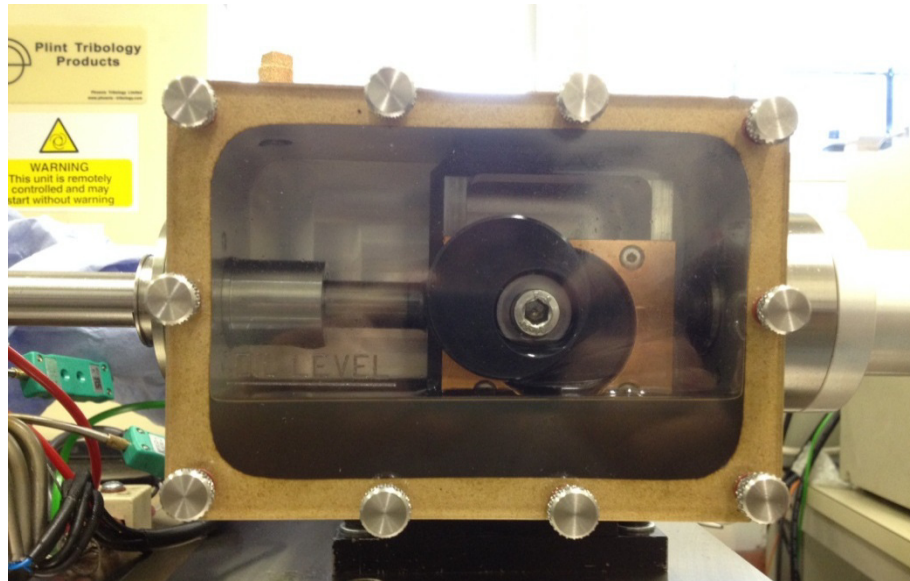
Figure 3.12: Mechanical drive unit that converts rotational motion into reciprocating motion

The load is applied by a spring acting through a lever stirrup mechanism (see Figure 3.11). The normal force is transmitted directly onto the moving specimen via needle-roller cam follower situated on the carrier head and the running plate on the loading stirrup (highlighted by red box in Figure 3.11). The applied load is measured using a strain gauge transducer mounted on the load lever. Friction force is measured using a piezo-electric transducer with sensitivity of 45.7 pC/N. The output range can be set to accommodate the range of expected friction coefficient during sliding. A charge amplifier is used to convert the charge from the piezo-electric transducer into proportional voltage signal using a fixed-scale graded mechanical unit (N/V). The coefficient of friction is calculated by dividing the measured friction force (r.m.s signal from the piezo-electric transducer) by the normal load. In addition, the contact potential and specimen temperature can also be continuously monitored. The specification of the TE-77 as given by the manufacturer is shown in Table 3.10. During the first 30 s, 900 s and the last 10 s of sliding, high-speed data at sampling rate of 1 kHz were captured. This provides friction hysteresis from which the work done to overcome the friction can be determined.

Table 3.10: Technical specification of the TE-77 high frequency reciprocating
tribometer

Contact type	Point contact, line contact
Type of movement	Sinusoidal, square and triangular
Load range	5-1000 N (in increments of 5 N)
Friction force	± 500 N maximum
Frequency of movement	1 Hz – 100 Hz

3.4   Electrochemical and immersion corrosion test
       methodology

Prior to all corrosion tests, the samples were sectioned and prepared by
metallographic techniques as detailed in section 3.2.1. For the electrochemical
corrosion tests, cylindrical specimens with a diameter of 8 mm were used. All
samples were ultrasonically cleaned in acetone for 30 minutes and dried for 24
hours prior to the test.

Test configurations and test sequence

The cylindrical sample was place into a specimen holder with a 6 mm diameter
window exposed to the solution. A rubber O-ring provides a watertight seal and
ensures that only the window area is exposed. Electrochemical measurements of
the samples were performed at room temperature in an aerated 3.5% NaCl
solution by using a Gamry Reference 600 potentiostat. For all tests, the reference
electrode is a Ag/AgCl electrode and a graphite rod was used as the counter
electrode. The specimen holders and all electrodes are protected within a Faraday
cage. The test sequence used for all electrochemical tests involve three main
stages, these are detailed in Table 3.11

Table 3.11: Summary of electrochemical test sequence

Stage	Description
Open circuit potential (OCP)	Specimen is held for 1 hour to achieve steady OCP
Electrochemical impedance spectroscopy (EIS)	Specimen is scanned at OCP over a frequency range of 100 kHz to 0.01 Hz using a sinusoidal AC voltage with amplitude of ± 10 mV
Potential-dynamic polarization	Specimen is subjected to a change in potential from -0.2 V to 0.1 V with respect to OCP at rate of change in potential of 0.167 mV s^{-1}

Following the electrochemical tests, the samples were cleaned with distilled water and dried. Post-test characterisation of the corroded surfaces and changes in chemical composition were carried out using SEM and EDS. The 3D morphology of the corroded surface and the change in surface roughness were evaluated by an optical profilometer (see section 3.3.1). Samples for immersion corrosion test were prepared by metallographic techniques as detailed in section 3.2.1. The samples were then mounted on non-conductive mount and submerge in 3.5 % NaCI solution for one week. The corrosion rates were determined by the gravimetric method outline in section 3.3.1.

4. Microstructure and physical properties of the PTA aluminium bronze coatings

The microstructure and adhesion of the coating produced by the PTA technique is strongly dependent on melting of the steel substrate during deposition. For wear protection application, it is common to increase the substrate melting to enhance adhesion at the expense of mechanical and wear resistance properties [26]. Thus to optimise the properties and adhesion, the effects of substrate melting on the microstructure of the coating must be fully understood. This section details the effects of increasing heat input resulting in elevating levels of substrate melting on the microstructure and mechanical properties of PTA Cu-Al-Fe aluminium bronzes coatings. In chapter 5 and 6 the findings from this section are used to explained failure of the coatings by wear and corrosion.

4.1   Microstructural characterisation

4.1.1   Chemical composition of the as deposited coating

In the present research, four coatings were produced from the same batch of gas atomized Cu-Al-Fe powder by deposition on to an E.N. 10503 steel substrate by using PTA technique. The compositions of the four coatings and the powder material are shown in Table 4.1.

Table 4.1: Composition of the Cu-Al-Fe powder and the coating in as-deposited condition (all in wt.%, averaged of 10 EDS from top surface of the coating)

		Cu	Al	Fe	Mn	Ni	Si	Cr
Increase substrate melting	Powder	76.9	15.5	4.6	1.2	0.6	0.2	0.2
	Coating 1	75.7	12.2	9.2	1.1	0.7	0.4	0.9
	Coating 2	67.3	8.4	21.5	1.0	1.3	0.3	0.2
	Coating 3	62.7	8.7	27.4	0.9	0.3	0.1	0.0
	Coating 4	54.8	6.8	35.3	1.0	1.2	0.3	0.6

Table 4.1 shows two important points. The Fe content in the coating is substantially higher than that of the powder. This strongly suggests that the Fe content was increased as a consequence of elevating level of steel substrate melting caused by the increase in heat input during deposition.

As the substrate melting increases, the amount of Fe in the coating also increased. To confirm that the increase in Fe is a result of substrate melting, a cross-section specimen of coating 4 was analysed by EDS as shown in Figure 4.1. Spectrum 1, 2 and 3 are EDS analyses of the splats. Spectrum 4 is the EDS analysis of the coating 4. The composition of spectrum 1, 2 and 3 closely resembles that of the powder as shown in Table 4.2. However, the composition of the coating exhibits substantially higher Fe content than the splats and the powder. This confirms that the increase in Fe content is due to melting of the steel substrate. From this point onwards and throughout this thesis the coatings will now be referred to by their Fe content as: 9Fe, 20Fe, 27Fe and 35Fe coating. This represents the four levels of heat input during deposition.
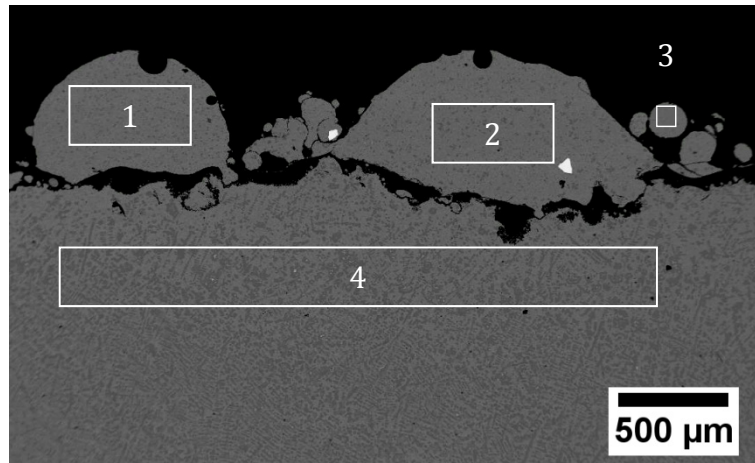
Figure 4.1: Backscattered electron image of coating 4 in as-deposited condition. The white boxes indicate position of EDS analysis

Table 4.2: EDS results of the splats (spectrum 1-3) and from within coating 4 (spectrum 4) (all in wt.%)

Spectrum	Cu	Al	Fe	Mn	Ni	Si	Cr
1	75.8	12.7	6.2	1.2	2.3	0.4	1.4
2	75.2	12.1	7.8	1.2	2.2	0.3	1.2
3	79.2	13.2	4.9	1.3	1.0	0.2	0.1
4	60.1	7.6	28.8	0.8	1.7	0.2	0.6

4.1.2   Phase identification

The increase in Fe content leads to changes to the Cu and Al content of the coating as shown in Table 4.2. The change in composition is expected to cause significant changes to the constituent phases in the coating. Phase identification was carried out using X-ray diffraction. The observed XRD patterns are shown in Figure 4.2. The identified phases in each coating are summarised in Table 4.3. The crystallographic information of the identified phases is shown in Table 4.4.

Table 4.3: Summary of identified phases in the coating

| Coating | Identified phases | | | | |
	Solid solution (Cu)	Ordered β_1	Martensitic β_1'	Intermetallic κ_1	bcc αFe
9Fe	x		x	x	
20Fe	x	x		x	
27Fe	x	x		X	
35Fe	x	x		x	x

In the previous work [21] on a coating with similar composition to the 20Fe and 27Fe coating, the following phases were identified: Cu_9Al_4 γ_1, Cu_3Al β_1 , FeAl and the Fe_3Al κ_1. However, in the present research, Cu_3Al β_1 and Fe_3Al κ_1 and (Cu) phase were identified. The possible reason for the differences in the observed phases might be due to the Al content in the coating and the cooling rate. As discussed in 2.3.1, the Cu_9Al_4 γ_1 phase is the first phase to form during the diffusion-controlled eutectoid decomposition of the ordered Cu_3Al β_1. Given that the reaction is diffusion-controlled, the presence of such phase indicates that sufficient time was given for the reaction to initiate. However, in the present research the high cooling rate achieved by the PTA process is expected to suppress the decomposition and thus the coating is retained as the ordered Cu_3Al β_1 as shown by the XRD. It is worth noting that the β_1 and κ_1 have very similar microstructure as shown in Table 4.4, thus to confirm the presence of these two phases, several complementary techniques such as EDS mapping and electro-polishing were employed. The results from that microstructure characterisation are detailed in the next section.
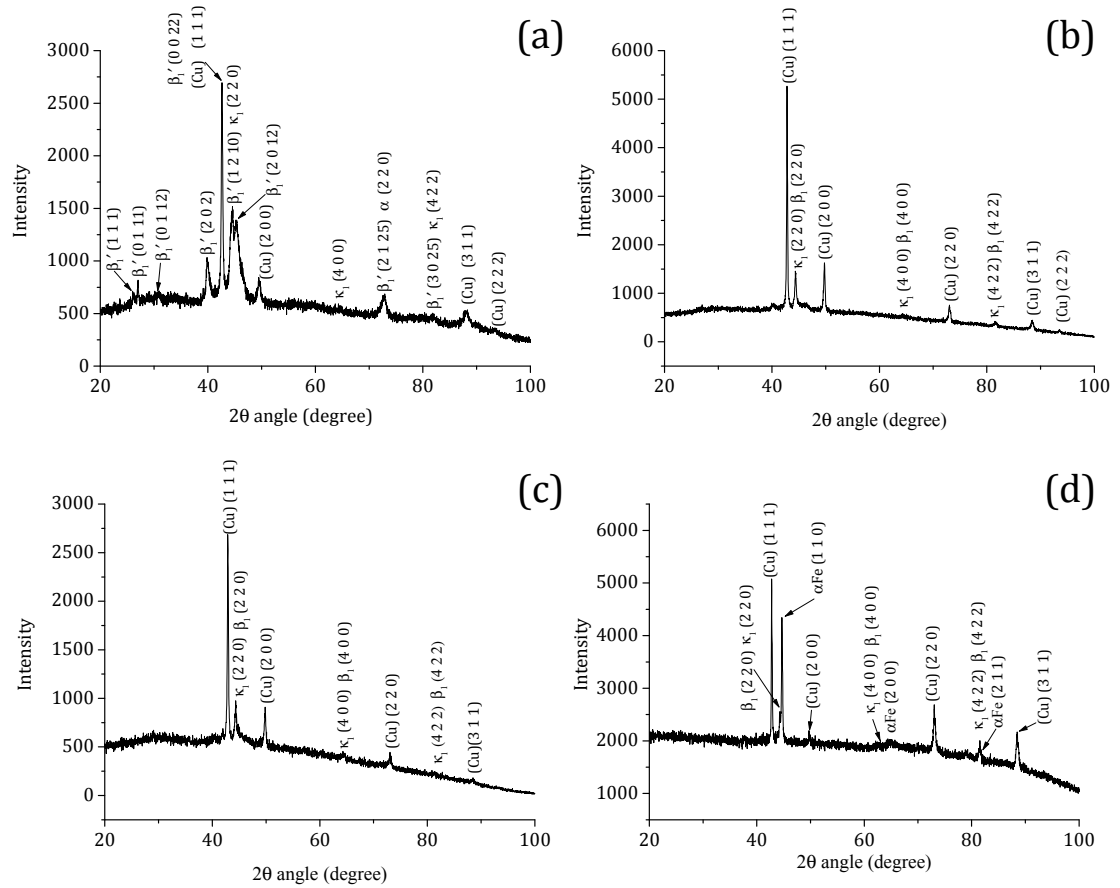
Figure 4.2: Observed XRD pattern showing the effects of increasing Fe content on the identified phase in the (a) 9Fe, (b) 20Fe, (c) 27Fe and (d) 35Fe PTA aluminium bronze coatings

Table 4.4: Crystallographic information of the identified phases

Phase	Structure type	Unit cell (Å)	PDF number	Reference
bcc αFe	bcc	2.868 2.868 2.868	1100108	
Solid solution (Cu)	fcc	3.654 3.654 3.654	9013019	
Ordered β_1	fcc	5.820 5.820 5.820	01-073-2762	[176]
Martensitic β_1'	Orthorhombic	4.520 5.210 4.230	00-028-0005	[177]
Intermetallic κ_1	fcc	5.791 5.791 5.791	00-045-1203	[178]

4.1.3   Microstructure of the PTA aluminium bronze coatings

The microstructure of the PTA aluminium bronze coatings revealed by backscattered electron (BSE) imaging and EDS mapping on mechanically polished samples are shown in Figure 4.3. The microstructure of the coating consists of a Cu-rich matrix (appearing bright in BSE) and a Fe-rich precipitate (appearing dark in BSE). Fine precipitates (appearing bright) such as those shown in Figure 4.3 b and c were observed inside the Fe-rich precipitates. In the 35Fe coating, the second Fe-rich phase was observed. This appears as light grey in BSE shown in Figure 4.3 d. In the 9Fe coating, fine Fe-rich precipitates about nm in size were observed throughout the matrix as shown in Figure 4.3 a, some of these precipitates were also observed in the 20Fe coating and very few were observed in the 27Fe and 35Fe coating. For all coatings, X-ray diffraction identified two Cu-rich phases. EDS maps of Al showed small variations in the Al content throughout the matrix. These two results suggest that the Al content can differentiate the two Cu-rich phases. However, as shown in Figure 4.3, preparation of the sample by mechanical polishing was unable to clearly reveal these two phases. Therefore electro-polishing was employed.
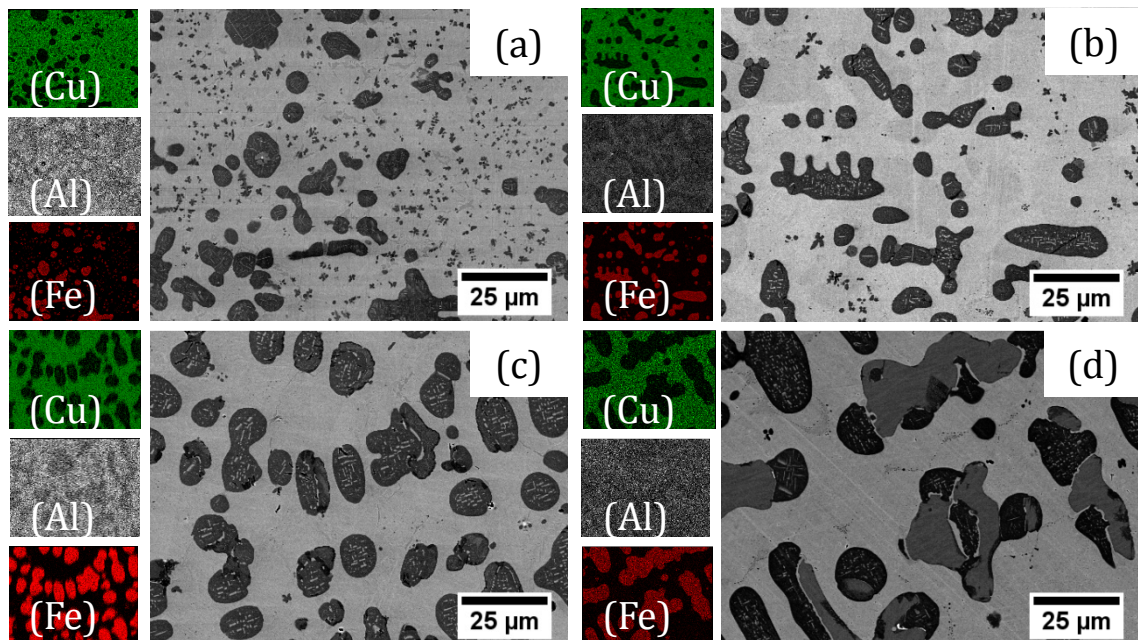
Figure 4.3: BSE image and EDS element map of the (a) 9Fe, (b) 20Fe (c) 27Fe and (d) 35Fe PTA aluminium bronze coatings

Due to the difference in electrochemical potential caused by the Al content, the two Cu-rich phases are electro-polished at different rates. This leads to deeper polishing on Cu-rich area as shown in Figure 4.4. The Fe-rich areas appeared unaffected by the electro-polishing. The composition of the areas removed and the unaffected area were determined using EDS analysis as shown in Table 4.5. The areas removed contain ∼5 at.% less Al than the unaffected area. By combining these EDS and XRD results as well as consideration of the stoichiometric ratio of Cu to Al, the area removed was identified as the solid solution (Cu) phase. The unaffected areas were identified as: the martensitic β_1' phase in the 9Fe coating and ordered β_1 phase in the 20Fe, 27Fe and 35Fe coating. Figure 4.4 also shows that the area and thus the volume fraction of the solid (Cu) phase increased with increasing Fe content in the coating (see Table 4.6).
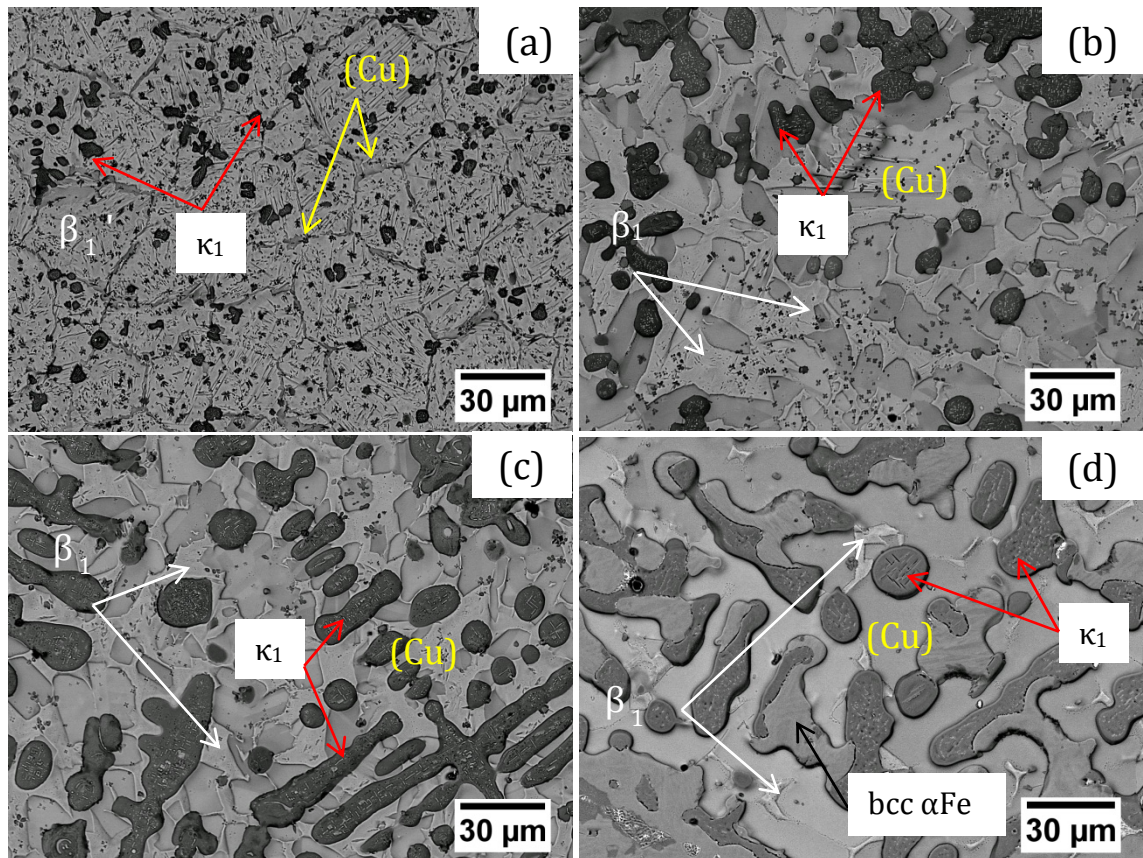
Figure 4.4: BSE image of electro-polished (a) 9Fe, (b) 20Fe (c) 27Fe and (d) 35Fe PTA aluminium bronze coatings showing two Cu-rich phases in the matrix (the Fe-rich precipitates = dark)

Table 4.5: Chemical composition of the area removed and unaffected area (all in at.%)

		Cu	Al	Fe	Mn	Ni	Identified phase
9Fe	removed	79.0	17.8	2.1	0.6	0.4	(Cu)
	unaffected	74.4	22.6	1.5	1.0	0.5	β_1'
15Fe	removed	77.7	17.7	2.7	0.7	1.3	(Cu)
	unaffected	74.1	22.2	1.9	0.8	1.0	β_1
20Fe	removed	79.2	16.8	3.1	0.5	0.4	(Cu)
	unaffected	74.4	21.8	2.6	0.8	0.5	β_1
37Fe	removed	73.5	18.8	5.5	1.1	1.2	(Cu)
	unaffected	65.1	27.0	3.5	1.2	3.2	β_1

By combining the XRD and EDS results, the Fe-rich precipitate (appearing dark in Figure 4.3 and Figure 4.4) was identified as the Fe_3Al intermetallic κ_1 phase. The size and distribution of this intermetallic phase was observed to change with the Fe content. The increase in the Fe content leads to an increase in the size of the Fe-rich phase as well as its density in the matrix as shown in Figure 4.5. To quantify the volume fraction occupied by the intermetallic and other continent phases, the area fractions occupied by these phases were determined by analysing low magnification BSE images such as those shown in Figure 4.5. Assuming that there are no significant mismatch between the orientation of the plane and the orientation of the phase(s) then the area fraction can be assumed to be equal to the volume fraction. For the image analysis, the BSE image was first converted into a binary image as shown in Figure 4.6. Automatic measurement of the area was carried out on the converted image using ImageJ software [179]. In certain areas, manual area measurement was also employed. The results are presented in Table 4.6.
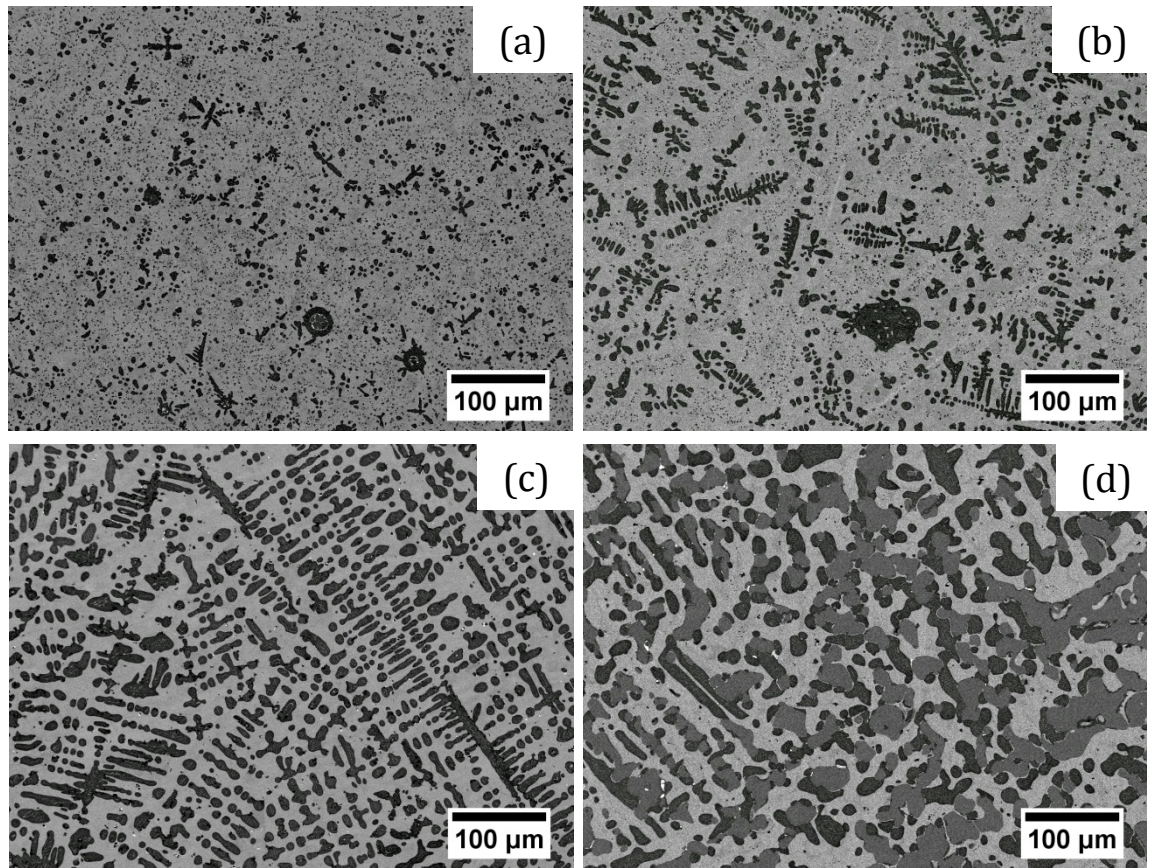
Figure 4.5: Backscattered electron image showing the effects of heat input on the morphology and distribution of the κ_1 phase (a) 9Fe, (b) 20Fe (c) 27Fe and (d) 35Fe PTA aluminium bronze coatings
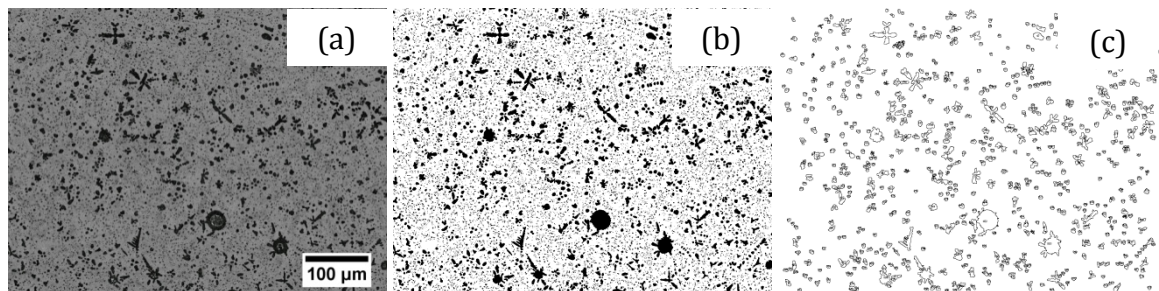
Figure 4.6: Sequence of images showing (a) the conversion of BSE image into (b) binary image, which is use for automatic particle size analysis. The individual particles are outline as shown in image (c)

Table 4.6: Relationship between Fe content in the coating and volume fraction
of the constituent phases in the PTA aluminium bronze coatings

Fe content in the coating (wt.%)	Volume of each phase [%]				
	Solid solution (Cu)	Ordered β_1	Martensitic β_1'	Intermetallic κ_1	bcc αFe
9	5.8	-	80.2	14.0	-
20	29.5	51.3	-	19.2	-
27	33.7	28.1	-	38.3	
35	48.9	2.2	-	25.4	23.4

Table 4.6 shows that with increasing Fe content, the volume fraction of the intermetallic κ_1 and the solid solution (Cu) phase increases. In the 20Fe, 27Fe and 35Fe coating, the volume fraction of the ordered β_1 decreases with increasing Fe content. The results suggest the increase in Fe content has an effecting in promoting the formation of the solid solution (Cu). Figure 4.3 shows fine precipitates appearing bright at the centre of the κ_1 phase. However, due to the close proximity between this phase and the surrounding κ_1 phase, accurate EDS analysis was difficult. An etching solution (detailed in section 3.2.1) was used in an attempt to remove the κ_1 phase. The effect of the etching on the κ_1 phase is shown in Figure 4.7. For the 20Fe, 27Fe and 35Fe coating, the etching solution removed the κ_1 phase to reveal rod and plate shaped structures. EDS analysis (see Table 4.7) confirms that these structures are Cu-rich with composition close to that of the solid solution (Cu) phase. For the 9Fe coating the needle-shaped phase and the surrounding matrix are removed. Due to its size, accurate EDS of the needle-phase structure is was not possible.
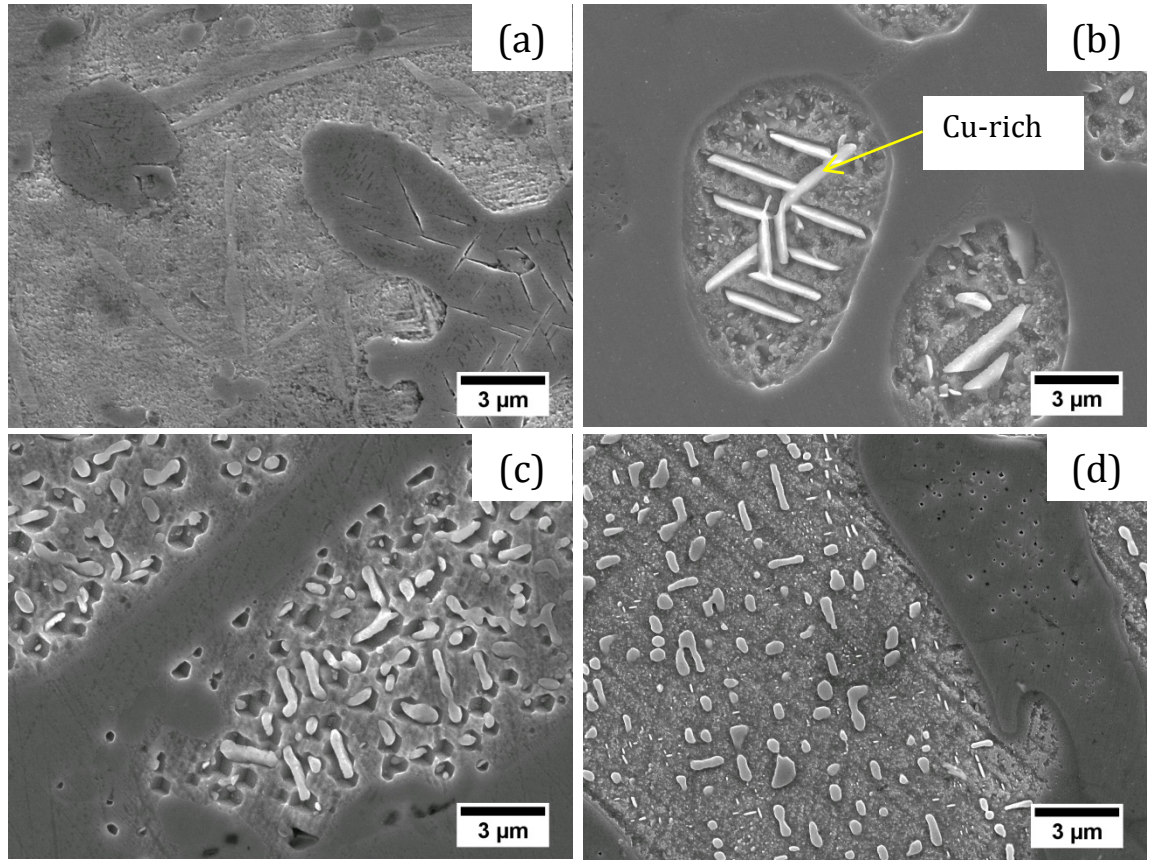
Figure 4.7: Secondary electron image showing the effects of etching on the κ_1 phase in (a) 9Fe, (b) 20Fe, (c) 27Fe and (d) 35Fe coating

Table 4.7: EDS results of the rod and plate shaped structures at the centre of the κ_1 phase (all in wt.%)

		Cu	Al	Fe	Mn	Ni	Si	Cr
20Fe	Cu-rich	64.3	8.8	24.7	0.8	0.7	0.6	0.2
	κ_1 phase	25.7	7.7	63.0	1.2	1.0	1.0	0.4
27Fe	Cu-rich	62.8	9.2	26.3	0.8	0.2	0.5	0.1
	κ_1 phase	14.8	8.6	74.1	1.2	0.4	0.6	0.2
35Fe	Cu-rich	39.3	7.1	50.5	0.9	1.1	0.5	0.7
	κ_1 phase	20.7	7.6	68.2	1.0	1.3	0.6	0.6

From the observed XRD pattern of the 35Fe coating, two Fe-rich phases were identified: Fe_3Al intermetallic κ_1 phase and the bcc αFe phase. These two phases have different contrast under BSE observation as shown in Figure 4.5 d.

When exposed to the etching solution, only certain areas of these Fe-rich phases were removed as shown in Figure 4.8. To ascertain the composition of these two Fe-rich areas EDS analyses were carried out. The results shown in Table 4.8 indicate that the area removed by the etching solution has ~ 6 wt.% higher Cu contents than the unaffected area and has composition similar to that of the κ_1 phase observed in other coatings. The higher Fe content of the unaffected area and the lack of Cu-Al precipitate strongly suggest that the unaffected area is the bcc αFe phase.
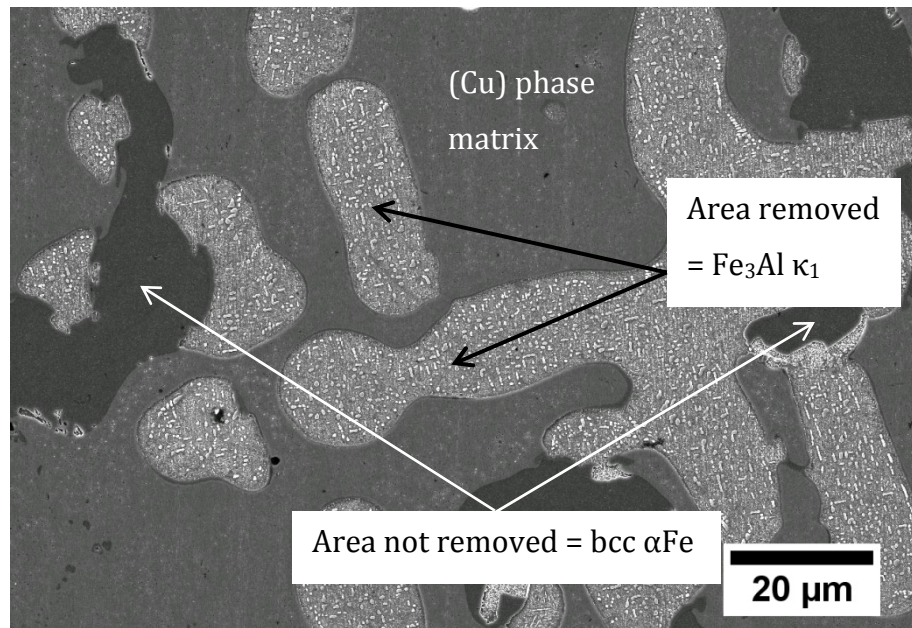
Figure 4.8: SE image showing the effects of etching on the Fe-rich areas in the 37Fe PTA aluminium bronze coating

Table 4.8: EDS analysis of the Fe-rich areas in the 35Fe coating after etching (all in wt.%)

	Cu	Al	Fe	Mn	Ni	Si	Cr	Phase identified
Area not removed	13.7	5.9	76.5	0.9	1.4	0.4	1.2	bcc αFe
Area removed	19.8	7.4	69.1	0.8	1.3	0.8	0.8	κ_1

4.1.4   EBSD analysis of the coating matrix

Crystallographic information related to the grain size and orientations were investigated using EBSD on electro-polished specimens. From the EBSD phase maps shown in Figure 4.9, it is clear that not all phases were indexed.
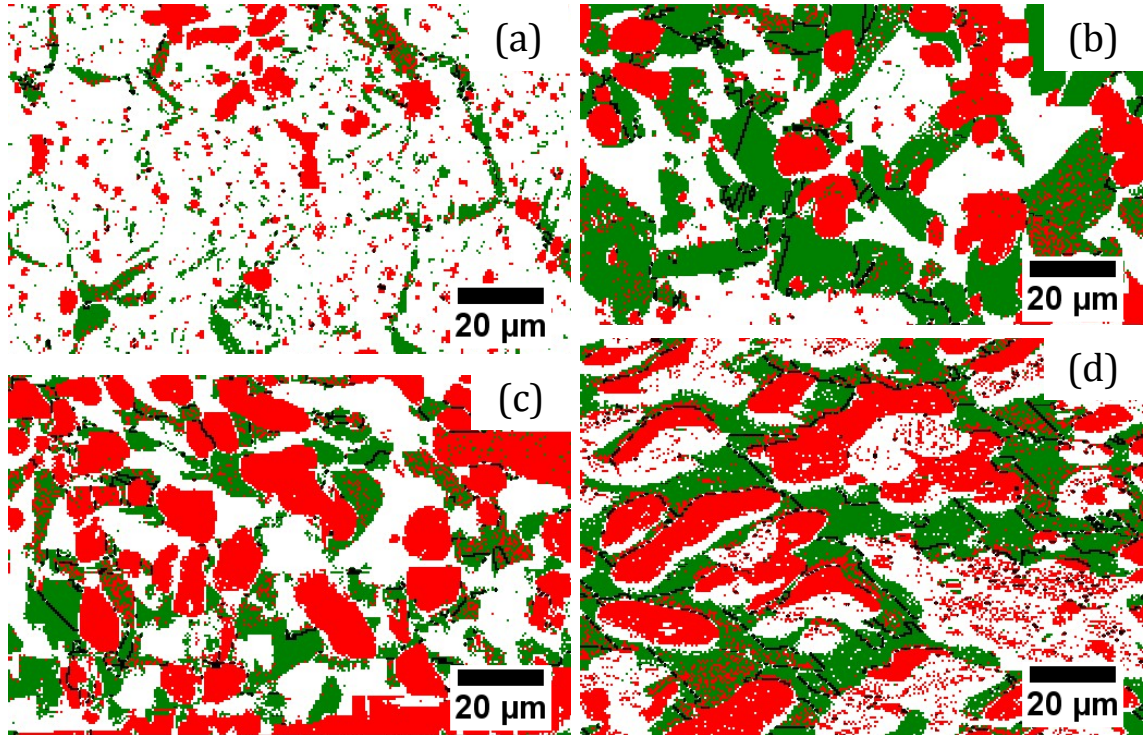
Figure 4.9: EBSD phase map (green: (Cu) phase, red: κ_1 phase, white: not indexed, black lines: grain boundaries)

The EBSD phase map and SEM observation in backscattered mode (see Figure 4.10) show that it was possible to index the solid solution (Cu) phase and the intermetallic κ_1 phase only.   Thus the un-indexed areas (appearing white) represent: martensitic β_1' phase for 9Fe coating, the ordered β_1 phase for 20Fe and 27Fe coating and the ordered β_1 phase or bcc αFe for the 35Fe coating. The mean grain sizes of the solid solution (Cu) phase and the intermetallic κ_1 phase obtained from EBSD mapping of the coating matrix are shown in Table 4.9. With increasing heat input, the size of the (Cu) phase increases to a maximum at the composition of the 20Fe coating.
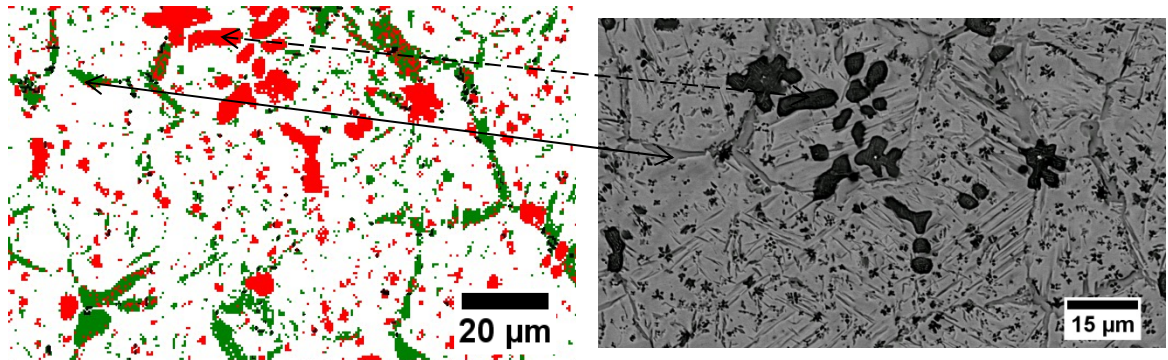
Figure 4.10: EBSD phase map and corresponding BSE image of the 9Fe PTA aluminium bronze coating

This is due to the increase in heat input during deposition, which allows more energy for grain growth. However, with further increase in heat input, the (Cu) grain size decreases. This is due to the effects of the intermetallic κ_1 that limits the growth of the (Cu) grain. The grain size of the intermetallic κ_1 phase increases with the heat input and reaches a maximum at the composition of the 27Fe coating. Further increase in the heat input doesn't lead to an increase in the grain size of the intermetallic κ_1 phase. This might be due to the formation of the bbc αFe phase.

Table 4.9: Mean grain size of the (Cu) and κ_1 obtained from EBSD mapping of the matrix of the 9Fe, 20Fe, 27Fe and 35Fe PTA aluminium bronze coatings (all in μm)

Coating	Solid solution (Cu) phase	Intermetallic κ_1
9Fe	3.4	3.5
20Fe	6.3	5.9
27Fe	4.3	7.2
35Fe	5.5	4.7

The pole figures (Figure 4.11) and the misorientation angle plots (Figure 4.12) of the (Cu) phase indicate no texture. This is expected because the turbulence generation during deposition will promote random grain growth. The same observations were observed for the Fe_3Al intermetallic κ_1 phase.
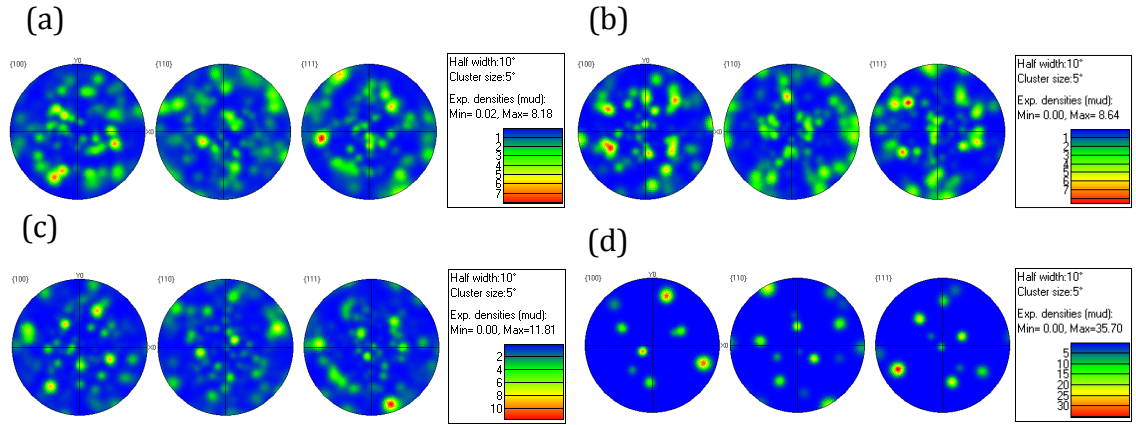
Figure 4.11: Pole figures plot for the solid solution (Cu) phase in (a) 9Fe, (b) 20Fe, (c) 27Fe and (d) 35Fe PTA aluminium bronze coating
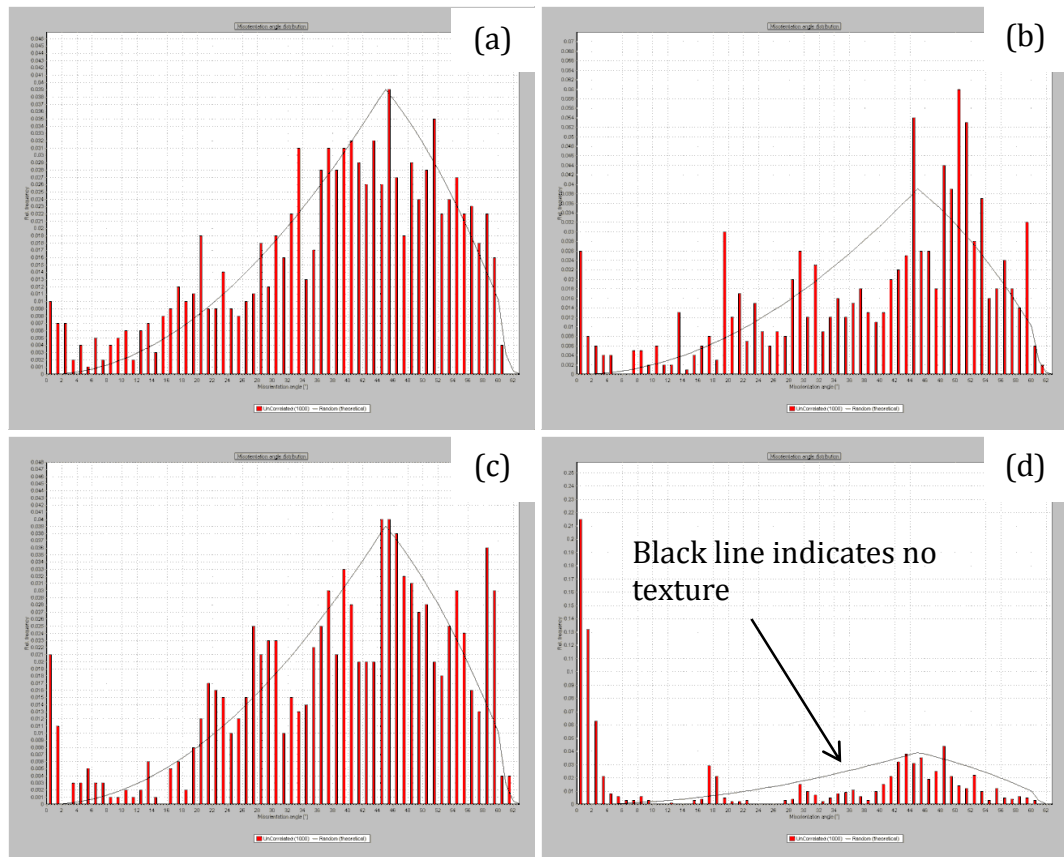
Figure 4.12: Misorientation angle plots for the solid solution (Cu) phase in (a) 9Fe, (b) 20Fe, (c) 27Fe and (d) 35Fe PTA aluminium bronze coatings showing that the (Cu) phase has no texture

102

4.1.5   Hardness and Young's modulus of the coatings

The effects of the microstructure changes on hardness and Young's modulus of the PTA aluminium bronze coatings were investigated by depth-sensing nano-indentation. Due to the different phases present in the coating, hardness mapping of the coating surface is necessary as conventional micro-hardness will only provide an average hardness of the phases present. The 2D plots of measured hardness are shown in Figure 4.13. It is clear from the plot that the 9Fe coating has the most uniform hardness. This is due to the homogeneous distribution of the κ_1 phase. As the Fe content increased the hardness of the coating is less homogenous. The increase in Fe also reduced the matrix's hardness by $\sim$ 2 GPa (201 HV) as shown by the hardness map in Figure 4.13, this is due to the phase change from a martensitic β_1' phase to a solid solution (Cu) phase, which has lower hardness.
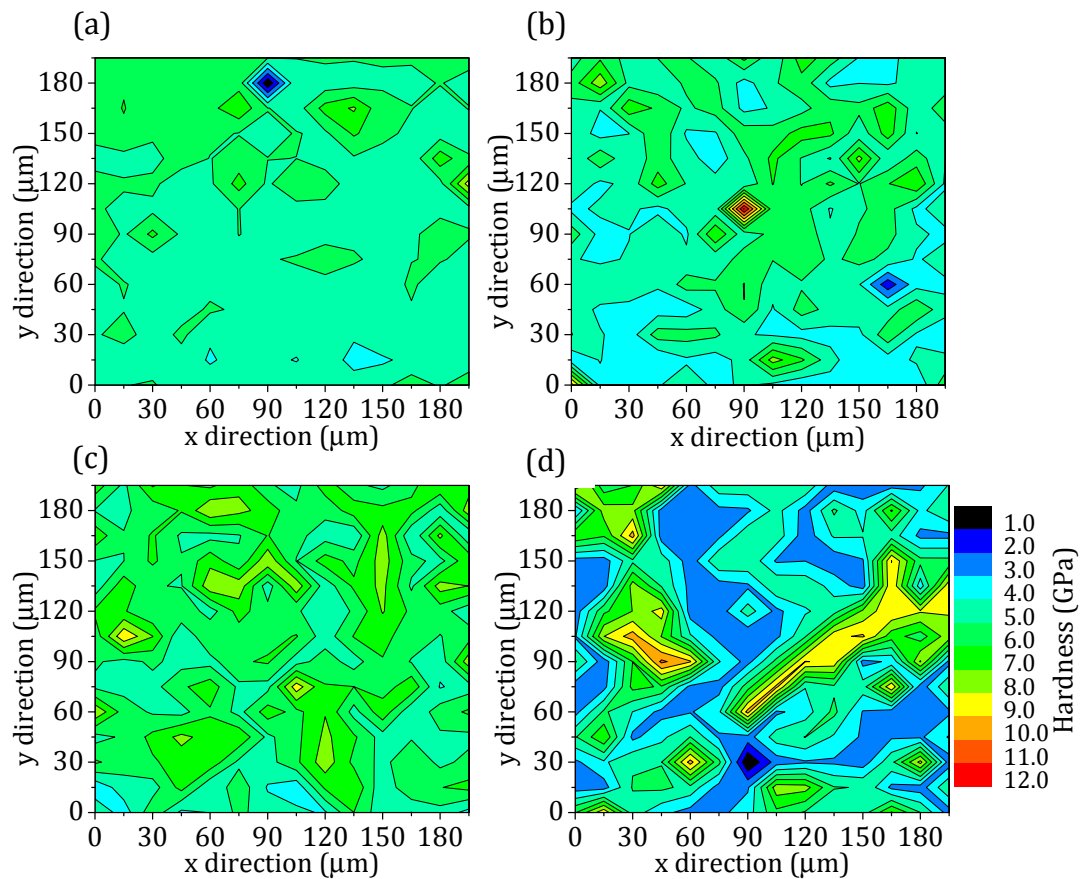
Figure 4.13: 2D plot of measured hardness from 196 indent points for: (a) 9Fe, (b) 20Fe, (c) 27Fe and (d) 35Fe aluminium bronze coatings. (Measurements were made on the top surface of the coating)

Information regarding the hardness and Young's modulus of the individual phases that are present in the 20Fe, 27Fe and 35Fe coating was obtained by combing the measured hardness measurements with BSE images of the indent map as shown in Figure 4.14 b and c. Due to the fine size of the κ_1 phase (see Figure 4.14 a) and the small quantity of α phase present in the 9Fe coating, accurate measurements of these phases were not possible. The measured properties of these phases are shown in Table 4.10.
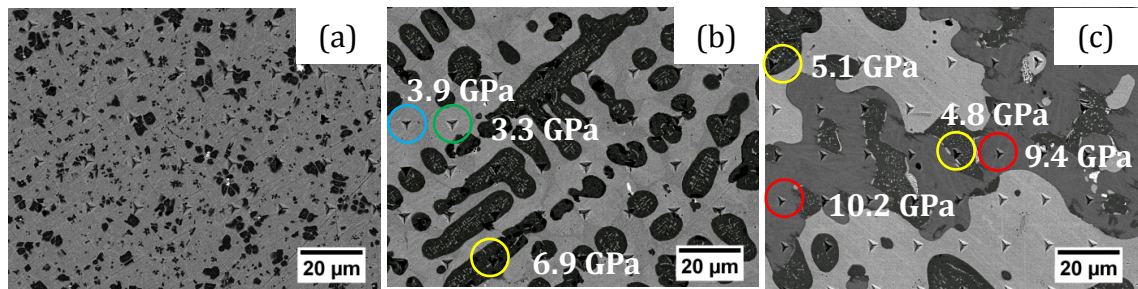
Figure 4.14: BSE image showing selected area of the indent map on the 9Fe, 27Fe and 35Fe PTA aluminium bronze coatings

The measured hardness values are comparable with the literature values (see Table 4.11). The subsurface influence of the phase present beneath the hardness indent is the primary source of error in the measurement, which leads to some of the observed differences between the measured value and the literature value. The measured hardness for the bcc αFe of 8.1 GPa (825.9 HV) in the 35Fe coating is significantly higher than the 0.8 GPa (81.6 HV) expected for the ferrite phase. This might be due to the solid solution strengthening effects of Cu and Al.

Table 4.10: Measured Hardness and Young's modulus of the PTA aluminium bronze coatings

Fe content (wt.%)	9Fe	20Fe	27Fe	35Fe
Matrix phase (bright)	β_1'	(Cu) and β_1	(Cu) and β_1	(Cu)
(Cu) hardness (GPa)	-	3.5	3.6	2.6
β_1 hardness (GPa)	-	4.5	4.3	
κ_1 hardness (GPa)	-	6.2	7.1	4.8
bcc αFe (GPa)				8.1
Averaged hardness H (GPa)	4.9	4.7	5.6	4.6
Averaged Reduced Modulus E* (GPa)	121.7	147.6	165.1	160.6

Table 4.11: Literature values for the hardness of the phases present in the coating [21]

Phase	Reported hardness (GPa) (converted from HV)
(Cu)	1.9-2.6
κ_1	> 6.7
β_1	2.8-3.9

Hardness prediction using the rules of mixture

The properties of a multiphase material can be predicted from the proportion of the constituent phases present in the material. This can be achieved by using several methods such as finite element method and the rule of mixtures. The rule of mixture is one of the simplest methods for estimating the effective mechanical properties in terms of the proportion of the constituent phases [180]. To investigate whether the hardness of the PTA coatings can be predicted using the rules of mixture. Predictions of the hardness were made using the volume fraction obtained by image analysis (see Table 4.6) and hardness of the individual phases obtained from nano-indentation (see Table 4.10). Depending on the orientation of the constituent phases within the coating, the load distribution changes as shown in Figure 4.15. The effective hardness of the coating for the iso-stress (lower bound) and iso-strain (upper bound) conditions can be calculated by Equation 4.1 and Equation 4.2 respectively.

Iso-stress   Iso-strain
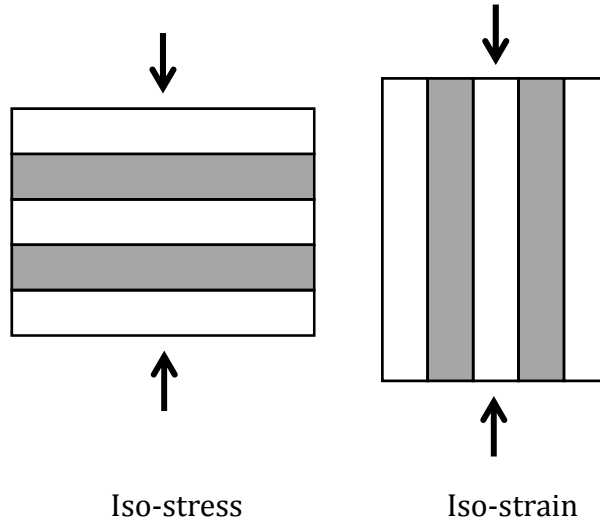
Figure 4.15: Schematic showing the effects of constituent phase distribution on the overall load distribution with in the coating

$$H_{\text{upper}} = V_{\text{phase 1}} H_{\text{phase 1}} + V_{\text{phase 2}} H_{\text{phase 2}} \quad \text{Equation 4.1 [36]}$$

$$H_{\text{lower}} = \cfrac{1}{\cfrac{V_{\text{phase 1}}}{H_{\text{phase 1}}} + \cfrac{V_{\text{phase 2}}}{H_{\text{phase 2}}}} \qquad \text{Equation 4.2 [36]}$$

The hardness prediction using the rules of mixture is shown in Table 4.12. The results show that using the rules of mixture the hardness of the PTA aluminium bronze coating can be predicted with high accuracy (within < 0.5 GPa from the H_{upper} value). As shown by the SEM images and EBSD results in section 4.1.3, the constituent phases in the PTA aluminium bronze coatings have no preferred orientation, therefore the iso-stress condition assumed for the H_{upper} deviates slightly from the actual condition. Additionally, the hardness value of the individual phases obtained by nano-indentation is also influenced by the phase present beneath the indent. The differences between the microhardness measurements and hardness measurements obtained from nano-indentation will be discussed in Chapter 7.

Table 4.12: Comparisons between the predicted hardness of the PTA aluminium bronze coatings using the rules of mixture and the measured values from micro hardness measurements and nano-indentation measuremetns

Coating	H_{upper} (GPa)	H_{lower} (GPa)	Micro hardness (GPa)	Averaged hardness from 196 indent points (GPa)
9Fe	5.0	4.9	3.1	4.9
20Fe	4.5	4.4	2.4	4.7
27Fe	5.1	4.7	2.9	5.6
35Fe	4.5	3.6	3.6	4.6

4.2   Coating steel substrate interface microstructure

The service life and performance of any coating is strongly dependent on the adhesion between the coating and the substrate material. In this section, the results from the characterisation of the areas between the PTA aluminium bronzes coating and the steel substrate will be presented.

4.2.1   Microstructure and composition of the coating-steel substrate interface

The backscattered electron image of the cross section through the coating and steel substrate and the corresponding EDS elemental mapping are shown in Figure 4.16. Under backscattered electron imaging, the Cu-rich coating appears much brighter than the Fe-rich steel substrate. This leads to a clearly defined Fe-Cu boundary (shown by the yellow lines in Figure 4.16). As the Fe content in the coating increases, Fe-rich dendrites were also observed to protrude from the Fe-Cu boundary as shown by the BSE image and EDS mapping in Figure 4.16 c and d.
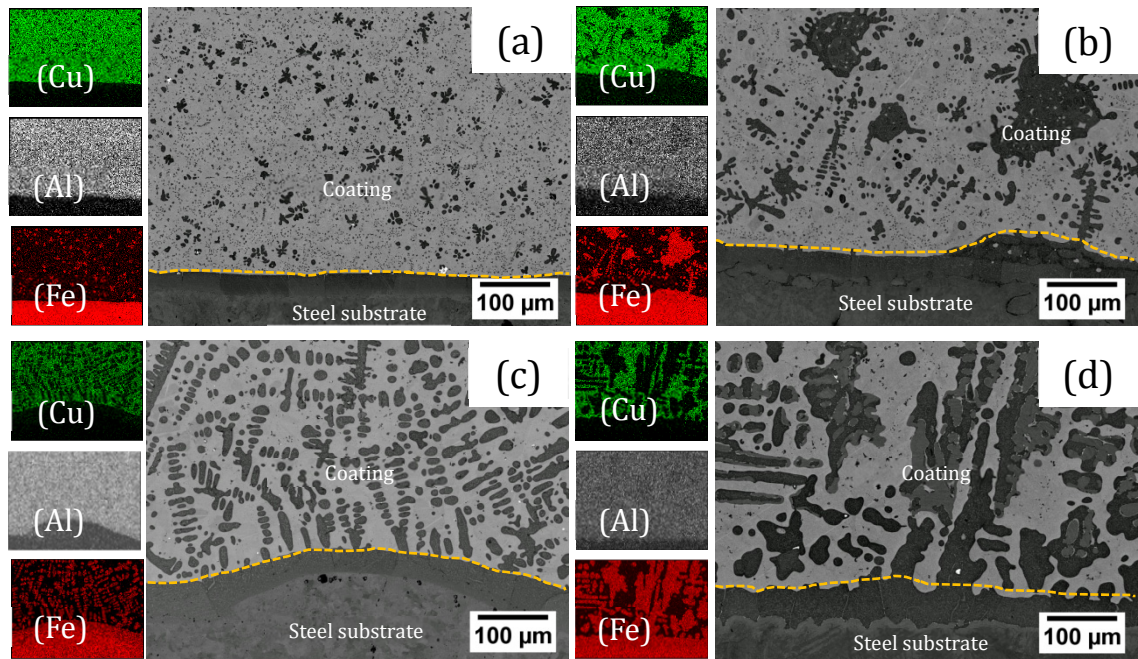
Figure 4.16: BSE image and EDS element of the section through the coating-steel substrate interface for (a) 9Fe, (b) 20Fe, (c) 27Fe and (d) 35Fe coatings (yellow lines = Fe-Cu boundary)

The PTA aluminium bronze coating has a dense microstructure that is s similar to cast material as show in Figure 4.17 b. Compared to other coatings such as that shown in Figure 4.17 a, fewer voids (appearing black in the optical microscopy in in Figure 4.17 a) were observed. This is expected to improve the mechanical properties of the coatings as voids are known to act as stress concentration site where cracks can initiate.
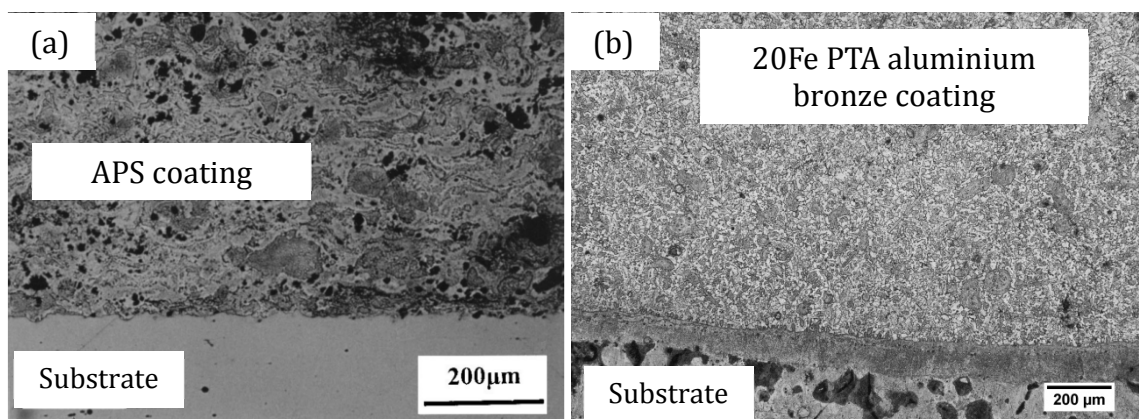
Figure 4.17: Optical microscopy image of (a) plasma sprayed Cu-10Al coating [22] and (b) 20Fe PTA aluminium bronze coatings

High magnification backscattered electron images of the area between the coating and the steel substrate are shown in Figure 4.18. No cracks were detected, however, in certain areas such as those highlighted in Figure 4.18 a and Figure 4.19 evidences of liquid penetration into the grain boundaries of the Fe-rich phase were observed. Fine precipitates, (appearing bright in the dark region of Figure 4.18) were observed in the interface region.
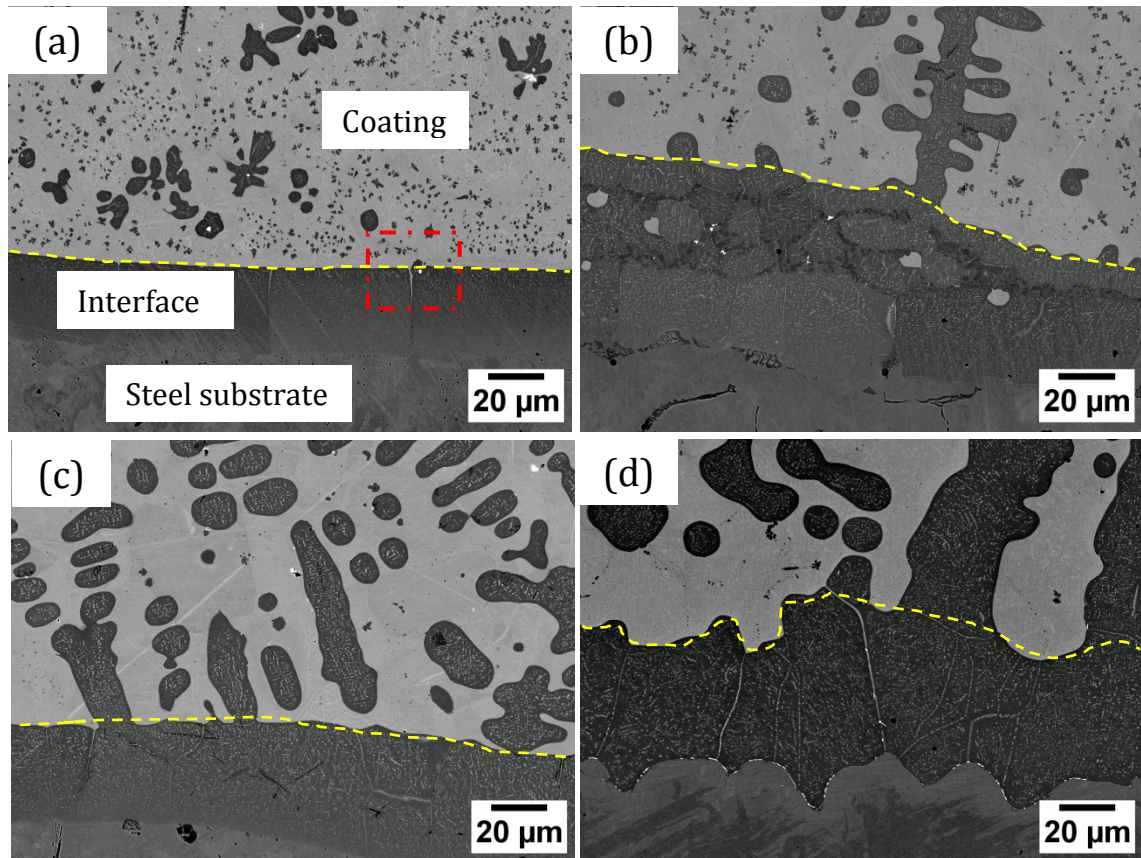
Figure 4.18: High magnification backscattered electron image of the (a) 9Fe, (b) 20Fe, (c) 27Fe and (d) 35Fe PTA aluminium bronze coatings (yellow line= approximate boundary of the interface layer on the coating side)

The bright contrasts of these precipitates suggest that they might be rich in Cu. The size and density of these precipitates increased with the Fe content in the coating. The presence of precipitates indicates that during deposition, some Cu and Al were also transferred from the molten aluminium bronzes droplets to the Fe-rich steel substrate. To determine the composition of the interface layer, five EDS analyses were conducted at various positions on the layer. The averaged compositions are shown in Table 4.13.

The EDS results show that the interface layer is rich in Fe with some Cu and Al. The high Fe content suggests that the interface layer originated from the steel substrate. The EDS results also show that as the heat input during deposition increased, the amount of Cu and Al in the interface layer also increases. The transfer of these elements is expected to modify the mechanical properties of the interface layer. The mechanical properties of the interface layer will be discussed in section 4.2.3.

Table 4.13: Composition of the interface layer from an average of five EDS analyses (all in wt.%)

		Cu	Al	Fe	Mn	Ni	Si	Cr
Increase heat input	9Fe	0.9	3.4	91.6	1.0	0.3	0.6	0.2
	20Fe	1.2	2.9	93.2	0.8	0.9	0.5	0.6
	27Fe	1.3	3.1	94.1	0.8	0.4	0.2	0.2
	35Fe	20.6	6.6	69.8	0.6	1.0	0.6	0.9

To investigate the depth which Cu and Al are transferred into the interface layer, EDS element line scans across the coating-substrate interface were measured. The results are shown in Figure 4.19. The approximate boundary of the interface layer on coating side (shown as solid black line in Figure 4.19) is used as the datum point for distance calculation. By combining the BSE image and the intensity information from the EDS element mapping, the depth in which Cu and Al were detected inside the steel substrate was determined; this is shown as the dotted line in Figure 4.19. Within the interface region, the intensity of Cu and Al decreased almost linearly away from the coating side of the interface. Beyond the interface region (on the steel substrate side) no Cu and Al were detected, this indicates that the transfer of Cu and Al into the Fe-rich area is limited to within the interface layer. Based on this information, the thickness of the interface layer was measured from high magnification BSE images as shown in Figure 4.20. The average thickness of the interface as measured from the BSE images shows that the thickness of the layer increases significantly from 27.3 µm for the 9Fe coating to 50.2 µm for the 35Fe coating. The interface layer thickness for the 20Fe and 27Fe are 41.9 µm and 42.5 µm respectively.
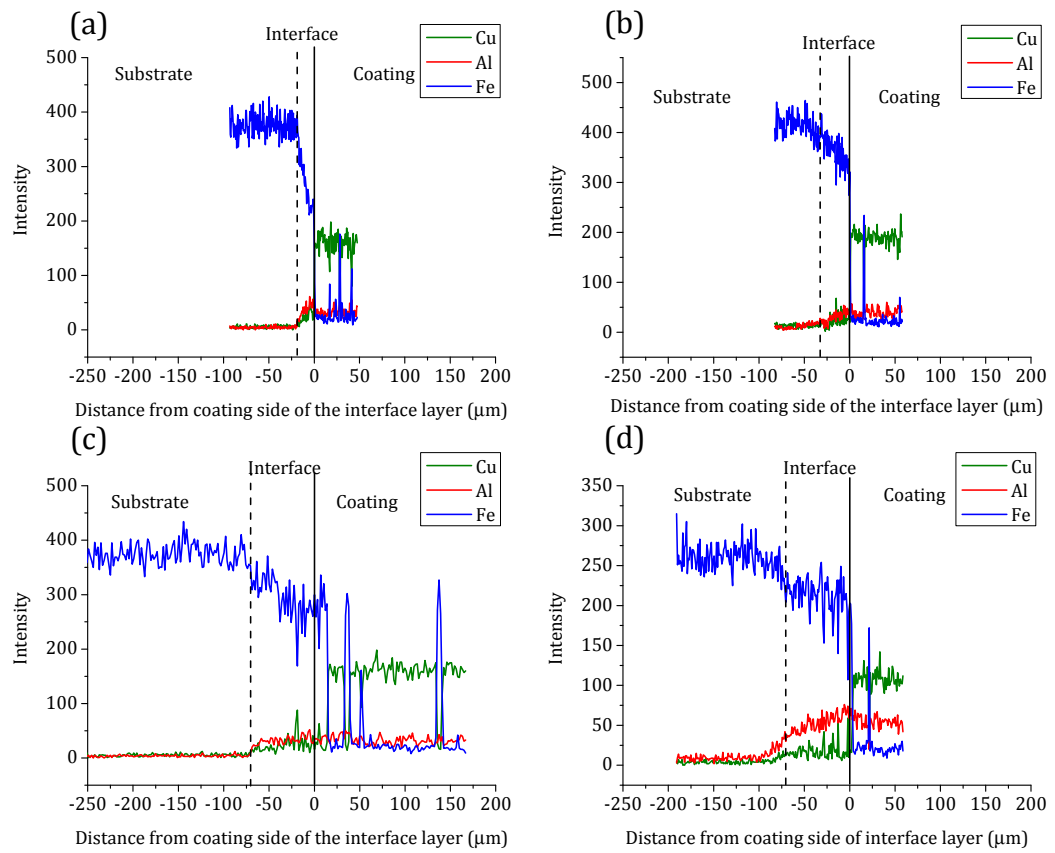
Figure 4.19: EDS line profiles showing elemental distribution across (a) 9Fe, (b) 20Fe, (c) 27Fe and (d) 35Fe PTA aluminium bronze coatings
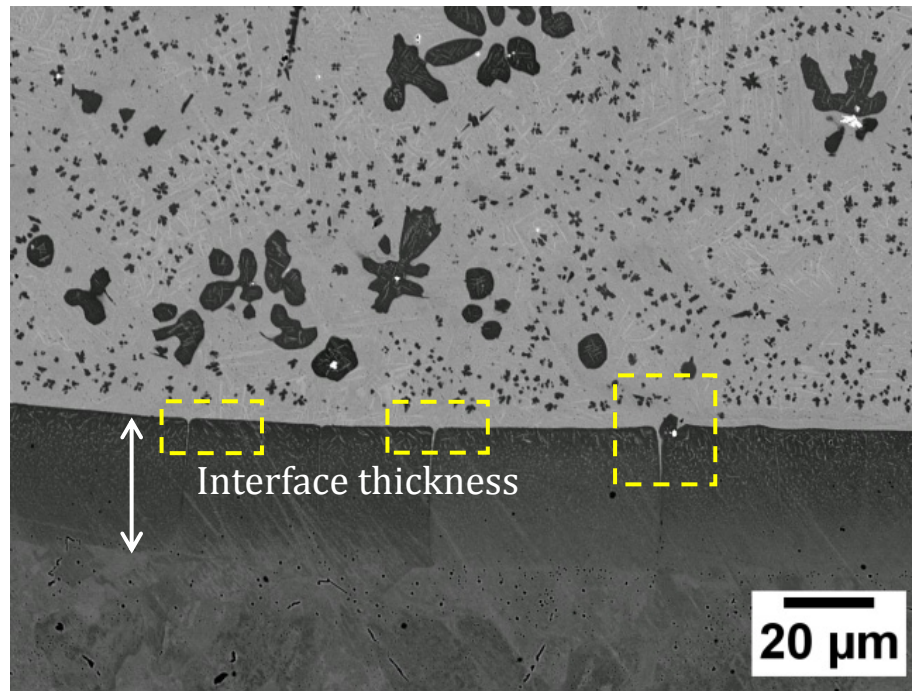
Figure 4.20: Measurement of the interface thickness from a BSE image

4.2.2   EBSD mapping of the interface layer

The steep temperature gradient at the un-melted and the melted steel substrate might lead to texture in the interface layer. To investigate this EBSD was employed. The EBSD phase maps and the corresponding pole figures (Figure 4.21) and the misorientation angle plots (Figure 4.23) indicates there is no texture in the interface layer. By combining the EBSD orientation map and the BSE image, it was possible to show that all the Fe-rich dendrites that extend from the interface layer have orientation that are identical the layer below them (see Figure 4.21 c and d). This suggests these dendrites originate from the same grains as those on the interface layer.
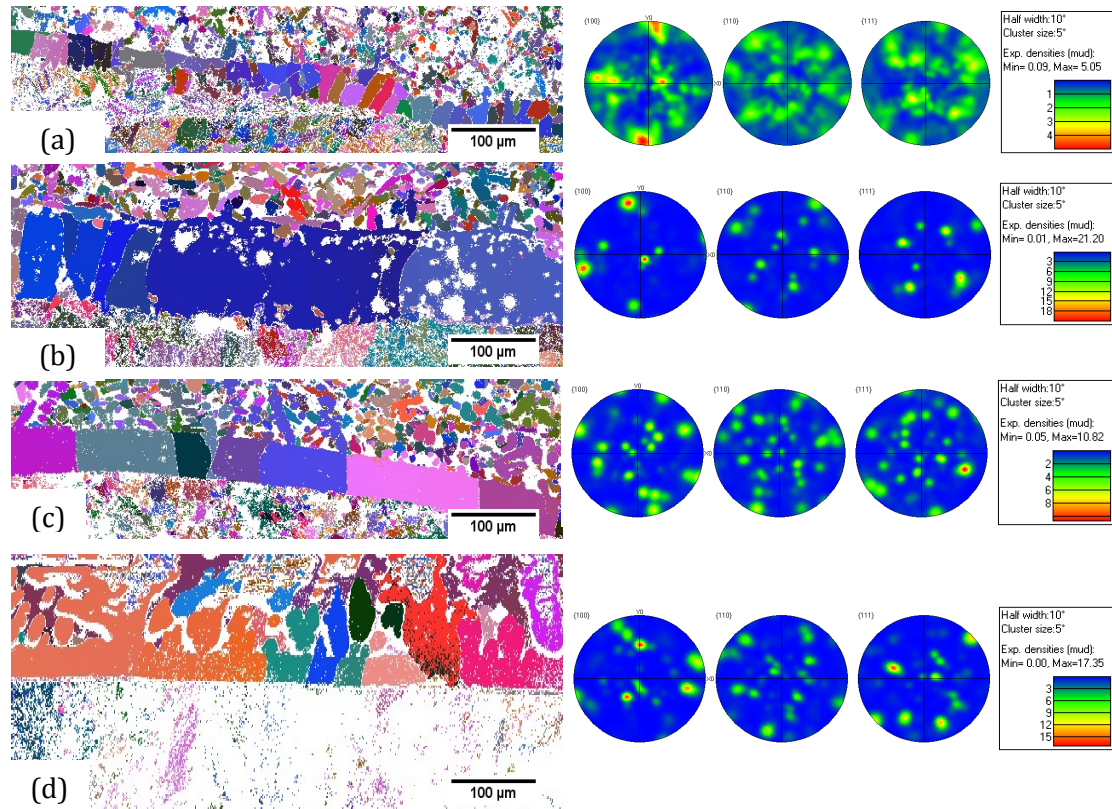
Figure 4.21: EBSD orientation map and corresponding pole figure plots of the Fe phase of (a) 9Fe, (b) 20Fe, (c) 27Fe and (d) 35Fe PTA aluminium bronze coating (for all maps white = not indexed)
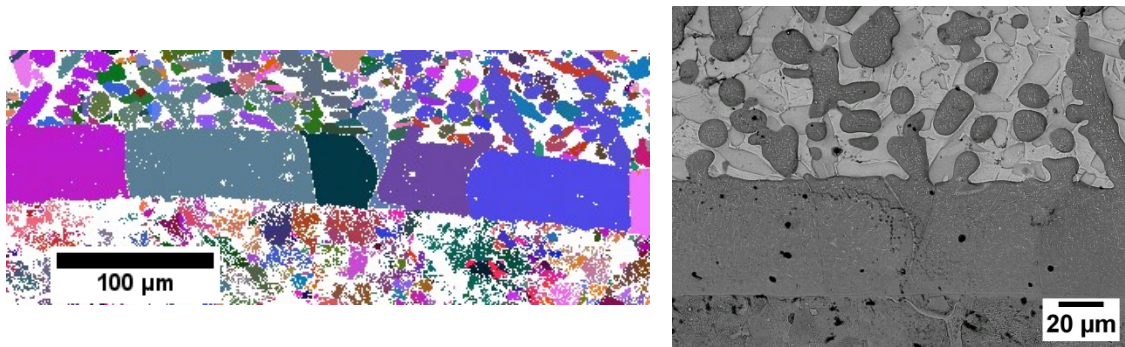
Figure 4.22: EBSD orientation map and the corresponding BSE image of the cross section through the interface between the 27Fe PTA aluminium bronze coating and the steel substrate
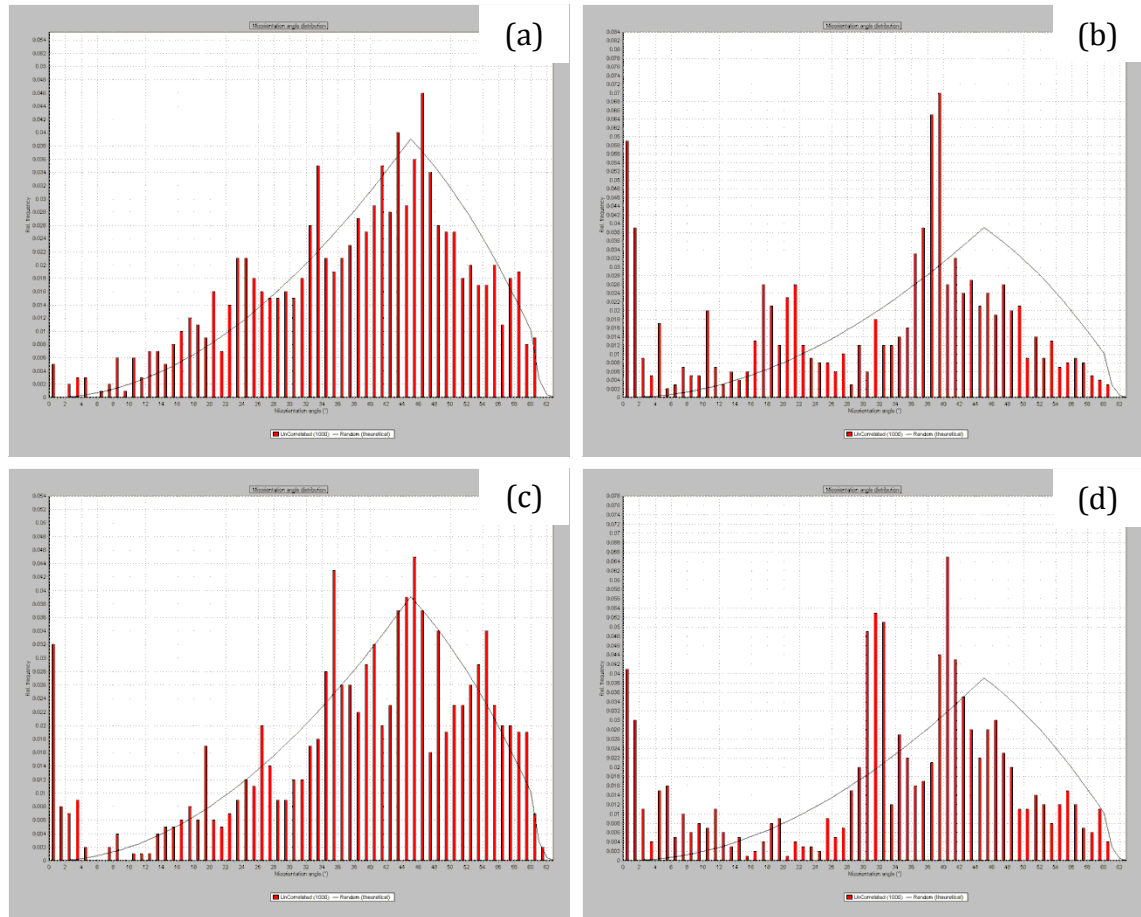
Figure 4.23: Misorientation angle plots for the Fe-rich phase at the interface layer of the a) 9Fe, (b) 20Fe, (c) 27Fe and (d) 35Fe PTA aluminium bronze coatings showing that the Fe-rich phases at the interface has no preferred orientation

Based on this interpretation of the results, the actual molten region of the steel substrate might be located at a significant distance away from the interface layer and thus the interface layer may actually be the re-solidified steel substrate which has been alloyed by Cu and Al due to the turbulence generated during deposition by PTA technique. The EBSD phase map and the low magnification backscattered electron image of the interface layer is shown in Figure 4.24 and Figure 4.25 respectively. The grains in the interface region were indexed as bcc αFe phase. The maps show that with increasing heat input during deposition, the grain size of the Fe-rich phase at the interface region increased with the Fe content in the coating as shown in Table 4.14. This might be due to the increase in heat input during deposition.

Table 4.14: Mean grain size of the Fe-rich phase at the interface region obtained from the EBSD analysis of the interface region (all in µm)

9Fe	20Fe	27Fe	35Fe
10.7	11.0	11.7	17.3
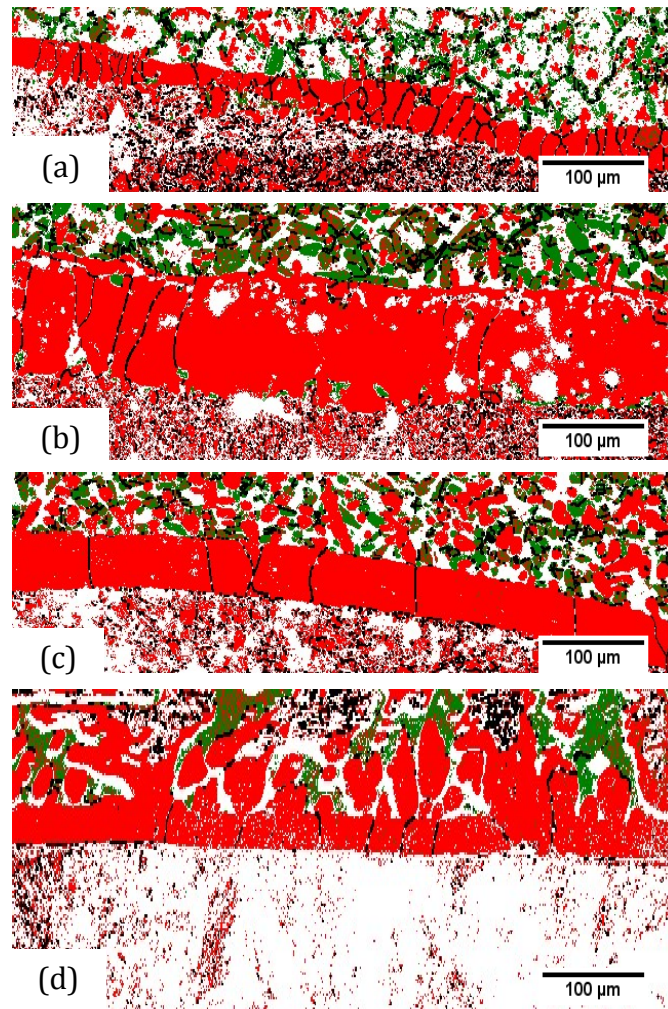
Figure 4.24: EBSD phase map of (a) 9Fe, (b) 20Fe, (c) 27Fe and (d) 35Fe coating-steel substrate interface (red = bcc αFe, green = (Cu) phase, for all maps white = not indexed)
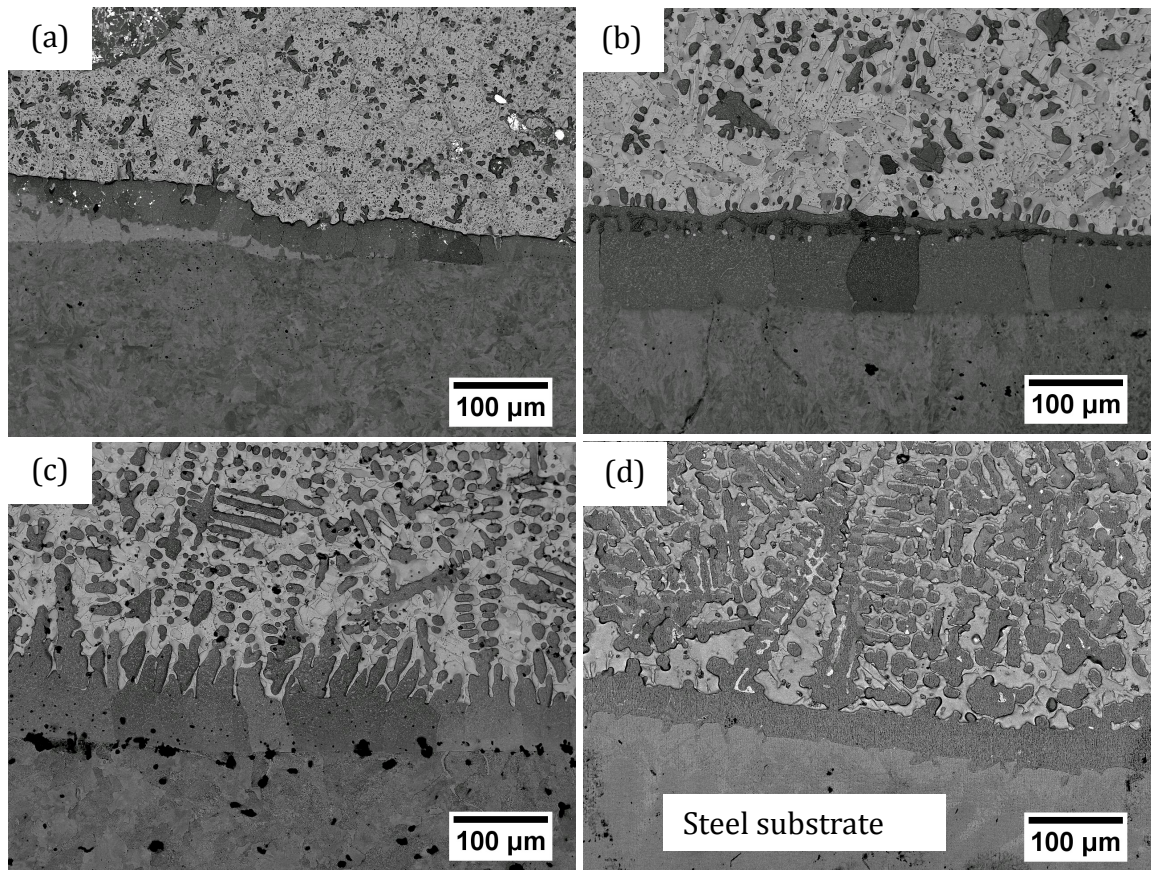
Figure 4.25: Low magnification backscattered electron image of the cross section through the interface between (a) 9Fe (b) 20Fe (c) 27Fe and (d) 35Fe PTA aluminium bronze coating and the steel substrate

Due to the small thickness of the interface region, accurate phase identification of the phase present at the interface layer using XRD was not possible due to the strong influence from both the coating and the steel substrate. However, by using the information obtained by EDS analysis and EBSD phase map it is possible to confirm that the interface layer consists of bcc αFe phase and Cu-rich precipitates. The lack of intermetallic phase formation might be the reason for the lack of cracks in the interface layer. The presence of Cu-rich precipitates and Al in the interface region is expected to have strong influence on the mechanical properties of the interface layer. To investigate this, depth-sensing nano-indentation was employed. The results are presented in the next section.

4.2.3   Hardness of the interface layer

The EDS results in Table 4.13 show the presence of Cu and Al into the interface layer. EBSD phase maps show that despite the additional Cu and Al, the interface region is still bcc αFe phase. However, these elements can be expected to cause solid solution strengthening and thus increases the hardness of the interface layer. Depth-sensing nano-indentation was used to produce a hardness map of a section through the coating-steel substrate interface and the results are shown in Figure 4.26. The map of measured hardness showed that the interface region has hardness between 5-7 GPa. This is substantially higher than the 2 GPa of the unaffected steel substrate (shown blue in in Figure 4.26 a and b). The increase in hardness is expected to improve the load carrying capacity of the coating. The hardness map also shows that as the heat input during deposition increases, the depth of the heat affected zone also increased (see Figure 4.26 c and d where the area below the interface region has high hardness of ~4 GPa). It is worth noting that the change in grain size at the interface as shown by in Table 4.14 has no significant effects on the hardness. This indicates that the main contribution for the hardness increase is the solid solution and precipitate strengthening caused by the increased Cu and Al content. However, the interface layer of the 9Fe coating, which has the largest proportion of small grains, can be expected to have higher ductility than the interface layer on the 35Fe coating.
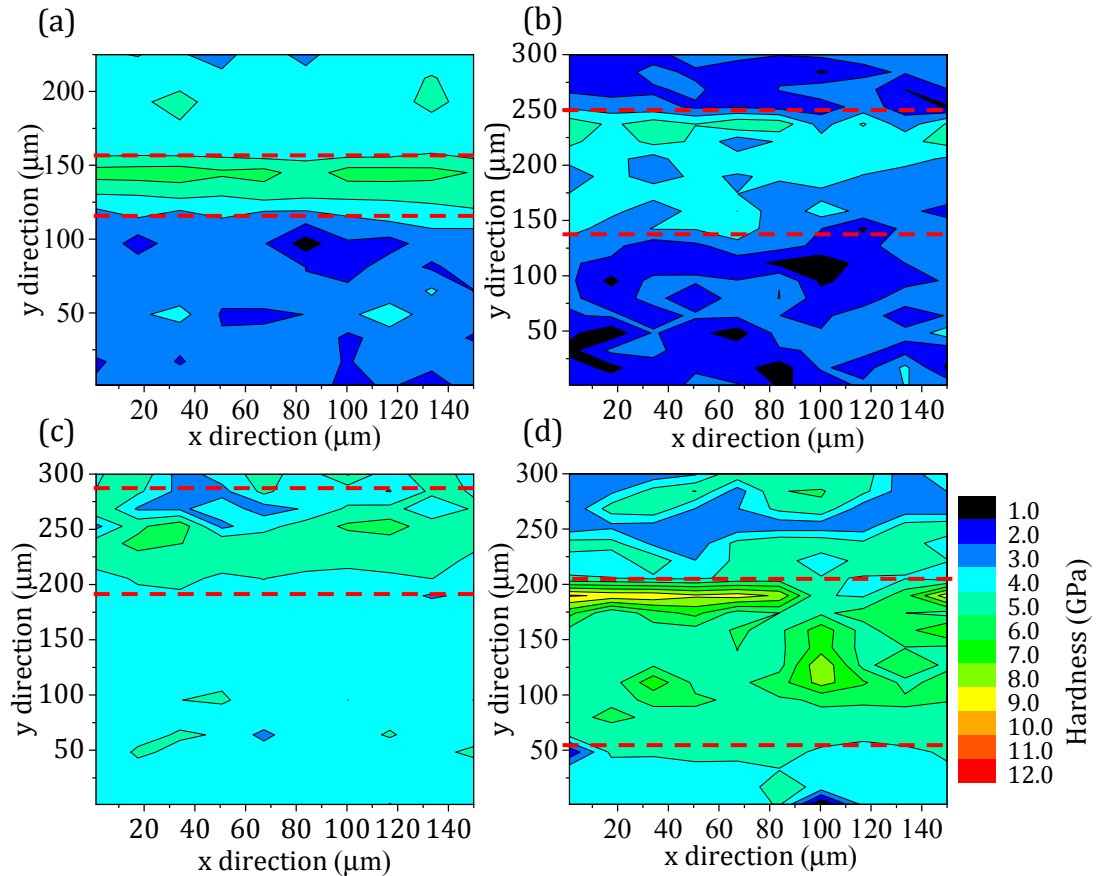
Figure 4.26: 2D plot of measured hardness of a cross-section through the coating-steel substrate interface for (a) 9Fe, (b) 20Fe, (c) 27Fe and (d) 35Fe PTA aluminium bronze coatings (red lines = approximate boundaries of interface layer)

4.3   Summary of microstructure characterisation

In this section, the effects of increasing substrate melting on the microstructure of the coatings were investigated. The results show that the increase in heat input during deposition leads to elevating substrate melting. This leads to an increase in the Fe content in the coating. Using several complementary techniques, the increase in Fe content in the coating leads to the following changes to the microstructure:

•   Change in matrix phase from a martensitic β_1' phase to a solid solution α phase

•   An increase in size of the Fe_3Al intermetallic κ_1 phase

•   Formation of the bcc αFe phase in the coating containing 35 wt.%Fe

These changes to the microstructure have the following effects on the mechanical properties of the coating:

- Reduction in matrix hardness from 4.1 GPa to ~2.5 GPa

- Inhomogeneous hardness distribution due to the presence of large Fe_3Al intermetallic κ_1 phase in the soft solid solution α matrix

The increase in heat input during deposition leads to the following changes to the area between the coating and steel substrate:

- Formation of Fe-rich interface layer containing Cu-rich precipitates and Al solutes. The thickness of the layer increased with heat input during deposition.

- Growth of the Fe-rich dendrites from the interface layer into the coating

- Increase in grain size of the interface region

These microstructural changes have the following effects on the mechanical properties of area between the coating and the steel substrate:

- The interface layer is characterised by area of high hardness of ~ 7 GPa, this is higher than that of the steel substrate and coating material

- With increasing substrate melting, the size of the heat-effected zone below the interface layer also increased

5. Tribological properties

For sheet metal forming dies application, high wear resistance and stable friction coefficient are two critical properties. In this chapter, the results detailing the effects of PTA induced microstructural changes on the friction and wear characteristics of the coating are first presented. This is then followed by wear test results showing the performance comparison between the coating and the currently used AISI D2 tool steel under dry sliding condition against stainless steel with different hardness. The chapter concludes with a summary on the coating's friction and wear characteristics and their relationship with the microstructure.

5.1 Influence of microstructure on the wear characteristics

The increase in Fe content induced during PTA deposition leads to significant changes to the microstructure and hardness of the coating as shown in Table 4.10. To investigate the influence of these changes on the wear characteristics, the coatings were worn against AISI 52100 bearing steel under dry reciprocating sliding condition. The AISI 52100 was chosen due to its high hardness of 915 HV ($\sim$ 8.9 GPa), which is significantly higher than that of the coating (see Table 4.10). This is expected to simplify the interpretation of the wear result, as the majority of the wear will occur in the coating. In this subsection, the results detailing the effects of microstructure on the wear characteristics will be presented.

5.1.1 Dry sliding friction coefficient

For most tribological systems, the onset of wear is nearly always accompanied by friction, thus the analysis of the coefficient of friction (CoF) provides the initial information about the wear process. The coefficient of friction measurements during dry sliding between the PTA aluminium bronzes coatings and AISI 52100 at four different loads are shown in Figure 5.1. For all coatings, the CoF decreased with increasing load. This decrease is the most apparent in the 35Fe coating as shown in Figure 5.1 d. With the exception of the 35Fe coating, all coatings exhibit an initial spike in CoF during the first 30 s of the test.

As it will be discussed later in this chapter, the spike is due to the shearing of the oxide film during the initial sliding. The 9Fe coating exhibits the most stable CoF as shown in Figure 5.1 a. However, for the 20Fe and 35Fe coatings, the CoF increase with time as shown in Figure 5.1 b and d. The increase in CoF can be attributed to the increase in wear damage on the two surfaces. The 35Fe coating also exhibits the highest CoF at a given load, whilst the value of CoF for the 9Fe, 20Fe and 27Fe coating are ~ 0.4 for all loads. Due to the similarities in the crystal structure of the bcc αFe phase and the AISI 52100 bearing steel, the solid solubility between these two phases are high. This increases the tendency for adhesive junction to form upon loading. As the number of junctions increases, the tangential force required to shear these junctions to enable relative motion is also high, resulting in the observed high CoF for the 35Fe coating.
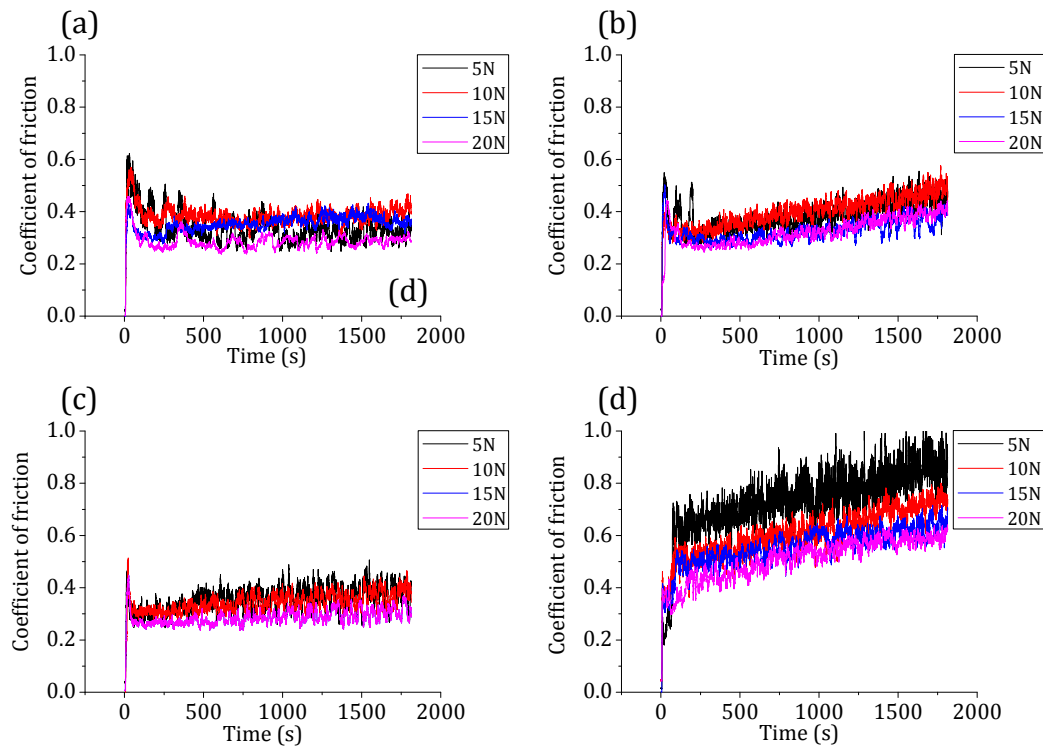
Figure 5.1: Measured coefficient of friction during dry reciprocating sliding wear test against AISI 52100 and (a) 9Fe, (b) 20Fe, (c) 27Fe and (d) 35Fe PTA aluminium bronze coatings

5.1.2   Morphology and chemical composition of the worn PTA aluminium bronze coating surfaces

The morphologies of all worn coating surfaces were observed using an optical microscope. Some of the images are presented in Figure 5.2. The optical images show several important points:

- With increasing Fe content, the wear mechanism changes from abrasive (shown by the scratches in Figure 5.2 a) to a mixture of abrasive and adhesive/delamination wear as evidenced by the wear debris and the scratches shown in Figure 5.2 d.
- The optical images also show accumulation of wear debris (appearing dark in Figure 5.2) at both ends of the worn surfaces.
- The width of the wear track on the 9Fe coating is smaller than the 20Fe, 27Fe and 35Fe coating. This suggests that the 9Fe coating has higher wear resistance than the other coatings as shown in Figure 5.3.

To investigate the depth generated by the wear processes, 3D surface profile of the worn coating surfaces were obtained using optical profilometer. From these 3D surface profile, the depth profiles of the worn surfaces in the direction parallel and perpendicular to the sliding direction were obtained. The depth profile on the 20Fe coating in a direction perpendicular to the sliding direction is shown Figure 5.5 a. Significant pile-up of materials was observed as shown by the increase in height of the surface near the edge of the worn surface. Similar pile-ups of materials were also observed for the 27Fe and 35Fe coatings. Due to the ductile nature of the solid solution (Cu) phase in the 20Fe, 27Fe and 35Fe coatings, pile-up of material is expected [181]. In contrast to this, no material pile-up was observed in the 9Fe coating as shown in Figure 5.4 a. This is thought to be mainly due to the brittle nature of the martensitic β_1' phase.
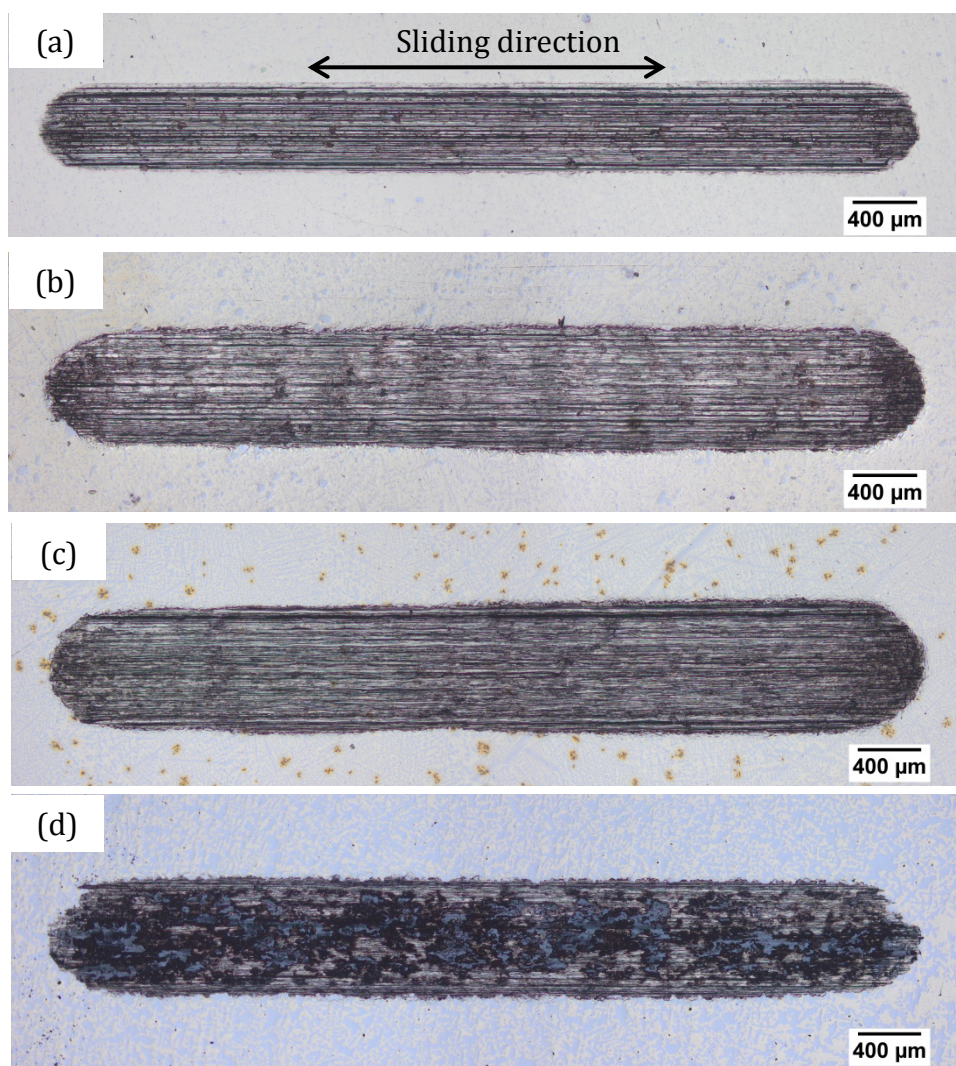
Figure 5.2: Optical images of the worn (a) 9Fe, (b) 20Fe, (c) 27Fe and (d) PTA aluminium bronze coatings after dry sliding wear test against AISI 52100 at a load of 5N
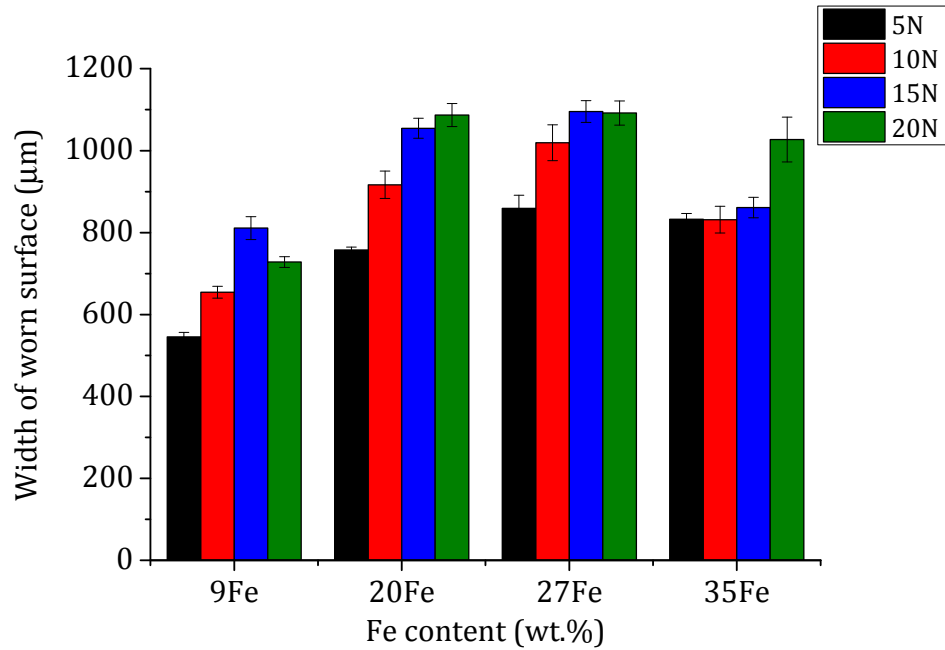
Figure 5.3: The effects of normal load on the width of the worn surface of the PTA aluminium bronzes coatings worn against AISI 52100 bearing steel

The depth profile of the 20Fe coating in a direction parallel to the sliding direction is shown in Figure 5.5 b. The profile shows that wear is not uniform as evidenced by local peaks and valleys. This might be due to the non-uniform hardness distribution caused by the large volume fraction of hard κ_1 intermetallic phase. The hard κ_1 is expected to have higher wear resistance than the surrounding softer solid solution (Cu) phase, which leads to difference in wear rates observed. Comparing to the 20Fe coating, wear on the 9Fe coating is more uniform as shown by Figure 5.4 a. This is due to the homogeneous distribution of fine intermetallic κ_1. The results thus far show that the 9Fe coating with martensitic structure appears to have higher wear resistance than the 20Fe, 27Fe and 35Fe coatings, which have a solid solution (Cu) phase structure. To further investigate the difference between the wear characteristic of these two microstructure and the effects of the constituent phases on the wear characteristic of the coatings, SEM and EDS analysis were employed.
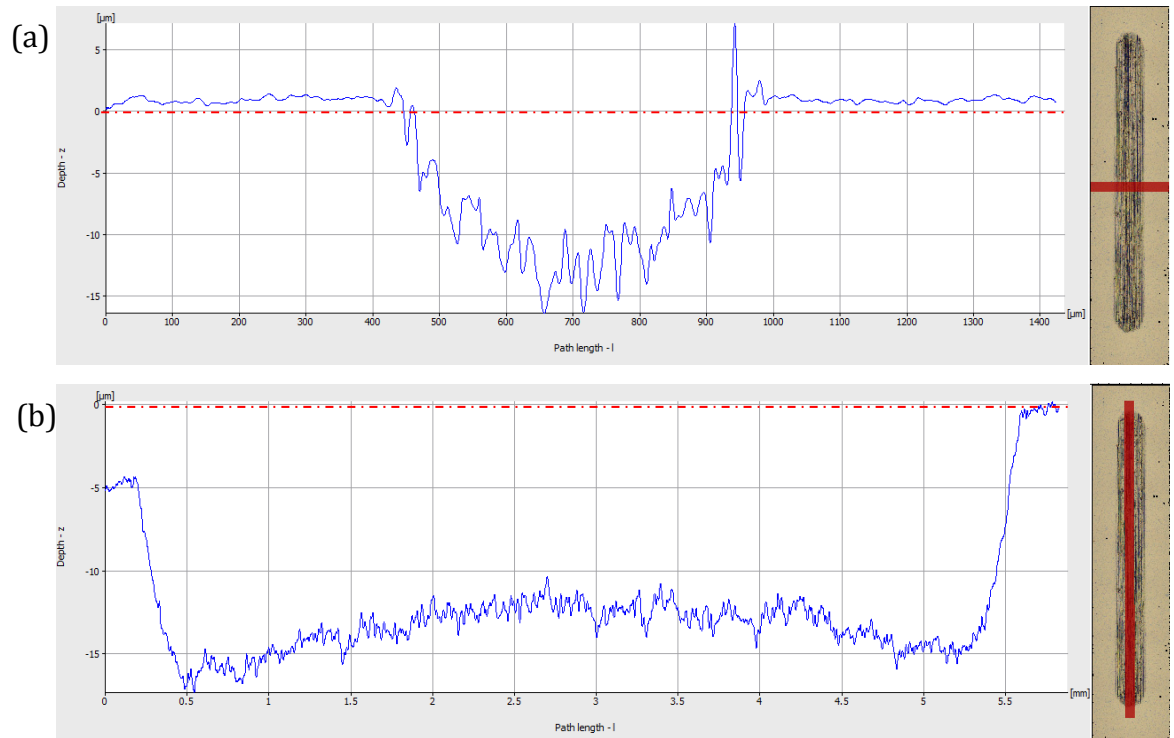
Figure 5.4: Line profile (a) across the worn surface of the 9Fe coating worn against AISI 52100 at 5 N (b) along the centre of the worn surface of 20Fe coating (red lines indicate datum point)
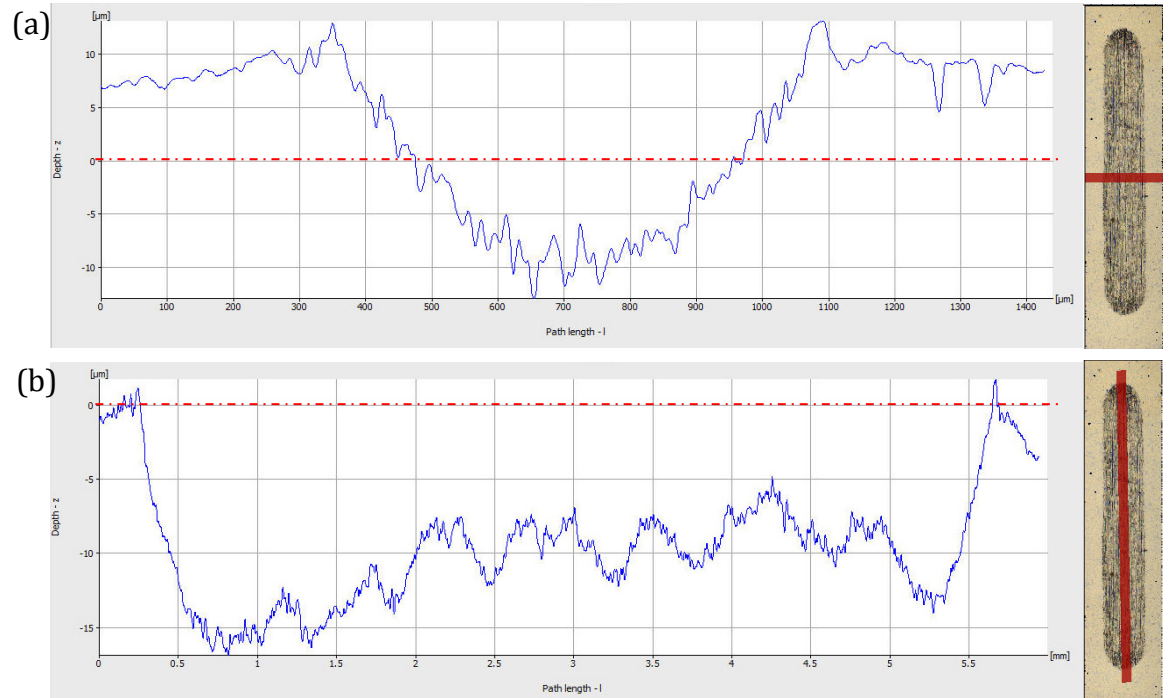
Figure 5.5: Line profile (a) across the worn surface of the 20Fe coating worn against AISI 52100 at 5 N (b) along the centre of the worn surface of 20Fe coating (red lines indicate datum point)

The worn surface of the 9Fe coating is characterised by fine scratches and small wear debris as shown by the secondary electron image in Figure 5.6 a. The scratches are indicative of abrasive wear, which was highlighted earlier by the optical images. The worn surfaces of the 20Fe, 27Fe and 35Fe coatings are characterised by deep scratches and presence of large wear debris as shown in Figure 5.6 b-d. The large wear debris indicates that for the 20Fe, 27Fe and 35Fe coatings, adhesive and or delamination has also taken place in addition to the abrasive wear process.
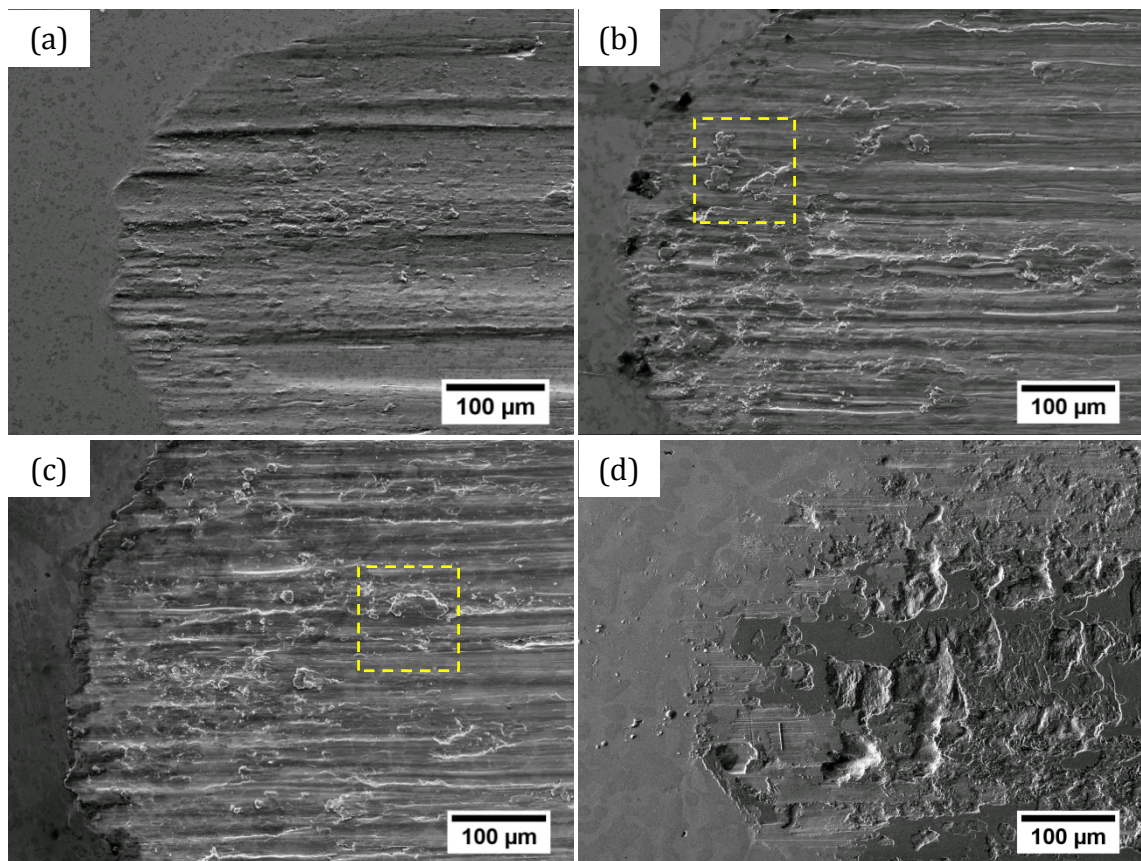
Figure 5.6: Secondary electron images of the worn (a) 9Fe, (b) 20Fe, (c) 27Fe and (d) 35Fe PTA aluminium bronzes coating worn against AISI 52100

The high magnification secondary electron image of the 20Fe coating in Figure 5.7 shows clear sign of adhesive wear. Fine surface cracks (highlighted by red arrows in Figure 5.7) were observed around the edges of the locations where material was removed. Formation and coalescence of these cracks is expected to reduce the cohesive strength of the material near the surface of the coating.

Under the applied normal load, adhesive junctions are formed between the coating and the AISI 52100 counter material. The strength of these junctions may exceed the cohesive strength of the material near the surface, which has been reduced by the formation and propagation of cracks. Consequently the surface begins to peel off and create more cracks as shown in Figure 5.8. Once the crack reaches a critical length, the entire piece is removed from the surface leaving damage on the surface of the coating as shown in Figure 5.9. The same type of worn microstructure was also observed on a 27Fe and 35Fe coatings.
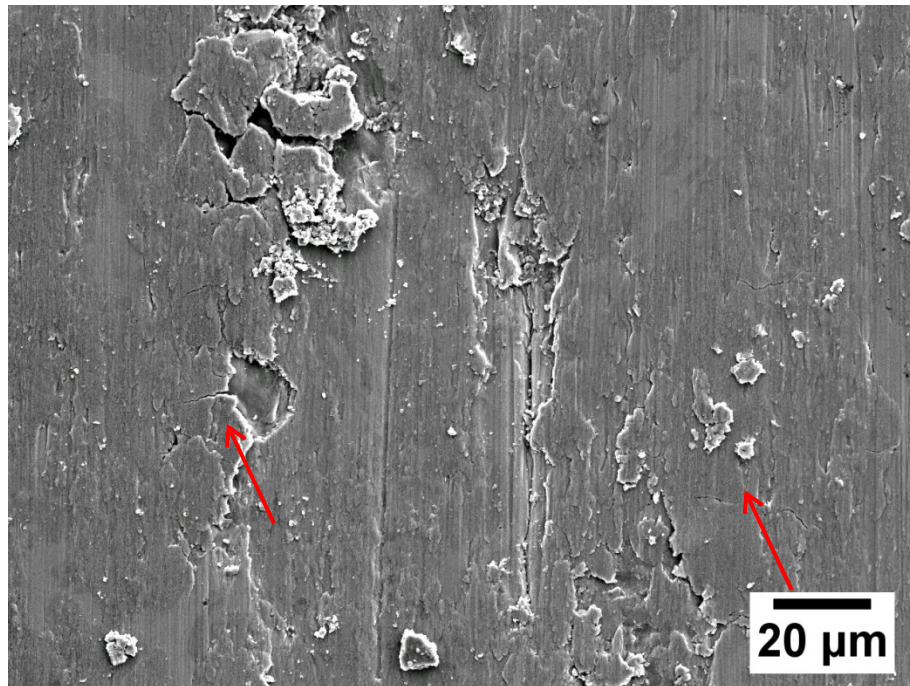
Figure 5.7: High magnification SE image showing adhesive wear and surface cracks 20Fe PTA aluminium bronze coating worn against AISI 52100
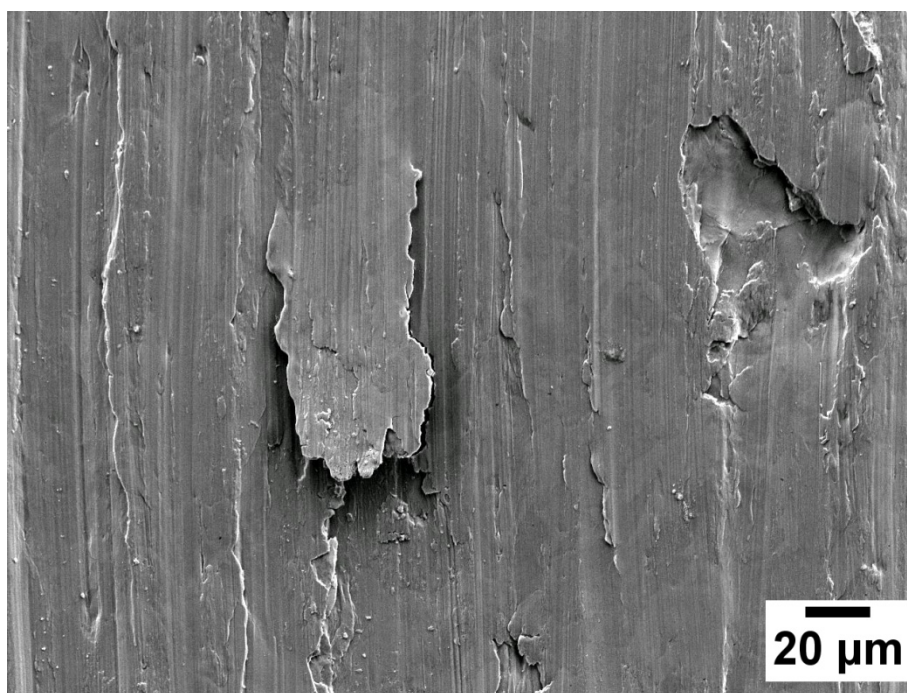
Figure 5.8: High magnification secondary electron image showing removal of material from the 27Fe PTA aluminium bronze coating worn against AISI 52100
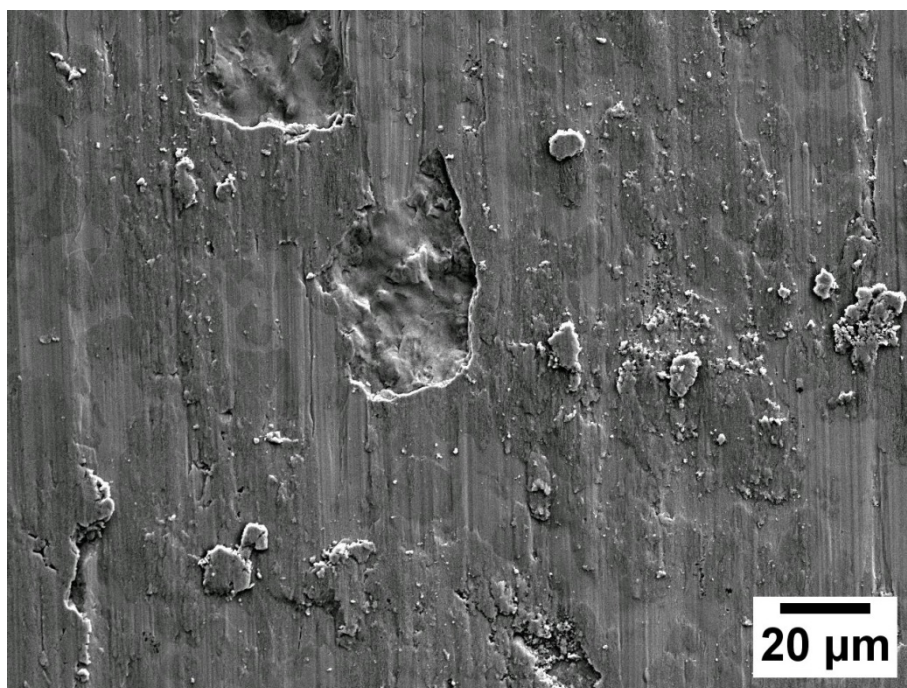
Figure 5.9: High magnification SE image showing removal of material from the 20Fe PTA aluminium bronze coating worn against AISI52100

The removed material can be transferred to the AISI 52100 counter material and/or it can act as abrasive wear particles. The hardness maps in Figure 4.13 b-d show that large differences in hardness exist between the intermetallic κ_1 phase and the solid solution (Cu) phase. The boundary between these two phases is a stress concentration region where cracks might initiate. A low magnification BSE image of the worn coating surface is shown in Figure 5.10. Compared to the surrounding unworn surfaces, damage involving the intermetallic κ_1 phase (appearing dark) was observed on the entire worn surface of the coating. The damage to the larger size κ_1 phase in the 20Fe, 27Fe and 35Fe coatings appears to be more extensive as evidence by the larger shape changes in the form of an increase in length in the direction of sliding.
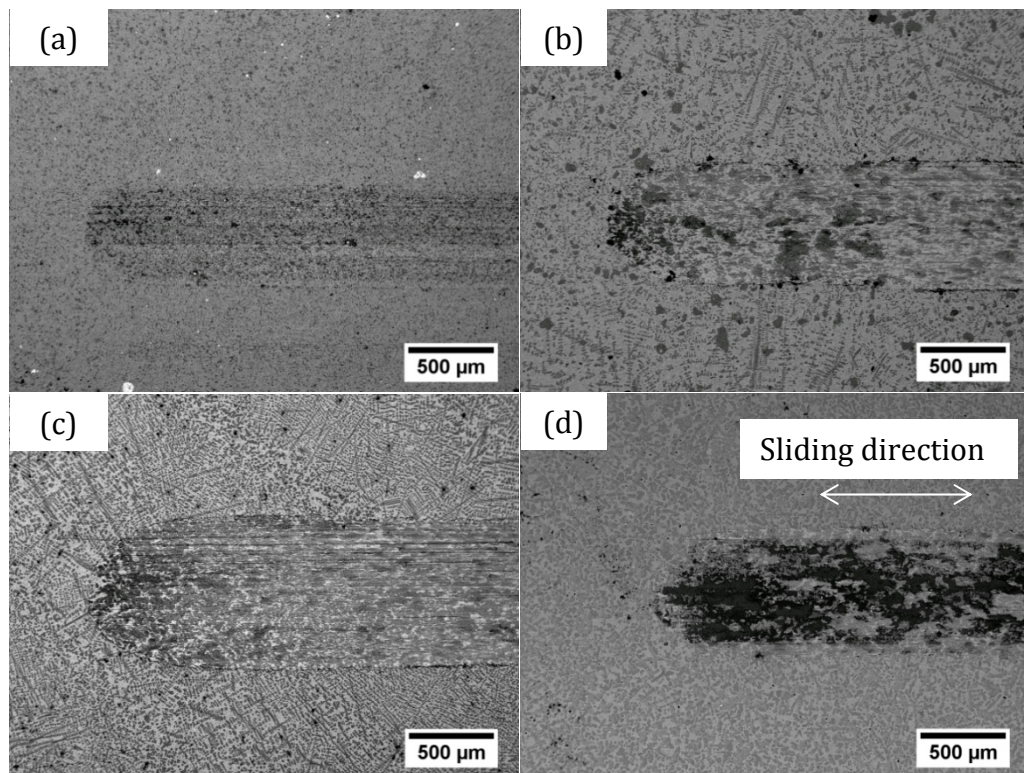
Figure 5.10 Low magnification BSE image showing the damage involving the intermetallic κ_1 phase in (a) 9Fe, (b) 20Fe, (c) 27Fe and (d) 35Fe PTA aluminium bronzes coating following dry sliding wear test against AISI 52100

At the boundaries between the worn and unworn regions of the coating, intersecting slip lines were observed on the 20Fe, 27Fe and 35Fe coatings but not on the 9Fe coating as shown in Figure 5.11. In the 20, 27 and 35Fe coatings, the solid solution (Cu) phase with fcc crystal structure has more slip systems than the martensitic β_1' phase of the 9Fe coating that has an orthorhombic crystal structure. Consequently, less force is required to activate slip. As shown in Figure 5.11 c, the slip lines are also localized to certain areas of the Cu-rich part of the coating. The compositions of these areas have been identified by EDS to be close to that of the solid solution (Cu) phase. The inverse pole figures (see Figure 5.13) of the (Cu) phase in the 20Fe, 27Fe and 35Fe coatings show strong {111} orientation on the Z-axis. The schematic showing the {111} orientation in the fcc system is shown in Figure 5.14. Upon loading, in the Z direction, a preferential slip on this plane will lead to sliding of the surface (similar to sliding a deck of cards). During sliding, several slip systems can be activated, this leads to the intersecting slip lines as shown in Figure 5.11 b and d. Pile-up of slip lines was also observed at the intermetallic κ_1 phase in the form of a decrease in the spacing between slip lines. Near the pile-up sites, some cracks/voids were observed as shown in Figure 5.11 b, c and Figure 5.13. The presence of these cracks might be due to the stress concentration generated by the pile-up of dislocations. Coalescence of these cracks might lead to the delamination of the coating material shown in Figure 5.7 - Figure 5.9. This suggests that for the 20Fe, 27Fe and 35Fe coatings the stress-induced activation of these slip system might play an important role in the mechanisms of wear in these coatings.
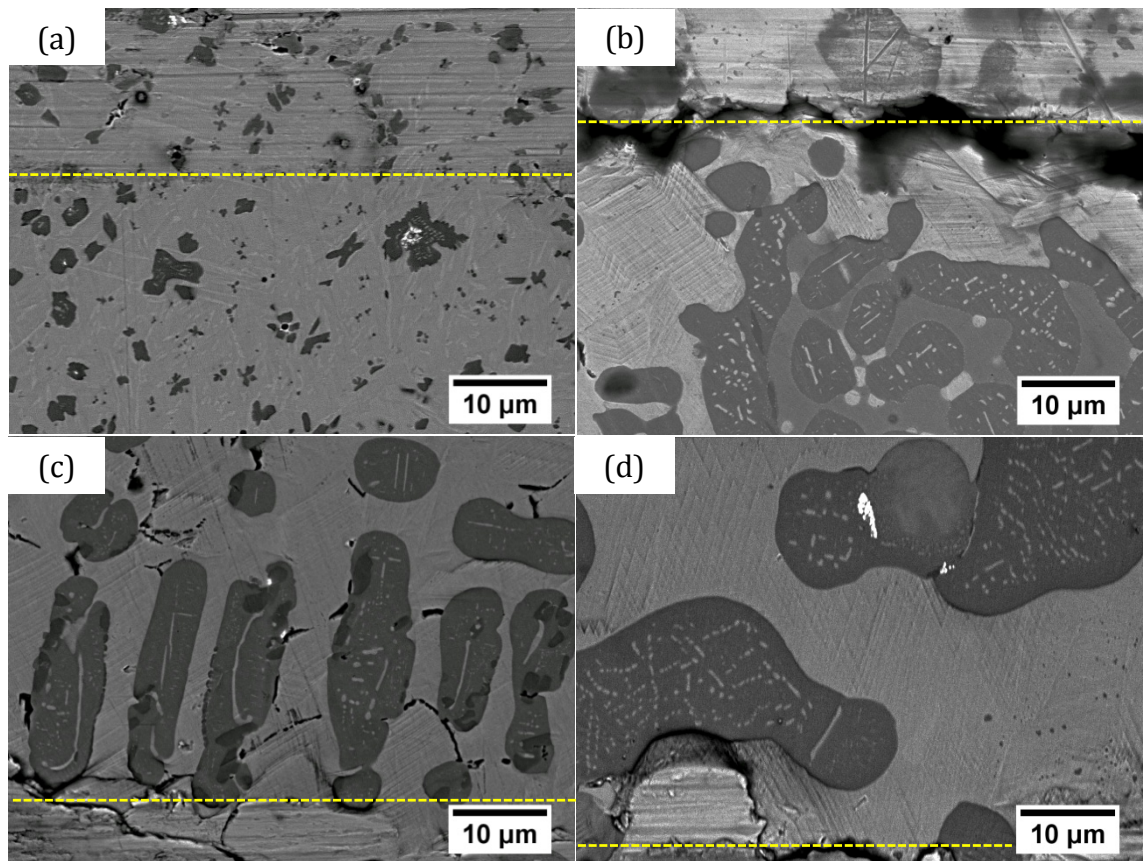
Figure 5.11: High magnification BSE image of the boundaries between the worn-unworn surface of the (a) 9Fe, (b) 20Fe, (c) 27Fe and (d) 35Fe PTA aluminium bronzes coating (yellow lines indicates approximate position of the wear track boundary)
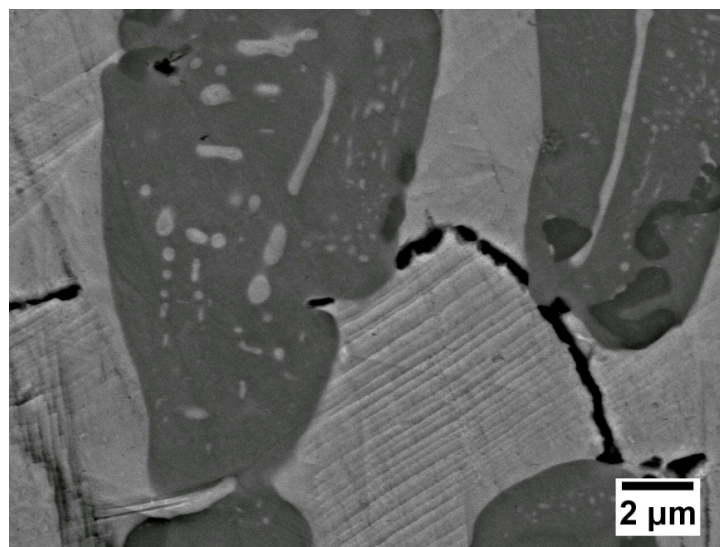
Figure 5.12: Backscattered electron image showing the presence of cracks near the pile up of slip lines at the intermetallic κ_1 phase
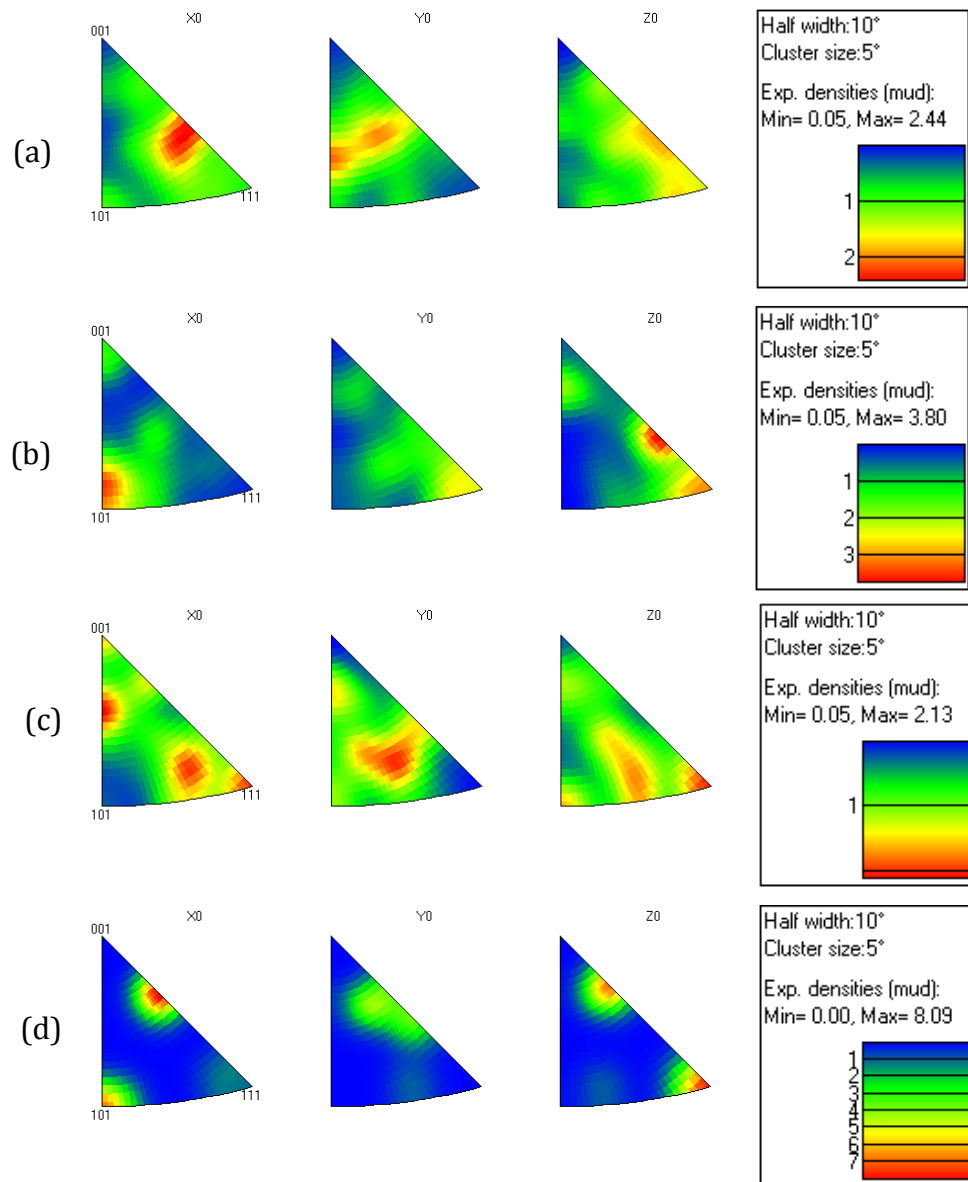
Figure 5.13: Inverse pole figures of the solid solution (Cu) phase obtained from EBSD mapping of the (a) 9Fe, (b) 20Fe, (c) 27Fe and (d) 35Fe PTA aluminium bronze coatings
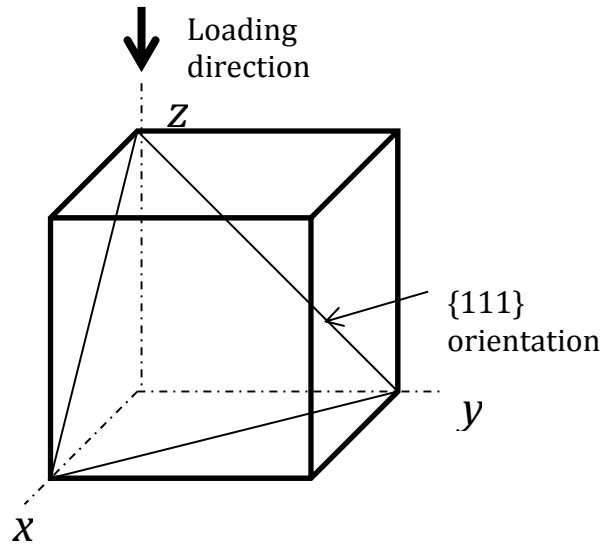
Figure 5.14: Schematic showing (111) orientation in the fcc crystal structure.

The results indicate that for the 20Fe, 27Fe and 35Fe coatings coalescence of surface cracks lead to the removal of the coating material. In the 9Fe coating no surface cracks were observed and the coating failed mainly by abrasive wear. Coalescence of sub-surface cracks is another mechanism that can generate wear particles. To investigate whether subsurface cracks are also present, the worn surfaces of the 9Fe coating and the 27Fe coating were sectioned using Focused Ion Beam (FIB) and observed using ion imaging contrast as shown Figure 5.15 and Figure 5.17 respectively. The ion imaging contrast of the 9Fe coating revealed an ultra-fine grain top layer of $\sim$ 700 nm thickness. The intermetallic κ_1 (appearing dark) appears to be largely un-deformed. Below 1000 nm from the surface, the martensitic structure of the β_1' phase is clearly visible. A small fracture, thought to be a subsurface crack was observed as shown by the yellow box in Figure 5.16.
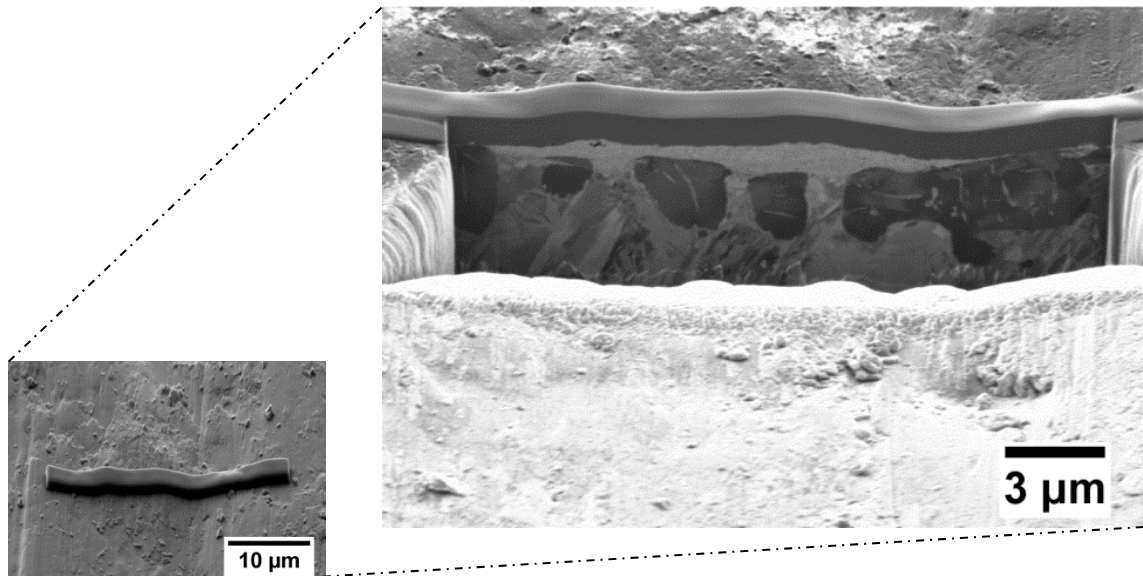
Figure 5.15: SE image of the cross section site and ion contrast image showing the FIB cross section through the wear track of the 9Fe PTA aluminium bronze coating
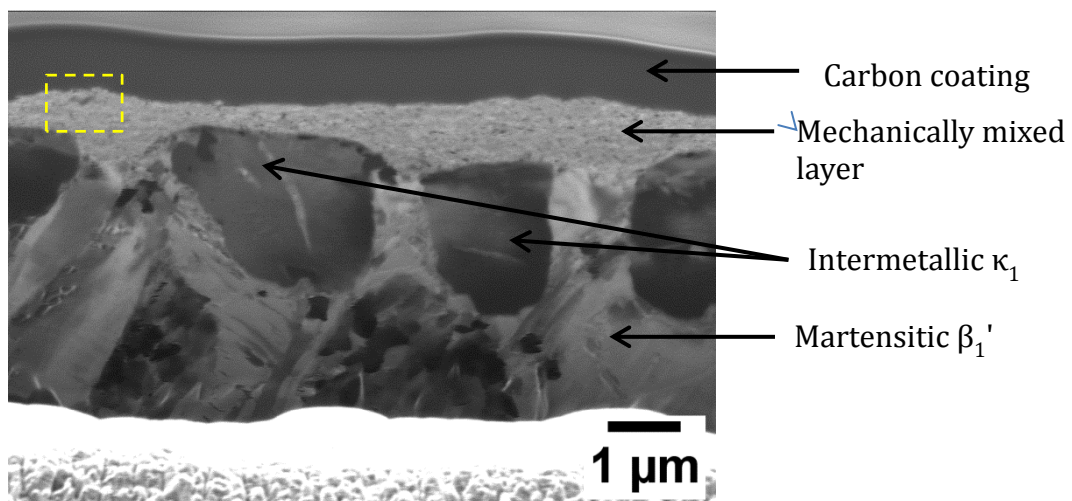
Figure 5.16: High magnification Ion contrast image showing the FIB cross section through the wear track of the 9Fe PTA aluminium bronze coating

However, due to the limited number of cross sections made, it was not possible to conclude whether subsurface cracks are present in the worn surface of the 9Fe coating. The subsurface microstructure of the 27Fe coating contains more deformation as shown in Figure 5.17. The microstructure at $\sim$ 2.5 μm below the worn surface is a mechanically mixed layer characterised by fine grains and plastic flow around the intermetallic particles. Below the mechanically mixed layer is a grain-refined layer of $\sim$ 3 μm thick.

Compared to the 9Fe coating, the deformation of the κ_1 in the 27Fe coating is more extensive as evidenced by the large changes. The plastic flow around the κ_1 phase was also observed as shown in Figure 5.17.

Mechanically mixed layer

Grain-refined layer

Intermetallic κ_1
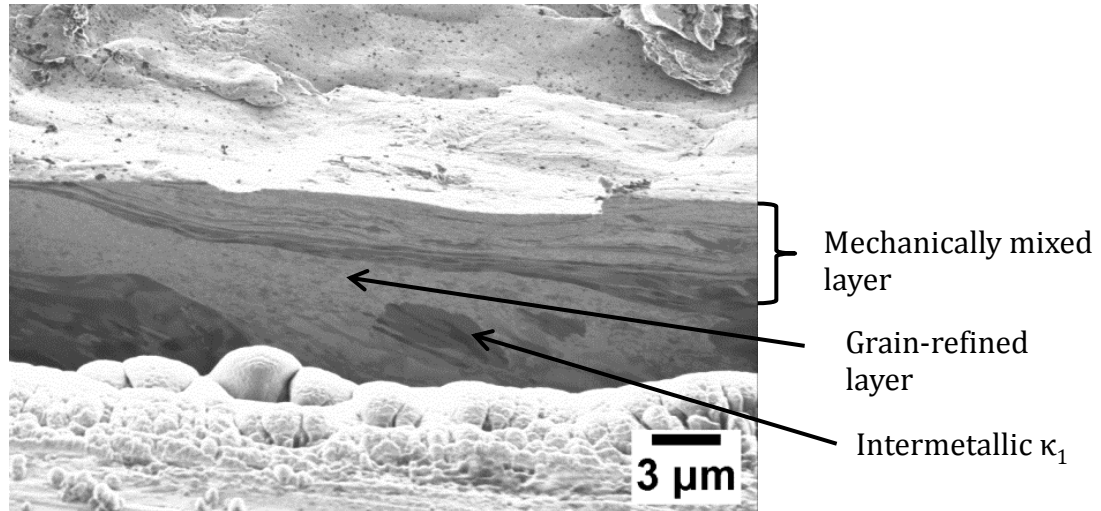
Figure 5.17: Ion contrast image showing the FIB cross section through the wear track of the 27Fe coating after wear test against AISI 52100 bearing steel

The plots of hardness variations across the worn surfaces of the PTA aluminium bronze coatings are shown in Figure 5.18. In the coating with solid solution phase (Cu), the hardness increase is higher than the coating with a martensitic phase β_1'. The stress induced during sliding increases the dislocation density in the coating. Due to the repulsive strain interaction between dislocations, the increase in the dislocation density limits its movement thereby increasing the hardness. The limited slip systems in the martensitic phase β_1' phase impedes the movement of dislocation, therefore the effects of dislocation hardening is less than the solid solution (Cu) phase which has more slip systems. The increase in hardness of the worn region also indicates that the wear debris generated can have hardness that is approximately double that of the unworn region. This can promote abrasive wear.
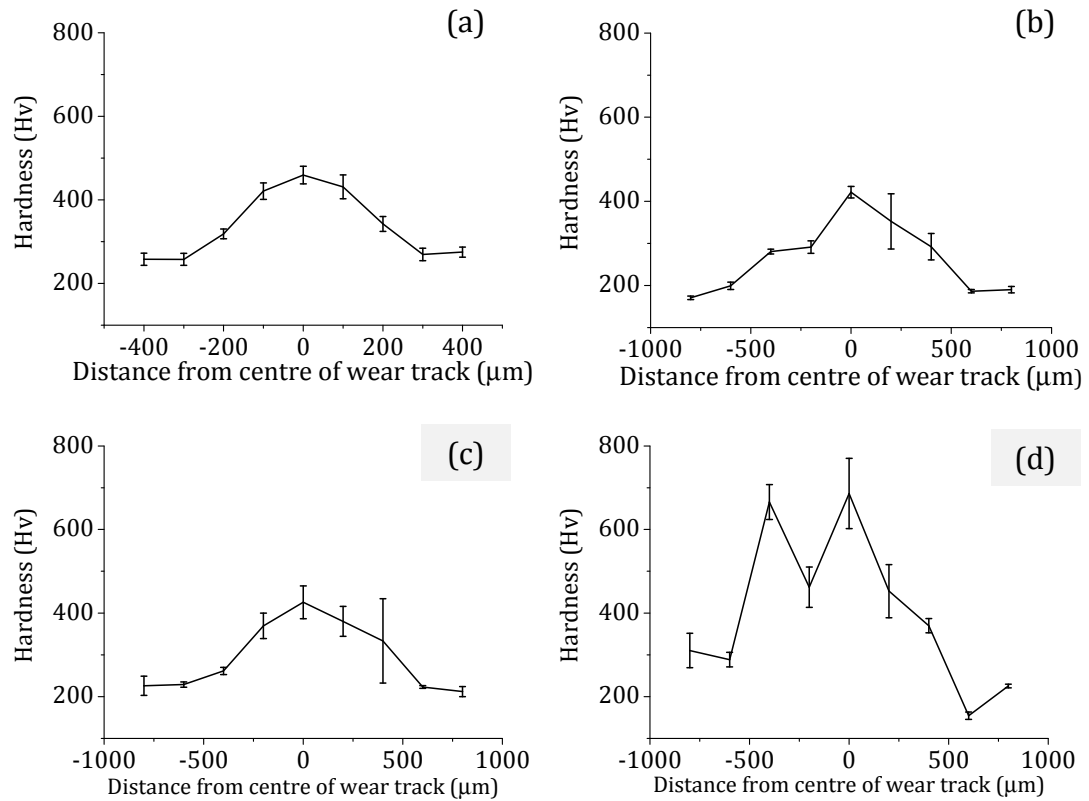
Figure 5.18: Variations in the hardness across the worn surface of the (a) 9Fe, (b) 20Fe, (c) 27Fe and (d) 35Fe PTA aluminium bronzes coatings after dry sliding wear test against AISI 52100 at 5N (error bars represent standard deviation of six measurements)

5.1.3   Material transfer to the AISI 52100 bearing steel

In section 5.1.2, wear debris have been shown to originate from the coalescence of surface cracks. Some of the wear debris may remain on the surface and can act as an abrasive wear particle; other wear debris may be removed and transferred to the AISI 52100 counter material. To investigate whether the coating material has been transferred to the AISI 52100, SEM-EDS observations were made. The secondary electron images of AISI 52100 pins in Figure 5.19 show clear evidence of debris on the surface. EDS analyses of these debris (see Table 5.1) show that they are rich in Cu, which confirms that these debris have been transferred from the coating to the pin.

The transfer of coating material on to the pin prevented direct contact between the coating and the AISI 52100 counter material. With increasing load, the abrasive wear promotes more coating material transfer onto the surface of the AISI 52100 counter material as shown in Figure 5.19 this further reduces the contact area between the two solids, which leads to the observed decrease in CoF as shown Figure 5.1. This indicates that the composition and the stability of the transferred material strongly influence the friction and wear characteristics under dry sliding condition.
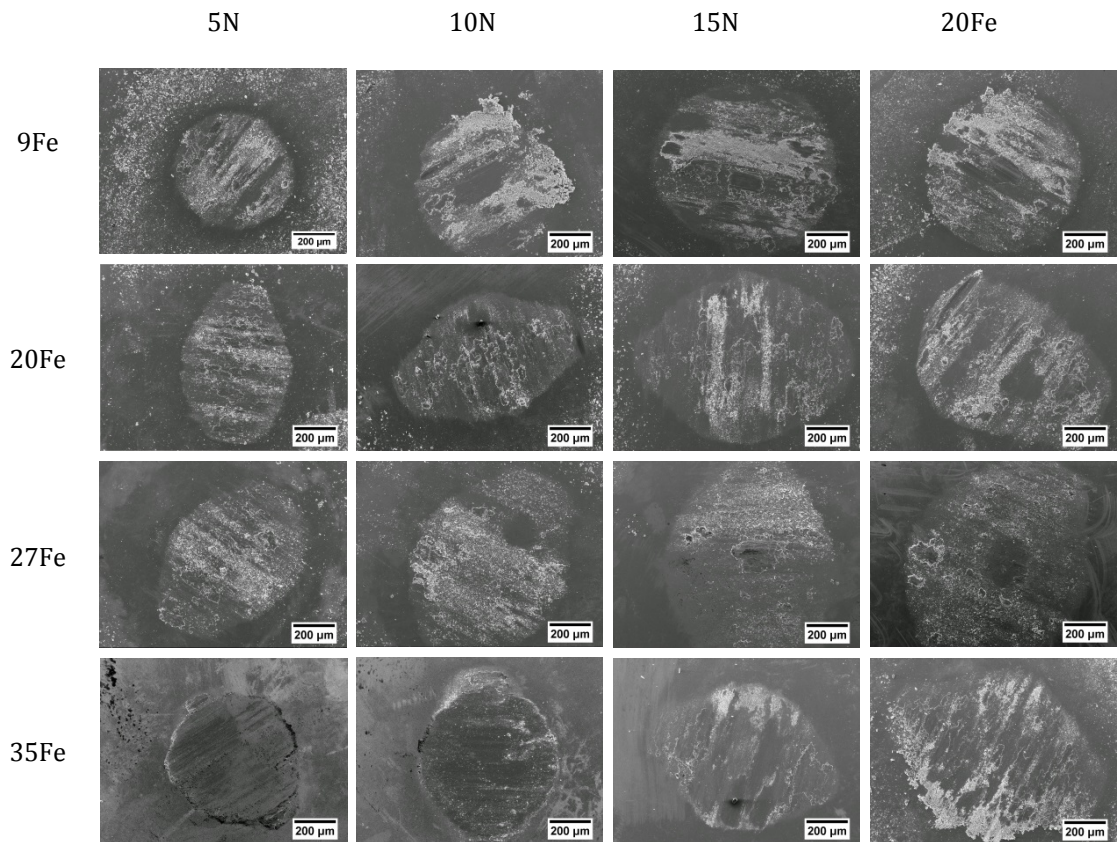
Figure 5.19: Secondary electron images showing the morphology of the AISI 52100 ball after dry reciprocating sliding test against the coatings

Table 5.1: EDS results of the wear debris on the AISI 52100 pin (all in wt.%)

	Cu	Al	Fe	Mn	Ni	Si	Cr	O
9Fe	61.4	10.0	13.6	0.9	0.7	0.3	0.7	12.3
15Fe	55.1	8.4	23.3	0.8	1.0	0.2	0.5	10.7
20Fe	51.0	8.1	32.4	0.7	0.4	0.2	0.2	6.9
37Fe	36.5	6.3	41.0	0.8	1.4	0.2	0.7	13.1

Evidence in the literature shows that the frictional heat generated during dry sliding is sufficient to cause transfer of materials [48] as well as promoting segregation of elements to the surface [150]. To investigate this, EDS analysis was carried out across the worn surfaces to investigate the composition change. The change in oxygen content between the worn and the unworn surfaces of the coatings is shown in Figure 5.20. Although there are uncertainties regarding the detection of oxygen by EDS, for all coatings an increase in oxygen content compared to unworn surface was observed. This indicates that the surface has been oxidised following the wear process.
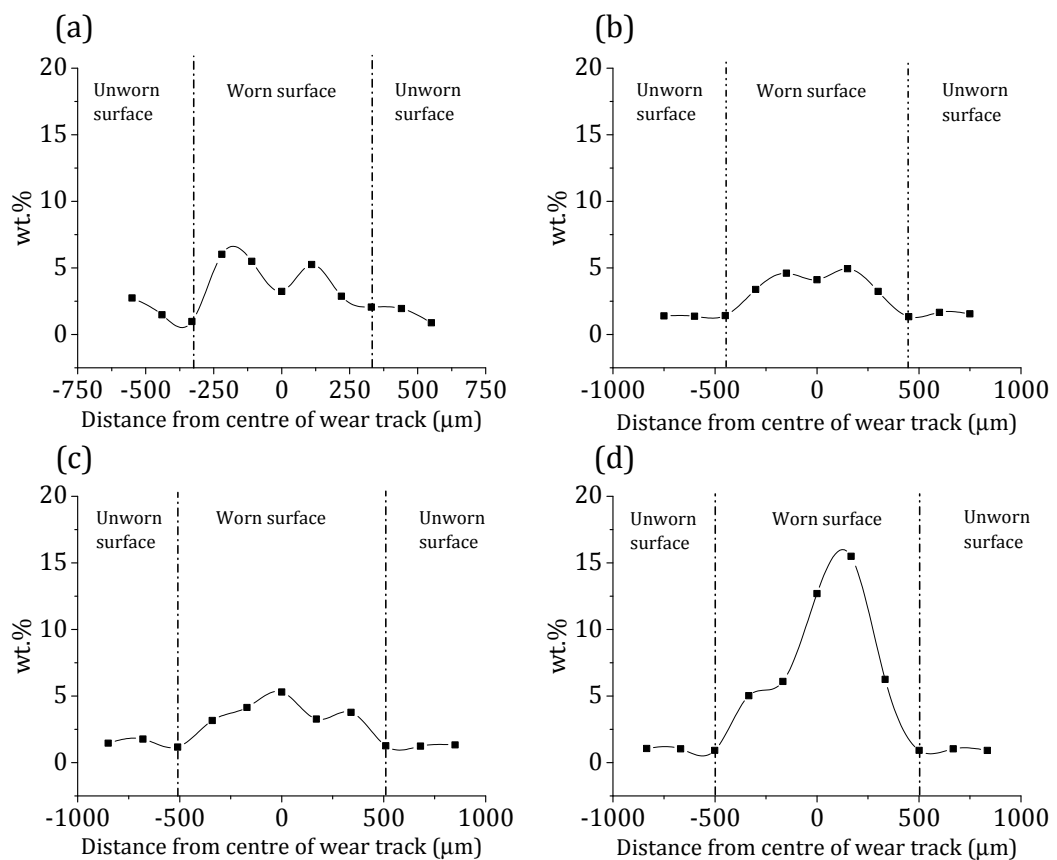
Figure 5.20: Variations in Oxygen across the between the worn and unworn surfaces of (a) 9Fe, (b) 20Fe, (c) 27Fe and (d) 35Fe PTA aluminium bronzes coating after dry sliding test against AISI 52100

Oxidation of the surface is expected to have a strong influence on the composition of the primary alloying elements of the coating. The change in Cu content between the worn and unworn surfaces is shown in Figure 5.21. The 35Fe coating shows the most significant reduction in the Cu content as shown in Figure 5.21 d.

This indicates that during sliding between the 35Fe coating and the AISI 52100, formation of Cu-oxides can be expected. For the other coatings, the Cu content remains at approximately the same level as the unworn surface as show in Figure 5.21 b-c. This indicates that for these coatings, the oxides produced during sliding are different to that formed on the 35Fe coating.
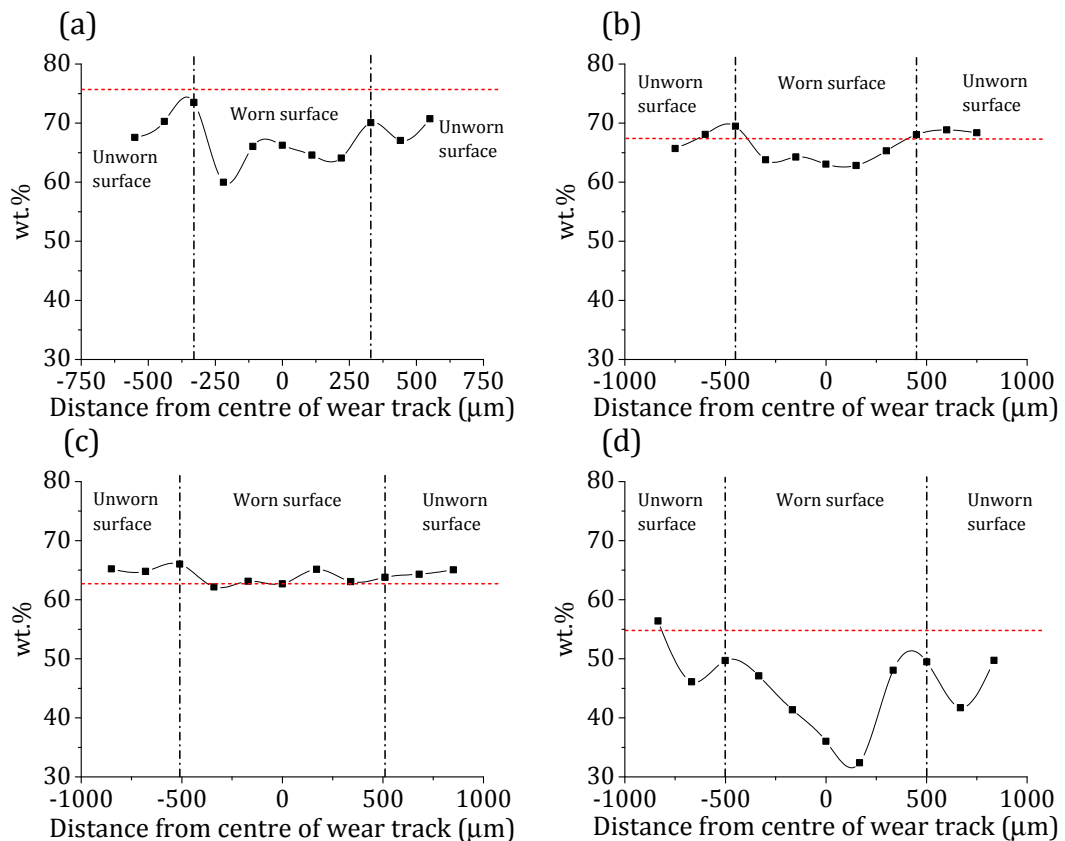
Figure 5.21: Variations in Cu content across the worn and unworn surfaces of (a) 9Fe, (b) 20Fe, (c) 27Fe and (d) 35Fe PTA aluminium bronzes coating after dry sliding test against AISI 52100 (red lines mark the Cu content in as sprayed condition)

The change in Al content as a result of the wear process is shown in Figure 5.22. For 9Fe, 20Fe and 27Fe PTA aluminium bronze coatings, an increase in the Al content was observed. This increase is most apparent in the 9Fe coating. The increase in Al might be due to the surface segregation of Al caused by the heat generated during dry sliding. Segregation of Al has also been observed during dry sliding of Cu-Al alloys [150][152] and has been associated with the formation of Al_2O_3 layer on the surface.

In the 35Fe coating, the Al content remains at approximately the same level as the unworn surface as shown in Figure 5.22 d. This suggests that during sliding the surface of the 35Fe coating is mostly covered with Cu-oxide while the surface of the 9Fe, 20Fe and 27Fe coatings are covered with Al_2O_3. From the SEM images shown in Figure 5.19, the Al_2O_3 layer appears to have stronger adhesion the AISI 52100 bearing steel substrate than the Cu-oxide. This is evident by the lower number of debris observed on the AISI 52100 counter material.
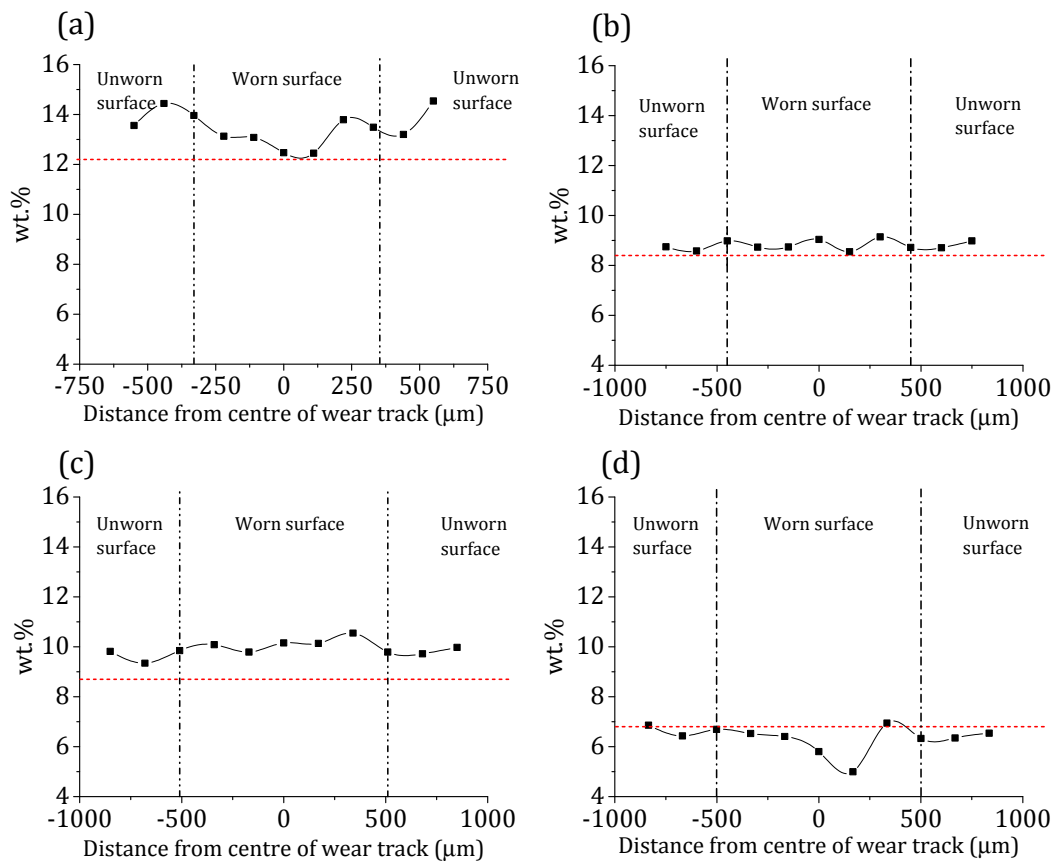
Figure 5.22: Variations in Al across the between the worn and unworn surfaces of (a) 9Fe, (b) 20Fe, (c) 27Fe and (d) 35Fe PTA aluminium bronzes coating after dry sliding wear test against AISI52100 (red lines mark the Cu content in as sprayed condition)

5.1.4   Effects of increasing load on the specific wear rates

The change in microstructure induced by the PTA process has a significant impact on the specific wear rate as shown in Figure 5.23. Up to 15 N, the specific wear rate increased with the increasing load. At 20 N the specific wear rate decreases as shown in Figure 5.19. The increase in load promotes the transfer of more oxides to the surface of the AISI 52100 counter material, this minimised the contact area between the two surfaces, which is evident as a reduction in the CoF as shown in Figure 5.1. The reduction in CoF also reduced the shear stress, which minimized the probability of crack formation on the surface of the coating. This leads to the observed reduction in the specific wear rate. The decrease in specific wear rate at 20 N might be due to the influence of adhesive wear that promotes more transfer of material on to the surface of the coating. This reduces the weight loss that leads to an apparent reduction in specific wear rate.
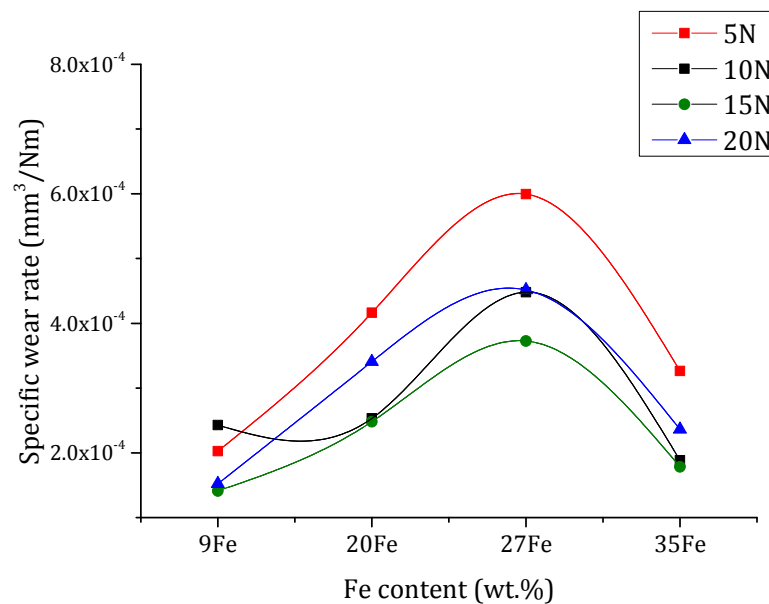
Figure 5.23: The effects of PTA induced Fe increase on the specific wear rate of the coating worn against AISI 52100 bearing steel

5.2   Effects of the microstructure on the galling resistance

In sheet metal forming processes, the transfer and built up of adhesive sheet metal debris on the surface of the forming dies can result in a high friction coefficient, seizure and wear of both forming dies as well as the sheet metal. The problem is commonly referred to as galling, which can classify as a severe form of adhesive wear. One of the solutions to galling is the application of a surface coating. Several coating systems have been investigated; however their performance was only evaluated against a limited type of sheet metals, which are typically Zn-coated steel and high strength steel. Stainless steel is a commonly used sheet metal that has been reported to suffer for galling. In the present research, the galling resistance of the PTA aluminium bronze coatings under dry sliding condition against stainless steels with different hardness was evaluated. The aim is to investigate the effects of sheet metal hardness on the wear characteristic of the coating. The currently used AISI D2 tool steel was tested under the same condition for comparison. The results from the tests are presented in this section.

5.2.1   Dry sliding friction coefficient

The galling process can be distinguished in to three separate stages as discussed in section 2.1.1. The first stage involves pure sliding followed by abrasive microscopic scratches, which upon further sliding leads to accumulation and growth of the transferred sheet metal and macroscopic scratching. The end of the initial stage of galling is typically marked by an increase in friction, which can be hard to resolve from the friction diagram. Furthermore, in some materials macroscopic scratching is not observed even though there has been significant transfer of sheet material [32]. The observed friction coefficients during dry sliding between the coatings and stainless steel substrate are shown in Figure 5.24. With the exception of the 35Fe coating, no significant changes in friction coefficient were observed with increasing counter material hardness. The 9Fe coating has the lowest and most stable coefficient of friction. While the 35Fe coating has the highest and most unstable CoF as evident by the large fluctuation particularly at ~1000 s (see Figure 5.24 d). Note that the measured coefficient of friction for all coatings are lower than that of the AISI D2 tool steel tested under the same condition.
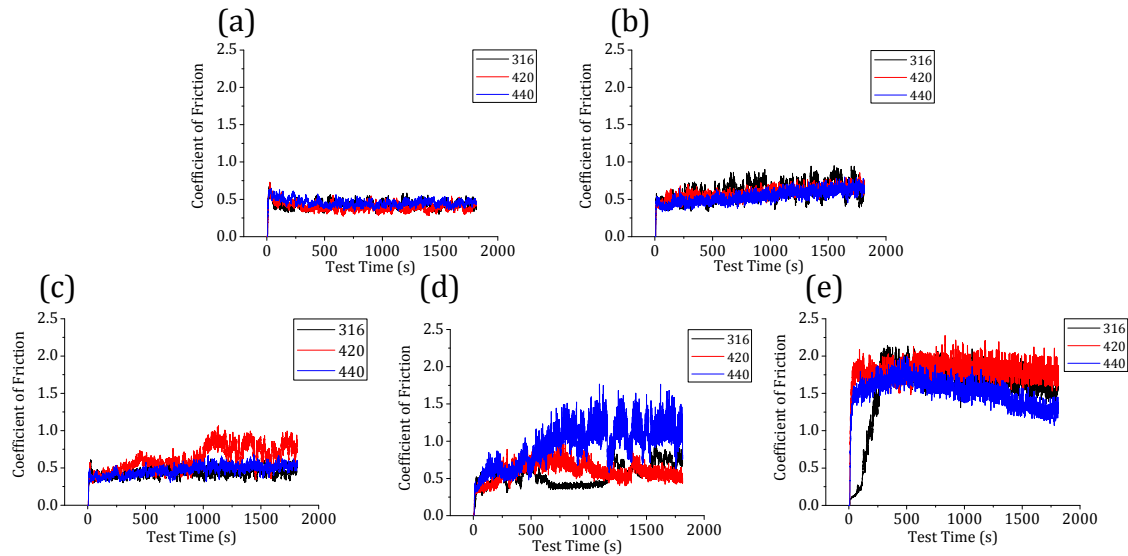
Figure 5.24: Measured coefficient of friction during dry reciprocating sliding between AISI 316, 420 and 440 against (a) 9Fe (b) 20Fe (c) 27Fe and (d) 35Fe PTA aluminium bronze coating and (e) AISID2 tool steel

Figure 5.24 also shows the use of friction coefficient as a criterion for galling is difficult as the rise in CoF occurs over a very short period of time and is hard to resolve on the friction vs. time plots, particularly for the 9Fe and 20Fe coating. Therefore, in the present research high-speed friction data was collected at a sampling rate of 1 kHz during the first 30 s, 900 s and at the last 10 s of the test. Some of the high-speed data collected during the first 10 s of the test is shown in Figure 5.25. The high-speed data is presented in the form of friction force (N) vs. sliding distance (mm). The area inside the hysteresis represents the energy required to overcome friction in each cycle. These areas were determined using numerical integration and are presented in Figure 5.26. A rise in the friction force can be associated with shearing of adhesive junction. From the high speed data the sudden increase in friction force was observed on the 27Fe and 35Fe coating, particularly at approximately the -2 and 2 mm positions. This is expected as at these positions, the relative velocity between the two materials is momentarily zero, which allows time for formation of adhesive junction. As the moving specimen accelerates back in the opposite direction, the shear force generated during sliding breaks the adhesive junction, which leads to the observed increase in friction force.

These sudden increases in friction force were not observed on the 9Fe and 20Fe. It is worth noting that the energy required to overcome friction for the AISI D2 coating is ~3 times more than the amount required for the PTA aluminium bronzes coatings.
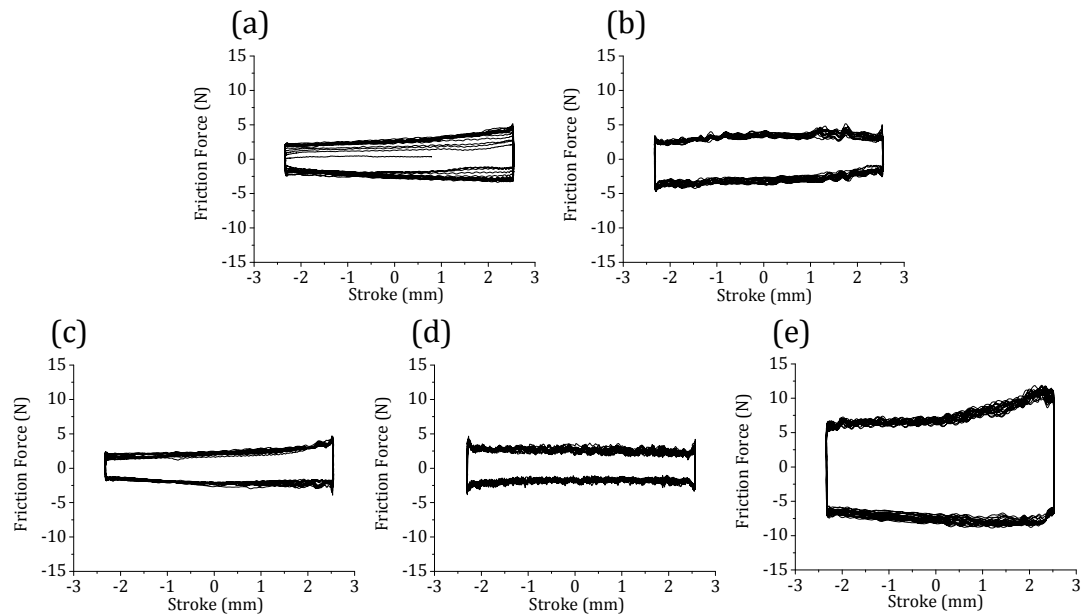
Figure 5.25: High speed friction data from the first 10 seconds of the of dry sliding wear test between AISI 420 and (a) 9Fe, (b) 20Fe, (c) 27Fe, (d) 35Fe coating and (e) AISI D2 tool steel
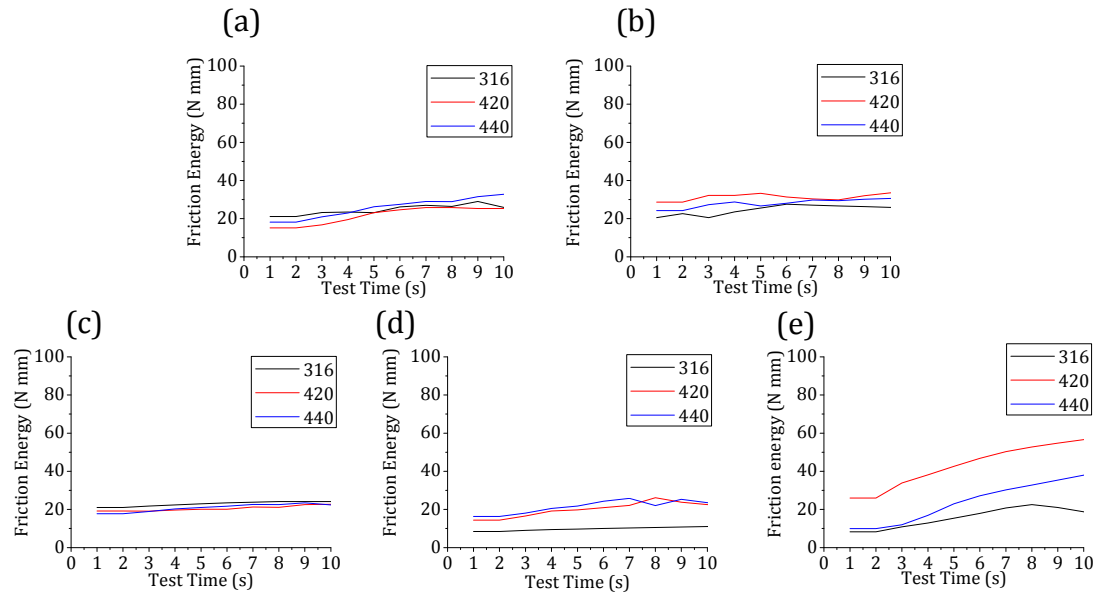
Figure 5.26:Energy consumption during first 10s of the dry sliding test between (a) 9Fe, (b) 20Fe, (c) 27Fe, (d) 35Fe coating and (e) AISI D2 tool steel against the AISI 316, 420 and 440 stainless steel

The plots showing the friction force vs. sliding distance during the last 10 s of the test are shown in Figure 5.27. For the 9Fe, 20Fe and 27Fe PTA coatings; the energy required to overcome friction is approximately constant for all three-counter materials tested. However, for the 35Fe and the AISI D2 tool steel, different energy consumptions were observed as shown by Figure 5.28 d and e. This indicates that friction characteristics of the 9Fe, 20Fe and 27Fe are not strongly affected by the counter material hardness.
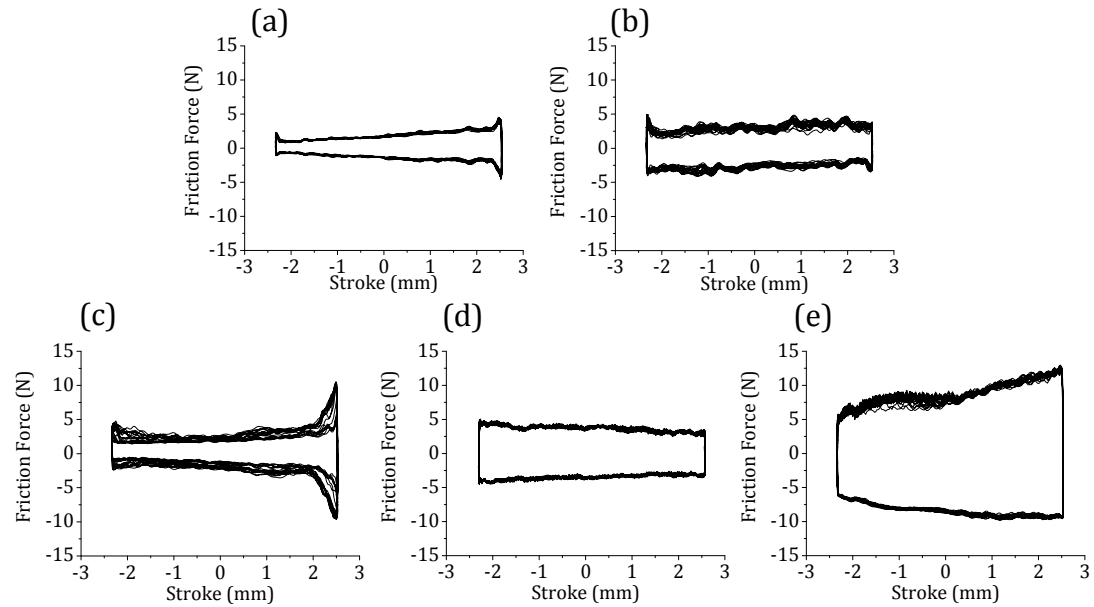
Figure 5.27: High speed friction data from the last 10 seconds of the of dry sliding test between AISI 420 and (a) 9Fe, (b) 20Fe, (c) 27Fe, (d) 35Fe coating and (e) AISI D2 tool steel
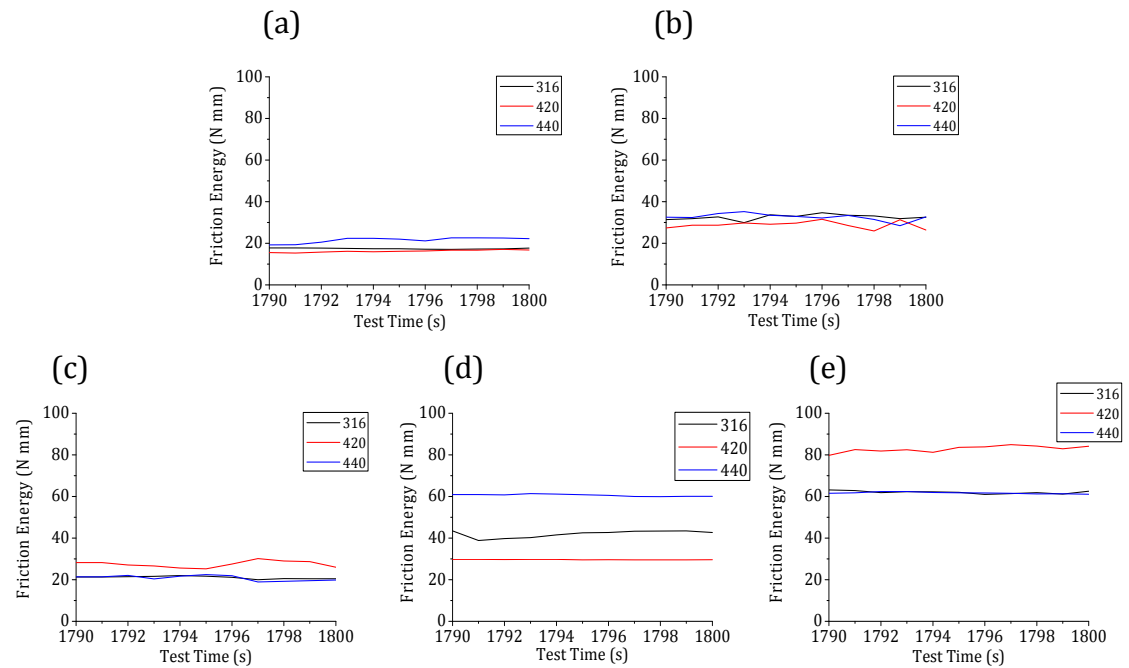
Figure 5.28: Energy consumption during the last 10 seconds of the dry sliding test between (a) 9Fe, (b) 20Fe, (c) 27Fe, (d) 35Fe coating and (e) AISI D2 tool steel against the AISI 316, 420 and 440 stainless steel

5.2.2   Morphology and chemical analysis of the worn coating surfaces

The morphology of the worn 9Fe coating is shown in Figure 5.29. The optical images show that with increasing hardness, the abrasive wear becomes more dominant as indicated by the deep scratches shown in Figure 5.29 b and c. The worn surfaces of the coating with solid solution (Cu) phase (represented here by the 27Fe coating) are shown in Figure 5.30. Compared to the coating with martensitic phase matrix, the worn surfaces are substantially wider. More wear debris (appearing black) were also observed on the worn surfaces of the 27Fe coating particularly at the both ends of the track. With increasing counter material hardness, abrasive wear also increases as indicated by the scratches that are similar to those observed on the 9Fe coating. With increasing counter material hardness, significant variations in the morphology of the worn AISI D2 were observed as shown in Figure 5.31. Similarly to the worn coating surfaces, wear debris were observed at both ends of the wear track. To quantify the effects of increasing counter material hardness on the depth of the wear scar, optical profilometry was used. Figure 5.32 shows that as the counter material hardness increases, the depth of the scratches also increases. For a given counter material hardness, the 27Fe coating has the deepest scratch; this might be due to the low hardness of the matrix phase and the large volume fraction of the hard intermetallic phases that can be displaced and act as abrasive wear particles. The 35Fe coating has the shallowest scratch; this might be due to the influence of the adhesive wear debris, which can reduce the depth of the abrasive wear. To determine the composition of the wear debris and to observe the worn surfaces in more detail SEM observations and EDS analyses of the worn surfaces and wear debris were made.
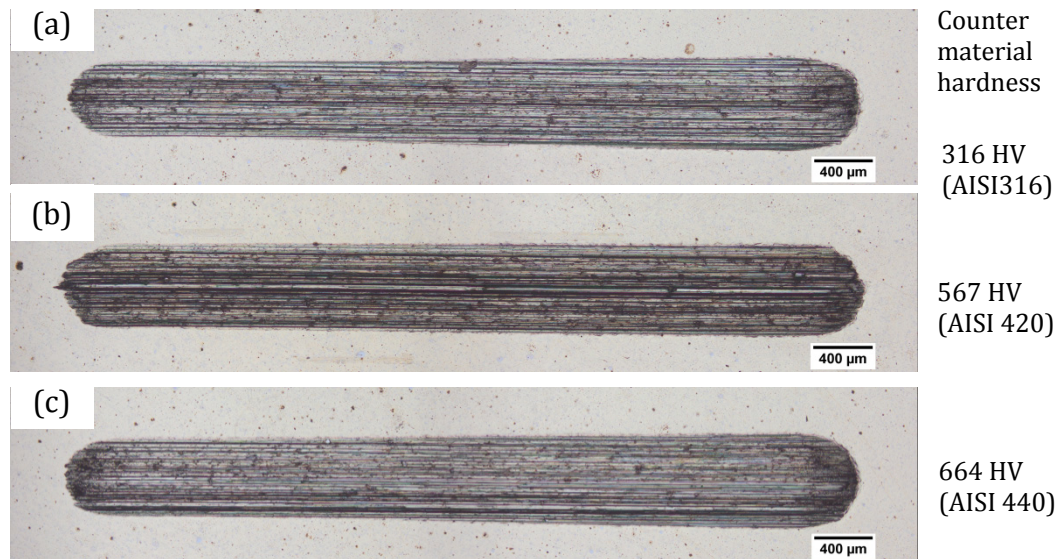
Figure 5.29: Optical images showing the worn surfaces of the 9Fe PTA aluminium bronze coating after dry sliding wear test against (a) AISI 316, (b) AISI 420 and (c) AISI 440 stainless steel
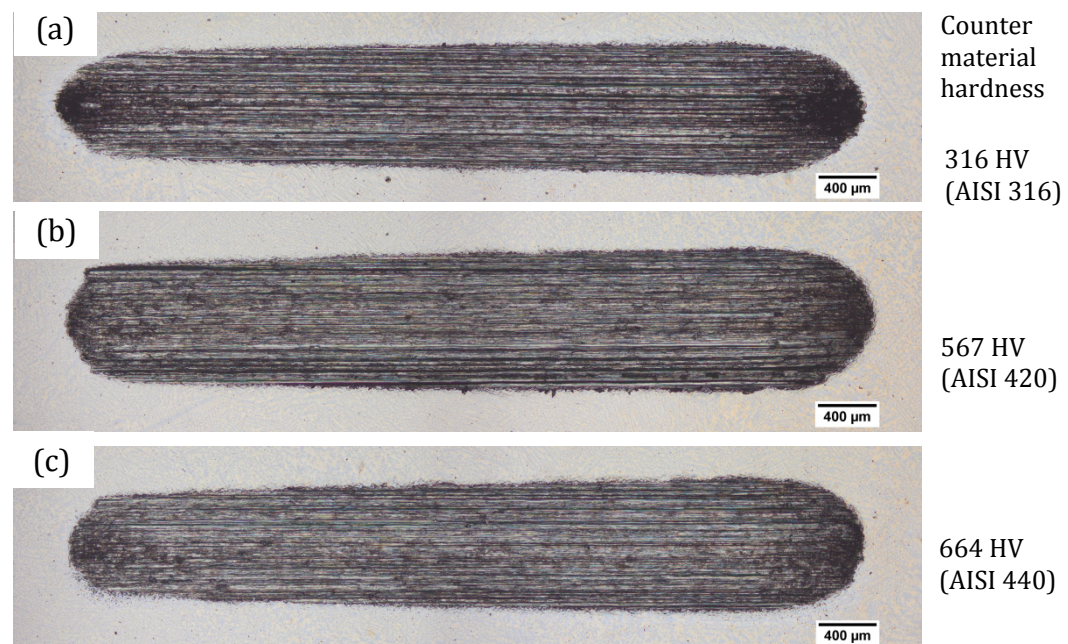
Figure 5.30: : Optical images showing the worn surfaces of the 27Fe PTA aluminium bronze coating after dry sliding wear test against (a) AISI 316, (b) AISI 420 and (c) AISI 440 stainless steel

(a)

Counter
material
hardness

316 HV
(AISI 316)

(b)

567 HV
(AISI 420)

(c)

664 HV
(AISI 440)
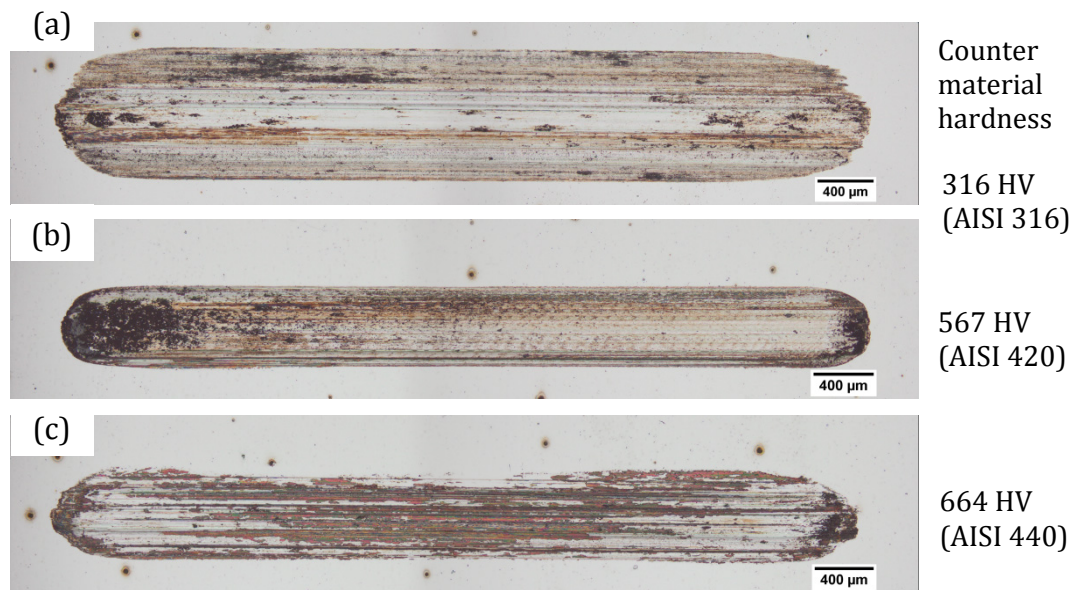
Figure 5.31: Optical images showing the worn surfaces of the AISID2 tool steel after dry sliding wear test against (a) AISI 316, (b) AISI 420 and (c) AISI 440 stainless steel
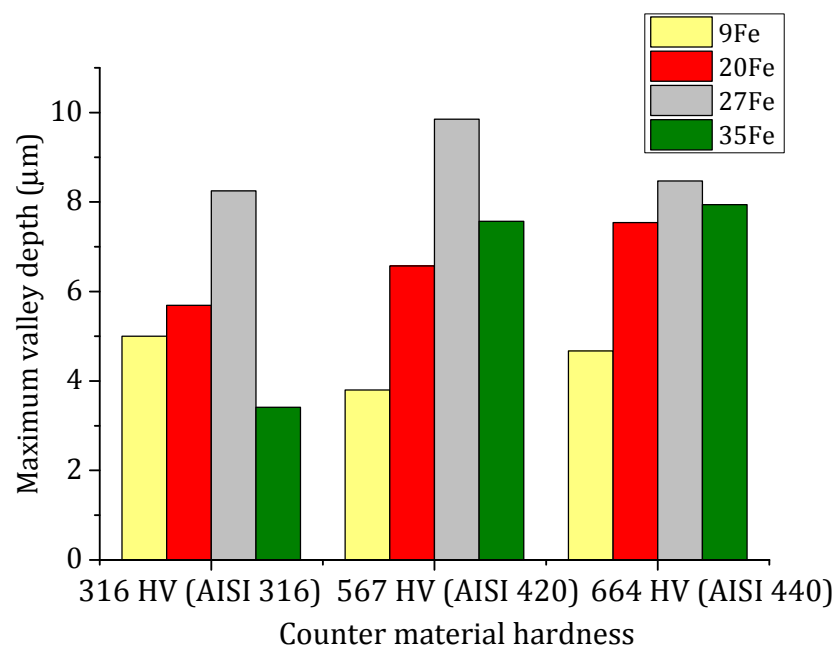
Figure 5.32: The effects of increasing counter material hardness on the maximum depth of the wear scar on the worn surface

The SEM observations of the worn PTA aluminium bronze coating and AISI D2 surfaces are shown in Figure 5.33. Comparing the four coatings, the worn surfaces of the 9Fe coating mainly consists of microscopic scratches which indicates the presence of abrasive wear. As the Fe content in the coating increases, adhesive wear dominates. This is evident by the increase in wear debris on the worn surfaces as shown in Figure 5.33. EDS analysis shows that the debris originating from the coating material are Cu-oxide with typical composition shown in Figure 5.34. Some Fe-rich debris were also observed as shown in Figure 5.35. The high Fe and Cr content suggest that the debris originated from the stainless steel counter material. The wear debris on the surface of the AISI D2 are mainly Fe oxides with typical composition shown in Figure 5.36. Due to the similarities in composition of the AISI D2 tool steel and the stainless steels it was difficult to determine whether material transfer took place. However, based on the hardness difference, material transfer from the AISI 316 stainless steel to AISI D2 tool steel is expected. This is due to the lower hardness of the AISI 316 stainless steel.
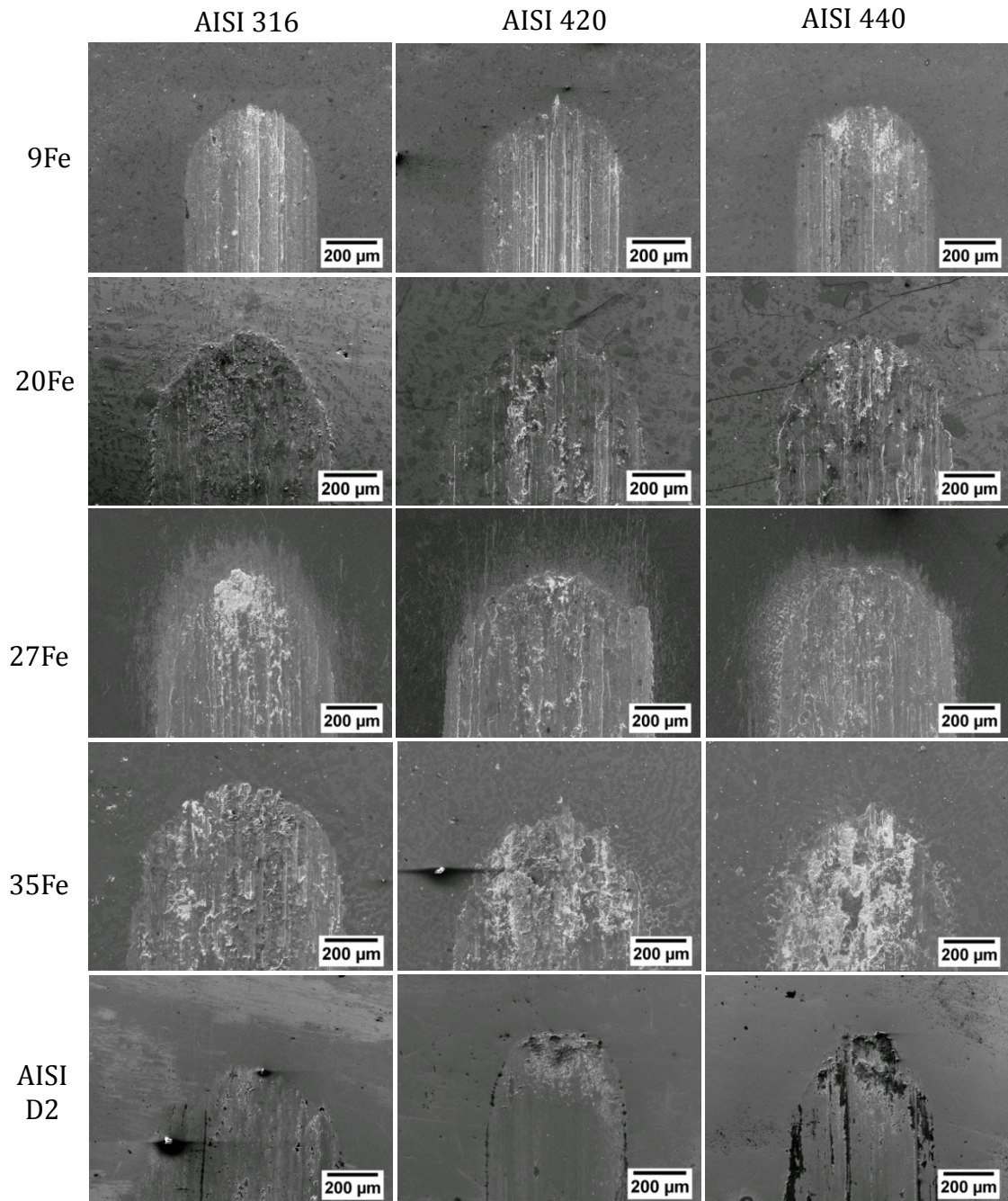
Figure 5.33: Secondary electron images of the worn PTA aluminium bronze coatings and AISI D2 tool steel after dry sliding wear test against AISI 316, 420 and 440 stainless steels

All in wt.%						
Cu	Al	Fe	Mn	Ni	Si	O
52.1	8.4	18.9	1.0	1.0	0.1	18.56
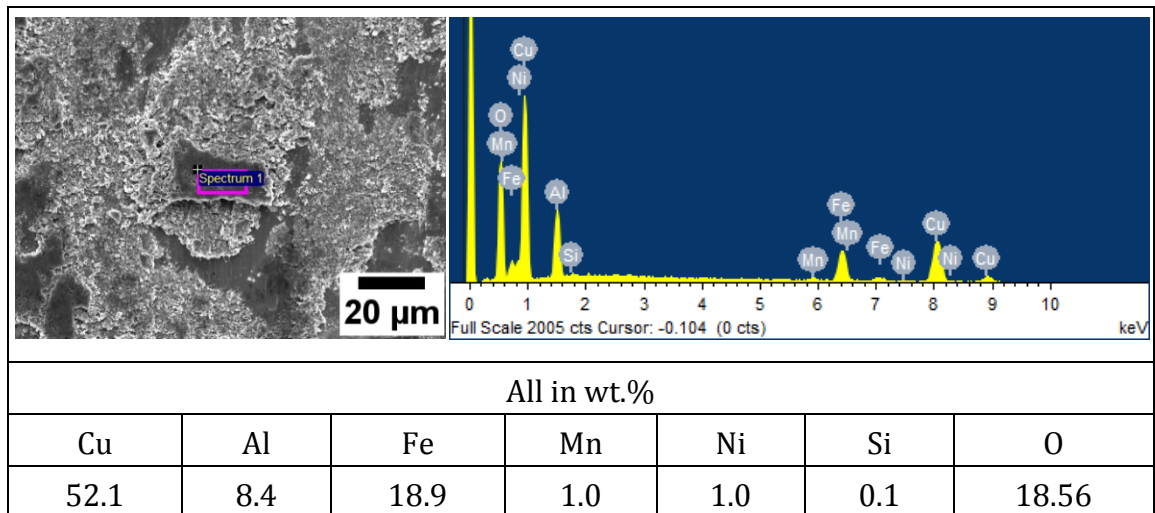
Figure 5.34: EDS analysis of the Cu-rich debris on the surface of the worn 20Fe PTA aluminium bronze coating after dry sliding test against 440 stainless steel

All in wt.%								
C	O	Al	Si	Cr	Mn	Fe	Co	Cu
3.31	2.42	2.70	2.83	20.77	1.53	53.86	3.85	8.72
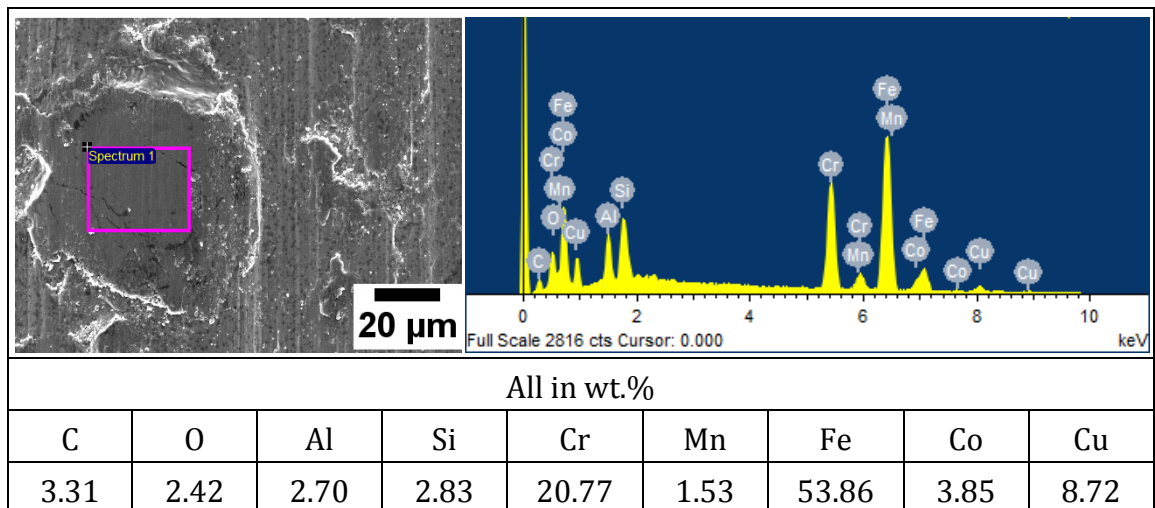
Figure 5.35: EDS analysis of the Fe-rich debris on the surface of the worn 9Fe PTA aluminium bronze coating after dry sliding test against 420 stainless steel

All in wt.%				
O	Si	Cr	Fe	Mo
31.7	0.8	5.75	60.36	1.4
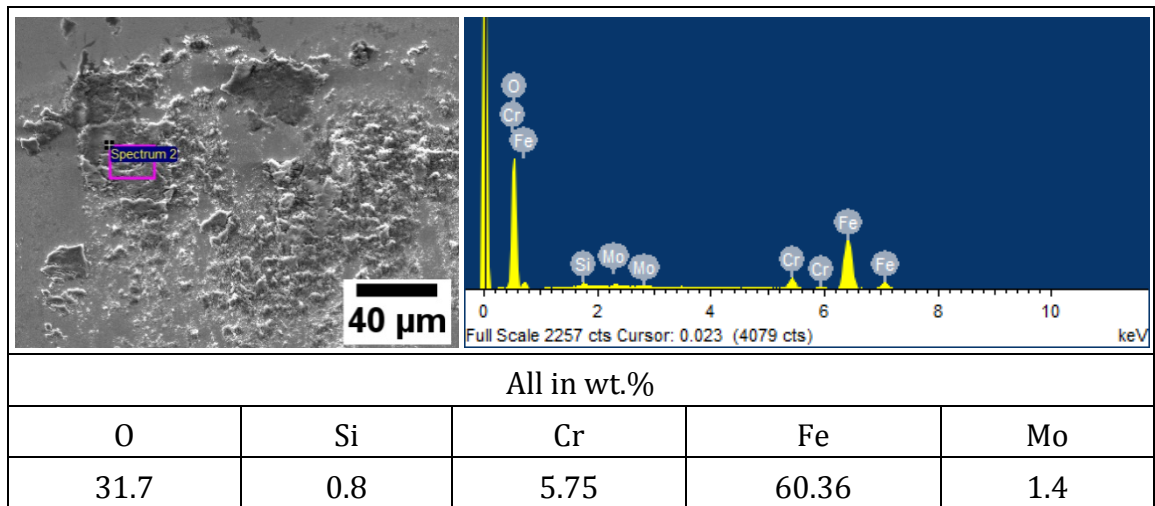
Figure 5.36: EDS analysis of the Fe-rich debris on the surface of the worn AISI D2 tool steel after dry sliding test against 420 stainless steel

A high magnification SE image of the worn surface on the 35Fe coating is shown in Figure 5.37. Surface cracks similar to those in Figure 5.7 were observed. This indicates that the wear mechanism described in section 5.1 is also applicable. The morphology of the worn 9Fe coating is shown in Figure 5.37; compared to the 35Fe coating, no surface cracks were observed and the scratches on the surface are also significantly more shallow.
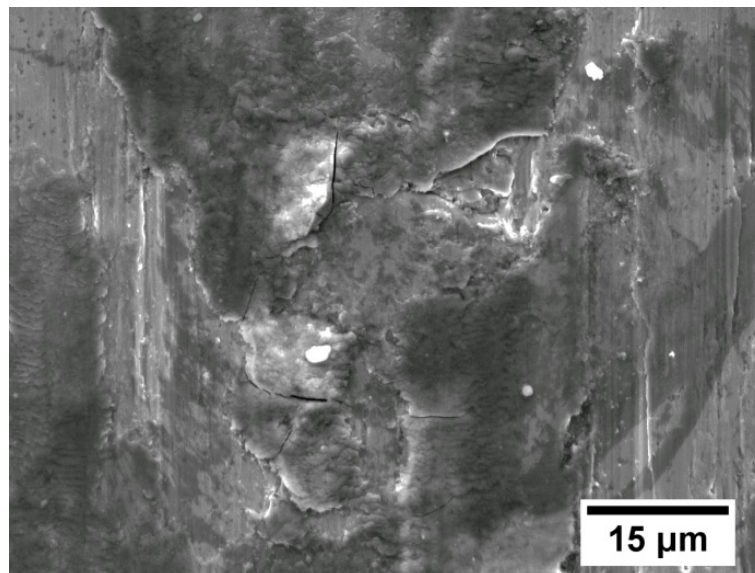
Figure 5.37: High magnification SE image of the worn surface on the 35Fe coating after wear test against an AISI 316 stainless steel
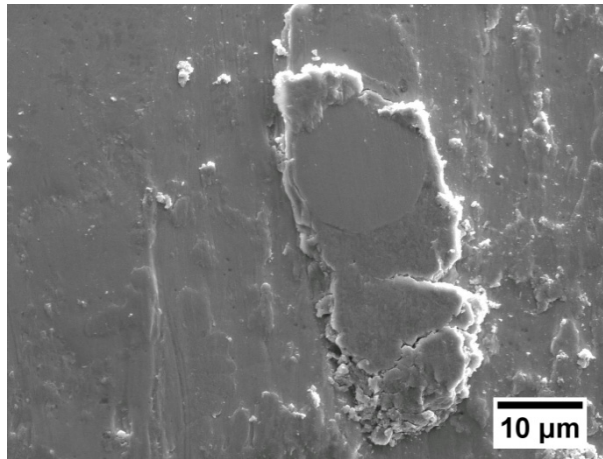
Figure 5.38: High magnification SE image of the worn surface on the 9Fe coating
after wear test against an AISI 316 stainless steel

High magnification SE image of the worn AISI D2 surface in Figure 5.39 shows a
crack. EDS analysis in Figure 5.40 shows that the crack is located near the
boundary between the carbides and the surrounding Fe-rich matrix. Beach marks
are also clearly visible, which suggests that the observed cracks might originate
from the cyclic loading during the reciprocating sliding test. This highlights the
need to optimise the size of the reinforcement particle size to reduce possible
stress concentration point that can lead to crack initiation.
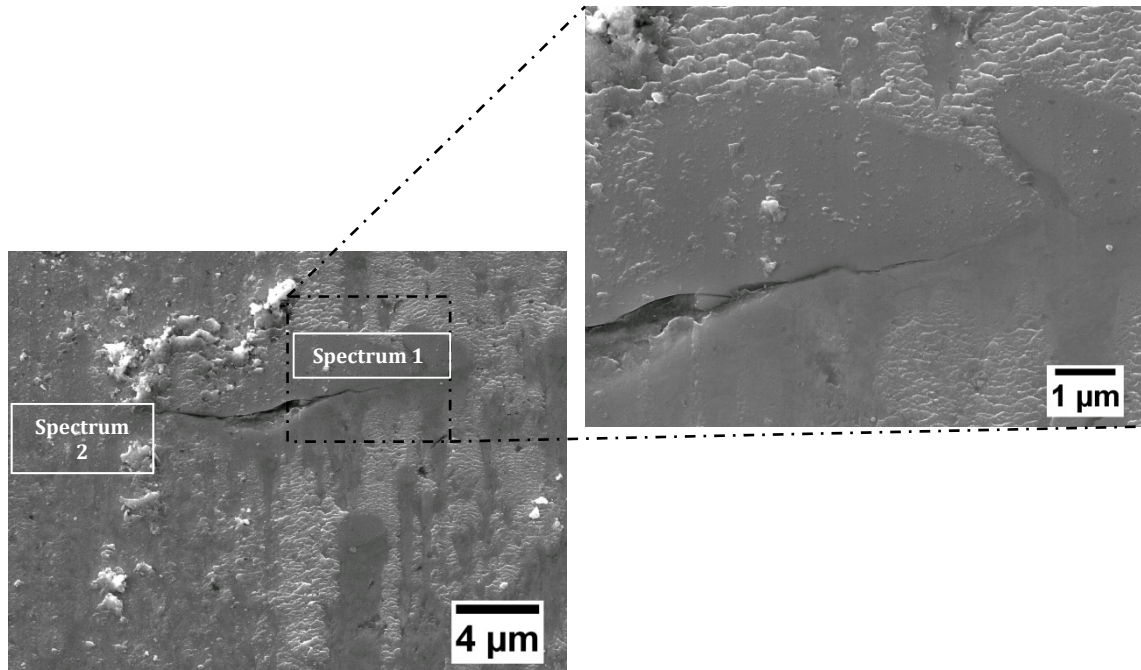
Figure 5.39: High magnification SE image of the worn surface on the AISI D2 tool steel after wear test against AISI 316 stainless steel

All in wt.%						
Spectrum	C	V	Cr	Fe	Mo	Si	O
1	5.9	6.6	39.7	37.1	10.6		-
2	1.6	0.44	8.37	83.75	2.93	0.7	2.27
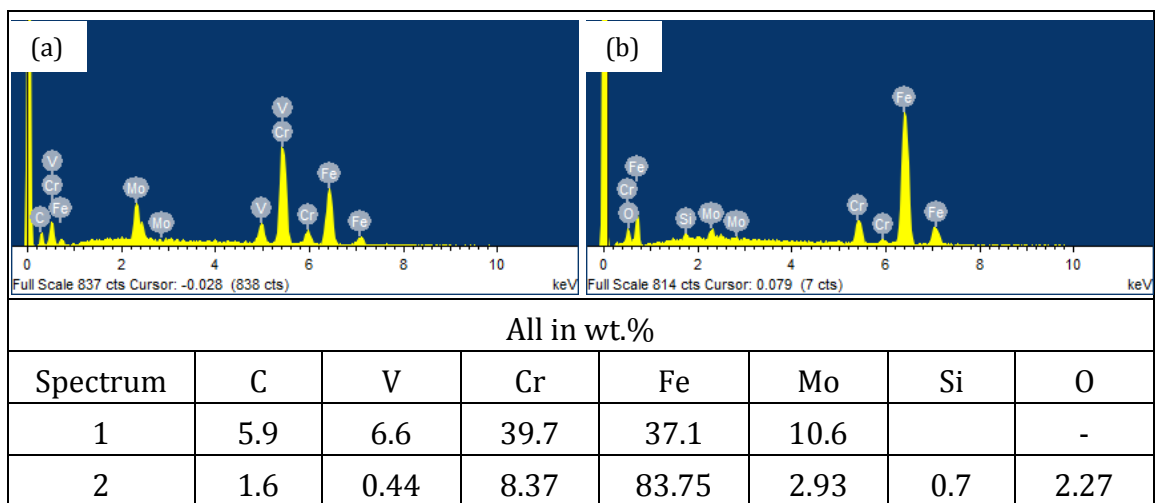
Figure 5.40: EDS spectra and results from the (a) Cr-rich area and (b) the worn surfaces of the AISI D2 tool steel after wear test against AISI 316 stainless steel

5.2.3   Morphology and composition of the stainless steel counter material

Although the primary function of the coating is to protect the forming dies from wear, it is also important to recognise that the coating should not introduce substantial wear on the sheet material.

Following the wear tests, the morphology of all stainless steel pins were imaged by SEM using both secondary (SE) and backscattered electron (BSE) imaging. The contrast difference in the BSE image was used to identifying the presence of wear debris on the surface of the pins, while the SE images were used to reveal the morphology of the debris. The representative morphology of the stainless steel pins worn against the 9Fe coating is shown in Figure 5.5 a. Wear debris (appearing dark) are clearly visible in the centre of the worn surface. The typical morphologies of the stainless steel pins worn against the 20Fe, 27Fe and 35Fe coating are shown in Figure 5.5 b. The worn surfaces of the stainless steels against 20Fe, 27Fe and 35Fe coatings are larger than the worn surfaces of the pins worn against the 9Fe coating (see Figure 5.5 a and b). This indicates that the indentation of the stainless steel into 20Fe, 27Fe and 35Fe coating is deeper than that in the 9Fe coating. This observation contradicts the initial indentation depth predicted using the hardness in Table 3.9. This indicates that for multiphase material, the hardness alone cannot be used to predict the wear characteristic. To determine the composition of the wear debris, extensive EDS analyses were carried out. The results show that the debris are Cu-rich with an average composition shown in Table 5.2. The high Cu content confirms that the wear debris were transferred from the PTA aluminium bronze coatings.
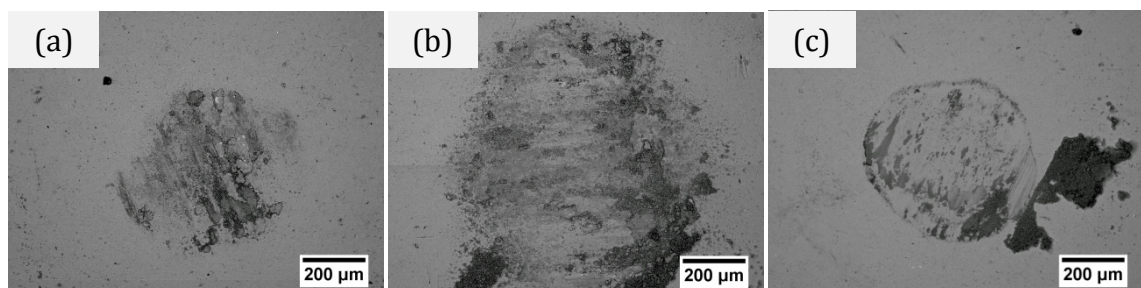
Figure 5.41: Low magnification BSE image of the AISI 420 pin after wear test against (a) 9Fe, (b) 27Fe PTA aluminium bronze coatings and (c) AISI D2 tool steel.

Wear debris were also observed on the surface of the AISI 420 pin worn against the AISI D2 tool steel. The size of the worn area is similar to that of the 9Fe coating. EDS analysis of the debris shows the present of Fe oxides with an average composition shown in Table 5.2.

The Cu-rich debris transferred from the 9Fe coating appears to be more strongly adhered to the stainless steel than the debris transferred from the 20Fe, 27Fe and 35Fe coating as shown in Figure 5.42. Large debris were also observed on the surface of the pin worn against the AISI D2. However, the majority of the debris observed are located on the edge of the worn surface as shown in Figure 5.43. This leads to direct contact between the stainless steel pin and the AISI D2 tool steel, which resulted in high friction coefficient and wear on the surface of the stainless steel pin as shown in Figure 5.44. Beach marks similar to that observed in Figure 5.39 were also commonly observed on the worn surface of the stainless pins worn against the AISI D2 tool steel.
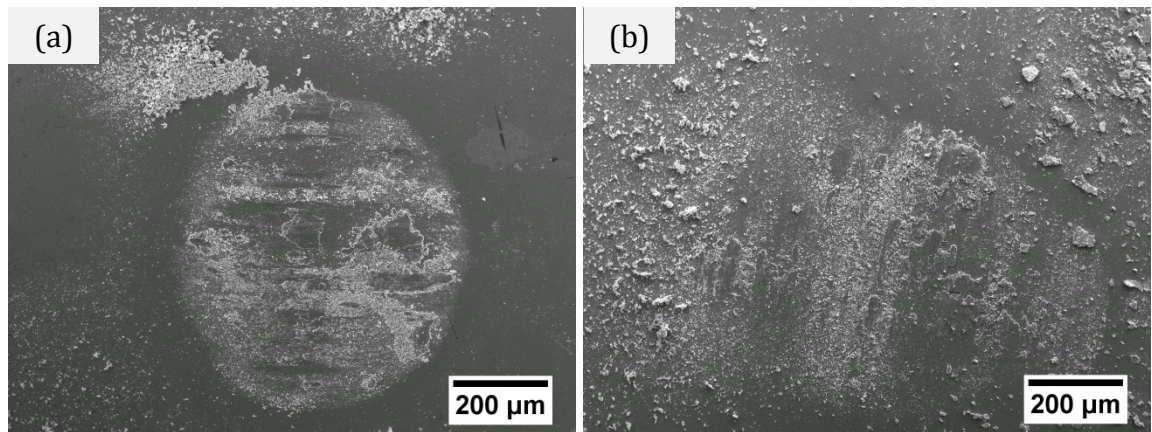
Figure 5.42: Secondary electron image showing the worn surface of the AISI 440 stainless steel after wear test against (a) 9Fe and (b) 27Fe PTA aluminium bronze coatings.

Table 5.2: Averaged composition of the debris found on the surface of the worn stainless steel after wear test against PTA aluminium bronzes coating and AISI D2 tool steel (all in wt.%)

	Cu	Al	Fe	Mn	Ni	Si	Cr	O	Mo	C
9Fe	50.4	9.1	20.6	1.2	1.1	0.3	3.6	13.3		
20Fe	42.2	7.1	30.4	0.9	1.7	0.2	2.7	14.8		
27Fe	41.5	7.5	36.8	1.3	1.0	0.2	2.1	10.3		
37Fe	29.6	5.0	44.4	1.1	2.5	0.2	4.4	12.7		
AISID2			59.6			0.4	10.0	26.5	1.0	2.6
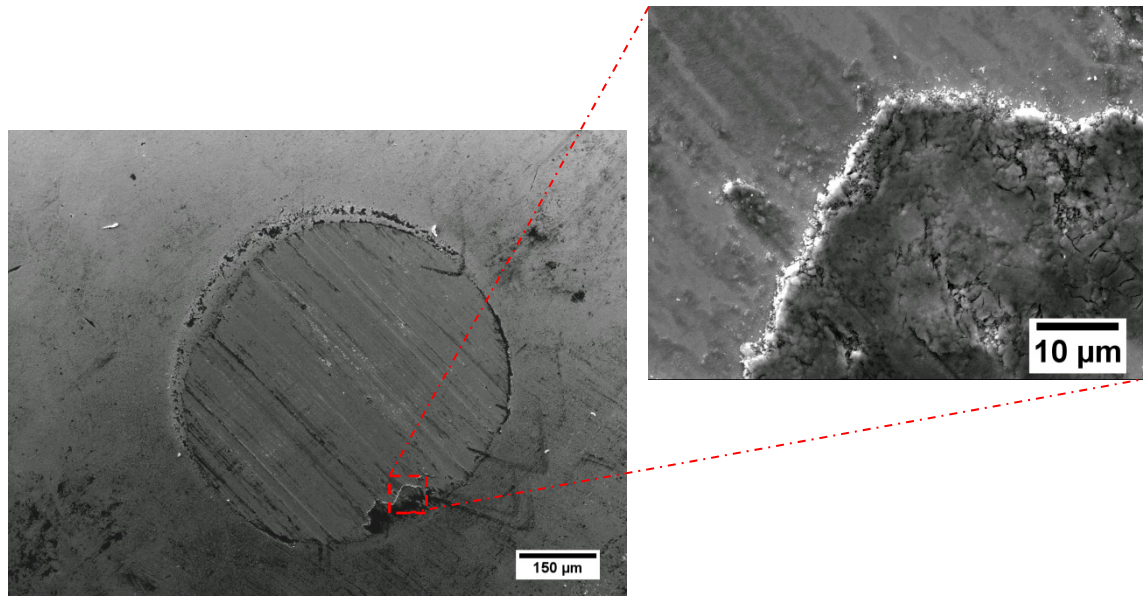
Figure 5.43: Secondary electron image showing agglomeration of debris on the edge of the worn AISI 440 stainless steel surface after wear test against AISI D2
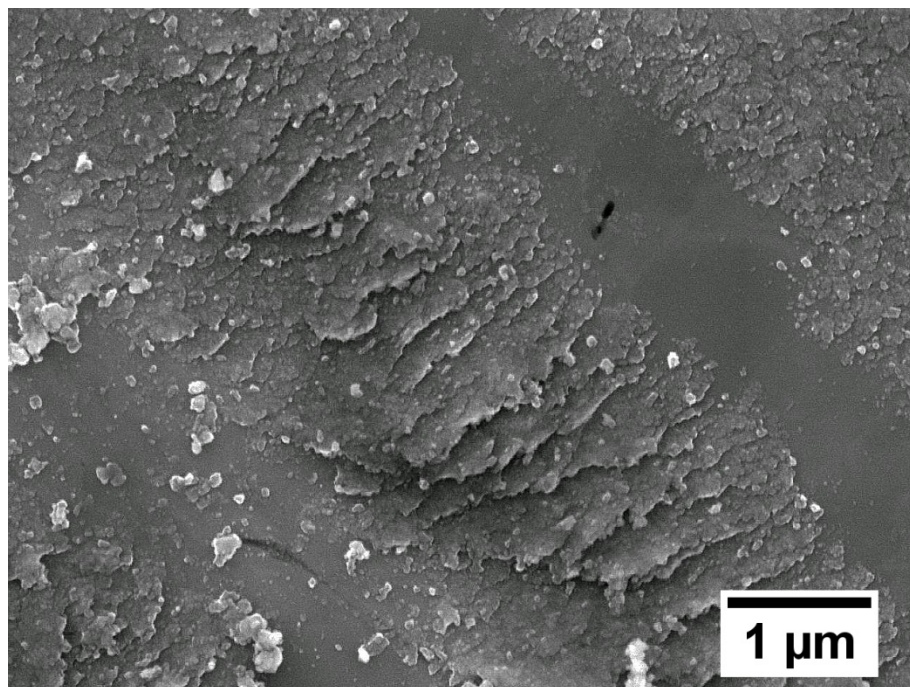
Figure 5.44: High magnification secondary electron image showing damage on the surface of the AISI 440 pin after wear test against AISI D2 tool steel

5.2.4   Influence of stainless steel pin hardness on material transfer

The morphology of the stainless steel worn against the AISID2 tool steel shows significant variations (Figure 5.45). Large wear debris were observed on the AISI 316 stainless steel as shown in Figure 5.45 a. Due to the lower hardness of the AISI 316 stainless steel compared to the AISI D2 tool steel, the majority of wear is expected to take place in the AISI 316 stainless steel pins. This leads to the production of wear debris as shown in Figure 5.45 and high mass loss as shown in Figure 5.47. As the stainless steel pin hardness increases, more signs of abrasive wear were observed as shown in Figure 5.45 b and c. The mass loss of the pins also decreases (see Figure 5.47). In contrast, the morphologies of the stainless steel worn against the PTA aluminium bronze coatings show fewer variations in the morphology as shown in Figure 5.46. No significant correlation between the hardness of the stainless steel and its mass loss were observed as shown in Figure 5.47.
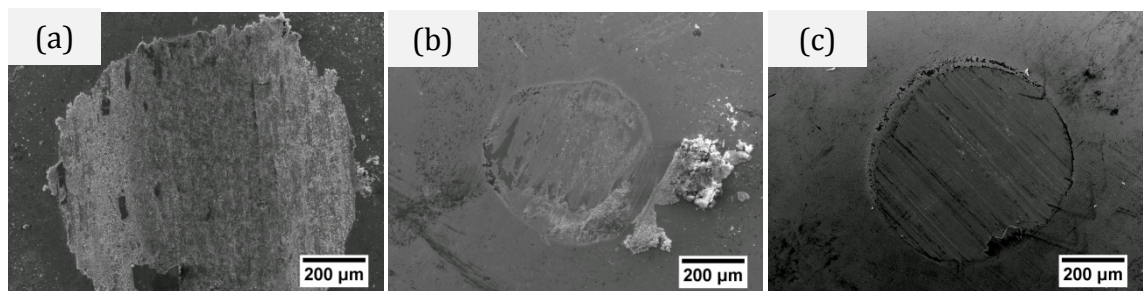
Figure 5.45: Secondary electron images showing the morphology of (a) AISI 316, (b) AISI 420 and (c) AISI 440 after dry sliding wear test against AISID2 tool steel
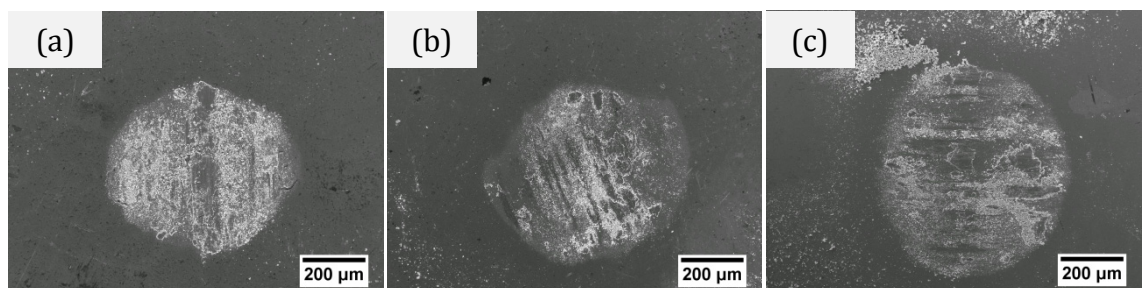
Figure 5.46: Secondary electron images showing the morphology of (a) AISI 316, (b) AISI 420 and (c) AISI 440 after dry sliding wear test against the 9Fe PTA aluminium bronze coating
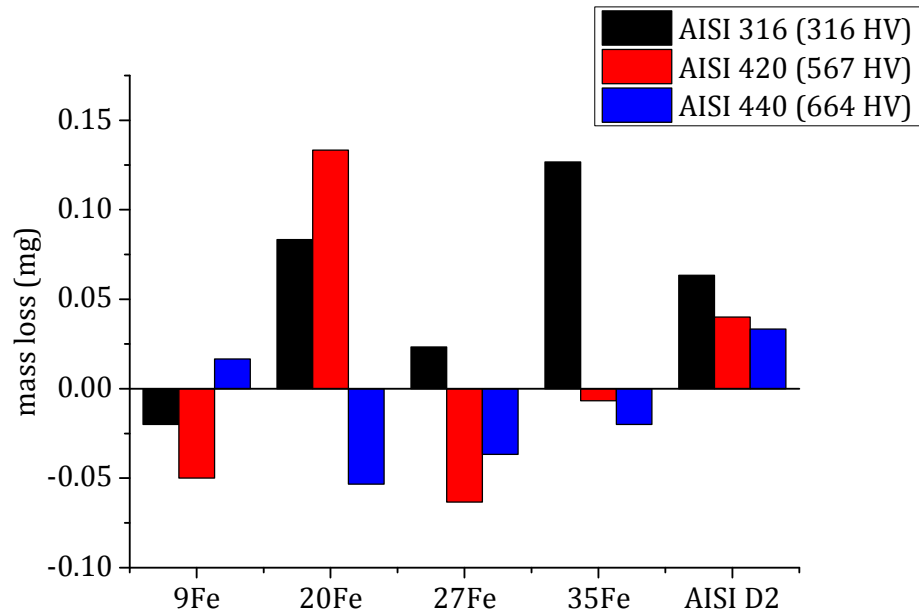
Figure 5.47: The averaged change in mass (from three repeated test) of the AISI 316, 420 and 440 stainless steel following dry sliding wear test against PTA aluminium bronzes coatings and AISI D2 tool steel (negative value = mass gain)

5.2.5   Specific wear rate of the PTA aluminium bronze coatings and the AISI D2 during dry sliding against stainless steels

The specific wear rates of the PTA aluminium bronze coatings and the AISI D2 tool steel after dry sliding wear tests against AISI 316, 420 and 440 stainless steels are shown in Figure 5.48. The specific wear rates of the coatings are approximately an order of magnitude lower than that of the AISI D2 tool steel. The specific wear rates for the 9Fe coating are the lowest and are also approximately constant for all counter materials testes. This might be due to the strong adhesion of the transferred material, which prevents direct contact between the 9Fe coating and the stainless steel. In the 20Fe, 27Fe and 35Fe coating the specific wear rate increase with increasing sheet metal hardness. This is due to the combined effects of both delamination and abrasive wear.

Due to the lower matrix hardness of these coatings, the effects of abrasive wear caused by the work hardened wear debris is more significant than in the 9Fe coating where the higher matrix hardness can provide better resistance against abrasive wear. Furthermore, the stress-induced delamination wear also leads to the production of more debris. Despite having higher hardness than the PTA aluminium bronze coatings, the specific wear rate of the AISI D2 tool steel is higher than that of the coatings. Coalescence of the cracks observed near the large carbides leads to the removal of large wear debris. These wear debris may also be entrained between the two surfaces, thus causing abrasive wear resulting in the high wear rates observed.
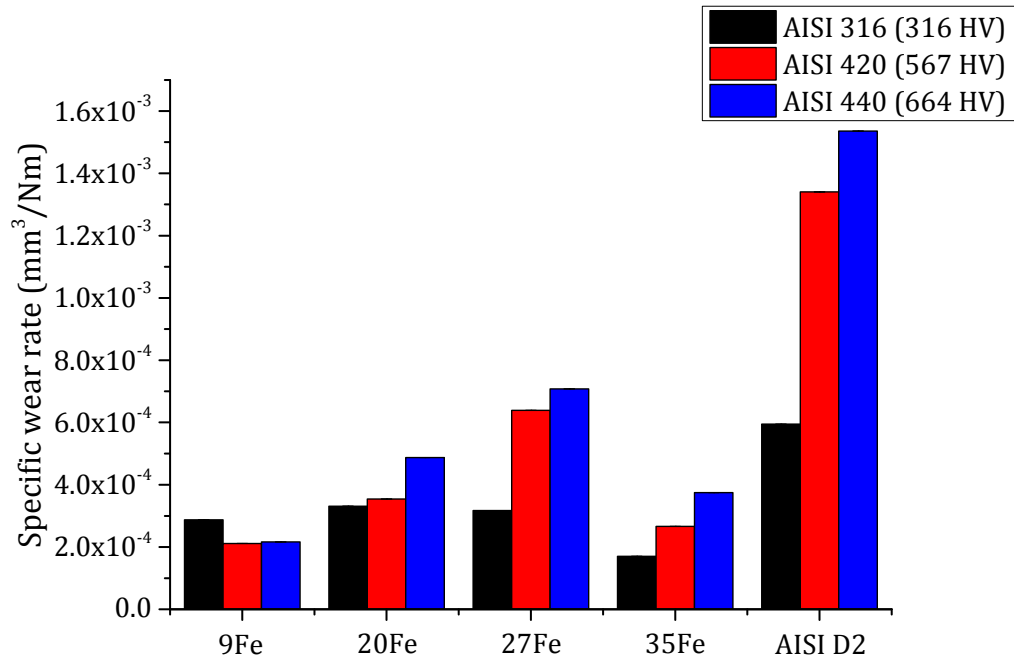
Figure 5.48: Specific wear rate of the PTA aluminium bronze coatings and AISI D2 tool steel worn against stainless steel with different hardness

5.3   Summary of the relationship between microstructure and tribological properties and optimum microstructure for wear resistance

The effects of the microstructure resulting from the PTA process on the friction and wear characteristics of the coating were investigated by using dry sliding wear tests. The results show that PTA induced phase change from a martensitic β_1' phase to a solid solution (Cu) phase leads to an increase in specific wear rate. In the solid solution (Cu) phase with fcc crystal structure, activation of slip is easier than in the orthorhombic structure of the martensitic β_1' phase that has limited slip systems. Upon loading, several slip systems in the solid solution (Cu) phase were activated. Pile-up of slips on the hard intermetallic κ_1 phase increases the stress, resulting in the formation of voids and cracks on the surface. Coalescence of these cracks reduces the cohesive strength of the material near the surface. Due to the strong adhesion between the Al_2O_3 that forms on the surface of the coating and the AISI 52100 steel substrate, the contact between the two materials leads to the formation of a strong adhesive junction. During sliding, the surface is removed and transferred on to the surface of the counter material pin.

The friction coefficient of the coating during dry sliding was found be strongly influence by the surface oxide film. In the 9Fe coating, the high Al content in the matrix ($\sim$ 12 wt.%) promotes the growth of Al_2O_3, which has strong adhesion to the bearing steel and stainless steels tested. The transfer of the oxides and the coating materials to the steel surface during the test prevents direct contact between the two solids. This modifies the properties near at interface, which leads to a stable CoF of $\sim$ 0.4. As the sliding continues, the heat generated by friction promotes segregation of Al to the surface as shown by the EDS. This prevents contact between the solids, which keeps the CoF at a constant level. However, in the 35Fe coating, the Al content in the matrix is limited ($\sim$ 6 wt.%), this favours the growth of Cu oxides over the Al_2O_3 oxide. The Cu oxides are known to be lubricious, resulting in lower CoF. However, its low load carrying capacity leads to direct contact between the 35Fe coating and the steel counter material.

Due to the presence of a large volume fraction of Fe-rich phases such as the bcc αFe and the intermetallic κ_1 phase, the cohesive force between the two materials promotes adhesive wear. The resistance to galling of the coatings was evaluated through a dry sliding test against three different stainless steels with increasing hardness. The results show that the 9Fe, 20Fe and 27Fe coatings have a stable CoF value of $\sim$ 0.5 against all stainless steel tested. This is significantly lower than the CoF value of $\sim$ 2.0 observed for the AISI D2 under the same condition. However, in the 35Fe coating, high and unstable CoF between 1-1.5 were observed. The transfer of oxides on to the surface of the stainless is responsible to the observed CoF value for the 9Fe, 20Fe and 27Fe coatings. With increasing stainless steel hardness, more oxide layers are sheared and transferred on to the surface of the stainless steel, thus preventing the contact between the two surfaces and keeping the CoF at a constant level.

In the 35Fe coating, the oxide film does not prevent direct contact between the two surfaces. Therefore the CoF is dependent on the microstructure of the coating. The 35Fe coating contains a high volume fraction of Fe-rich phases. Consequently, high CoF were observed due to the strong cohesive force between the Fe-rich phases in the 35Fe coating and the stainless steel. The stable CoF observed for the 9Fe, 20Fe and 27Fe coatings leads to lower wear rate when compared to the currently used AISI D2 steel as shown in Figure 5.48. The 9Fe coating has the lowest specific wear rate while the 27Fe has the highest. The wear mechanism of the coating against stainless steel follows the same mechanism as described during wear test against the AISI 52100 steel. For the 20Fe, 27Fe and 35Fe coatings, the specific wear rate increases with the stainless steel hardness. This is due to the promotion of abrasive wear. The 9Fe coating with a martensitic β_1' phase matrix and submicron size intermetallic κ_1 particles provided the highest wear resistance and the most stable CoF. This makes it the most suitable microstructure for sheet metal forming die application amongst the four coatings investigated.

6. The influence of microstructure on corrosion characteristics of PTA aluminium bronze coating in aerated 3.5% NaCI solution

In this chapter, results from electrochemical and immersion corrosion tests are presented and analysed in conjunction with a post-test characterisation of the corroded surfaces using SEM and EDS analysis. The chapter concludes with a summary on the effects of Fe on the corrosion resistance of the coating.

6.1   Electrochemical corrosion tests in 3.5% NaCI

6.1.1   Variations in open circuit potential over the exposure period

The change in open circuit potential (OCP) over the exposure period can be used to monitor the corrosion behaviour of the coating. A rise in OCP in a positive direction indicates formation of a passive film, while a change in potential towards the negative direction indicates the dissolution of the passive film or no film formation. The change in OCP measured against an Ag/AgCl electrode is shown in Figure 6.1. This decrease in the open circuit response was also observed in Nickel aluminium bronze coating in sea water [153]
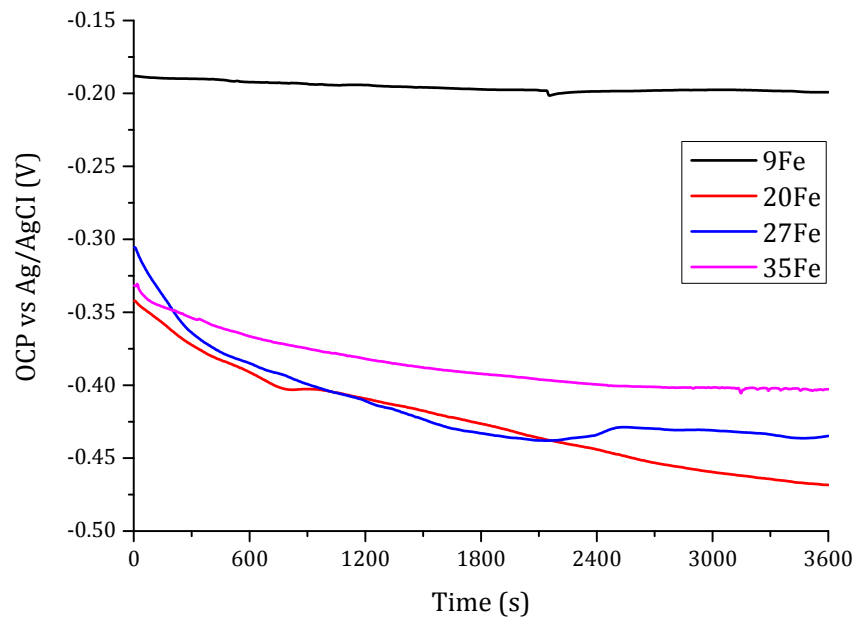
Figure 6.1: Open circuit potential against exposure time in aerated 3.5% NaCl solution for 9Fe, 20Fe, 27Fe and 35Fe coating

With increasing Fe content, the initial OCP tends to be more negative. The 9Fe coating has an initial OCP of -0.19 V, while the 20Fe, 27Fe and 35Fe coatings have an initial OCP between -0.30 V to -0.35 V. This suggests that the increase in Fe content changed the nature of the passive film on the coating. The passive film on aluminium bronze consists of a Cu-oxide outer layer and an Al_2O_3 inner layer. Formation of Al_2O_3 is dependent by the Al content in the coating. The increase in Fe resulted in the reduction of Al available in the matrix, which restricts formation of Al_2O_3 in the 20Fe, 27Fe and 35Fe coatings. The rate of change of the OCP with respect to time for 20Fe, 27Fe and 35Fe coatings is also higher than the 9Fe coating as evident by the steeper gradient in the initial part of the graph shown in Figure 6.1. This indicates that the passive films on the 20Fe, 27Fe and 35Fe coatings dissolve faster than the passive film on the 9Fe coating. To investigate the role of the passive film and the nature of the electrochemical interface between the coating and the surround 3.5% NaCI solution, electrochemical impedance spectroscopy (EIS) was performed at the OCP. The EIS results are presented in the next section.

6.1.2   Electrochemical Impedance Spectroscopy

The electrochemical impedance spectroscopy (EIS) is a non-destructive method used to investigate the electrochemical interface between the electrode and the solution. The nature of the interface is typically interpreted by modelling of the observed spectra using electrical equivalent circuits [182] that usually consist of resistor, inductor and capacitor arranged in series and/or parallel combinations. The physical representation of these equivalent circuit components will be discussed in conjunction with the results presented in this section. The information obtained from EIS is commonly presented by using Nyquist and Bold plots as shown in Figure 6.4 and Figure 6.5 respectively. The Nyquist plots for the 20Fe, 27Fe and 35Fe coatings shown in Figure 6.4 b-d are characterised by an initial linear section followed by an asymmetric semi-circular shape section. The linear section is indicative of a capacitive-resistive behaviour that is commonly observed when metals are immersed in solution. The resistive behaviour is due to the inherent resistance of the coating and the resistance of the solution. The capacitive behaviour originates from the adsorption of the ions on the surface of the electrode, which leads to the formation of an electrical double layer that is insulated by the resistance of the solution i.e. a capacitor (see Figure 6.6). The asymmetric semi-circular shape is related to a low frequency inductive behaviour that can be associated with several physical phenomena such as [183]:

- The adsorption of species on the surface of the coating
- Anodic dissolution of the alloy
- The increase in electrode surface area due to corrosion

Similar to the other coatings, the linear section on the Nyquist plot for the 9Fe coating can be related to the capacitive-resistive behaviour. However, the low frequency inductive behaviour was not present. Instead a second linear section was observed. The second linear section is indicative of a diffusion-controlled process at the surface of the coating. Further evidence for the diffusion-controlled process can also be seen on the phase angle of the 9Fe coating which tends towards -45 ° as shown in Figure 6.5 a. To model the observed behaviours, several equivalent circuits were considered.

Two models based on the modified Randle equivalent circuit shown in Figure 6.2 and Figure 6.3 provided the best fit. The best fit is here defined as the difference between the calculated impedance and the measured impedance and has average values in the order of 10^{-3} for all EIS data. The corresponding values obtained from the modelling using these two equivalent circuits are presented in Table 6.1 - Table 6.3.
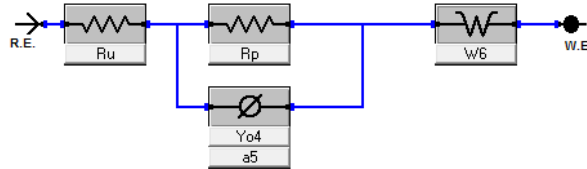
Figure 6.2: Equivalent circuit used to model the electrochemical interface between the 9Fe PTA aluminium bronze coating and the aerated 3.5% NaCI solution
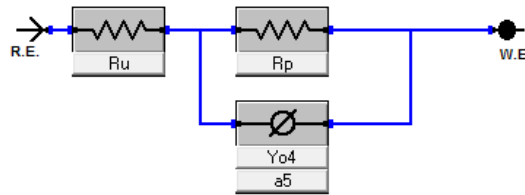
Figure 6.3: Equivalent circuit used to model the electrochemical interface between the 20Fe, 27Fe and 35Fe PTA aluminium bronze coatings and the aerated 3.5% NaCI solution

In both equivalent circuits, each symbol has the following meaning:

- R_u: Solution resistance

- R_p: Coating resistance

- Y_{o4}: Admittance of the Constant Phase Element (CPE)

- a_5: empirical exponent of the CPE with values $-1 \le a5 \le 1$

For both equivalent circuits, the constant phase element (CPE) was used instead of a pure capacitance element in order to account for the non-ideal behaviour of the capacitive element that may arise from several factors such as surface roughness and impurities in the coating.

The CPE impedance (Zcpe) is defined as:

$$Zcpe = [Yo4\,(j\omega)^{a5}]^{-1}$$

Equation 6.1

At the limiting *a5* values of 0, 1 and -1 the CPE can represent an ideal resistor, capacitor and inductor respectively. To account for the diffusion behaviour an infinite Warburg *W6* was used.
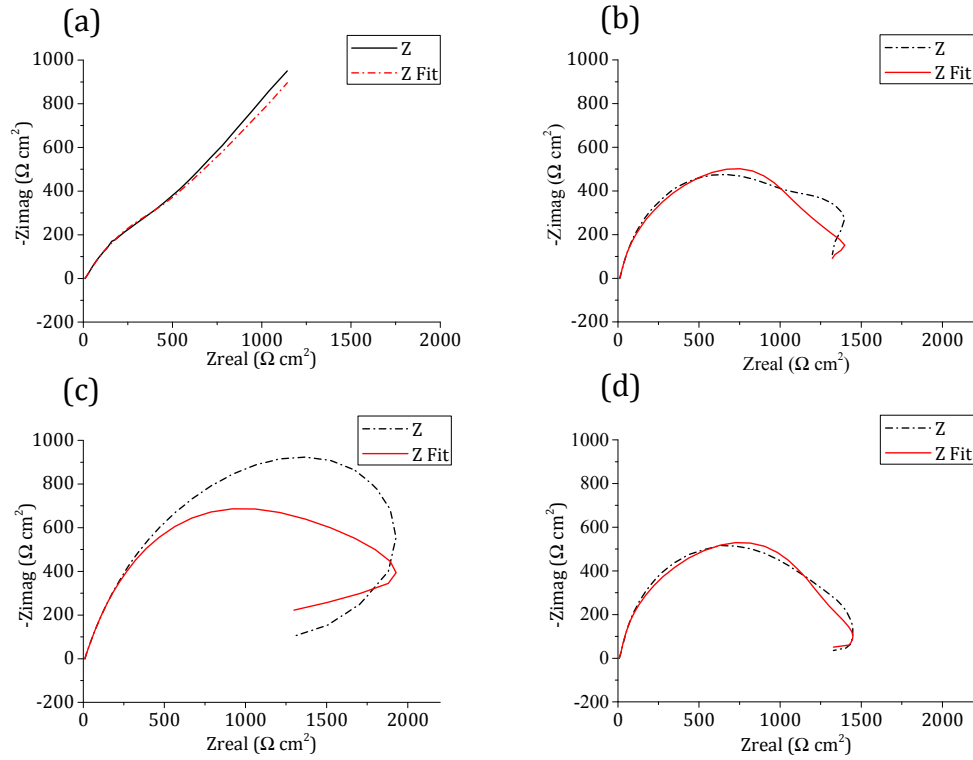
Figure 6.4: Nyquist plots of (a) 9Fe, (b) 20Fe, (c) 27Fe and (d) 35Fe PTA aluminium bronze coatings in aerated 3.5% NaCI solution (red line represents fitting.)
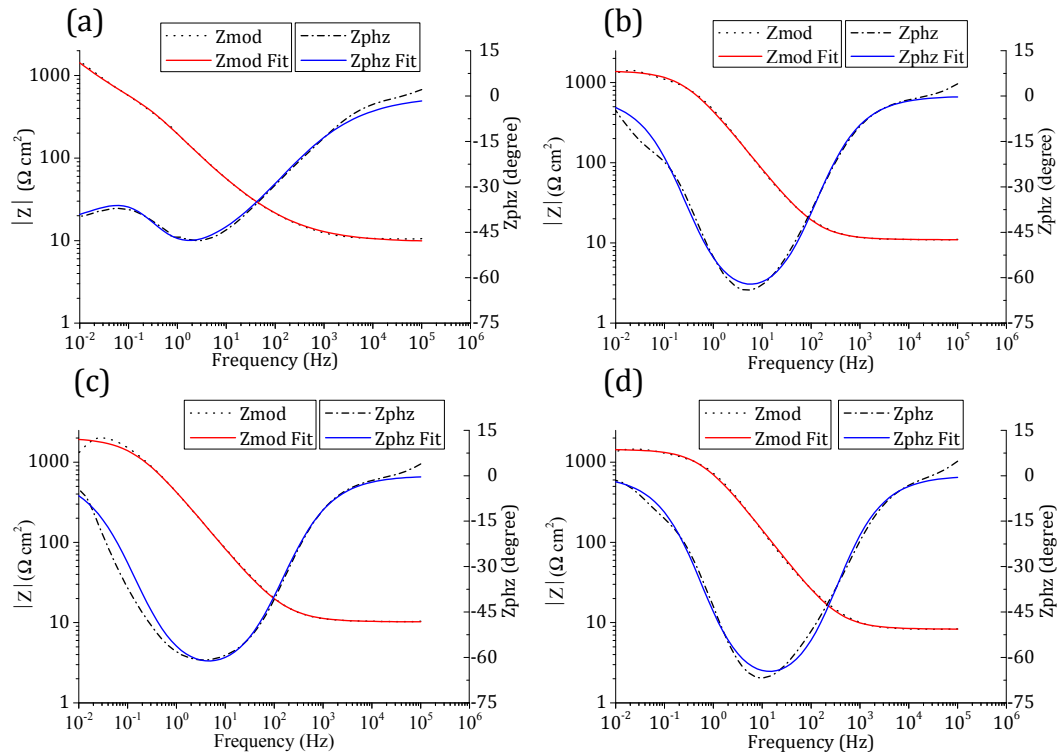
Figure 6.5: Bode plots for (a) 9Fe, (b) 20Fe, (c) 27Fe and (d) 35Fe PTA aluminium bronze coatings in aerated 3.5% NaCI solution (red=fitting, Zmod = modulus of impedance, Zphz = phase angle.)

Table 6.1: Solution and coating resistance values obtained from fitting the equivalent circuit

	Solution resistance R_u (Ω cm^2)	error	Coating resistance R_p (Ω cm^2)	error
9Fe	9.62	0.07	214	18
20Fe	10.95	0.06	1397	11
27Fe	10.22	0.06	2019	19
35Fe	8.29	0.05	1442	10

Table 6.2: Constant phase element parameters obtained from fitting the equivalent circuit

	Admittance of the CPE $Yo4$ (S*s a/ cm^2)	error	Empirical exponent of the CPE $a5$	error
9Fe	2.90×10^{-3}	12.29×10^{-5}	8.26×10^{-1}	23.4×10^{-3}
20Fe	4.66×10^{-4}	5.30×10^{-6}	7.94×10^{-1}	2.61×10^{-3}
27Fe	5.36×10^{-4}	5.39×10^{-6}	7.61×10^{-1}	2.37×10^{-3}
35Fe	2.44×10^{-4}	3.05×10^{-6}	8.08×10^{-1}	2.45×10^{-3}

Table 6.3: Infinite Warburg obtained from fitting the equivalent circuit

	Infinite Warburg $(S*s^{(1/2)} / cm^2)$	error
9Fe	3.2 x10^{-3}	68.8x10^{-6}

In all coatings, the solution resistance R_u has values between 8-11 Ω cm². This is within the 7-20 Ω cm² expected for a standard 3.5% NaCI solution. With increasing Fe content from 9 wt.% to 20 wt.%, the coating resistance R_p increased significantly from 214 to 1397 Ω cm². This might be due to the increase in volume fraction of the non-conductive intermetallic κ_1 as shown in Table 4.6. With further increase in Fe content, the coating resistance increased to a maximum value of 2019 Ω cm². However, further increase in Fe content to 35 wt.% leads to a reduction in coating resistance. The possible reason for this might be due to the formation of the conductive bcc αFe shown by the XRD results in 4.1.2. The increase in coating resistance impedes movement of electrons; this is expected to increase the corrosion resistance. For all coatings, the empirical exponent of the CPE tends towards a value of 1, which indicates a capacitive behaviour. The increase in Fe content doesn't affect the value of the empirical exponent $a5$. However, the increase in Fe content from 9 wt.% to 20 wt.% leads to an order of magnitude reduction in the admittance value as shown in Table 6.2. High admittance indicates that the material in between the charged double layers has high resistance. For the present physical system, the material between the charged double layers consists of the 3.5 % NaCI solution and the oxide film as shown by the schematic in Figure 6.6. The results in Table 6.1 show that the solution resistance is approximately the same; therefore the higher admittance in the 9Fe coating must result from the higher resistance of the oxide layer. This is a strong indication for the presence of Al_2O_3, which has high resistance. The higher resistance of the oxide layer might also be responsible for the observed differences in OCP between the coatings as shown in Figure 6.1. The effects of this highly resistive oxide layer on the corrosion rate were investigated using potential dynamic polarization. The results are presented in the next section.
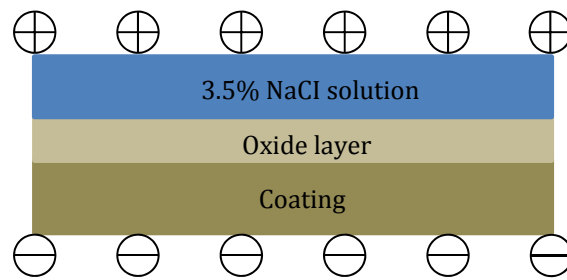
Figure 6.6: Schematic showing the presence of a charge double layer during immersion of PTA aluminium bronze coatings in aerated 3.5% NaCI solution

6.1.3   Potential dynamic polarization

The corrosion rate and the tendency for pitting for each coating were investigated using potential dynamic polarization in an aerated 3.5 % NaCl solution. The observed polarization curves are shown in Figure 6.7. The linear section of the polarisation curves displays an apparent Tafel [163] behaviour where the applied potential is proportional to the log of the corrosion current. By performing Tafel fit to this region (shown by the red line in Figure 6.7), the corrosion current density and thus the corrosion rate can be obtained. In the present research Gamry Echem Analyst software supplied by the manufacturer of the potentialstat was used for the fitting. The results are tabulated in Table 6.4. Following the test, the morphology of the corroded surfaces was observed using optical profilometer as shown in Figure 6.8.
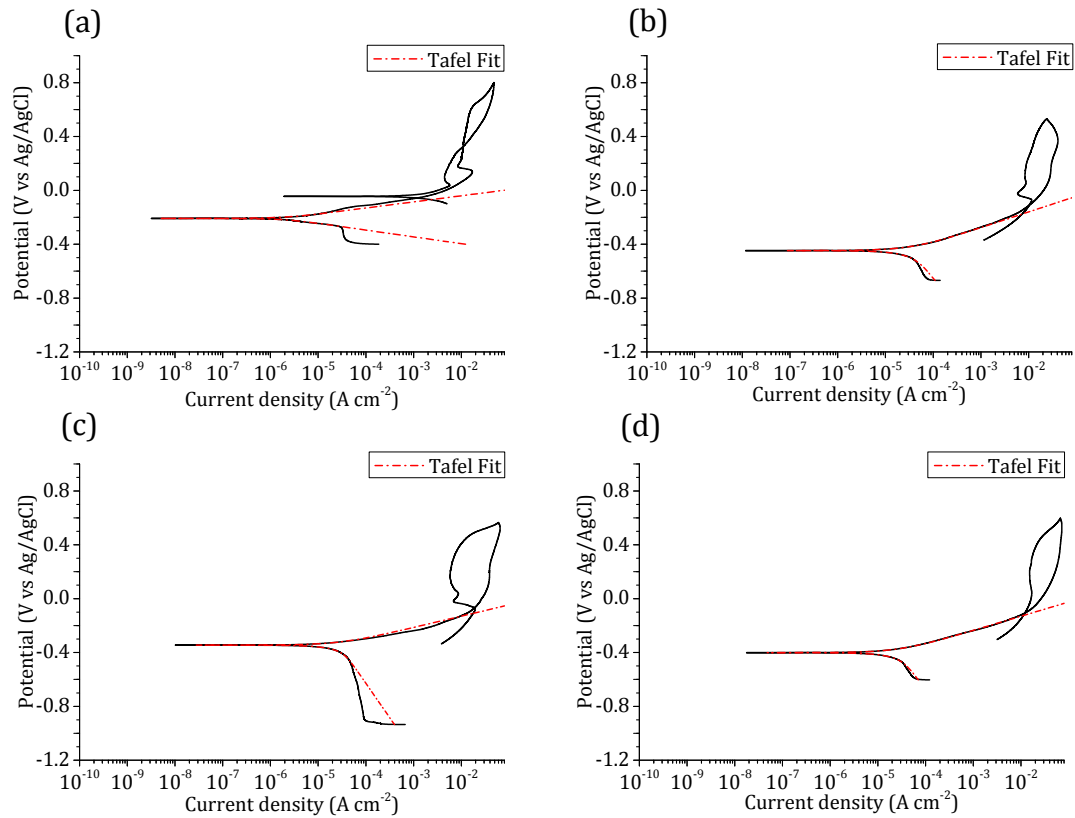
Figure 6.7: The observed potentiodynanic polarization curve for (a) 9Fe, (b) 20Fe, (c) 27Fe and (d) 35Fe PTA aluminium bronze coating in aerated 3.5 % NaCI solution

Table 6.4: The corrosion current and corrosion rates obtained by Tafel fitting of the linear section of the measured polarization curve

Fe content in the coating wt.%	9Fe	20Fe	27Fe	35Fe
Anodic potential (V/decade)	45.4×10^{-3}	116.5×10^{-3}	84.1×10^{-3}	105.4×10^{-3}
Cathodic potential (V/decade)	50.5×10^{-3}	443.3×10^{-3}	511.3×10^{-3}	489.8×10^{-3}
Corrosion current ($\mu A\ cm^{-2}$)	1.94	34.6	27.8	27.2
Corrosion potential (mV)	-208	-447	-345	-401
Corrosion rate (mm/year)	22.5×10^{-3}	400.7×10^{-3}	324.4×10^{-3}	315.0×10^{-3}
Goodness of Fit	37.8×10^{-6}	5.5×10^{-6}	19.2×10^{-6}	1.7×10^{-3}
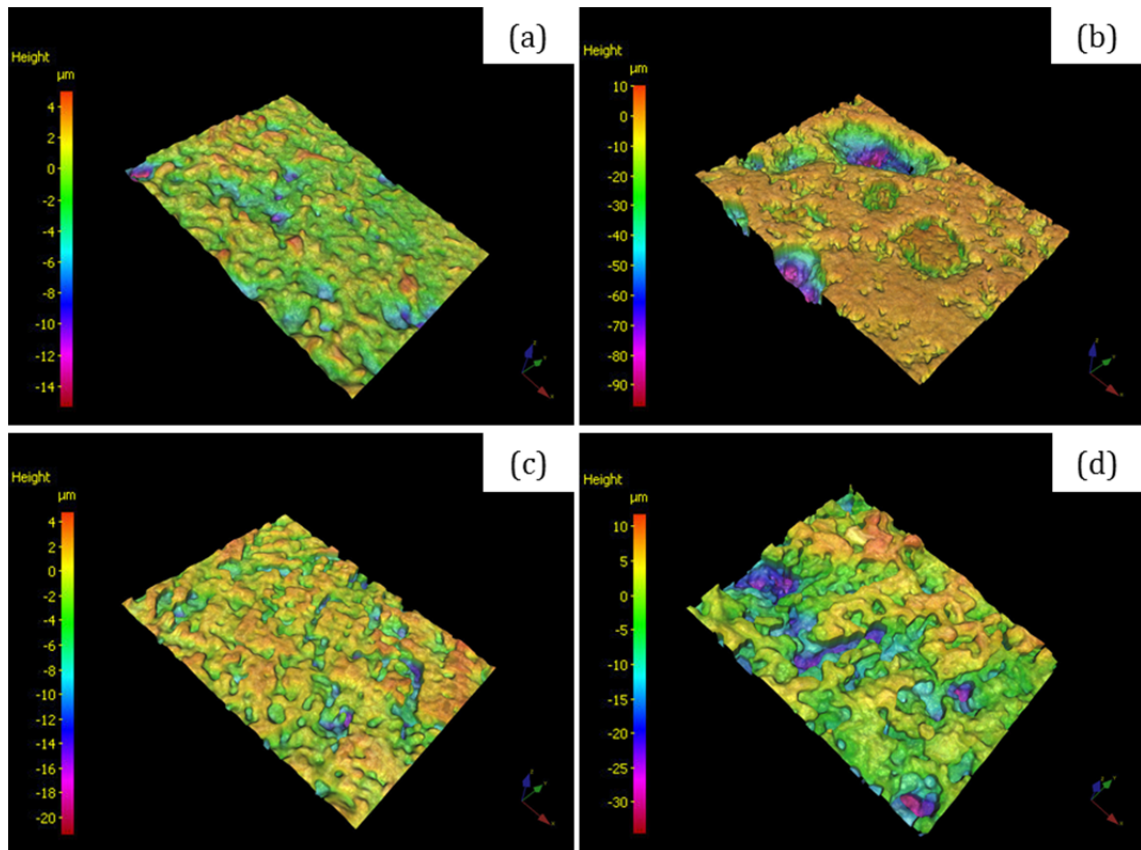
Figure 6.8: 3D images showing the surface of the (a) 9Fe, (b) 20Fe, (c) 27Fe and (d) 35Fe PTA aluminium bronze coatings after electro-chemical corrosion test in an aerated 3.5% NaCl solution

The polarization results show that with increasing Fe content the corrosion current and thus corrosion rate also increases. The 3D images of the corroded 20, 27 and 35Fe coating surfaces (see Figure 6.8 b-d) show clear evidence of localised corrosion attack. For each coating, five 3D images of the corroded surface were obtained; an averaged of the maximum depth from each side was calculated. The results are presented in Figure 6.9. The 9Fe coating has the shallowest depth of 18.0 μm. The 20Fe coating has the deepest depth of 49.8 μm. However, further increase in Fe content leads to a decrease in depth. This might be due to the formation of corrosion product in the pores.
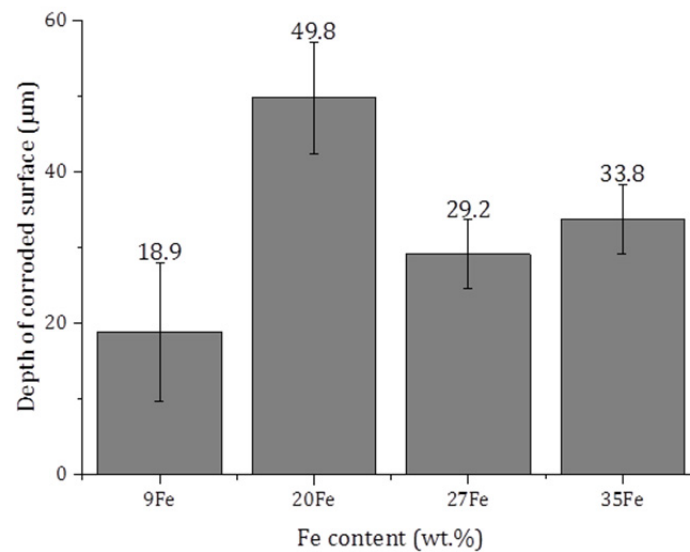
Figure 6.9: Maximum depth of the corroded surface obtain an average of from five 3D images on the 9Fe, 20Fe, 27Fe and 35Fe PTA aluminium bronze coatings after electrochemical test in an aerated 3.5% NaCI solution (error bars represent standard deviation)

The increase tendency for localised corrosion can also be related to the area bounded by the passivation loop shown in Figure 6.10. Numerical integration was carried out using Origin 9.1 software to determine the area bounded by the passivation loop. The results are presented in Table 6.5. The area of the passivation loop increases with the Fe content in the coating. This indicates greater tendency for pitting and is in good agreement with the observation of the corroded surface shown in Figure 6.8. Due to the limited number of data points, it was not possible to obtain the relationship between the area of passivation loop and the depth of the corroded area.
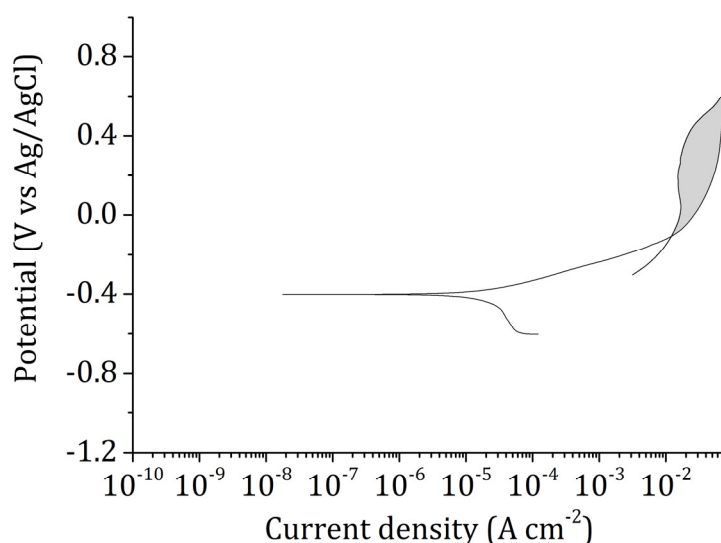
Figure 6.10: The observed potentiodynanic polarization curve for 37Fe PTA aluminium bronze coating in an aerated 3.5 % NaCI solution, grey area show the area bounded by the passivation loop

Table 6.5: Area of passivation loop obtained by numerical integration and potential difference between passivation potential and corrosion potential

Fe content in the coating (wt.%)	9Fe	20Fe	27Fe	35Fe
Area of passivation loop	0.0054	0.0114	0.0200	0.0201
Potential difference between passivation potential and Corrosion potential (V)	0.53	0.33	0.27	0.29

The ability of the coating to reform the passive layer also has significant effects on the corrosion rate. The larger the difference between the re-passivation potential (the potential where the passivation loop closes on the reverse scan) and the corrosion potential obtained in Table 6.4, the easier it is for the coating to re-passivate [184]. As shown in Table 6.5, the 9Fe coating exhibits the largest potential difference the re-passivation potential and the corrosion potential, which suggests that the coating can re-passivate more easily than other coatings. This might also be the reason for the stable OCP observed as shown in Figure 6.1.

6.2   Morphology and composition of the corroded surfaces

The results from optical profilometry showed clear evidence of localised corrosion in the 20Fe, 27Fe and 35Fe PTA aluminium bronze coatings. To investigate which area of the coating was selectively corroded, SEM observations in both secondary and backscattered electron modes were employed in conjunction with EDS analyses. The backscattered electron images comparing the as polished and the corroded 20Fe PTA aluminium bronze coatings are shown in Figure 6.11. The images show that the Fe_3Al intermetallic κ_1 phase (appearing dark in Figure 6.11 a) is completely removed after an electrochemical corrosion test. Similar observations were made for the 9Fe, 27Fe and 35Fe coatings as shown in Figure 6.12.
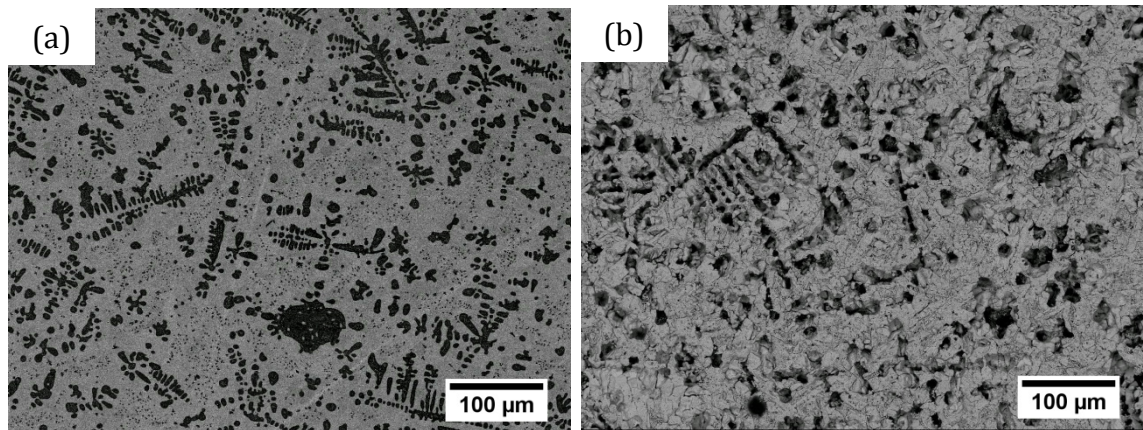
Figure 6.11: Backscattered electron image of the 20Fe PTA aluminium bronze coatings in (a) the as-polished condition and (b) after electrochemical corrosion test in 3.5% NaCI solution (the images were taken from two different samples)
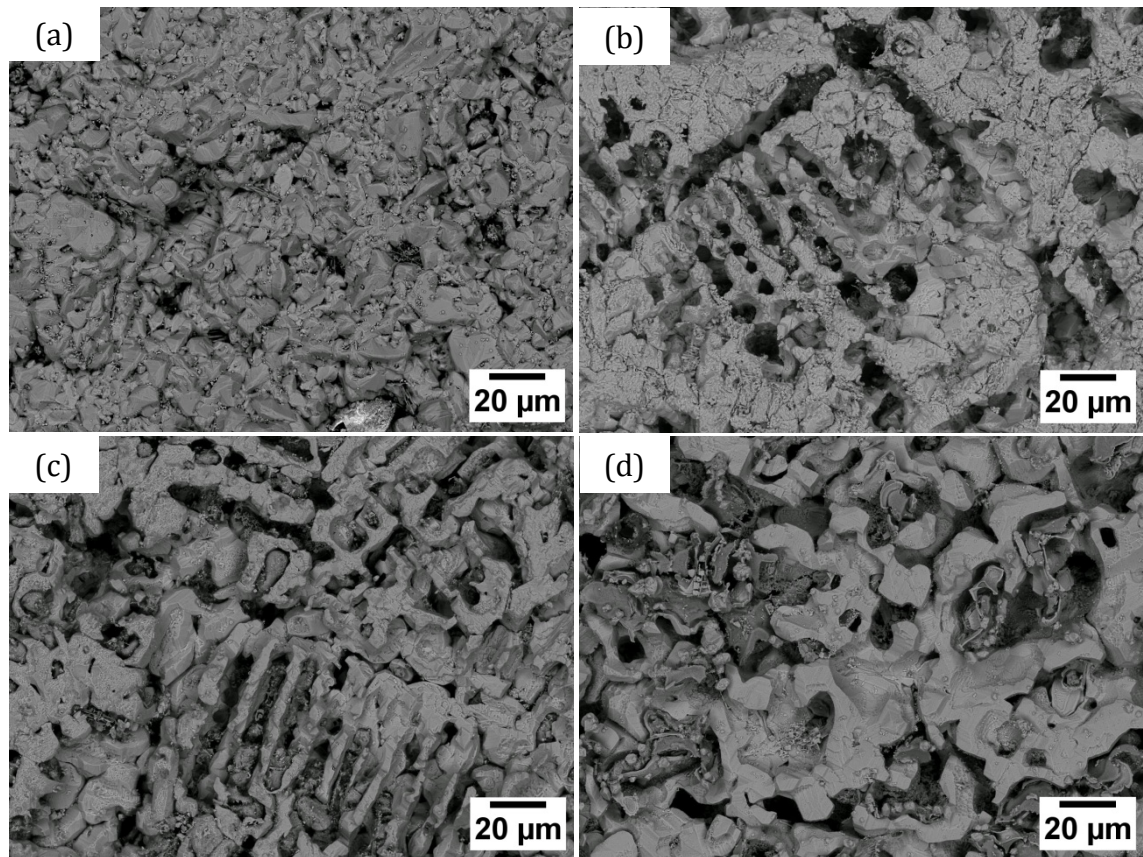
Figure 6.12: Backscattered electron image of the (a) 9Fe, (b) 20Fe, (c) 27Fe and (d) 35Fe coating surfaces after electrochemical corrosion test in an aerated 3.5% NaCI solution

To confirm the interpretation of the backscattered electron images and EDS analysis was carried out. The composition of the coatings after electrochemical corrosion tests is shown in Table 6.6. The results show significant reduction in both Fe and Al alloying element, which confirms that the intermetallic κ_1 phase has been selectively corroded.

Table 6.6: Composition of the coating after electrochemical corrosion test in aerated 3.5 % NaCI (all in wt.%)

	Cu	Al	Fe	Mn	Ni	Si	Cr	O
9Fe As sprayed	75.7	12.2	9.2	1.1	0.7	0.4	0.9	
9Fe After corrosion	80.3	6.4	7.5	1	0.7	0.2	1.4	2.4
20Fe As sprayed	67.3	8.4	21.5	1	1.3	0.3	0.2	
20Fe After corrosion	81.3	7.5	6.8	0.9	0.7	0.1	0.1	2.6
27Fe As sprayed	62.7	8.7	27.4	0.9	0.3	0.1	0	
27Fe After corrosion	76.8	7.1	10.5	0.6	0.4	0	0	4.6
35Fe As sprayed	54.8	6.8	35.3	1	1.2	0.3	0.6	
35Fe After corrosion	58.1	6.2	26.9	0.5	1.1	0.3	0.5	6.1

6.3   Immersion corrosion test in 3.5 % NaCI solution

The electrochemical tests yield a wealth of information regarding the mechanism and kinetics of the corrosion; however the test conditions differ from service condition, which lacks the presence of corrosion current. To investigate the corrosion behaviour of the coatings in the absence of corrosion current the coatings were immerse in an aerated 3.5 % NaCI solution for 7 days, post-test characterisation of the surface were carried out using SEM and EDS. The results are presented in the following sections.

6.3.1   SEM observation of the corroded surfaces

The SEM observations of the coating surface after 7 days immersion in 3.5 % NaCl is shown in   Figure 6.13. Compared   to the surface of   the coatings after electrochemical test, different corrosion characteristics were observed. In the electrochemical corrosion test, the intermetallic κ_1 phase was selectively corroded. However, for the immersion corrosion test, the intermetallic κ_1 phase appears unaffected as shown Figure 6.13. Corrosion damage involving the Cu-rich matrix appears non-uniform. In the 9Fe coating, the majority of the Cu-rich matrix was corroded. However, for the 20Fe, 27Fe and 35Fe coatings, only selected areas of the Cu-rich matrix are corroded.

The affected areas appear dark grey under backscattered electron imaging (Figure 6.13 b and d) and have higher roughness (Figure 6.13 c) compared to other Cu-rich areas.
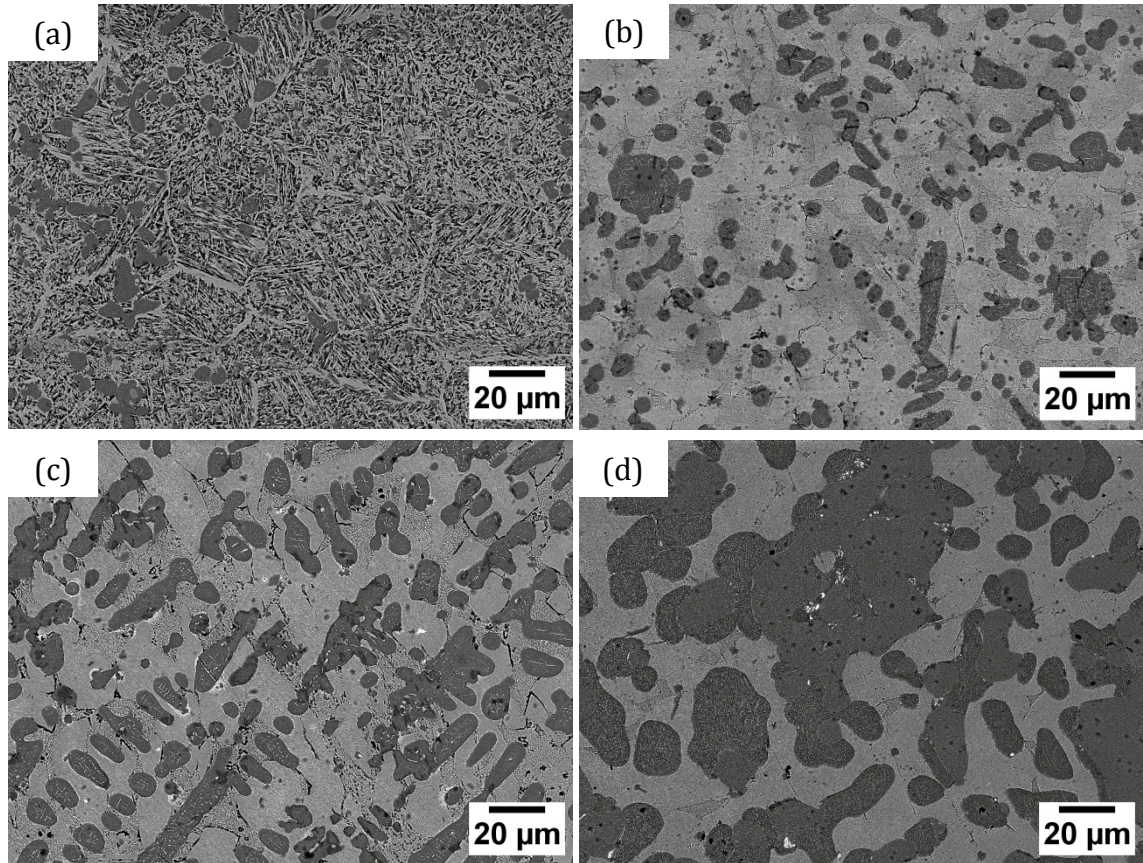
Figure 6.13: Backscattered electron images showing the surface of the (a) 9Fe, (b) 20Fe, (c) 27Fe and (d) 35Fe PTA aluminium bronze coatings after immersion corrosion test in an aerated 3.5 % NaCl solution

To determine which area of the Cu-rich matrix was selectively corroded, area EDS analysis was performed on the 35Fe coating as shown in Figure 6.14 and the results are presented in Table 6.7. The EDS data clearly shows that the corroded area contains ~5 wt.% higher Al content than the unaffected area. This composition corresponds to the β_1 as identified previously in Table 4.5. The same EDS analyses were carried out on all coatings and from the results it can be concluded that the corroded area is the β_1' phase of the 9Fe coating and the β_1 phase of the 20Fe and 27Fe coatings.
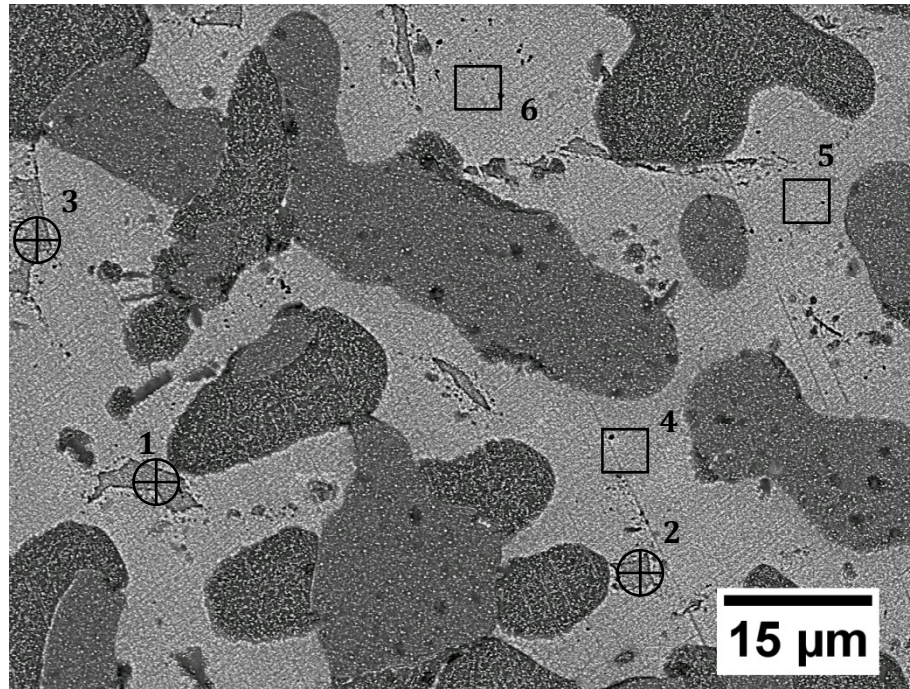
Figure 6.14: Backscattered electron image showing the position of the area EDS analysis performed on the corroded surface of the 35Fe PTA aluminium bronze coating

Table 6.7: EDS results from corroded and unaffected areas of the 37Fe PTA aluminium bronze coating after immersion corrosion test in an aerated 3.5% NaCl solution (all in wt.%)

	Cu	Al	Fe	Mn	Ni	Si	Cr	O	Phase
Corroded area	63.9	14.6	5.4	1.7	5.9	0.1	0	8.4	(Cu)
Area unaffected	68.1	10.4	8.4	1.7	2.7	0.0	0.2	8.5	β_1

A possible explanation for the selective attack may be related to differences in electrochemical potential between the phases. As shown by the EDS results in and in section 4.1.3 both the ordered β_1 phase and the martensitic β_1' phase have higher Al content than the solid solution (Cu) phase and the intermetallic κ_1 phase and thus have much lower electrochemical potential. Consequently, the β_1 and β_1' phase are oxidized when immersed in the 3.5 % NaCl solution and this leads to the observed localized corrosion. Based on this interpretation of the corrosion mechanism, the differences between the coatings can be explained by considering the proportion of the three main phases.

From the SEM images of the electro-polished samples Figure 4.4. The 9Fe coating mainly consists of the martensitic β_1' phase, therefore its matrix is uniformly corroded. As the Fe content in the coating increased, the depth of the localized attack increases. This results in an increase in corrosion rate as shown in Figure 6.15. The selective phase attack leads to a reduction in Cu content as shown in Table 6.8. However, the aluminium content in the coating remained largely unchanged. This indicates that dissolution of Cu might be the mechanism responsible for the observed corrosion behaviour.

Table 6.8: Composition of the coating before and after immersion corrosion test in an aerated 3.5% NaCI solution (all in wt.%)

	Cu	Al	Fe	Mn	Ni	Si	Cr	O
9Fe As sprayed	75.7	12.2	9.2	1.1	0.7	0.4	0.9	
9Fe after corrosion	59.3	12.0	13.7	1.4	1.4	0.5	1.2	10.5
20Fe As sprayed	67.3	8.4	21.5	1.0	1.3	0.3	0.2	
20Fe after corrosion	56.4	6.9	23.2	1.3	2.0	0.4	0.2	6.7
27Fe As sprayed	62.7	8.7	27.4	0.9	0.3	0.1	0	
27Fe after corrosion	49.7	8.8	32.7	1.4	0.9	0.1	0.0	6.4
35Fe As sprayed	54.8	6.8	35.3	1.0	1.2	0.3	0.6	
35Fe after corrosion	36.9	6.5	47.0	1.2	1.7	0.3	0.7	5.7
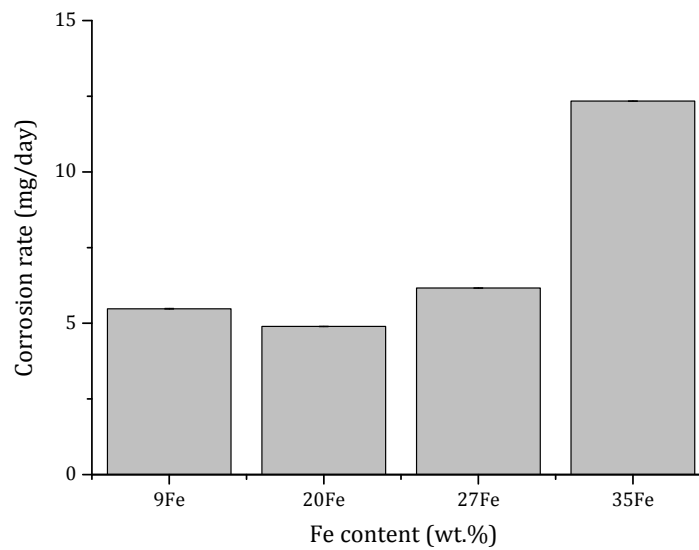
Figure 6.15: The effects of Fe content on the corrosion rate of PTA aluminium bronze coatings in aerated 3.5 % NaCI solution (error bars represent standard deviation)

6.4   Summary of the effects of microstructure on the corrosion characteristics of the PTA aluminium bronze coatings

The effects of PTA induced Fe increase on the corrosion characteristics of the coatings were investigated using electrochemical and immersion corrosion tests in an aerated 3.5 % NaCI solution. Results from electrochemical corrosion tests showed that the presence of the Al_2O_3 layers leads to low corrosion rate. The Al content in the coating was shown to have a strong influence on the coating's ability to form the passive Al_2O_3. In the coating system investigated, only the 9Fe coating was able for form this passive layer as indicated by the EIS results. For the 20Fe, 27Fe and 35Fe coatings, formation of Al_2O_3 is limited due to the lower Al content of the matrix, consequently the corrosion rate of these coatings are $\sim$ 20 times higher than that of 9Fe coating.

7. Discussion

In this chapter, first the microstructures of PTA aluminium bronze coatings are discussed. Variations in the microstructure of the coatings are rationalised with respect to the Fe increase resulting from the deposition. This is then followed by a discussion on the effects of microstructure on the friction, wear and corrosion resistance of the coatings. The influences of the constituent phase present in the coating on wear and corrosion properties are highlighted. The section concludes with recommendations for an optimal microstructure to improve wear and corrosion resistance.

7.1 Microstructure of PTA aluminium bronze coatings

7.1.1 Effects of PTA induced composition change and cooling rate on the constituent phases of the coatings

During the deposition process, the heat generated by the collimated plasma and the contact between high temperature molten aluminium bronzes causes the steel to melt [185]. Due to the high kinetic energy and rapid solidification, the melted Fe is sufficiently mixed and retained in the aluminium bronze droplet as shown schematically in Figure 7.1. This leads to an increase in the Fe content within the coatings as shown by the EDS result in Table 4.1.
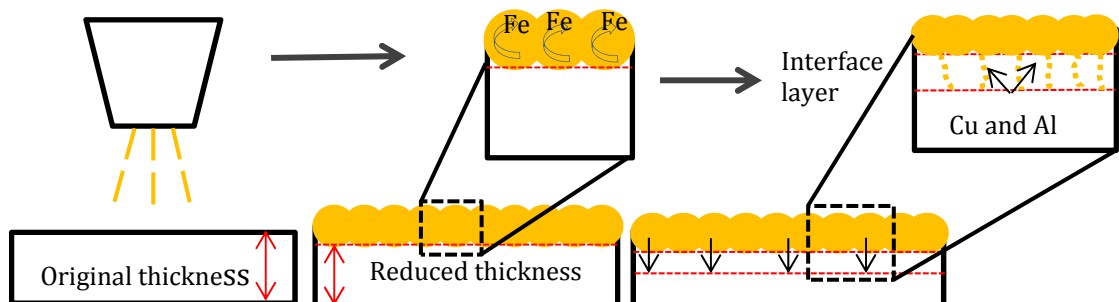
Figure 7.1: Schematic showing the a possible mechanism responsible for the composition change of the PTA aluminium bronze coating during deposition

One of the objectives of the present research is to investigate the influence of increase heat input during deposition on the microstructure of the coating. To achieve this, the PTA parameters were adjusted to increase the temperature during deposition. This increases the depth in which the steel substrate is melted during deposition thereby increasing the Fe content in the coating. In the present research, four coatings with Fe content of 9, 20, 27 and 35 wt.% were investigated. The Fe content investigated is substantially higher than the 2.5 wt.% Fe [15] and 11.5 wt.% Fe [133] achieved previously by rapid cooling and spin melting respectively. Information related to the effects of high Fe content on the microstructure of aluminium bronze is limited. Furthermore, most of the studies have only been carried out on alloys with composition in the (Cu) phase region of the Cu-Al phase diagram. Yutaka [138] showed that the addition of 3 wt.% Fe only slightly modify the binary Cu-Al phase diagram. Using X-ray diffraction, Krazanowski [139] showed that the addition of 12.3 wt.% Fe to the (Cu) alloys doesn't lead to any phase changes and the resulting microstructure consists of solid solution (Cu) phase and the bcc αFe phase. In the present research, the effects of high Fe content on alloys with composition in the β phase of the Cu-Al phase diagram were investigated.The microstructures of PTA aluminium bronze coatings consist of a Cu-rich matrix with iron aluminide particles of various sizes. Phase identification and confirmation were carried out using X-ray diffraction and SEM-EDS analyses of the electro-polished and etched samples. The results are presented in Table 7.1 together with previous works on other aluminium bronze coating and rapidly solidified Cu-Al and Cu-Al-Fe alloys.

Table 7.1: The constituent phases of the PTA aluminium bronze coating and other Cu-Al alloys

Coating nominal composition (wt.%)	Substrate material	Production method	Cu-rich phases	Fe-rich phases	Reference
Cu-5.9Al-9.3Fe	n/a	Magnetron sputtering	(Cu)	αFe	[139]
Cu-6.8Al-35.3Fe	Steel	PTA	(Cu) and β_1	κ_1 and αFe	This work
Cu-8.5Al-4.7Fe	Al-Si alloy	Laser cladding	(Cu) Cu_3Al Cu_9Al_4 Cu_2Al	-	[186]
Cu-8.4Al-21.5Fe	Steel	PTA	(Cu) and β_1	κ_1	This work
Cu-8.7Al-27.4Fe	Steel	PTA	(Cu) and β_1	κ_1	This work
Cu-8.63Al-3.23Fe	n/a	Casting + quench	(Cu) and β'	κ_1	[131]
Cu-9Al-4Fe	Steel	Electric arc deposition	(Cu) Cu_9Al_4	-	[187]
Cu-10Al-4Fe-4Ni	Cu-10Al-4Fe-4Ni	PVD	(Cu) Cu_9Al_4 NiAl	-	[13]
Cu-12.2Al-9.2Fe	Steel	PTA	(Cu) and β_1'	κ_1	This work

Table 7.1 shows that the increase in Fe content caused by the PTA deposition leads to a change in matrix phase from a martensitic β_1' phase to an ordered β_1 phase. This Fe induced phase change in the β phase alloy has not been observed previously. The increase in Fe content also promotes the formation of dendrites at the interface between the coating and the steel substrate as shown in section 4.2.

To explain the observed changes in phase and the microstructure of the PTA aluminium bronze coating, the first phase diagrams of ternary Cu-Al-Fe and binary Cu-Fe, Cu-Al and Fe-Al were analysed. The following key points were deduced:

- In the composition range relevant to the present coating system, no ternary phases are expected, thus consideration of the binary phase diagrams can provide an initial explanation for the observed phases.

- The Cu-Fe phase diagram in Figure 2.20 shows low solubility of Fe in Cu, no low temperature Cu-Fe phases have been reported. Therefore only Cu-Al and Fe-Al phases are expected in the coating. This is consistent with the XRD results shown in section 4.1.2, However, a miscibility boundary is known to exist [188]. This indicates that during rapid cooling such as in PTA process, liquid phase separation may occur [134]. The solubility of Fe in Cu or vice versa decreases significantly with temperature. Therefore rapid cooling from high temperature can lead to extension of solute trapping. This phenomena was observed during electric arc deposition of aluminium bronze on steel [187] .

- The Cu-Al phase diagram shows that the Al content has strong influence on which type of Cu-Al phase will be formed. The solid solution (Cu) phase is only stable for Al < 9 wt.%, while the disordered β is stable between 10-15 wt.% Al and only at high temperature. The microstructure of the solid solution (Cu) is not influence by the cooling rate. However, as discussed in section 2.3.1, the cooling rate has significant influence on the microstructure of the high temperature disordered β phase. The eutectoid decomposition of the high temperature disordered β phase into (Cu) and Cu_9Al_4 γ_1 phase follows a two-step process involving the $\beta \rightarrow \beta_1$ disordered to ordered reaction followed by diffusion controlled decomposition of the ordered β_1 phase.

- Slow cooling though the ~567 °C enables completion of the eutectoid decomposition. Rapid solidification leads to martensitic transformation of the order β_1 phase into β', β_1' and/or γ_1' depending on the Al content of the alloy as discussed in section 2.3.1. The disordered β can also transform to β_1 and (Cu) through a metastable eutectoid reaction $\beta \rightarrow \beta_1$ + (Cu) at ~500 °C [129].

- Considering the melting points of Cu, Al and Fe, the Fe rich phase is expected to be the first to solidify. Furthermore, steep temperature gradient in the region between the melted and un-melted steel substrate also accelerates the solidification process.

7.1.2   Solidification of the PTA aluminium bronze coatings

Considering the exit temperature at PTA orifice and the increase in Fe content discussed in section 7.1.1 it is certain that both aluminium bronze powder and the top surface of the steel substrate are in the liquid state during deposition. As the PTA system traverse across the surface of the steel (see Figure 2.11, the molten mixture of aluminium bronze and Fe begins to solidify. In the PTA process, the cooling rates in the range of $10^2 - 8 \times 10^3$ K s^{-1} [100] have been reported. Due to this high cooling rate and low solubility of Fe in Cu, the molten mixture separates into the Fe-rich and Cu-rich components both of which contain certain amount of Al solute. In addition, some Cu may also be retained in the Fe-rich component or vice versa. Such separation has also been reported during rapid solidification of Cu-Fe alloy [189] [190] [134]. The Fe-rich melt has significantly higher melting point than the Cu-rich melt and is thus the first to solidify as the temperature decreases below 1538 °C as indicated the Fe-Al phase diagram. As the temperature decreases, the Cu-rich component solidifies according to the Cu-Al phase diagram. Based on this solidification sequence and the review of the relevant phase diagrams the microstructure of the coatings can be explained as follows. In the 9Fe coating, the deposition temperature and the depth of substrate melting are the lowest. Consequently, the cooling rate expected for this coating is also the highest and the amount of Fe increase in this coating is the lowest.

At the interface between the molten mixture and un-melted steel substrate, the Fe-rich component solidified as Fe-rich globules, which later grows to form the interface layer as shown by the EBSD phase map in Figure 4.24 a. Due to the high cooling rate, the growth of these Fe-rich globules is limited, this leads to the submicron size grains at the interface layer as shown in Figure 4.24 a. At the same time, the Fe-rich melt that has been mixed into the Cu-rich component solidified as Fe-rich globules, which due to the high cooling rate also contains Cu and Al. Additionally, due to the steep concentration gradient between the solidified Fe and the surrounding Al-rich liquid, some Al solute may diffuse into the solidified Fe-rich globules. The diffusion of Al solute was also observed during diffusion bonding of $Fe_{72}Al_{28}$ iron aluminide using a pure Fe interlayer by Torun et al. [191] who reported major diffusion of Al from the $Fe_{72}Al_{28}$ matrix to the pure Fe interlayer. These effects lead to the reduction in the concentration of Al solute in the Cu-rich component. However, due to the limited Fe content in the 9Fe coating, the composition of the Cu-rich component is maintained in the β phase region. Upon rapid cooling from high temperature, the disordered β phase first undergoes an ordering reaction to form an ordered β_1 before transforming into a martensitic β_1' phase. This result is also consistent with previous works by Kwarciak et al. [118] and that of Nishiyama and Kajiwara [192]. The result also confirms that the cooling rate achieved during PTA is sufficient to avoid the undesired eutectoid reaction. With increasing Fe content, the deposition temperature and the depth in which the substrate material is melted also increases. This has the following effects on the temperature distribution:

- The increase in the depth of substrate melting leads to a temperature gradient within the molten mixture as shown schematically in Figure 7.2. The region nearest to the un-melted steel substrate will experience the highest temperature gradient and will solidify faster than the region away from the un-melted steel. Consequently solute trapping is enhanced in this region.

- The increase in deposition temperature enables more Fe to be dissolved in the Cu-rich component as shown by the Cu-Fe phase diagram. Rapid cooling from this temperature enables the retention of more Fe in the coating [134].

- The increase in deposition temperature also leads to larger heat affected zone around the molten region.
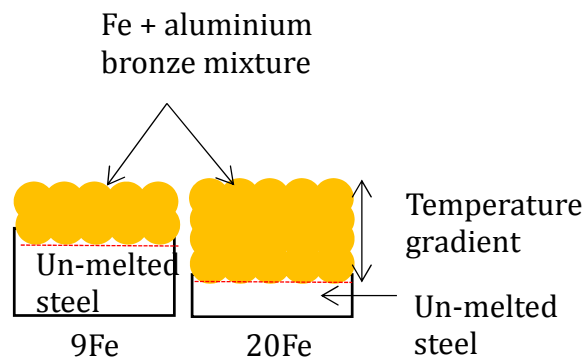
Figure 7.2: Schematic showing the influence of increase depth of substrate melting on the temperature gradient within the Fe and aluminium bronze mixture

These changes in the temperature distribution have the following effects on the microstructure of the interface region between the coating and the steel substrate:

Compared to the 9Fe coating, the grains at the interface layer of the 20Fe coating are larger as shown by the EBSD phase map in Figure 4.24 b. The increase in deposition temperature provides excess energy for the grains to grow. As the deposition temperature increases further, Fe-rich dendrites were observed to grow from the grains at the interface layer as shown by the EBSD orientation map for the 27Fe and 35Fe coatings in Figure 4.22 c and d respectively. The large temperature gradient in the molten mixture and high local under cooling are thought to be the main driving force for the observed dendrite growth in the 27Fe and 35Fe coatings. In the Cu-Fe system the speed of the dendrite has been reported to increase with the decree of under cooling as shown in Figure 7.3 [193].

The growth of the dendrites into the coating enhances the mechanical bonding by increasing the contact area between the coating and the steel substrate. Due to the limited availability of the sample it was not possible to obtain the bond strength values for the present coating. However, the results from previous tests on aluminium bronze coatings with similar interface microstructure showed high bond strength of up to 365.4 MPa [38], which is substantially higher than that of PVD and CVD coatings (see section 2.2.2.).
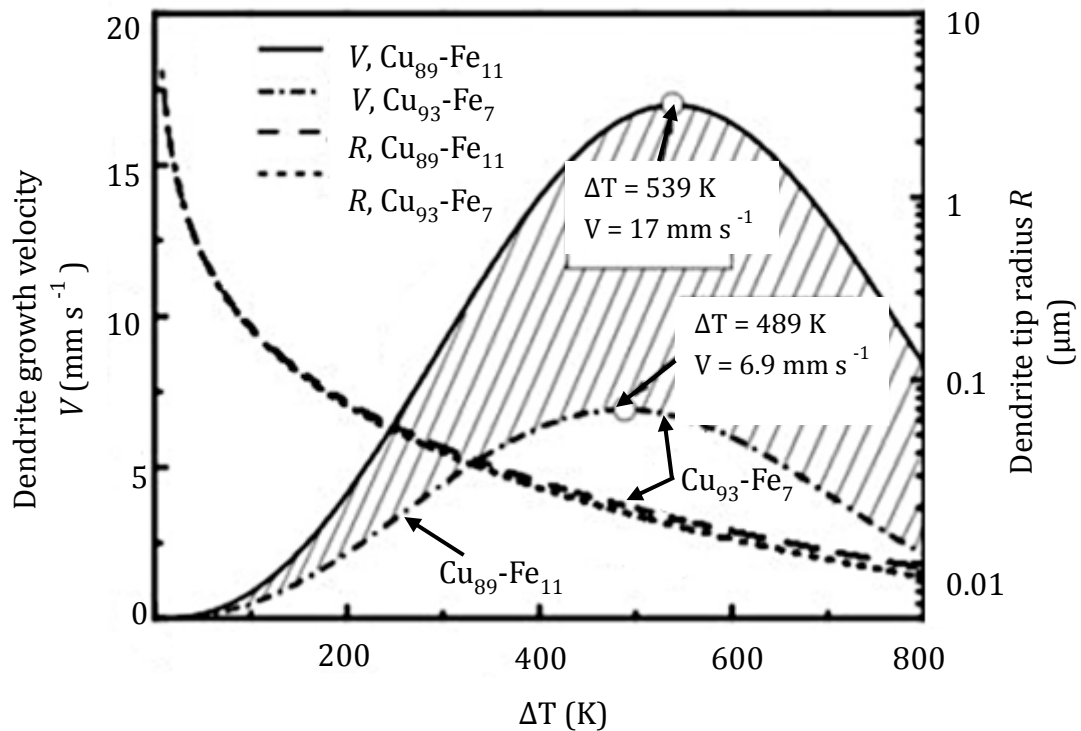
Figure 7.3: Calculated velocity of dendrite growth and tip radius for Cu 89-Fe 11 and Cu 93-Fe 7 alloy (adapted from [193])

In the region away from the interface layer the changes in the temperature distribution have the following effects on the microstructure:

The enhanced trapping of Cu and Al in the Fe-rich component caused by the increase in deposition temperature decreases the concentration of Al in the Cu-rich component. With increasing Fe content the composition of the Cu-rich component is shifted towards the (Cu)/β and (Cu) region of the Cu-Al phase diagram as indicated by the red arrow in Figure 7.4.

Upon cooling from high temperature metastable eutectoid reaction $\beta \rightarrow \beta_1 + (Cu)$ at ~500 °C [129] occurs. Consequently, the matrix of the 20Fe, 27Fe and 35Fe coatings consist of a two phases. These were identified by XRD and confirmed by SEM-EDS to be the solid solution α and the ordered β_1 phase. In the 20Fe, 27 Fe and 35Fe coating the eutectoid structures was also not observed. This further confirms that the cooling rate achieved is sufficient to avoid the eutectoid decomposition.
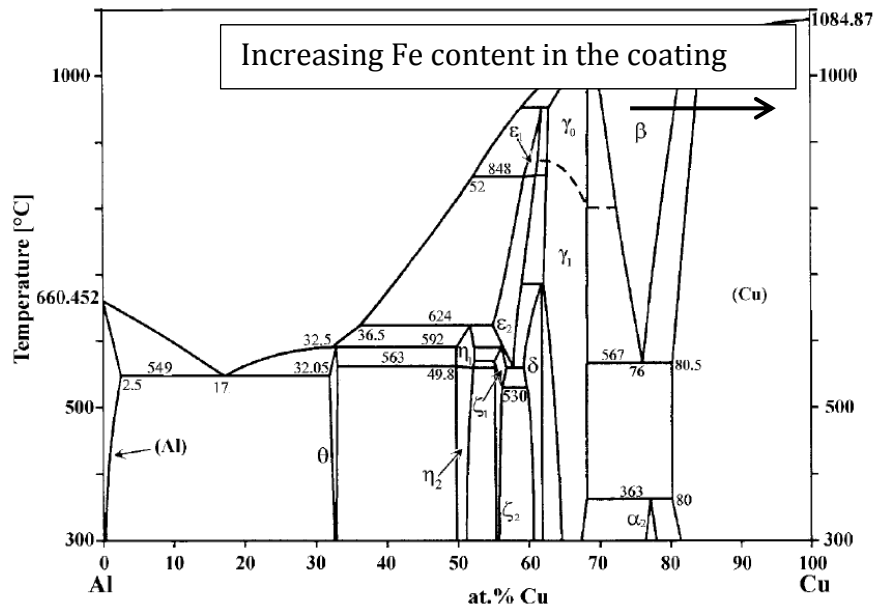
Figure 7.4: The effects of increasing Fe content due to elevating substrate melting during deposition on the composition of the Cu-rich melt. The arrow indicates a shift in composition towards the (Cu) phase region as the Fe content in the alloy increases (adapted from [123])

The Fe-rich component, which has been mixed into the Cu-rich component first solidified as the bcc αFe phase. As the temperature decreases to below 540°C, the bcc αFe phase transforms into the Fe_3Al intermetallic κ_1 phase as indicated by the Fe-Al phase diagram. In the 35Fe coating, the bcc αFe phase was also observed along with the intermetallic phase. A possible reason is due to the limited Al solute available for all the Fe to exist in the form of intermetallic phase. Once the entire Al is utilized to form the intermetallic phase, the remaining Fe-rich component solidifies as the bcc αFe phase. In previous works [158][131][17][157] on the characterisation of the aluminium bronze alloy, the κ_1 phase appeared to have a uniform microstructure.

However, in the present study, to the enhance solute trapping caused by the high deposition temperature and the high cooling resulted in precipitation of the Cu-rich particles inside the κ_1 phase as shown SEM-EDS analysis of the etched samples in Figure 4.7. Hardness measurements of κ_1 phase in the 20Fe, 27Fe and 35Fe coatings reveal that it has an average hardness of 6.2 GPa, 7.1 GPa and 4.8 GPa respectively. The hardness increase of the κ_1 phase from 6.2 GPa to 7.1 GPa might be due to the precipitation hardening cause by the Cu-rich precipitates. However, as the number of precipitates increases a decrease in hardness of the κ_1 phase was observed. This is not expected because the increase in hardness is expected to continue to rise. A possible reason for the observed decrease in hardness might be due to the reduction Al content in the intermetallic phase, which reduced the hardness. This interpretation of the results suggests that the Al is the main factor that governs the hardness of the intermetallic phase. In the next section, the effects of constituent phases on the hardness of the coating are discussed.

7.1.3 Influence of constituent phases on the hardness of the coatings

Hardness mapping using depth-sensing nano-indentation shows that the microstructure change has significant effect on the hardness and hardness distribution of the coating. The hardness of the coating with 9 wt.% Fe is the most uniform. This is due to the homogeneous distribution of the fine intermetallic κ_1 phase. With increasing Fe content the hardness of the coating becomes less uniform due to the presence of large intermetallic κ_1 phase. The change matrix phase from martensitic β_1' phase to the solid solution (Cu) phase also leads to a reduction in matrix hardness from 4.9 GPa to ~2.5 GPa. Comparing the hardness of the coating with solid solution matrix, the reduction in the Al solute also leads to hardness reduction of the solid solution (Cu) phase from 3.5 GPa for the 20Fe coating to 2.6 GPa in the 35Fe coating. This is due to the reduction in solid solution strengthening caused by the lack of Al solute. The analysis of the measured hardness indicates that the intermetallic κ_1 phase has the most significant influence on the mean hardness of the coating. Consequently, the 27 wt.% Fe coating has the highest mean hardness of 5.6 GPa, while the coating with 35 wt.% Fe has the lowest mean hardness of 4.7 GPa.

The difference between the hardness results obtained by micro-hardness and depth-sensing nano-indentation is also worth noting. The results obtained by nano-indentation are higher than that obtained by the micro hardness test. This is due to several reasons; the first reason is the influence of phase(s) present beneath of the indentation site. The second reason is due to the indentation size effects where the observed hardness increase with decreasing indentation size [194]. This effect is generally accepted to be a consequence of the large strain gradient caused by small indentation that leads to enhanced hardening. As it will be discussed later, the increase in hardness due to the presence of large κ_1 phase leads to a reduction in wear performance.

Table 7.2: Hardness difference between measurements obtained by micro hardness testing and depth-sensing nano-indentation

Coating	Mean micro-hardness (GPa)	Mean nano-hardness (GPa)	Difference between methods (micro-nano)
9Fe	3.1	4.9	-1.8
20Fe	2.4	4.7	-2.3
27Fe	2.9	5.6	-2.7
35Fe	3.6	4.6	-1.0

7.2   The influence of microstructure on the friction and wear characteristics of the PTA aluminium bronze coatings

Aluminium bronze alloys are some of the oldest and most frequently used material for bearing applications. Over the past century, numerous investigations have been dedicated to the understanding of the microstructural influence on the tribological properties of these alloys. However, with the advent of new processing techniques and addition of more alloying elements, the microstructure of the alloy becomes ever more complex. This makes the effects of microstructure on wear more difficult to interpret. Furthermore, complex oxide may also be present at the sliding interface due to the different oxidational properties of the different phases. The type and stability of these oxides are also expected to have a significant role in controlling the friction and wear of the coating [146].

7.2.1   The significant of the constituent phases on the wear characteristic of the coatings

In the present research, the microstructure of the coatings under investigation can be classified into two main groups:

- The martensitic β_1' phase matrix with submicron size intermetallic κ_1 phase (9Fe coating)

- The solid solution (Cu) phase matrix with micron size intermetallic κ_1 phase (20Fe, 27Fe and 35Fe coatings)

The 9Fe coating with the martensitic β_1' matrix has significantly lower specific wear rates than the coatings with a solid solution (Cu) phase as shown in Figure 5.23 and Figure 5.48. To investigate the influence of the constituent phases on the wear characteristic of the coating, SEM observations of all worn surfaces were conducted. Additionally, selected worn surfaces of the 9Fe and 27Fe coatings (representing the two groups of microstructure) were sectioned using FIB and observed by ion contrast imaging. In the 9Fe coating with β_1' martensitic matrix, the microstructure underneath the worn surface is characterised by a layer of fine grains nanometre in size. Dynamic recrystallization (DRX) induced during the wear test is thought to be the mechanism responsible for generation of the nanometre-sized grain. The presence of DRX in Cu-based alloys was first discovered in the 1977 [148] and confirmed by TEM during sliding wear of Cu pins against steel [147]. Beneath the fine grain layer, the microstructure of the martensite appears to be un-affected as shown in Figure 5.16. This is evident by the morphology of the κ_1 phase, which appears to retain the same morphology as in the un-deformed alloy thus indicating that the surrounding martensite is also un-deformed. A possible reason for the limited deformation of the martensite could be due to the energy dissipation among the interfaces within the martensite plates and matrix [146]. The subsurface microstructure of the 27Fe coating with a solid solution (Cu) phase is characterised by a mechanically mixed layer and a fine grain layer caused by DRX as shown in Figure 5.17. The observed microstructure is similar to that reported in [195][149].

Within the mechanically mixed layer, ion imaging reveals a layered structure that is thought to be a mixture of the substrate and the oxide layers that have been sheared and re-attached on to the surface during sliding. Beneath the mechanically mixed layer, a fine grain layer of nanometre in size also was observed. In the fine grain layer, significant plastic flow was also observed. This is evident by the elongation of the intermetallic κ_1 phase. This observation indicates that the solid solution (Cu) phase doesn't have sufficient strength to with stand the load. The inverse pole figures obtained from the EBSD mapping of the solid solution (Cu) phase (see Figure 5.13) show that it has a strong preference for slip to occur along $\langle 1\bar{1}0 \rangle$ direction within the {111} plane. Upon loading several slip systems were activated as shown by the intersecting slip lines in Figure 5.11. These slip lines propagate through the matrix and terminate at the intermetallic κ_1 phase as shown in Figure 5.12 The stress induced by the pile up of dislocation at the hard intermetallic κ_1 phase leads to the formation of voids on the surface as shown in Figure 5.11. The number of voids increases with the volume fraction of the solid solution (Cu) phase and the intermetallic κ_1 phase. Coalescence of these voids leads to surface cracks as shown in Figure 5.7. This reduced the strength of the surface layer that is enclosed by the cracks leading to the removal of the surface layer as shown in Figure 5.8 and production of flake-shaped wear debris. Consequently, coatings with high volume fraction of (Cu) phase and κ_1 phase such as the 27Fe coating have the high specific wear rate as shown in Figure 5.23 and Figure 5.48. The results are in good agreement with previous work in reference [196]. This mechanistic interpretation of the wear mechanism is similar to that postulate by the delamination theory of wear [49] except the lack of subsurface crack. This indicates that flake-shaped wear debris can also be formed by coalescence of surface cracks.

7.2.2   The influence of oxide properties on the friction and wear characteristics

In addition to the microstructure features, the properties of the oxide film also have a significant influence on the friction and wear characteristics, particularly for dry contact. Aluminium bronze naturally contains oxide layers of ~ 900 nm thick that consist of CuO/Cu_2O outer layer and an Al_2O_3 inner layer [167]. The volume fraction of the Al_2O_3 increases with the Al content in the coating [15]. It is also worth noting that that counter-materials used for all wear tests were not sputtered clean and therefore contain the natural oxide on the surface. Therefore, the chemical reaction between the alloying elements in the coating and the oxide on the counter material has influences on the friction and wear behaviours. During initial sliding, the high contact pressure and the shear stress lead to the removal of the initial oxide layer. In the 9Fe, 20Fe and 27Fe coatings this shearing of oxide is evident as spikes in friction coefficient during the first 30 s of sliding as shown in Figure 5.1 a-c. However, in the 35Fe coating, the spike in friction coefficient was not observed. A similar rise in friction coefficient during initial sliding was also observed in the wear test of Cu-12 wt % Al alloys with martensitic and eutectoid structure [146]. The increase in the friction coefficient indicates that different oxides are present on the surface of the coatings. In the 9Fe, 20 Fe and 27Fe coating, higher Al content is retained in the matrix as shown in Table 4.1. This enables formation of Al_2O_3, which is known to have high hardness. Therefore, shearing of the oxide requires high tangential force, which is evident by the increase in friction coefficient. In the 35Fe coating, the low Al content in the matrix limits the formation of Al_2O_3 layer. The CuO/Cu_2O is expected to form on the surface. Due to the lower shear strength of the CuO/Cu_2O compared to the Al_2O_3 the tangential force required to shear the layer is lower. Therefore no spike in friction coefficient was observed as shown in Figure 5.1 d. As the sliding continues, the coating surface is exposed to oxygen and the heat generated by friction. The EDS analyses show that the Al content in the worn surface of the 9Fe, 20Fe and 27Fe coatings are higher than in the unworn region. The possible reason for the increase in Al at the surface is due to segregation of Al by grain boundary diffusion [150].

Once at the surface, the Al reacts with oxygen and forms Al_2O_3 that links the counter material and coating surface as shown schematically in Figure 7.5. Due to the high chemical stability of the Al_2O_3 (indicated by the high melting point of 2270 °C) the bond strength generated between the Al_2O_3 and the counter material steel is stronger than the cohesive strength of the coating. Due to the tangential force generated by the relative movement, the bond breaks within the coating leading to the transfer of coating materials on to the surface of the steel as shown by the results in section 5.1.3. This prevents direct contact between the coating and steel modifies the shear strength at the interface between the two materials. Further segregation of Al to the surface leads to the reformation of the Al_2O_3 layer on the surface of the coating. Due to the high chemical stability of the Al_2O_3 that is now covering both surfaces, the shear strength at the contact interface is low. This leads to the low friction coefficient and wear.
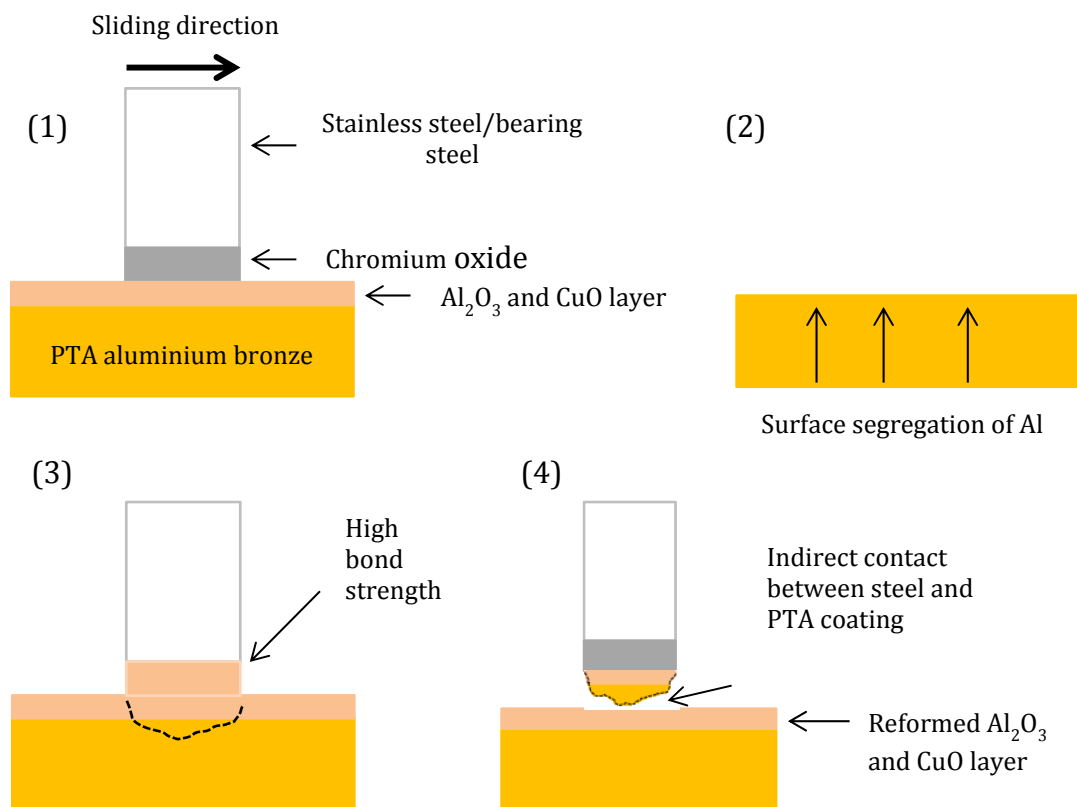
Figure 7.5: Schematic showing the influence of Al_2O_3 on the contact between the coating and the Fe-rich counter material

In the 35Fe coating, the initial shearing of the CuO/Cu_2O oxide exposes the Cu-rich surface. Due to the limited amount of Al in the matrix, segregation of the Al to the surface was not observed as shown by EDS result in Figure 5.22. However, EDS analysis shows that the Cu-rich surface is oxidised as shown by the high oxygen content and a decrease in Cu. Due to the low shear strength of re-formed Cu-oxide, it is easily removed from the coating surface. This leads to direct contact between the steel and the Fe-rich phases present in the 35Fe coating as shown schematically in Figure 7.6. The Fe-on-Fe contact has high tendency for adhesive junction formation due to the similarity in crystal structure and the high solubility. Consequently, high cohesive strength is formed. Therefore to enable relative motion, high tangential force is required. This results in high and unstable friction coefficient as shown in Figure 5.1. Due to the low hardness of the matrix phase in the 35Fe coating (see Figure 4.13) the shearing took place within the 35Fe coating, leading to transfer of material. As the sliding continues, some of the transferred material is re-attached onto the surface of the 35Fe coating as shown in Figure 5.6. This decreases the mass loss which leads to an apparent lower specific wear rate when compared with the 27Fe coating as shown in Figure 5.23 and Figure 5.48.
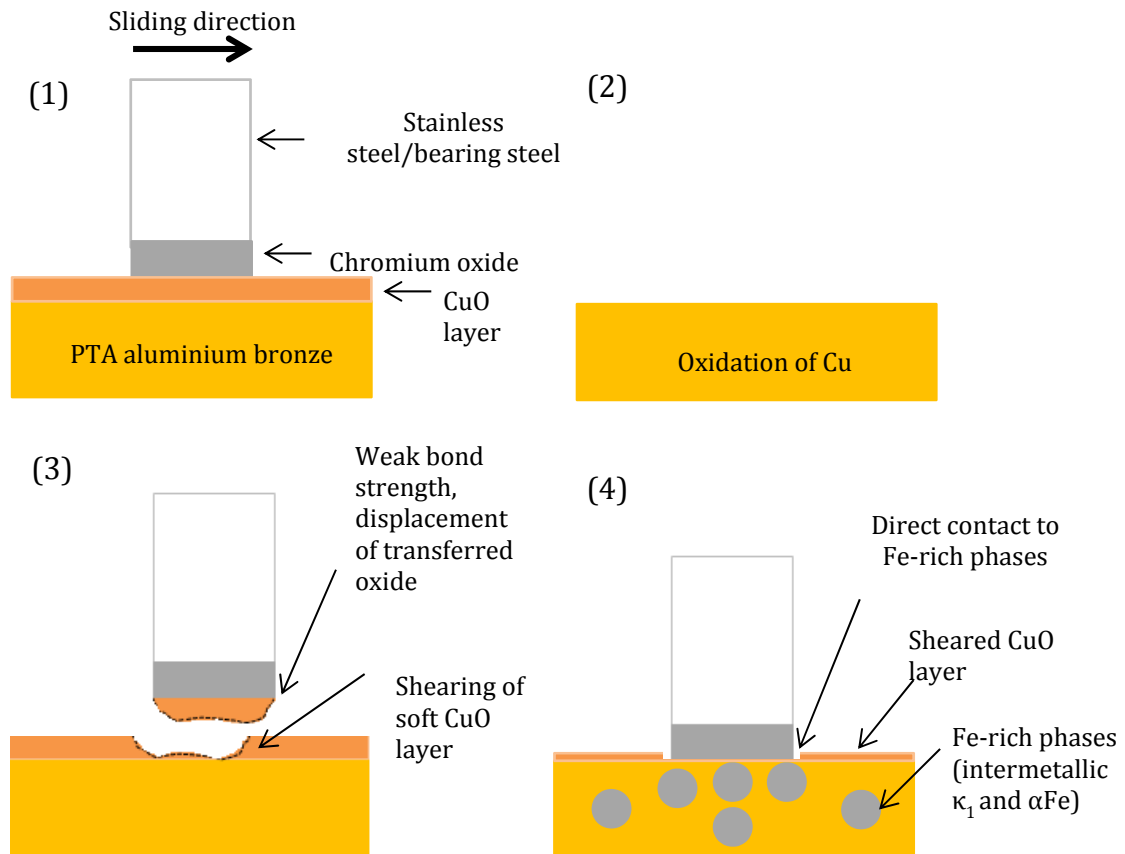
Figure 7.6: Schematic showing the contact between the 35Fe PTA aluminium bronze coating and the Fe-rich counter material

7.2.3   Wear characteristics of the coating against stainless steels

Surface coating has been used effectively to reduce wear on cutting tools, however the majority of the forming dies remain uncoated [197][12]. One of the main reasons for the low acceptance of the surface coating technology is due to the complex shape of the forming dies, which makes it difficult to apply the coating. Furthermore, hard coatings such as those used for protection of cutting tools have been reported to result in high friction coefficient and galling tendency when used in contact with the relatively softer sheet metals [198] such as austenitic stainless steel, Al, Ni and Ti based alloys. In this section, the friction and wear characteristics of the PTA aluminium bronze coatings during dry sliding against three different grades of stainless steels will be discussed with emphasis on the effects of stainless steel hardness and the role of oxide layer.

Influence of oxide layers on the friction coefficient during dry sliding against stainless steels

Stable friction coefficient is a critical requirement for a good surface finish of the product during SMF operation. The friction coefficient during dry sliding between the PTA aluminium bronze coatings and three different stainless steel grades are shown Figure 5.24. With the exception of the 35Fe coating, all coatings exhibit a stable friction coefficient of ~ 0.5. This is comparable with the measured value of 0.4 [199] and 0.46 [200] during dry sliding between high strength steel an (Ti,Al)N and TiN coatings respectively. However, unlike other coatings, the CoF for the PTA coating is not effected the change in counter material hardness. During sliding, the oxide layers are transferred and adhered strongly with stainless steel as shown in Figure 5.46. A similar observation was also observed in [201]. This prevents direct contact between the stainless steel pin and the coating leading to low CoF. With increasing counter material hardness, more oxides are removed and transferred on to the counter material pin. This further prevents the direct contact between the two surfaces. Therefore, the change in counter hardness does not lead to a significant change in friction coefficient as shown Figure 5.24.

The effects of stainless steel hardness on the friction and wear rates of the coatings

The specific wear rate of the coatings and the AISI D2 during dry sliding wear test against three different stainless steel grades are shown in Figure 5.48. For the 20Fe, 27Fe, 35Fe coatings and the AISI D2 tool steel, the specific wear rates increase with the hardness of the stainless steel. However, for the 9Fe coatings, the specific wear rate decreases with increasing counter material hardness. The 9Fe coating has the lowest specific wear rate of 200 x 10^{-6} mm^3/Nm. This is comparable to the 356 x 10^{-6} mm^3/Nm reported for aluminium bronze alloy during ASTM G65 abrasion test [202]. In relation to other coatings aimed at SMF processes, the observed specific wear rate for the 9Fe coating is comparable to the significantly harder WC-Co and DLC coatings which have a specific wear rate of ~170 x 10^{-6} mm^3/Nm and 160 x 10^{-6} mm^3/Nm respectively [53].

The lower specific wear rate of the 9Fe coating is due to resistant of surface crack of the matrix phase. This minimizes the removal of the coating material and enhances the resistance against abrasive wear. With increasing stainless steel hardness, the temperature during sliding increases. As discussed in section 7.2.1, the high temperature can promote segregation of Al to the surface, which leads to formation and transfer of Al_2O_3 onto the surface of the stainless steel as shown in schematically in Figure 7.5 Consequently the actual contact area between the stainless steel and the coating is minimized. This results in the reduction in specific wear rate observed. The high wear rates observed for the 20Fe, 27Fe and 35Fe coatings are due to the combined effects of delamination and abrasive wear. The 35Fe coating exhibits the highest adhesive wear as shown by the SEM image in Figure 5.33. This might be due to the strong cohesive force between the Fe-rich phases present in the coating and the stainless steel. The low hardness of the matrix phase in the 20Fe, 27Fe and 35Fe coatings also leads to an increase in abrasive wear rate.

In comparison with the currently used AISI D2 tool steels tested under the same condition, the specific wear rates of all coatings are substantially lower as shown in Figure 5.48. SEM observations of the AISI D2 worn surface show evident of abrasive micro scratches that are thought to initialise by the adhered material on the surface of the AISI D2. The abrading particles were observed at the end of the wear tracks. During the initial stage of sliding, material from the softer stainless steel pin is transferred to the AISI D2 surface by the adhesive wear mechanism discussed in section 2.1.2. Due to the large spacing of the carbides in the AISI D2 material, the adhesive failure is expected to be on the Fe-rich matrix. The smooth appearance of the carbide phase suggests that the carbide phase has a low adhesion to the stainless steel counter material. Similar observations were found in [32].

7.3   The effects of microstructure on the corrosion resistance of the coatings

The majority of the investigations on corrosion resistance of aluminium bronzes have been focused on the Cu-Al-Fe-Ni alloys containing up to 6 wt.% each of Ni and Fe [203][204][151]. However, there are limited numbers of studies on Cu-Al-Fe aluminium bronze with Al >10 wt.% and few report on the electrochemical kinetic at the interface. In the present research, extensive electrochemical and immersion corrosion tests were carried out in an aerated 3.5 % NaCI solution. In this section, the effects of microstructure changes on the corrosion resistance of the coating will be discussed.

7.3.1   The influence of Fe on the corrosion rate of the PTA aluminium bronze coatings

The corrosion current is an indication of the corrosion rate of a material. The corrosion current was obtained from the analysis of the polarization curves as shown in Table 6.4. The results show that the 9Fe coating with a martensitic matrix has the lowest corrosion current of 1.94 μA cm^{-2}. The change in matrix phase to a solid solution α phase leads to an increase in corrosion to 34.6 μA cm^{-2} for the 20Fe coating. However, further increase in Fe content in the coating with solid solution matrix, the corrosion current decreases to 27.2 μA cm^{-2} for the 35Fe coating. This might be due to the increase in volume fraction of the non-conductive intermetallic phase, which increases the resistance of the alloy. Compared to previous work on the solid solution Cu-6Al-xFe alloy by Collins et al. [133]. The high Fe content retained in PTA aluminium bronze coating leads to a decrease in corrosion current and thus corrosion rate as shown in Figure 7.7.
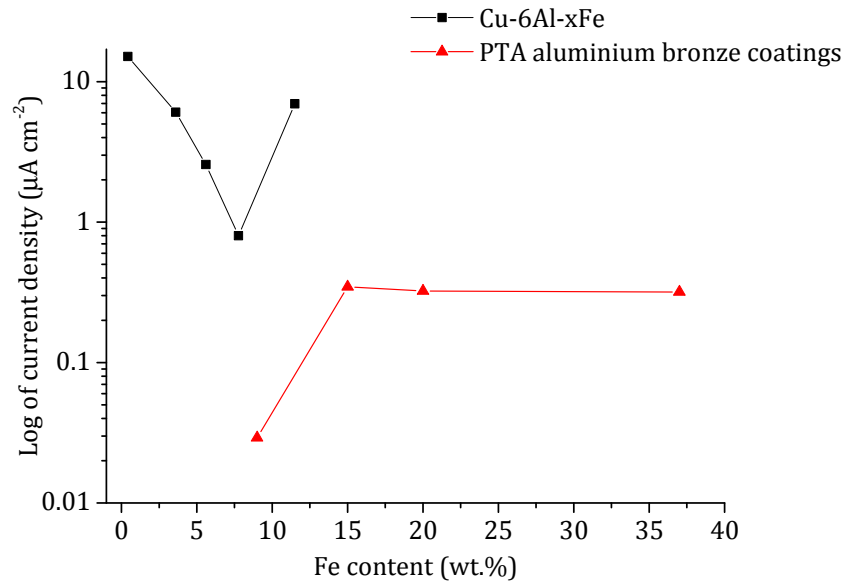
Figure 7.7: The effects of Fe content on the corrosion current of the PTA aluminium bronze coatings (data for Cu-6Al-xFe obtained from [133])

The 9Fe coating has the lowest corrosion rate from 22.5×10^{-3} mm/year. This is significantly lower than the 400×10^{-3} mm/year measured for the 20Fe coating. The observed corrosion rate for the 9Fe coating is comparable to the corrosion rate of more highly alloyed nickel aluminium bronze in seawater which has a reported corrosion rate of $15\text{-}500 \times 10^{-3}$ mm/year [16]. To explain the observed corrosion behaviour, first the corrosion mechanism of aluminium bronze in chloride media is considered. The corrosion of aluminium bronze in chloride media can be assumed to be similar to that of Cu [153]. The corrosion process involves an anodic dissolution of Cu and the cathodic reduction of oxygen as shown in Equation 7.1 and Equation 7.2 respectively. The anodic dissolution is the rate-determining step. It is govern by the mass transport of the $2Cl^-$ and the $CuCl^{2-}$.

$$Cu +\ e^- + 2Cl^-\ \rightarrow CuCl_2^- \qquad\qquad \text{Equation 7.1}$$

$$O_2 +\ H_2O + 4e^- \rightarrow 4OH^- \qquad\qquad \text{Equation 7.2}$$
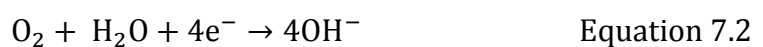
The anodic and cathodic current of the coatings are shown in Table 6.4. The results show that the 9Fe coating with a martensitic matrix has the lowest anodic current of 45.4×10^3 V/decade , this indicates that rate of the anodic reaction and thus the corrosion rate is limited. However, as the matrix phase changed to the solid solution phase, the anodic current increases significantly to 116.5×10^3 V/decade, which suggests that the change in structure may have an effect in promoting the anodic dissolution. The possible explanation for the low anodic current in the 9Fe coating is presence of protective Al_2O_3 layer on the surface, which is impermeable to the ions, thus reducing the anodic current.

Although no direct confirmation of the presence of Al_2O_3 was made in the present research, the EIS data and open circuit results provide strong evidence for the presence of Al_2O_3 in the 9Fe coating. The open circuit potential measurement shows that the 9Fe coating has the potential of approximately -0.2 V vs Ag/AgCl. Despite having significantly higher Al content, the observed value is comparable to an alloy with lower Al content such as the (Cu) and the (Cu)/β alloys, which have a reported potential of -0.22 V and -0.24 V respectively [205] As the Fe content increases, the more negative potential was observed. The 20Fe coating has the most negative potential at -0.47 V vs Ag/AgCl. This is significantly more negative than the value measured for the 9Fe coating, which suggests that in the 20Fe, 27Fe and 35Fe coating, the Al_2O_3 is incomplete or inexistent.

In addition to the limited amount of Al content in the matrix, formation of the intermetallic κ_1 phase is another possible reason for the incomplete formation of the oxide layer. García-Alonso et al. [168] showed that the κ_1 phase with low Cr content has low corrosion resistance due to the limited ability to form the protective Al_2O_3 layer. Another evidence that suggests the present of the Al_2O_3 in the 9Fe coating is the high admittance value of 2.9×10^3 S*s a/cm^2, which is an order of magnitude higher than the admittance value for the 20Fe, 27Fe and 35Fe coatings as shown in Table 6.2. The high admittance value indicates the present of Al_2O_3 that is known for its high electrical resistance. The 9Fe coating contains the highest Al content in the matrix of $\sim$ 12 wt.%. However, due to the increase in Fe content caused by melting of the steel substrate and the rapid solidification during deposition by PTA, the Al content in the matrix is reduced.

This limits the ability for the 20Fe, 27Fe and 35Fe coatings to form the protective Al_2O_3 layer resulting in the high corrosion rate observed. Without the applied current the corrosion characteristics of the coatings differ significantly from condition where a current is applied. The SEM image of the coating after one-week immersion in aerated 3.5% NaCI solution is shown in Figure 6.13.   Unlike the electro-chemical corrosion test, the immersion corrosion does not lead to selective attack on the κ_1 phase. However, SEM-EDS result in Figure 6.13 and Table 6.7 showed that the β_1' phase in the 9Fe coating and the β_1 phase in the 20Fe, 27Fe and 35Fe coating were selectively attacked. The EDS analysis of β_1' phase and the β_1 phase in Table 4.5 shows that both phases contain higher Al content than the solid solution α phase and the intermetallic κ_1 phase and therefore are expected to have much lower electrochemical potential. Consequently, these phases are oxidized by the chloride ion, which is a strong oxidizing agent.   In the 35Fe coating the localized attack on the β_1 phase is significantly deeper than in the 20Fe, 27Fe coating. Volume fraction analysis in Table 4.6 shows that the 35Fe coating mainly consists of the cathodic α phase and small volume fraction of the anodic β_1 phase. This combination leads to large driving force for corrosion provided by the (Cu) phase resulting in a high corrosion rate as shown in Figure 6.15.

7.4   Summary of and recommendation for improved adhesion and optimal microstructure for wear and corrosion resistance

Deposition of the coating by PTA promotes metallurgical bonding between the coating and the steel substrate. Increasing substrate melting during deposition promotes dendrite growth into the coating, which increases the contact area between the coating and the steel substrate resulting in higher bond strength. However, this improvement is achieved at the expense of a larger heat affected zone and grain growth in the interface region. The 9Fe coating with a β_1' martensitic matrix phase and fine intermetallic κ_1 phase has the highest wear resistance. This is due to the homogenous distribution of hard intermetallic κ_1 phase and the limited slip system of the martensitic phase that resist crack propagation. The 20Fe, 27Fe and 35Fe coatings exhibit lower wear resistance due

to the presence of the solid solution α phase, which promotes failure by planar slip. Pile-up of slip at the intermetallic phase leads to void formation. Propagation and coalescence of these voids lead to surface cracks and delamination of the surface material resulting in high wear rate. Complete formation of the protective Al_2O_3 in the 9Fe coating has been shown to improve the corrosion resistance. The Al_2O_3 forms a barrier, which limits the transport of ions thereby reducing the dissolution of the alloying elements. Although the high cooling rate of the PTA process enables the Fe to be retained in the form of an intermetallic phase, its inability to form protective oxide limits its benefit in improving the corrosion resistance. The optimal microstructural characteristic for improved wear resistance and corrosion resistance is a β_1' martensitic phase matrix and fine intermetallic κ_1 phase. Such a microstructure can be obtained by controlling of the relevant PTA parameter to minimize the increase in Fe content during deposition.

8. Conclusion

The effects of PTA deposition involve primarily an increase in Fe content of the coating caused by melting of the steel substrate. The increase in Fe combined with the enhanced solute trapping due to the rapid solidification were found to be the governing factors that control the microstructure of the PTA aluminium bronze coating. In the coating with 9 wt.% Fe, the combined results from all characterisation techniques show that it mainly consists of a Cu_3Al martensitic β_1' matrix phase and submicron size Fe_3Al intermetallic κ_1 phase. Coatings with Fe content of 20 and 27 wt.% have two phases in the matrix that consist of a solid solution (Cu) phase and an ordered β_1 phase as well as large intermetallic κ_1 phase of several microns in size. The coating with 35 wt.% Fe has the same microstructure as the 20 and 27 wt.% Fe coatings with the addition of the bcc αFe phase.

The hardness of the coatings increases with the Fe content up to a maximum value of 5.6 GPa in the coating with 27 wt.% Fe. The increase in volume fraction of the hard intermetallic κ_1 phase is the main reason for the rise in hardness. However, with further increase in Fe to 35 wt.%, the hardness decreases to 4.6 GPa, the lowest among all four coatings investigated. This is due to a reduction in solid solution strengthening caused by the decrease in Al solute in the matrix. Comparing all four coatings, the coating with 9 wt.% Fe has the most uniform hardness due to the homogeneous distribution of fine intermetallic κ_1 phase and matrix that mainly consists of the martensitic β_1' phase. The hardness of the PTA aluminium bronze coating can be predicted with high accuracy using the rules of mixture.

The interface between the coating and the steel substrate is a Fe-rich layer characterised by high hardness of approximately 7 GPa. The high hardness is due to the combined effects of precipitation hardening of the Cu precipitates and solid solution hardening. Despite the high hardness and the low solubility of Fe in Cu, observations using SEM show no cracks or voids in the interface layer.

The tribological characteristics of the coatings are controlled by the failure of the matrix phase and the property of the surface oxide layer. A relationship between the hardness and wear was observed. The coating with 9 wt.% Fe has the lowest specific wear rate with an average value of 2.38 x 10^{-4} mm^3/Nm for dry sliding against AISI 316, 420 and 440 stainless steel. This is significantly lower than the average specific wear rate of 11.57 10^{-4} mm^3/Nm for the currently used AISI D2 tool steel tested under the same condition. In the 9Fe coating with a martensitic phase matrix, the intermetallic κ_1 phase has positive effects in providing additional load carrying capacity and resisting crack propagation. However, in the coating with 20, 27 and 35 wt.% Fe, the intermetallic κ_1 phase has an adverse effect on the wear resistance. Pile-up of dislocation was observed at the intermetallic κ_1 phase, leading to formation of voids and surface cracks. Coalescence of surface cracks subsequently leads to the delamination of the coating, resulting in high wear rate. In dry sliding conditions, the friction coefficient of the coatings is strongly dependent on the transfer of the surface oxide layer from the coating to the counter material. The transfer of material prevents direct contact between the two solids resulting in a stable friction coefficient. With the exception of the coating with 35 wt.% Fe, all coatings exhibit a stable friction coefficient of ~ 0.4 regardless of the change in counter material. This is substantially lower than the friction coefficient of ~ 2 measured for the AISI D2 tool steel under the same condition.

The corrosion resistance of the coating is governed by the nature of the surface oxide. Due to the differences in Al content in the matrix, complete formation of the protective Al_2O_3 is only achieved in the coating with 9 wt.% Fe. The formation of Al_2O_3 acts as a protective layer that prevents the transport of ions. Consequently, the coating with 9 wt.% Fe has the lowest corrosion rate of 22.5 x10^{-3} mm/year. This is comparable to the more highly alloyed nickel aluminium bronze, which has a reported corrosion rate of 15 x10^{-3} mm/year. In the coating with 20, 27 and 35 wt.% Fe the lack of Al_2O_3 oxide layer leads to rapid dissolution of Cu resulting in high corrosion rate of 300-400 x10^{-3} mm/year. The increasing Fe content doesn't lead to significant improvement in the corrosion resistance of the coating.

Based on the results, it is clear that the wear and corrosion resistance of the coating increases when substrate melting is minimum. However, promoting substrate melting can increase the bond strength between the coating and the steel substrate. Therefore, a compromise solution is needed. In SMF application, wear resistance is the most important factor, therefore substrate melting should be limited by controlling the PTA parameters to ensure that the Fe content in the coating doesn't exceed 10 wt.%. This is to ensure that the resulting coating has a martensitic matrix β_1' phase and submicron size intermetallic κ_1 phase.

9. Future work

As the demand for production increases, there exists a need for continual development of environmentally friendly solutions for protection against wear. In the present research, an aluminium bronze coating with martensitic β_1' matrix and fine intermetallic κ_1 phase was shown to have high wear resistance and stable friction coefficient that is independent of the counter material hardness. However, the initial friction coefficient is relatively high. This can be a limitation in applications that constantly operate in the transient condition. A possible solution to this is to incorporate solid lubricant particles into the coating surface. Selection, characterisation and optimization of the particle size, distribution and its effects on the performance are possible research direction for further development of wear resistance coating based on aluminium bronze alloys.

The current wear test methodology is design to evaluate the steady-state wear performance of a material. From the preceding discussion, certain applications such as SMF do not reach steady state. As shown by the high-speed data obtained in the present research, the transient condition took place over a very short period and has a significantly different response to the steady state condition. Therefore the further development of new test methodology is required. This can be in the direction of the development of a new test rig that can enable interrupted testing and in-situ measurements of parameters such as the roughness and oxide film. This information can provide better understanding of the initial state of wear and enables better selection of material for non-steady state condition.

The fatigue property of the coating is also of significant importance. This is particularly true for multiphase material where the reinforcement particles (represented by intermetallic phases in the present coating system) has strong influence on the properties. However, there are limited number of investigation concerning the fatigue of multiphase material, particular those under tribological loading. As more multiphase material are being employed, further research in this area is deem critical as fatigue is one of the most commonly failure mode.

Prediction of the properties of a multiphase material is also important for the design process and failure analysis. The results in the present research shows that the hardness of the multiphase PTA aluminium bronze coatings can be predicted by using the rules of mixtures. This indicates the possibility to predict other properties such as the wear rate using similar analysis. The development of accurate models for predicting the wear of multiphase material is an important research direction, which can prove valuable for both material design and for predictive maintenance.

A significant portion of this research was dedicated to understanding the effects of manufacturing process and the inherent effects on the microstructure and properties of the resulting coating. The results and review of the literatures highlight a number of critical gaps in the fields of rapid solidification process and dissimilar metal joint. Although the works on the effects of high cooling rate on the structure formed have already started, there are limited published works on rapid solidification of multiphase material. Such understanding will also be beneficial for other emerging manufacturing processes such as in additive manufacturing, where technology such as high powered laser can result in cooling rates up to 1000 °C/s [206].

Appendix 1

Measured roughness of the as-polished PTA aluminium coatings, AISI D2 tool steel, AISI 316,420 and 440 stainless steels (all in μm)

	R_a	R_q	R_z	R_t
9Fe	0.008	0.017	0.052	0.443
20Fe	0.021	0.029	0.122	0.275
27Fe	0.011	0.015	0.070	0.165
35Fe	0.039	0.091	0.321	0.552
AISI D2	0.013	0.114	0.061	0.2892
AISI 316	0.127	0.158	0.327	1.237
AISI 420	0.128	0.166	0.510	1.491
AISI 440	0.110	0.134	0.259	0.982
AISI 52100	0.125	0.151	0.145	0.796

Measured micro hardness of PTA aluminium coatings, AISI D2 tool steel, AISI 316,420 and 440 stainless steels (all in HV, averaged from 10 indentation)

Material	Hardness (HV)
9Fe PTA aluminium bronze coating	311
20Fe PTA aluminium bronze coating	249
27Fe PTA aluminium bronze coating	292
35Fe PTA aluminium bronze coating	363
AISI D2Tool Steel	646
AISI 316 Stainless steel	316
AISI 420 Stainless steel	567
AISI 440 Stainless steel	664
AISI 52100 Bearing steel	915

Appendix 1

Chemical composition of the AISI D2 tool steel as determined by EDS analysis (all in wt.%)

Fe	Cr	Mo	V	Si	C
85.8	8.0	2.3	0.6	0.9	1.7

Chemical composition of the AISI 316 stainless steel as determined by EDS analysis (all in wt.%)

Fe	Si	Cr	Mn	Ni	Mo	C
66.0	0.7	16.6	0.9	9.9	2.5	3.3

Chemical composition of the AISI 420 stainless steel as determined by EDS analysis (all in wt.%)

Fe	Si	S	Cr	C
84.0	0.6	0.0	13.2	2.1

Chemical composition of the AISI 440 stainless steel as determined by EDS analysis (all in wt.%)

Fe	Si	Mo	Cr	C
76.0	0.5	0.5	18.1	4.8

Chemical composition of the AISI 52100 bearing steel as determined by EDS analysis (all in wt.%)

Fe	Si	Mn	Cr	C
95.2	0.3	0.4	1.6	2.5

Nominal compositions of cast aluminium bronzes and nickel aluminium bronzes as listed by the CDA (all in wt. %)

	Cu		Pb		Sn		Zn		Fe		P		Ni		Al		Mg		Mn		Si		Others	
	Min	Max	Min	Max	Min	Max	Min	Max	Min	Max	Min	Max	Min	Max	Min	Max	Min	Max	Min	Max	Min	Max	Min	Max
95200	86								2	4					8.5	9.5								
95210	86			0.05		0.1		0.5	2.4	4				1	8.5	9.5		0.05		1		0.25		
95220		Rem							2.5	4				2.5	9.5	10.5				0.5				
95300	86								0.8	1.5					9	11								
95400	83								3	5				1.5	10	11.5				0.5				
95410	83								3	5			1.5	2.5	10	11.5				0.5				
95420	83.5								3	4.3				0.5	10.5	12				0.5				
95430		Rem												0.5	10.5	12				0.5				
95500	78								3	5			3	5.5	10	11.5				3.5				
95510	78								3	5			3	5.5	10	11.5				3.5				
95520	74.5			0.02		0.25		0.3	4	5.5			4.2	6	10	11.5				1.5		0.15		0.20Co,0.05Cr
95600	88													0.25	6	8					1.8	3.2		
95700	71								2	4			1.5	3	7	8.5			11	14		0.1		
95710	71			0.05		1		0.5	2	4		0.05	1.5	3	7	8.5			11	14		0.15		
95720	73			0.03		0.1		0.1	1.5	3.5			3	6	6	8			12	15		0.1		
95800	79			0.03					3.5	4.5			4	5	8.5	9.5			0.8	1.5		0.1		
95810	79			0.09				0.5	3.5	4.5			4	5	8.5	9.5		0.05	0.8	1.5		0.1		
95820	77.5			0.02		0.2		0.2	4	5			4.5	5.8	9	10				1.5		0.1		
95900		Rem							3	5				0.5	12	13.5				1.5				

Appendix 1

Nominal compositions of wrought aluminium bronzes and nickel aluminium bronzes as listed by the CDA (all in wt. %)

	Cu		Pb		Sn		Zn		Fe		P		Ni		Al		Mn		Si		Others	
	Min	Max	Min	Max	Min	Max	Min	Max	Min	Max	Min	Max	Min	Max	Min	Max	Min	Max	Min	Max	Min	Max
60800		Rem		0.1						0.1					5	6.5					0.02As	0.35As
61000		Rem		0.02				0.2		0.5					6	8.5				0.1		
61300		Rem		0.01	0.2	0.5		0.1	2	3		0.015		0.15	6	7.5		0.2		0.1		
61400		Rem		0.01				0.2	1.5	3.5		0.015			6	8		1				
61500		Rem		0.015									1.8	2.2	7.7	8.3						
61550		Rem		0.05		0.05				0.2			1.5	2.5	5.5	6.5		1				
61800		Rem		0.02				0.02	0.5	1.5					8.5	11				0.1		
61900		Rem		0.02		0.6		0.8	3	4.5					8.5	10						
62200		Rem		0.02				0.02	3	4.2					11	12				0.1		
62300		Rem				0.6			2	4				1	8.5	10		0.5		0.25		
62400		Rem				0.2			2	4.5					10	11.5		0.3		0.25		
62500		Rem							3.5	5.5					12.5	13.5		2				
62580		Rem		0.02				0.05	3	5					12	13				0.04		
62851		Rem		0.02				0.02	3	5					13	14				0.04		
62852		Rem		0.02				0.2	3	5					14	15				0.04		
63000		Rem				0.2		0.3	2	4			4	5.5	9	11		1.5		0.25		
63010	78					0.2		0.3	2	3.5			4.5	5.5	9.7	10.9		1.5				
63020	75.5			0.03		0.25		0.3	4	5.5			4.2	6	10	11		1.5				
63200		Rem		0.02					3.5	4.3			4	4.8	8.7	9.5	1.2	2		0.1		
63280		Rem		0.02					3	5			4	5.5	8.5	9.5	0.6	3.5				
63380		Rem		0.02		0.15			2	4			1.5	3	7	8.5	11	14		0.1		
63400		Rem		0.05		0.2		0.5		0.15				0.15	2.6	3.2			0.25	0.45	0.09As	
64200		Rem		0.05		0.2		0.5		0.3				0.25	6.3	7.6		0.1	1.5	2.2	0.09As	

List of References

[1]   "Tribology: saving cost and improving safety across industries," 2016. [Online]. Available: http://www.southampton.ac.uk/engineering/research/impact/preventing_wear_and_tear.page. [Accessed: 08-Nov-2016].

[2]   A. Roescher and A. H. . Tinnemans, "A new coating for deep drawing with preservation–lubricant–primer properties," *Prog. Org. Coatings*, vol. 43, pp. 111–122, 2001.

[3]   N. Bay, A. Azushima, P. Groche, I. Ishibashi, M. Merklein, M. Morishita, T. Nakamura, S. Schmid, and M. Yoshida, "Environmentally benign tribo-systems for metal forming," *CIRP Ann. - Manuf. Technol.*, vol. 59, pp. 760–780, 2010.

[4]   C. Mitterer, F. Holler, F. Üstel, and D. Heim, "Application of hard coatings in aluminium die casting — soldering, erosion and thermal fatigue behaviour," *Surf. Coatings Technol.*, vol. 125, pp. 233–239, 2000.

[5]   S. Bayen, J. P. Obbard, and G. O. Thomas, "Chlorinated paraffins: a review of analysis and environmental occurrence," *Environ. Int.*, vol. 32, pp. 915–29, 2006.

[6]   "Anon (1999) European Union Risk Assessment Report, alkanes, C10-13, chloro (CAS No. 85535-84-8)."

[7]   K. Taube, "Carbon-based coatings for dry sheet-metal working," *Surf. Coatings Technol.*, vol. 98, pp. 976–984, 1998.

[8]   S. Kataoka, M. Murakawa, T. Aizawa, and H. Ike, "Tribology of dry deep-drawing of various metal sheets with use of ceramics tools," *Surf. Coatings Technol.*, vol. 177–178, pp. 582–590, 2004.

[9]   K. P. Rao and C. L. Xie, "A comparative study on the performance of boric acid with several conventional lubricants in metal forming processes," *Tribol. Int.*, vol. 39, pp. 663–668, 2006.

[10] K. G. Budinski and S. T. Budinski, "Interpretation of galling tests," *Wear*, vol. 332–333, pp. 1185–1192, 2015.

[11] V. Fox, A. Jones, N. . Renevier, and D. . Teer, "Hard lubricating coatings for cutting and forming tools and mechanical components," *Surf. Coatings Technol.*, vol. 125, pp. 347–353, 2000.

[12] B. Podgornik and S. Hogmark, "Surface modification to improve friction and galling properties of forming tools," *J. Mater. Process. Technol.*, vol. 174, pp. 334–341, May 2006.

[13] W. Liang, X. Xiaolei, X. Jiujun, and H. Zukun, "Microstructures and properties of PVD aluminum bronze coatings," *Thin Solid Films*, vol. 376, pp. 159–163, Nov. 2000.

[14] Z. Shi, a. Bloyce, Y. Sun, and T. Bell, "Influence of surface melting on dry rolling-sliding wear of aluminium bronze against steel," *Wear*, vol. 198, pp. 300–306,1996.

[15] P. J. Macken, *The Aluminium Bronzes Properties and Production Processes*. London, United Kingdom, Copper Development Association, 1966.

[16] H. Meigh, *Cast and Wrought aluminium bronzes properties, processes and structure*. Cambridge: IOM Comminication Ltd, 2000.

[17] D. V. Kudashov, R. Zauter, and H. R. Müller, "Spray-formed high-aluminium bronzes," *Mater. Sci. Eng. A*, vol. 477, pp. 43–49, 2008.

[18] Y. Li, "Mechanical, friction and wear behaviors of a novel high-strength wear-resisting aluminum bronze," *Wear*, vol. 197, pp. 130–136, 1996.

[19] W. S. Li, Z. P. Wang, Y. Lu, Y. H. Jin, L. H. Yuan, and F. Wang, "Mechanical and tribological properties of a novel aluminum bronze material for drawing dies," *Wear*, vol. 261, pp. 155–163, 2006.

[20] H. A. Sundquist, "Ion-plated Aluminium bronze Coating for Sheet Metal Forming Dies," *Thin Solid Films*, vol. 73, pp. 309–314, 1980.

[21] W. Li, Y. Liu, Z. Wang, C. Ma, and S.C Wang, "Effects of Ce in novel bronze and its plasma sprayed coating," *Trans. Nonferrous Met. Soc. China*, vol. 22, pp. 2139–2145, 2012.

[22] S. Alam, S. Sasaki, and H. Shimura, "Friction and wear characteristics of aluminum bronze coatings on steel substrates sprayed by a low pressure plasma technique," *Wear*, vol. 248, pp. 75–81, 2001.

[23] C. Sudha, P. Shankar, R. V. S. Rao, R. Thirumurugesan, M. Vijayalakshmi, and B. Raj, "Microchemical and microstructural studies in a PTA weld overlay of Ni–Cr–Si–B alloy on AISI 304L stainless steel," *Surf. Coatings Technol.*, vol. 202, pp. 2103–2112, 2008.

[24] V. Balasubramanian, A. K. Lakshminarayanan, R. Varahamoorthy, and S. Babu, "Application of Response Surface Methodoloy to Prediction of Dilution in Plasma Transferred Arc Hardfacing of Stainless Steel on Carbon Steel," *J. Iron Steel Res. Int.*, vol. 16, pp. 44–53, 2009.

[25] F. Fernandes, B. Lopes, a. Cavaleiro, a. Ramalho, and a. Loureiro, "Effect of arc current on microstructure and wear characteristics of a Ni-based coating deposited by PTA on gray cast iron," *Surf. Coatings Technol.*, vol. 205, pp. 4094–4106, 2011.

[26] F. Fernandes, T. Polcar, A. Loureiro, and A. Cavaleiro, "Effect of the substrate dilution on the room and high temperature tribological behaviour of Ni-based coatings deposited by PTA on grey cast iron," *Surf. Coatings Technol.*, vol. 281, pp. 11–19, 2015.

[27] A. T. Adorno and R. A. G. Silva, "Ageing behavior in the Cu–10wt.%Al and Cu–10wt.%Al–4wt.%Ag alloys," *J. Alloys Compd.*, vol. 473, pp. 139–144, Apr. 2009.

[28] D. K. Karupannasamy, J. Hol, M. B. de Rooij, T. Meinders, and D. J. Schipper, "Modelling mixed lubrication for deep drawing processes," *Wear*, vol. 294–295, pp. 296–304, 2012.

List of References

[29] M. Y. Demeri, "Deep Drawing," in *ASM Handbook Vol 14B Metal working*, ASM International, 2006.

[30] D. Hortig and D. Schmoeckel, "Analysis of local loads on the draw die profile with regard to wear using the FEM and experimental investigations," *J. Mater. Process. Technol.*, vol. 115, pp. 153–158, 2001.

[31] J. F. Archard, "Contact and rubbing of flat surfaces," *J. Appl. Phys.*, vol. 24, pp. 981–988, 1953.

[32] A. Gåård, P. Krakhmalev, and J. Bergström, "Influence of tool steel microstructure on origin of galling initiation and wear mechanisms under dry sliding against a carbon steel sheet," *Wear*, vol. 267, pp. 387–393, 2009.

[33] R. Beardmore, "Bonding/Forming/ Deep drawing and Spinning," 2013. [Online]. Available: http://www.roymech.co.uk/Useful_Tables/Manufacturing/Deep_Drawing.html. [Accessed: 29-Oct-2013].

[34] H. Kim, S. Han, Q. Yan, and T. Altan, "Evaluation of tool materials, coatings and lubricants in forming galvanized advanced high strength steels (AHSS)," *CIRP Ann. - Manuf. Technol.*, vol. 57, pp. 299–304, 2008.

[35] H. Kim, T. Altan, and Q. Yan, "Evaluation of stamping lubricants in forming advanced high strength steels (AHSS) using deep drawing and ironing tests," *J. Mater. Process. Technol.*, vol. 209, pp. 4122–4133, 2009.

[36] W. D. J. Callister, *Materials Science and Engineering an Introduction*, 7th ed. John Wiley & Sons, Inc.

[37] S. Bayen, J. P. Obbard, and G. O. Thomas, "Chlorinated paraffins: a review of analysis and environmental occurrence.," *Environ. Int.*, vol. 32, pp. 915–29, 2006.

[38] W. Li, Y. Lu, K. Yuan, and C. Yuan, "Effects of cerium on microstructure and bonding strength of Cu-14Al-4.5Fe bronze plasma sprayed coating," *J. Rare Earths*, vol. 29, pp. 363–369, 2011.

[39] H. P. Jost, "Tribology-Origin and Future," *Wear*, vol. 136, pp. 1–17, 1990.

[40] H. Kim and N. Kardes, "Friction and Lubrication," in *Sheet Metal Forming-Fundamentals*, T. Altan and A. E. Tekkaya, Eds. ASM International, 2012, pp. 89–103.

[41] J. Williams, "Wear and surface damage," in *Engineering Tribology*, Cambridge: Cambridge University Press, pp. 166–199.

[42] H. Gohar, R., Rahnejat, "Dry friction and wear," in *Fundamentals of Tribology*, London: Imperial Colleage Press, 2008, pp. 51–75.

[43] P. K. Saha and W. R. D. Wilson, "Influence of plastic strain on friction in sheet metal forming," *Wear*, vol. 172, pp. 167–173, 1994.

[44] "ASTM G40-13 Terminology relating to wear and erosion," in *ASTM Annual Book of Standards Vol .03.02*, West Conshohocken PA, 2013.

[45] E. Rabinowicz, *Friction and wear of materials*, 2nd ed. John Wiley & Sons, Inc, 1995.

[46] M. Cartier, J. M. Curtis, and T. A. Polak, *Handbook of Surface Treatments and Coatings*. London: Professional Engineering Publishing Limited, 2000.

[47] P. Karlsson, "The early stage of galling," Karlstad University, 2012.

[48] E. van der Heide and D. J. Schipper, "Galling initiation due to frictional heating," *Wear*, vol. 254, pp. 1127–1133, 2003.

[49] P. N. Suh, "The delamination theory of wear," *Wear*, vol. 25, pp. 111–124, 1973.

[50] J. Wei, A. Erdemir, and G. . Fenske, "Dry lubricant films for aluminum forming," *Tribol. Trans.*, vol. 43, pp. 535–541, 2000.

[51] A. Erdemir, "Tribological properties of boric acid and boric-acid-forming surfaces. Part I. Crystal chemistry and mechanism of self-lubrication of boric acid," *Lubr. Eng.*, vol. 47, pp. 168–173, 1991.

List of References

[52] W. Wang, X. Zheng, M. Hua, and X. Wei, "Influence of surface modification on galling resistance of DC53 tool steel against galvanized advanced high strength steel sheet," *Wear*, vol. 360–361, pp. 1–13, 2016.

[53] M. Murakawa, N. Koga, S. Watanabe, and S. Takeuchi, "Tribological behavior of amorphous hard carbon films against zinc-plated steel sheets," *Surf. Coatings Technol.*, vol. 108–109, pp. 425–430, 1998.

[54] Z. Hu, A. Schubnov, and F. Vollertsen, "Tribological behaviour of DLC-films and their application in micro deep drawing," *J. Mater. Process. Technol.*, vol. 212, pp. 647–652, 2012.

[55] T. Sato and T. Besshi, "Anti-galling evaluation in aluminum sheet forming," *J. Mater. Process. Technol.*, vol. 83, pp. 185–191, Nov. 1998.

[56] T. Sato, T. Besshi, I. Tsutsui, and T. Morimoto, "Anti-galling property of a diamond-like carbon coated tool in aluminum sheet forming," *J. Mater. Process. Technol.*, vol. 104, pp. 21–24, 2000.

[57] S. Kataoka, A. Motoi, K. Tamaoki, M. Murakawa, H. Noguchi, and J. Kihara, "Improvement in DLC Thin Film Adhesion and Its Application to Dry Deep Drawing," *Japan Soc. Technol. Plast.*, vol. 46, pp. 412–416, 2005.

[58] W. Daodon, V. Premanond, W. Wongpisarn, and P. Niranatlumpong, "Vanadium nitride and titanium nitride coatings for anti-galling behavior in ironing of aluminum alloy cups," *Wear*, vol. 342–343, pp. 279–287, 2015.

[59] F. Klocke, T. Maßmann, K. Bobzin, E. Lugscheider, and N. Bagcivan, "Carbon based tool coatings as an approach for environmentally friendly metal forming processes," *Wear*, vol. 260, pp. 287–295, 2006.

[60] P. Carlsson, "Surface Engineering in Sheet Metal Forming," Uppsala Universitet, 2005.

[61] J. Adamus, J. M. Lackner, and Major, "A study of the impact of anti-adhesive coatings on the sheet-titanium forming processes," *Arch. Civ. Mech. Eng.*, vol. 13, pp. 64–71, 2013.

[62] B. Podgornik, S. Hogmark, and O. Sandberg, "Proper coating selection for improved galling performance of forming tool steel," *Wear*, vol. 261, pp. 15–21, 2006.

[63] M. Meiler and H. Jaschke, "Lubrication of Aluminium Sheet Metal within the Automotive Industry," in *11th International conference on sheet metal*, 2005, pp. 551–558.

[64] M. Meiler, M. Pfestorf, M. Geiger, and M. Merklein, "The use of dry film lubricants in aluminum sheet metal forming," *Wear*, vol. 255, pp. 1455–1462, 2003.

[65] M. Tolazzi, M. Meiler, and M. Merklein, "Tribological investigations on Coated Steel Sheets Using Dry Film Lubricant Drylube E1," *Adv. Mater. Res.*, vol. 6–8, pp. 565–572, 2005.

[66] K. Mori, T. Murao, and Y. Harada, "Multi-Stage Cold Deep Drawing of Long Pure Titanium Cups Using Coloured Sheets for Prevention of Seizure," *CIRP Ann. - Manuf. Technol.*, vol. 52, pp. 237–240, 2003.

[67] O. Sandberg, B. J. Hogman, and A. Thuvander, "New tool concept for stamping of HSS and AHSS," in *Proceed. Int. J. Microstructure and Materials Properties*, 2008, pp. 391–100.

[68] X. Roizard, J. M. Pothier, J. Y. Hihn, and G. Monteil, "Experimental device for tribological measurement aspects in deep drawing process," *J. Mater. Process. Technol.*, vol. 209, pp. 1220–1230, 2009.

[69] E. van der Heide, M. Burlat, P. J. Bolt, and D. J. Schipper, "Wear of soft tool materials in sliding contact with zinc-coated steel sheet," *J. Mater. Process. Technol.*, vol. 141, pp. 197–201, 2003.

[70] T. Murakawa, M, Koga, N, Kumagai, "Deep-drawing of aluminium sheets without lubricant by use of dimond-like carbon coated dies," *Surf. Coatings Technol.*, vol. 77, pp. 553–558, 1995.

List of References

[71] W. Tillmann, P. Hollingsworth, I. Baumann, L. Hiegemann, C. Weddeling, A. E. Tekkaya, S. Rausch, and D. Biermann, "Thermally sprayed finestructured WC-12Co coatings finished by ball burnishing and grinding as an innovative approach to protect forming tools against wear," *Surf. Coatings Technol.*, vol. 268, pp. 134–141, 2015.

[72] S.-Y. Yoon, J.-K. Kim, and K. H. Kim, "A comparative study on tribological behavior of TiN and TiAlN coatings prepared by arc ion plating technique," *Surf. Coatings Technol.*, vol. 161, pp. 237–242, 2002.

[73] F. Clarysse, W. Lauwerens, and M. Vermeulen, "Tribological properties of PVD tool coatings in forming operations of steel sheet," *Wear*, vol. 264, pp. 400–404, 2008.

[74] Y. Iriyama and S. Yoshihara, "DLC Coating on Magnesium Alloy Sheet by Low-Temperature Plasma for Better Formability," in *Magnesium Alloys-Corrosion and Surface Treatments*, F. Czerwinski, Ed. Rijeka: InTech, 2006, pp. 305–327.

[75] J. Witulski, M. Trompeter, A. E. Tekkaya, and M. Kleiner, "High wear resistant deep drawing tools made of coated polymers," *CIRP Ann. - Manuf. Technol.*, vol. 60, pp. 311–314, 2011.

[76] A. Brosius and A. Mousavi, "Lubricant free deep drawing process by macro structured tools," *CIRP Ann. - Manuf. Technol.*, vol. 65, pp. 253–256, 2016.

[77] E. Brinksmeier, O. Riemer, and S. Twardy, "Tribological behavior of micro structured surfaces for micro forming tools," *Int. J. Mach. Tools Manuf.*, vol. 50, no. 4, pp. 425–430, 2010.

[78] V. Franzen, J. Witulski, A. Brosius, M. Trompeter, and A. E. Tekkaya, "Textured surfaces for deep drawing tools by rolling," *Int. J. Mach. Tools Manuf.*, vol. 50, pp. 969–976, 2010.

[79] ASTM, "Standard Test Method for Galling Resistance of Materials, G98," in *ASTM Standards, vol. 03.02,* .

[80] P. A. Swanson, L. K. Ives, E. P. Whitenton, and M. B. Peterson, "A study of the galling of two steels using two test methods," *Wear*, vol. 122, pp. 207–223, 1988.

[81] B. Podgornik, S. Hogmark, and J. Pezdirnik, "Comparison between different test methods for evaluation of galling properties of surface engineered tool surfaces," *Wear*, vol. 257, pp. 843–851, 2004.

[82] S. R. Hummel and B. Partlow, "Threshold galling load and frictional behavior of stainless steel couples in line contact," *Wear*, vol. 255, pp. 504–508, 2003.

[83] S. R. Hummel, "An application of frictional criteria for determining galling thresholds in line contact tests," *Tribol. Int.*, vol. 35, pp. 801–807, 2002.

[84] H. Kim, J. Sung, F. E. Goodwin, and T. Altan, "Investigation of galling in forming galvanized advanced high strength steels (AHSSs) using the twist compression test (TCT)," *J. Mater. Process. Technol.*, vol. 205, pp. 459–468, 2008.

[85] H. Holleck and V. Schier, "Multilayer PVD coatings for wear protection," *Surf. Coatings Technol.*, vol. 76–77, pp. 328–336, 1995.

[86] A. Kenneth, Holmberg and Matthews, *Coating Tribology Properties, Mechanism, Techniques and Applications in Surface Engineering*, 2nd ed. Elsevier B.V., 2009.

[87] F.-W. Bach, A. Laarmann, and T. Wenz, Eds., *Modern Surface Technology*. Weinheim: Wiley-VCH, 2004.

[88] H. A. Jehn, "PVD and ECD-competition, alternative or combination?," *Surf. Coatings Technol.*, vol. 112, pp. 210–216, 1999.

[89] P. A. Steinmann, Y. Tardy, and H. E. Hintermann, "Adhesion testing by the scratch test method: The influence of intrinsic and extrinsic parameters on the critical load," *Thin Solid Films*, vol. 154, pp. 333–349, 1987.

[90] W.-J. Wu and M.-H. Hon, "The effect of residual stress on adhesion of silicon-containing diamond-like carbon coatings," *Thin Solid Films*, vol. 345, pp. 200–207, 1999.

[91] J. Pujante, M. Vilaseca, D. Casellas, and M. D. Riera, "High temperature scratch testing of hard PVD coatings deposited on surface treated tool steel.," *Surf. Coatings Technol.*, vol. 254, pp. 352–357, 2014.

[92] L. Y. Huang, K. W. Xu, and J. Lu, "Evaluation of scratch resistance of diamond-like carbon films on Ti alloy substrate by nano-scratch technique," *Diam. Relat. Mater.*, vol. 11, pp. 1505–1510, 2002.

[93] P. Lu, X. Xiao, M. Lukitsch, A. Sachdev, and Y. K. Chou, "Interface characterizations of diamond-coated tools by scratch testing and simulations," *Surf. Coatings Technol.*, vol. 206, pp. 1860–1866, 2011.

[94] C. Pierlot, L. Pawlowski, M. Bigan, and P. Chagnon, "Design of experiments in thermal spraying: A review," *Surf. Coatings Technol.*, vol. 202, pp. 4483–4490, 2008.

[95] *ASM Handbook Volume 5: Surface Engineering*. ASM International, 1994.

[96] H. Warlimont, Rybicki, and J. R. Shadley, "An Improved Specimen Geometry for ASTM C633-79 to Estimate Bond Strengths of Thermal Spray Coatings," *J. Therm. Spray Technol.*, vol. 2, pp. 145–150, 1993.

[97] "Standard Test Method for Adhesion or Cohesion Strength of Thermal Spray Coatings," in *ASTM International*, 2008.

[98] A. Gatto, E. Bassoli, and M. Fornari, "Plasma Transferred Arc deposition of powdered high performances alloys: Process parameters optimisation as a function of alloy and geometrical configuration," *Surf. Coatings Technol.*, vol. 187, pp. 265–271, 2004.

[99] F.-W. Bach, K. Möhwald, T. Rothardt, J. Prehm, L. Engl, K. Hartz, and B. Drößler, "Particle image velocimetry in thermal spraying," *Mater. Sci. Eng. A*, vol. 383 , pp. 146–152, 2004.

[100] R. L. Deuis, J. M. Yellup, and C. Subramanian, "Metal-matrix composite coatings by PTA surfacing," *Compos. Sci. Technol.*, vol. 58, pp. 299–309, 1998.

[101] N. Avenue, "The wear properties of plasma transferred arc cladded stellite specimens," *Surf. Coatings Technol.*, vol. 71, pp. 196–200, 1995.

[102] E. Sigolo, J. Soyama, G. Zepon, C. S. Kiminami, W. J. Botta, and C. Bolfarini, "Wear resistant coatings of boron-modified stainless steels deposited by Plasma Transferred Arc," *Surf. Coatings Technol.*, vol. 302, pp. 255–264, 2016.

[103] H. J. Kim, B. H. Yoon, and C. H. Lee, "Wear performance of the Fe-based alloy coatings produced by plasma transferred arc weld-surfacing process," *Wear*, vol. 249, pp. 846–852, 2001.

[104] P. Skarvelis and G. D. Papadimitriou, "Plasma transferred arc composite coatings with self lubricating properties, based on Fe and Ti sulfides: Microstructure and tribological behavior," *Surf. Coatings Technol.*, vol. 203, pp. 1384–1394, 2009.

[105] P. Skarvelis and G. D. Papadimitriou, "Microstructural and tribological evaluation of potential self-lubricating coatings with additions produced by the plasma transferred arc technique," *Tribol. Int.*, vol. 42, pp. 1765–1770, 2009.

[106] C. Y. Su, C. P. Chou, B. C. Wu, and W. C. Lih, "Plasma transferred arc repair welding of the nickel-base superalloy IN-738LC," *J. Mater. Eng. Perform.*, vol. 6, pp. 619–627, 1997.

[107] K. Siva, N. Murugan, and R. Logesh, "Optimization of weld bead geometry in plasma transferred arc hardfaced austenitic stainless steel plates using genetic algorithm," *Int. J. Adv. Manuf. Technol.*, vol. 41, pp. 24–30, 2009.

[108] E. H. Takano, D. De Queiroz, and A. S. C. M. D'Oliveira, "Avaliação dos Parâmetros de Processamento por PTA nas Superfícies Processadas," *Soldag. e Insp.*, vol. 13, pp. 210–218, 2008.

[109] L. Bourithis and G. D. Papadimitriou, "The effect of microstructure and wear conditions on the wear resistance of steel metal matrix composites fabricated with PTA alloying technique," *Wear*, vol. 266, pp. 1155–1164, 2009.

[110] J. B. Cheng, B. S. Xu, X. B. Liang, and Y. X. Wu, "Microstructure and mechanical characteristics of iron-based coating prepared by plasma transferred arc cladding process," *Mater. Sci. Eng. A*, vol. 492, pp. 407–412, 2008.

[111] K. Gurumoorthy, M. Kamaraj, K. P. Rao, A. S. Rao, and S. Venugopal, "Microstructural aspects of plasma transferred arc surfaced Ni-based hardfacing alloy," *Mater. Sci. Eng. A*, vol. 456, pp. 11–19, 2007.

[112] Q. Y. Hou, J. S. Gao, and F. Zhou, "Microstructure and wear characteristics of cobalt-based alloy deposited by plasma transferred arc weld surfacing," *Surf. Coatings Technol.*, vol. 194, pp. 238–243, 2005.

[113] "Annual Data 2016 - Copper Supply and Consumption," 2016.

[114] "Application Datasheet Standard Designation for Wrought Copper Alloys," 2014.

[115] F. Hasan, A. Jahanafrooz, G. W. Lorimer, and N. Ridley, "The Morphology , Crystallography , and Chemistry of Phases in As-Cast Nickel-Aluminum Bronze," *Metall. Trans. A*, vol. 13A, pp. 1337–1345, 1982.

[116] M. D. Fuller, S. Swaminathan, a. P. Zhilyaev, and T. R. McNelley, "Microstructural transformations and mechanical properties of cast NiAl bronze: Effects of fusion welding and friction stir processing," *Mater. Sci. Eng. A*, vol. 463, pp. 128–137, 2007.

[117] X. . Liu, I. Ohnuma, R. Kainuma, and K. Ishida, "Phase equilibria in the Cu-rich portion of the Cu–Al binary system," *J. Alloys Compd.*, vol. 264, pp. 201–208, 1998.

[118] H. Kwarciak, J, Bojarski, Z, Morawiec, "Phase transformation in martensite of Cu-12.4% AI," *J. Mater. Sci.*, vol. 21, pp. 788–792, 1986.

[119] T. B. Massalski, A. J. Perkins, and J. Jaklovsky, "Extension of solid solubility during massive transformations," *Met. Trans.*, vol. 3, pp. 687–694, 1972.

[120] N. Nakanishi, "The Crystal Structure of B' Martensite in Cu-Al Binary Alloys," *Trans. JIM*, vol. 2, pp. 79–86, 1960.

[121] J. L. Murray, "The aluminium-copper system," *Int Met Rev*, vol. 30, pp. 211–233, 1985.

[122] P. Riani, L. Arrighi, R. Marazza, D. Mazzone, G. Zanicchi, and R. Ferro, "Ternary Rare-Earth Aluminum Systems With Copper: A Review and a Contribution to Their Assessment," *J. Phase Equilibria Diffus.*, vol. 25, pp. 22–52, 2004.

[123] N. Ponweiser, C. L. Lengauer, and K. W. Richter, "Re-investigation of phase equilibria in the system Al - Cu and structural analysis of the high-temperature phase h 1 -Al 1 À d Cu," *Intermetallics*, vol. 19, pp. 1737–1746, 2011.

[124] J. Kwarciak, "Kinetics of Phase Transformations in Cu-Al and Cu-Zn-Al Alloys," *J. Therm. Anal.*, vol. 31, pp. 1279–1287, 1986.

[125] G. Roulin and P. Duval, "Initial Stages of Ordering Obtained By Tempering of the Disordered Martensitic Phase of Cu-Al Alloys," *Scr. Mater.*, vol. 37, pp. 45–51, 1997.

[126] N. Cheetham, D., Ridley, "The Kinetics of Isothermal and Isovelocity Pearlite Growth in Cu-Al Eutectoid Alloy," *Met. Trans.*, vol. 4, pp. 2549–2556, 1973.

[127] H. Warlimont, "Die Struktur der Mantensitphase B' im System Kupfer-Aluminium," *Z. Met.*, vol. 55, pp. 382–387, 1964.

[128] A. T. Adorno, M. R. Guerreiro, and A. V. Benedetti, "Isothermal aging kinetics in the Cu–19 at.%Al alloy," *J. Alloys Compd.*, vol. 315, pp. 150–157, 2001.

[129] B. Çorlu and M. Ürgen, "Modification of copper surfaces with cathodic arc aluminum plasma," *Surf. Coatings Technol.*, vol. 205, pp. 540–544, 2010.

[130] Y. Li, R. K. Shiue, S. K. Wu, and L. M. Wu, "Infrared brazing Fe3Al intermetallics using the Cu filler metal," *Intermetallics*, vol. 18, pp. 422–428, Apr. 2010.

[131] F. Hasan, J. Iqbal, and N. Ridley, "Microstrcture of as-cast aluminium bronze containing iron," *Mater. Sci. Technol.*, vol. 1, pp. 312–315, 1985.

[132] X. F. Zhang and F. Liang, "The effect of stacking fault energy on the cavitation erosion resistance of α-phase aluminum bronzes.pdf," *Wear*, vol. 253, pp. 1105–1110, 2002.

[133] L. E. Collins and V. Mitrovic-Scepanovic, "Improved Corrosion Resistance of Rapidly Solidified Fe-AI Bronzes *," *Mater. Sci. Eng.*, vol. 99, pp. 493–496, 1988.

[134] A. Munitz, "Liquid Separation Effects in Fe-Cu alloys Solidified Under Different Cooling Rates," *Metall. Trans. B*, vol. 18B, pp. 565–575, 1987.

[135] J. He and J. Zhao, "Behavior of Fe-rich phase during rapid solidification of Cu-Fe hypoperitectic alloy," *Mater. Sci. Eng. A*, vol. 404, pp. 85–90, 2005.

[136] V. Raghavan, "Al-Cu-Fe (Aluminum-Copper-Iron)," *J. Phase Equilibria Diffus.*, vol. 31, pp. 449–452, 2010.

[137] Y. Z. Chen, F. Liu, G. C. Yang, X. Q. Xu, and Y. H. Zhou, "Rapid solidification of bulk undercooled hypoperitectic Fe–Cu alloy," *J. Alloys Compd.*, vol. 427, pp. L1–L5, 2007.

[138] A. Yutaka, "The Equilibrium Diagram of Iron-bearing Aluminium Bronze," *Nippon Kinzohu Gakkai-Si*, vol. 5, pp. 136–155, 1941.

[139] J. E. Krzanowski, "Characterization of Fe-Supersaturated Fe-AI Bronze Coatings Fabricated by Magnetron Sputter Deposition," *Mater. Charact.*, vol. 35, pp. 207–212, 1995.

[140] F. Haidara, M.-C. Record, B. Duployer, and D. Mangelinck, "Phase formation in Al–Fe thin film systems," *Intermetallics*, vol. 23, pp. 143–147, 2012.

[141] J. Roucka, I. Macasek, K. Rusin, and J. Svejcar, "Possibilities of applying aluminium bronze in the production of cast tools for sheet drawing," *Solidif. Technol. foundry casthouse*, pp. 392–397, 1983.

[142] M. Kanamori, S. Ueda, and S. Matsuo, "On the Properties of Cu-Al-Ni-Fe Alloys in Slowly-Cooled Castings," *Nippon Kinzohu Gakkai-Si*, vol. 24, pp. 265–268, 1960.

[143] S. Thapliyal and D. K. Dwivedi, "Microstructure evolution and tribological behavior of the solid lubricant based surface composite of cast Nickel Aluminum Bronze developed by friction stir processing," *J. Mater. Process. Technol.*, vol. 238, pp. 30–38, 2016.

[144] J. Chen, J. Yang, X. Zhao, Y. An, G. Hou, J. Chen, and H. Zhou, "Preparation and properties of poly-(p)-oxybenzoyl/aluminum bronze composite coating by atmosphere plasma spraying," *Surf. Coatings Technol.*, vol. 253, pp. 261–267, 2014.

[145] J. J. Pamies-Teixeira, N. Saka, and N. P. Suh, "Wear of copper-based solid solutions," *Wear*, vol. 44, pp. 65–75, 1977.

[146] P. J. Blau, "Effect of heat treatment and electron beam surface melting on the friction and wear behavior of a Cu-12wt.% Al Alloy," *Wear*, vol. 94, pp. 1–12, 1984.

[147] J. Dautzenberg, "The role of dynamic recrystallization in dry sliding wear," *Wear*, vol. 60, pp. 401–411, 1980.

[148] R. C. Bill and D. Wisander, "Recrystallization as a controlling process in the wear of some F.C.C. metals," *Wear*, vol. 41, pp. 351–363, 1977.

[149] Z. Shi, Y. Sun, A. Bloyce, and T. Bell, "Unlubricated rolling-sliding wear mechanisms of complex aluminium bronze aganist steel," *Wear*, vol. 193, pp. 235–241, 1996.

[150] J. Ferrante and D. H. Buckley, "Auger Electron Spectroscopy Study of Surface Segregation in Copper-Aluminum Alloys," National Aeronautics and Space Administration, Washington D.C., 1970.

List of References

[151] A. Schussler and H. E. Exner, "The corrosion of nickle-aluminium bronzes in seawater-I. Protective layer formation and the passivation mehcanism," *Corros. Sci.*, vol. 34, pp. 1793–1802, 1992.

[152] R. a. Poggie, J. J. Wert, and L. a. Harris, "The effects of surface oxidation and segregation on the adhesional wear behavior of aluminum—bronze alloys," *J. Adhes. Sci. Technol.*, vol. 8, pp. 11–28,1994.

[153] J. A. Wharton, R. C. Barik, G. Kear, R. J. K. Wood, K. R. Stokes, and F. C. Walsh, "The corrosion of nickel-aluminium bronze in seawater," *Corros. Sci.*, vol. 47, pp. 3336–3367, 2005.

[154] B. G. Ateya, E. A. Ashour, and S. M. Sayed, "Stress Corrosion Behavior of α-Aluminum Bronze in Saline Water," *Corrosion*, vol. 50, pp. 20–25, 1994.

[155] B. Upton, "Corrosion Resistance in Sea Water Of Medium Strength Aluminum Bronzes," *Corrosion*, vol. 19, pp. 204t–209t, 1963.

[156] Z. Wu, Y. F. Cheng, L. Liu, W. Lv, and W. Hu, "Effect of heat treatment on microstructure evolution and erosion-corrosion behaviour of a nickel-aluminium bronze alloy in chloride solution," *Corros. Sci.*, vol. 98, pp. 260–270, 2015.

[157] G. Culpan, E.A, Rose, "Microstructural characterization of cast nickel aluminium bronze," *Mater. Sci.*, vol. 13, pp. 1647–1657, 1978.

[158] A. Jahanafrooz, E. Hasan, G. W. Lorimer, and N. Ridley, "Microstructural Development in Complex Nickel-Aluminum Bronzes," *Metall. Trans. A*, vol. 14A, pp. 1951–1956, 1983.

[159] C. H. Tang, F. T. Cheng, and H. C. Man, "Laser surface alloying of a marine propeller bronze using aluminium powder: Part II: Corrosion and erosion–corrosion synergism," *Surf. Coatings Technol.*, vol. 200, pp. 2594–2601, 2006.

[160] Z. Tanabe, "Effect of metal composition and heat treatment on de-aluminification of Cu⬚Al alloys," *Corros. Sci.*, vol. 4, pp. 413–423, 1964.

[161] Z. Han and H. Zhao, "Effect of β martensite transformation on dealuminification behavior of Cu–9Al–2Mn alloy in a marine environment," *Mater. Sci. Eng. A*, vol. 345, pp. 8–13, 2003.

[162] R. Heidersbach, "Clarification of the Mechanism of the Dealloying Phenomenon," *Corrosion*, vol. 24, pp. 38–44, 1968.

[163] G. Kear, B. D. Barker, and F. C. Walsh, "Electrochemical corrosion of unalloyed copper in chloride media––a critical review," *Corros. Sci.*, vol. 46, pp. 109–135, 2004.

[164] A. M. Alfantazi, T. M. Ahmed, and D. Tromans, "Corrosion behavior of copper alloys in chloride media," *Mater. Des.*, vol. 30, pp. 2425–2430, 2009.

[165] A. V. Benedeti, P. T. A. Sumodjo, K. Nobe, P. L. Cabot, and W. G. Proud, "Electrochemical studies of copper, copper-aluminium and copper-aluminium-silver alloys: Impedance results in 0.5M NaCl," *Electrochim. Acta*, vol. 40, pp. 2657–2668, 1995.

[166] E. A. Ashour and B. G. Ateya, "Electrochemical behaviour of a copper-aluminium alloy in concentrated alkaline solutions," *Electrochim. Acta*, vol. 42, pp. 243–250, 1997.

[167] J. A. Wharton, R. C. Barik, G. Kear, R. J. K. Wood, K. R. Stokes, and F. C. Walsh, "The corrosion of nickel–aluminium bronze in seawater," *Corros. Sci.*, vol. 47, , pp. 3336–3367, 2005.

[168] M. . García-Alonso, M. . López, M. . Escudero, J. . González-Carrasco, and D. . Morris, "Corrosion behaviour of an Fe3Al-type intermetallic in a chloride containing solution," *Intermetallics*, vol. 7, pp. 185–191, 1999.

[169] V. S. Rao, "A review of the electrochemical corrosion behaviour of iron aluminides," *Electrochim. Acta*, vol. 49, pp. 4533–4542, 2004.

[170] L. I. Wen-sheng, W. Zhi-ping, and L. U. Yang, "Preparation , mechanical properties and wear behaviors of novel aluminum bronze for dies," *Trans. Nonferrous Met. Soc. China*, vol. 16, pp. 607–612, 2005.

List of References

[171] X. Liu, J. Yang, L. Yang, and X. Gao, "Effect of Ce on Inclusions and Impact Property of 2Cr13 Stainless Steel," *J. Iron Steel Res. Int.*, vol. 17, pp. 59–64, 2010.

[172] D. L. Perry, *Handbook of Inorganic Compounds*, 2nd ed. Florida: CRC Press, 2011.

[173] P. Kuisma-Kursula, "Accuracy, precision and detection limits of SEM-WDS, SEM-EDS and PIXE in the multi-elemental analysis of medieval glass," *X-Ray Spectrom.*, vol. 29, pp. 111–118,2000.

[174] A. C. Fischer-Cripps, "Nanoindentation Testing," in *Nanoindentation*, 1st ed., vol. 1, New York, NY: Springer New York, 2011, pp. 21–38.

[175] "Rules and procedures for the assesment of surface texture." ISO 4288:1996.

[176] I. Tarora, "The transformation process of beta-phase of Cu-Al system and the effect of Mn addition upon it. V on the relationship among the metastable phase," *J. Japan Inst. Met.*, vol. 13, pp. 1–4, 1949.

[177] G. Kurdjumov, V. Mireckij, and T. Stelleckaja, "Transformations in eutectoid alloys of Cu-Al. V. Structure of the matensitic phase gamma' and the mechanism of beta1-gamma' transformation," *Zhurnal Tekhnicheskoi Fiz.*, vol. 8, pp. 1959–1972, 1938.

[178] E. Popiel, M. Tuszynski, M. Zarek, and W. Rendecki, "Investigation of Fe3-x Vx Al alloys with DO3 type structure by X-ray, magnetostatic and Moessbauer effect methods," *J. Less-Common Met.*, vol. 146, pp. 127–135, 1989.

[179] K. W. Schneider, C A, Rasband, W S, Eliceiri, "NIH Image to ImageJ: 25 years of image analysis," *Nat. Methods*, vol. 9, pp. 671–675, 2012.

[180] H. S. Kim, "On the rule of mixtures for the hardness of particle reinforced composites," *Mater. Sci. Eng. A*, vol. 289, pp. 30–33, 2000.

[181] M. Cabibbo, D. Ciccarelli, and S. Spigarelli, "Nanoindentation Hardness measurement in piling up SiO2 coating," *Phys. Procedia*, vol. 40, pp. 100–112, 2013.

[182] D. D. MacDonald, "Reflections on the history of electrochemical impedance spectroscopy," *Electrochim. Acta*, vol. 51, pp. 1376–1388, 2006.

[183] M. a. Maleeva, a. a. Rybkina, a. I. Marshakov, and V. V. Elkin, "The effect of atomic hydrogen on the anodic dissolution of iron in a sulfate electrolyte studied with impedance spectroscopy," *Prot. Met.*, vol. 44, pp. 548–556, 2008.

[184] E. García-Lecina, I. García-Urrutia, J. a. Díez, J. Fornell, E. Pellicer, and J. Sort, "Codeposition of inorganic fullerene-like WS2 nanoparticles in an electrodeposited nickel matrix under the influence of ultrasonic agitation," *Electrochim. Acta*, vol. 114, pp 859-867, 2013.

[185] T. A. Mai and A. C. Spowage, "Characterisation of dissimilar joints in laser welding of steel-kovar, copper-steel and copper-aluminium," *Mater. Sci. Eng. A*, vol. 374, pp. 224–233, 2004.

[186] A. H. Wang and C. S. Xie, "Microstructural study of laser-clad Fe-Al bronze on Al-Si alloy," *J. Mater. Sci.*, vol. 36, pp. 1975–1979, 2001.

[187] V. V. Karzhavi, L. T. Plaksina, and B. A. Potekhin, "Investigation of the properties of layers of electric arc deposits of aluminium bronze on steel," *Weld. Int.*, vol. 25, pp. 37–41, 2011.

[188] S. Curiotto, R. Greco, N. H. Pryds, E. Johnson, and L. Battezzati, "The liquid metastable miscibility gap in Cu-based systems," *Fluid Phase Equilib.*, vol. 256, pp. 132–136, 2007.

[189] X. Lu, C. Cao, and B. Wei, "Microstructure evolution of undercooled iron–copper hypoperitectic alloy," *Mater. Sci. Eng. A*, vol. 313, pp. 198–206, Aug. 2001.

[190] I. Magnabosco, P. Ferro, F. Bonollo, and L. Arnberg, "An investigation of fusion zone microstructures in electron beam welding of copper-stainless steel," *Mater. Sci. Eng. A*, vol. 424, pp. 163–173, 2006.

[191] C. Turun.O, Gurler.R, Baksan.B, "Diffusion bonding of iron aluminide Fe72Al28 using a pure iron interlayer," *Intermetallics*, vol. 13, pp. 801–804, 2005.

[192] K. Zenji, N., Setsuo, "Electron Microscope study of the Crystal Structure of the Martensite in a Copper-Aluminium Alloy," *Jpn. J. Appl. Phys.*, vol. 2, pp. 478–486, 1963.

[193] S. Luo, W. Wang, L. Li, Z. Xia, and B. Wei, "Dendritic Growth Characteristics of Cu-Rich Zone within Phase Separated Fe50Cu50 Alloy," *Mater. Sci. Forum*, vol. 817, pp. 299–306, 2015.

[194] W. D. Nix and H. Gao, "Indentation size effects in crystalline materials: A law for strain gradient plasticity," *J. Mech. Phys. Solids*, vol. 46, pp. 411–425, 1998.

[195] X. Chen, Z. Han, and K. Lu, "Wear mechanism transition dominated by subsurface recrystallization structure in Cu-Al alloys," *Wear*, vol. 320, pp. 41–50, 2014.

[196] S. Jahanmir, N. P. Suh, and E. P. Abrahamson, "The delamination theory of wear and the wear of a composite surface," *Wear*, vol. 32, pp. 33–49, 1975.

[197] F. Clarysse, W. Lauwerens, and M. Vermeulen, "Tribological properties of PVD tool coatings in forming operations of steel sheet," *Wear*, vol. 264, pp. 400–404, 2008.

[198] V. Imbeni, C. Martini, E. Lanzoni, G. Poli, and I. M. Hutchings, "Tribological behaviour of multi-layered PVD nitride coatings," *Wear*, vol. 251, pp. 997–1002, 2001.

[199] J. Eriksson and M. Olsson, "Tribological testing of commercial CrN, (Ti,Al)N and CrC/C PVD coatings — Evaluation of galling and wear characteristics against different high strength steels," *Surf. Coatings Technol.*, vol. 205, pp. 4045–4051, 2011.

[200] P. Harlin, U. Bexell, and M. Olsson, "Influence of surface topography of arc-deposited TiN and sputter-deposited WC/C coatings on the initial material transfer tendency and friction characteristics under dry sliding contact conditions," *Surf. Coatings Technol.*, vol. 203, pp. 1748–1755, 2009.

[201] R. A. Poggie and J. J. Wert, "The role of oxidation in the friction and wear behavior of solid solution Cu-Al alloys in reciprocating sliding contact with sapphire and D2 tool steel," *Wear*, vol. 156, pp. 315–326, 1992.

[202] E. van der Heide, E. D. Stam, H. Giraud, G. Lovato, N. Akdut, F. Clarysse, P. Caenen, and I. Heikillä, "Wear of aluminium bronze in sliding contact with lubricated stainless steel sheet material," *Wear*, vol. 261, pp. 68–73, Jul. 2006.

[203] S. Fonlupt, B. Bayle, D. Delafosse, and J. L. Heuze, "Role of second phases in the stress corrosion cracking of a nickel-aluminium bronze in saline water," *Corros. Sci.*, vol. 47, pp. 2792–2806, 2005.

[204] R. . Chen, Q. Liang, Z, W. . Zhang, D. . Zhang, Z. . Luo, and Y. . Li, "Effect of heat treatment on microstructure and properties of hot-extruded nickel-aluminum bronze," *Trans. Nonferrous Met. Soc. China*, vol. 17, pp. 1254–1258, 2007.

[205] J. C. Rowlands, "Electrochemical Aspects of Preferential Phase Corrosion in Complex Alloys," *Corros. Sci.*, vol. 2, pp. 89–94, 1962.

[206] M. H. Farshidianfar, A. Khajepour, and A. P. Gerlich, "Effect of real-time cooling rate on microstructure in Laser Additive Manufacturing," *J. Mater. Process. Technol.*, vol. 231, pp. 468–478, 2016.